PHOTOCATALYTIC AND ELECTROCHEMICAL PROCESSES FOR GENERATION OF HYDROGEN AND DECONTAMINATION OF WATER

A THESIS

submitted by

M. SATHISH

for the award of the degree

of

DOCTOR OF PHILOSOPHY

DEPARTMENT OF CHEMISTRY
INDIAN INSTITUTE OF TECHNOLOGY MADRAS
CHENNAI – 600 036

APRIL 2006

Dedicated to my parents

&

Grandparents

THESIS CERTIFICATE

This is to certify that the thesis entitled "**PHOTOCATALYTIC AND ELECTROCHEMICAL PROCESSES FOR GENERATION OF HYDROGEN AND DECONTAMINATION OF WATER"** submitted by **M. Sathish** to the Indian Institute of Technology Madras, Chennai for the award of the degree of **Doctor of Philosophy** is a bonafide record of research work carried out by him under my supervision. The contents of this thesis, in full or in parts, have not been submitted to any other Institute or University for the award of any degree or diploma.

Chennai – 600 036

Prof. R.P. Viswanath
Research Guide

Date:

ACKNOWLEDGEMENTS

I am deeply indebted to **Prof. R.P. Viswanath,** my research guide for his incessant encouragement, thought providing discussions and unfailing guidance at every stage of the research programme. It gives me immense pleasure to have been associated with him. It is my privilege to express my gratitude to him for introducing me in to fields of catalysis. I am deeply indebted to him for his patient guidance, open discussions, constant encouragement, unbounded enthusiasm and interest and I owe him a great intellectual and inspirational debt.

I express my sincere gratitude to **Prof. B. Viswanathan** for his inspiring, invaluable guidance, constant encouragement and thought provoking discussions through out the research work. I am really grateful to him for providing opportunities to learn various fields in catalysis. I feel privileged to have been associated with him.

I sincerely thank, **Prof. S. Vancheesan** (late), **Prof. M. N. Sudheendra Rao,** the former Heads and **Prof. G. Sundararajan**, the present Head of the Department of Chemistry, IIT Madras for providing the necessary infrastructural facilities during my research.

I express my thanks to all my doctoral committee members **Prof. R. Dhamodharan, Dr. G. Ranga Rao, Prof. A. Ramesh** and **Prof. T. S. Panda** for their constant encouragement and suggestions.

I express my thanks to **Dr. C.S. Gopinath, Scientist, National Chemical Laboratory, Pune** for providing the XPS facility, his valuable suggestions and cooperation.

I am also thankful to **Prof. M.S. Subramanian, Prof. T.K. Varadarajan** and **Prof. N. Balasubramanian,** for their suggestions at various stages of research.

I gratefully acknowledge **UGC, New Delhi**, for the financial assistance.

My sincere thanks are due to all the staff members of chemistry department. I thank the **Head and staff members of CGBS, SAIF and Department of Metallurgy** IIT Madras for providing the necessary instrumentation facilities. I am thankful to **Mr. A. Narayanan, Mrs. Latha, Mr Esakimuthu, Mr. Ramkumar, Mr. P. Amulraj, K.S. Narashima Rao** and **Mrs Bhavani Kumar** for their untiring and immediate help.

Words are inadequate to express my heartful gratitude to **Mr V. Chidambaram, Mr. M. Sankaran, Mr. P. Suresh, Dr S. Deepa, Mr. V. Ramesh, Mr. G Raguraman, Miss Gayathri, Mrs A. Suvitha** and **Mrs Shyamala**, with whom I have spent many memorable occasions and who have been very helpful & supportive both in personal and academic.

I would like to place my sincere thanks to my senior lab mates, **Dr. Paul Wilson, Dr. Ganesan, Dr. Raghuveer, Dr. Subramanian, Dr. Rajesh, Dr. Aulice Scibio, Dr. Shanmugham, Dr. B. G. Mishra, Dr. Jothiramalingam** and **Dr. Jesudurai**, for their timely help, friendship and encouragement, which they have extended to me at IIT Madras.

I thank my colleagues **Mr. Magesh, Mr. Srimurugan, Mr. Navaladian, Mr. Indra Neel, Mr. Himakumar, Mr. Venkateshwara Rao, Mr. Kishore, Mr. Meiyalagan Ms. Chandravadhanam, Miss Janet, Miss. Rajeshwari, Miss. Helan and Mr. Rambabu** for their help in all aspects.

I am also thankful to **Dr. Raja, Dr. Lakshiminarashiman, Dr, Sudhakar, Dr. Karthikeayan, Dr. Dhlip, Mr. Narayanan, Mr. Vivek, Mr. Arun, Mr. Vijayasankar, Mr. Senthil Kumar, Miss Nithya, Mr. Vimalan, Mr. Danialraj Miss. Sabiah, Mr. K. Saminathan, Dr. S. Sakthivel, Dr. Siva, Mr. Bala Murugan, Mr. S. Karappanan and Mr. Durairaj,** for their help at various stage of my research.

I extremely grateful to **Dr. P. Subramani, Mrs Tamilarasi, Mr. P. Velusamy** and their family for the constant support and encouragement throughout my educational career.

My thanks are due to **Mr. Raja, Mr. Kumar, Mr. Anbu, Mr. Umapathi, Mrs. R. Tamilselvi** of M/**s. Raja Xerox** for their printing and Xeroxing throughout the programme.

Last but not least I owe everything to **my parents and relatives** for their constant support and encouragement whenever needed

M. Sathish

ABSTRACT

KEY WORDS: Photocatalysis, CdS nanoparticles, mesoporous CdS, heteroatom doped TiO_2, hydrogen production, water electrolysis, phenol decomposition, arsenic removal

Hydrogen generation and water decontamination processes are necessary owing to energy and environmental concerns. Extensive research has been carried out in these areas from early 70s by photochemical and electrochemical processes. The present work deals with the efforts made to realize these two processes and enhance the activity to meet the current requirements. Of late, the chemistry of nanoparticles is an emerging area and this has initiated interests in nanoparticle technology. CdS nanoparticles show light absorption in the visible region and widely used for hydrogen generation by photocatalysis. In our studies, CdS nanoparticles were prepared by various routes and the nanoparticles obtained were characterized. Photocatalytic activity of CdS nanoparticles has been measured for the decomposition of water. Various noble metal (Pt, Pd, Rh and Ru) loaded CdS nanoparticles have been prepared and photocatalytic activity for hydrogen production has been evaluated. Utilization of TiO_2, a promising material for water decontamination, is limited to UV region alone due to its wide band gap. In order to make the TiO_2 active in the visible region, alteration of its electronic structure have to be carried out. In the present study, anion doped TiO_2 was prepared by various routes and have been characterized. Photocatalytic activity of the doped TiO_2 samples for the decomposition of methylene blue was investigated both in UV and visible regions and compared with that of commercial TiO_2 (Degussa P25). Similarly, N, S co-doped TiO_2 has been prepared, characterized and the visible light induced photocatalytic activity was evaluated. Cluster model DFT and density of states calculations have also been carried out for

the hetero atom doped TiO_2 and results are compared with the experimental observations.

A compartmentalized electrolytic cell has been designed for hydrogen generation and environmental applications like water decontamination. The effect of various parameters like nature of the electrolyte, electrode materials and cell design on the hydrogen generation activity have been studied. Electrochemical oxidation of synthetic water containing phenol and removal of arsenic by reduction have been carried out in anodic and cathodic compartments respectively. The mechanistic aspects of phenol decomposition in different supporting electrolyte media are discussed.

TABLE OF CONTENTS

Table of Contents (Contd.,) **Page No.**

Table of Contents (Contd.,) **Page No.**

Table of Contents (Contd.,) **Page No.**

Table of Contents (Contd.,) **Page No.**

Table of Contents (Contd.,) **Page No.**

LIST OF TABLES

LIST OF FIGURES

List of Figures (Contd.,) **Page No.**

List of Figures (Contd.,) **Page No.**

List of Figures (Contd.,) **Page No.**

LIST OF SCHEMES

ABBREVATIONS

AR	-	Analytical Reagent
atm	-	atmosphere
deg	-	degrees
FID	-	Flame Ionization Detector
GC	-	Gas Chromatography
TCD	-	Thermal Conductivity Detector
Hz	-	Hertz
IR	-	Infrared Spectroscopy
ml	-	milliliter
mmol	-	millimoles
ppm	-	parts per million
MPa	-	Mega Pascal
SEM	-	Scanning electron microscopy
TG	-	Thermogravimetry
TEM	-	Transmission Electron Microscopic
UV-Vis	-	Ultraviolet-Visible
XRD	-	X-ray Diffraction
XPS	-	X-ray Photoelectron Spectroscopy
ZSM	-	Zeolite synthesized by Moil Oil Corporation
BE	-	Binding Energy
DOS	-	Density of States
ACE	-	Average Current Efficiency
COD	-	Chemical Oxygen Demand
FAS	-	Ferrous Ammonium Sulfate

NOTATIONS

eV	-	electron volt
m^2/g	-	Squre meter per gram
K	-	Kelvin
G	-	gram
Å	-	Angstrom
d	-	Interplanar spacing planar
r	-	Radius
λ	-	Wavelength
cm	-	Centimeter
nm	-	Nanometer
mA	-	milli Amps
V	-	Volts
wt	-	Weight
kJ	-	Kilo Joule
h	-	hour
θ	-	Bragg angle
ν	-	Frequency
cc	-	Cubic centimeter
%	-	Percentage
°C	-	Degree Celsius
kCal	-	Kilo Calories
μmol	-	Micro mole

CHAPTER 1

INTRODUCTION

1.1 GENERAL INTRODUCTION

Hydrogen is a well known energy carrier because of its higher energy content per unit weight, which is approximately three times more than the gasoline. Hydrogen burns completely without hazardous gas emission and it leaves no residue either, which makes hydrogen as an environmentally friendly fuel. It dissipates rapidly in the air, which avoids the explosion and it can be easily transported from one place to another even by pipelines.

Hydrogen is not only used in the energy systems, but also in electricity generation and electrical energy conversion systems. It is also used as a coolant for large generators, motors and frequency changing equipments circulating in a closed gas circuit. Even though, hydrogen is the most abundant element, it is always present in combined form in nature.

1.2 GENERATION OF HYDROGEN

Hydrogen today is mostly and primarily obtained from naphtha or carbon linked precursors like coal and natural gas. It is used as chemical feedstock, for the production of chemical intermediates and specialty chemicals. Steam reforming of methane and naphtha is the primary method of hydrogen production (Das and Veziroglu, 2001; Chen *et al.*, 2004; Haryanto *et al.*, 2005). This is a catalytic process and produces hydrogen and carbon dioxide. This technology therefore requires highly efficient catalysts for the reformation process and also good separation techniques for

separating the product gas into hydrogen and carbon-di-oxide. This is a commercially viable process at present and current demand for hydrogen is largely satisfied by this method.

Another method is the partial oxidation of fossil fuels for producing hydrogen, from feedstocks including natural gas, heavy oils, coal and solid biomass. This process also produces carbon dioxide as a by-product and needs energy input for the progress of the reaction.

1.3 HYDROGEN PRODUCTION BY WATER DECOMPOSITION

Hence, as the primary energy sources for hydrogen production are fast depleting, one should look for alternatives (in the form of renewable) energy sources to fulfill the future requirements of the energy needs. Though, hydrogen is more abundant element, it is generally stored by nature in the combined state. One such abundantly available hydrogen source is water. The production of hydrogen form water by splitting into hydrogen and oxygen requires unique energy in the form of thermal, photon or electrical. Though, there are various routes under investigation for decomposition of water for hydrogen production, essentially all of them are based on any one of the following methodologies:

1. Thermal decomposition of water
2. Electrolysis of water
3. Photocatalytic decomposition of water
4. Biological methods for decomposition of water

The reliability of any of these methods, being developed for water splitting, is an essential criterion for its adoption. In addition it should be economical in terms of

energy consumption. The thermal decomposition of water directly into hydrogen and oxygen will occur only above 4000 K. With the available thermal energy source, the required temperatures to split water is not readily available. Attempts have been made to reduce the decomposition temperature by various thermo-chemical routes (Funk and Reinstrom, 1966; Velzen and Langenkamp**,** 1977). Even then, the splitting of water by thermo-chemical methods require temperatures around 1500 K. Only limited heat sources are available like nuclear reactor, which can provide this high temperature. Therefore, this method is not readily amenable for the production of large quantities of hydrogen.

In electrolytic method, one can theoretically obtain pure hydrogen and oxygen by splitting the water molecule to its components at a theoretically reversible applied potential of 1.23 V. However in practice, the potential required for decomposition of water is around 1.7 V, due to the hydrogen and oxygen over potentials at the respective electrodes (Vogel, 1961). Various research investigations are aimed at reducing the hydrogen or oxygen over potentials by modifying the nature of the electrode or electrode surfaces. Due to this over potential, the cost of production of pure hydrogen is higher and hence this method is resorted to only where the electricity is cheap or when very pure hydrogen is a must.

Photocatalytic and photoelectrochemical splitting of water for hydrogen production is the other possible route, where one can use sustained energy source *i.e.* sunlight. Though it appears to be a convenient, low cost and suitable method for hydrogen production, the maximum efficiency attained so far for this process is only around 18 % in the laboratory scale (Licht *et al.,* 2001). This can be improved by choosing a suitable photocatalyst. Various materials like CdS, TiO_2, Fe_2O_3, ZnO, $SrTiO_3$ etc have

been investigated for this purpose (Litter, 1999; Kamat, 1993; Gurunathan, 2004; Kato and Kudo, 1998; Takahashi *et al.,* 1999; Daneshvar *et al.,* 2004; Chakrabarti and Dutta, 2004). The band gap and position of band edges with respect to the potential for the water decomposition reaction are the limiting factors that need to be addressed for success of this technology. In addition, the light absorption ability of these materials also plays an important role in the efficiency of the process so far.

The biological or biochemical methods for the production of hydrogen by splitting water have also been under investigation (Rozendal *et al*., 2006; Liu *et al.,* 2005). Micro organisms are capable of producing H_2 via either fermentation (Fumiaki *et al*., 1996; Yokoi *et al*., 1997) or photosynthesis (Lichtl *et al*., 1997; Hansel and Lindblad, 1998; Matsunaga *et al*., 2000). The former is generally preferred, because it does not rely on the availability of light sources and the transparency of the mixed liquor (Hart, 1997). Production of H_2 by fermentation has been studied with a large group of pure fermentative bacteria, such as *Clostridia* (Heyndrickx *et al.,* 1991; Fumiaki *et al*., 1993) and *Enterobacteria* (Rachman *et al.,* 1997; Kumar and Das, 2000). Since the enzymes and bacteria are sensitive to pH and temperature, it is essential to maintain the required conditions to achieve water splitting. Generally, enzyme-hydrogenase (Dabrock *et al.,* 1992), green algae-scenedesmus (Gaffron and Rubin, 1942), cyanobacteria and anabaena cylindrical (Greenbaum *et al.,* 1995; Benemann and Weare, 1974; Stal and Moezelaar, 1979) are extensively studied for the splitting of water. The oil crisis in 1973 prompted research on biological hydrogen production, including photosynthetic production, as part of the search for alternative energy technologies. Green algae are known as light-dependent, water-splitting catalysts, but the characteristics of the hydrogen production using them are not practical for exploitation. Hydrogenase is also oxygen-labile for sustainable hydrogen production:

light-dependent hydrogen production ceases within a few to several tens of minutes since photosynthetically produced oxygen inhibits or inactivates hydrogenases. A continuous gas flow system designed to maintain low oxygen concentrations within the reaction vessel, has been employed in basic studies (Greenbaum, 1988), but has not been found to be practically applicable so far.

1.4 DECONTAMINATION OF POLLUTANTS

The environment receives more and more pollutants in these days due to more population and increase of the industry waste. Basically our environment can be divided into three portions namely air, water and soil. The permissible limits of pollutants depend on the medium in which they are present and degree of hazardous nature of the individual pollutants. The remediation of pollutants in water has attracted considerable interest in recent days, because most of the pollutants are soluble in water. Water comprising over 70% of the earth's surface, is undoubtedly the most precious natural resource. When it is unfit for its intended use, it is considered as polluted. Generally the solvents, volatile organics, chlorinated volatile organics, dioxins, pesticides, chlorophenols, asbestos, heavy metals and arsenic compounds are the major contaminants in water. The main sources of pollution in surface water and ground water are industrial discharge, excess use of pesticides, fungicides, fertilizers and the domestic waste (Hoffmann *et al.*, 1995).

Treatment of wastewater has various steps like mechanical, biological, physical, and chemical processes (Hoffmann *et al.,* 1995). The particular treatment employed, depends on the nature of the pollutant. The solid wastes are removed by filtration and then the dissolved pollutants are oxidized by using advanced oxidation technology (AOT). In AOTs, free hydroxyl radicals are produced. These radicals have a high

oxidizing power than other oxidants. The remediation of pollutants can be carried out by various methods like, photocatalytic, electrocatalytic, chemical, thermal and biological decomposition (Grimm *et al.*, 1998; Chen, 2004). The current methods adopted for the decontamination of water are introducing another pollutants during the removal process especially the chemical based oxidation processes. In addition, the energy input in all this methods is high except in photocatalysis. In photocatalysis one can use sunlight as energy source and the possibility of introducing another pollutant is also ruled out. The most important advantage of solar energy is its ecological purity and it offers the possibility of accomplishing energy cycles without pollution of the environment and additional heating of the earth.

1.5 PHOTOCATALYSIS

Essentially the photocatalysed reactions have generated considerable interest after the photocatalytic splitting of water on TiO_2 electrodes was first demonstrated by Fujishima and Honda in 1972 (Fujishima and Honda, 1972). Subsequently, various kinds of photocatalysts have been employed for hydrogen production and remediation of pollutants from water. They have been classified into two groups: (a) dye and other photoactive molecules in homogeneous systems such as Ru $(bipy)_3^{2+}$ and metal porphyrin systems (b) semiconductors in heterogeneous systems (Viswanathan *et al.*, 2002). In homogeneous systems, the thermal reverse electron transfer between the redox products limits the efficiency. Studies in organized molecular assemblies, such as micelles, vesicles and microemulsions, show some promise in controlling to some extent the light induced charge separation (Kiwi *et al.*, 1982). Dispersed heterogeneous semiconductor surface provides a fixed environment that influences the chemical reactivity of a variety of adsorbates. Simultaneous oxidation and reduction

reaction occurs on the surface of the catalyst on photoexcitation. The other advantages are, easy separation of catalyst after the reaction by centrifugation, availability of large surface area, low cost and stability.

In heterogeneous photocatalytic systems, simultaneous adsorption of the reactant and absorption of the light are essential requirements for successful photocatalysis. In addition, it should be stable at the reaction conditions employed and it should be chemically inert. Among the available materials like metals, semiconductors and insulators, the semiconductors have been used because the band gap of semiconductor is optimum, band edge positions are suitable for oxidation/reduction of water and one can use sunlight as energy source to excite the electron from the valence band. The insulators do possess favorable energy levels to oxidation/reduction of water. However, the higher value of the band gap, demands high-energy photons to create the necessary excitons for promoting both the reactions. In metals, only one energy level is available because of overlaying of valence and conduction bands and they can not be used as photocatalyst. The oxidation and reduction potentials have the same value, thus not suitable for H_2/O_2 evolution from water. In addition to the favorable band gap and band positions, semiconductors are inexpensive, non-toxic, easily recoverable and capable of retaining the catalytic activity. Also, loading of metal on the semiconductor surface and coupling of two semiconductors can increase the efficiency of the semiconductor photocatalysed reaction. Even though the light absorption is essential, other parameters like band gap, surface area, crystal phase, morphology, rate of interfacial charge transfer, carrier density and stability are also essential for photocatalytic activity.

1.5.1 Semiconductor photocatalysis

Photocatalysis involves the initial absorption of photons by a semiconductor to excite electron from occupied state to unoccupied state. This results in the formation of electron-hole pair within semiconductor. Unlike metals (which have continuous electronic states, and the excess charge is squeezed on the surface) semiconductors have energy gap (band gap), which restrict the recombination of photogenerated electron-hole pair. The field is penetrated into the bulk to a few angstroms (space charge region) Fig.1.1. The thickness of the Garret space charge region is inversely proportional to the carrier concentration. As carrier concentration increases the thickness of the space charge region decreases (Bard, *et al.,* 2002). The formation of surface states (additional energy levels with in the band gap), on the surface of the semiconductor and bulk, plays an important role in photocatalysis. The formation of these states is due to termination of periodic crystal at the surface, or doping of the materials. The surface states are classified into two types; intrinsic and extrinsic. Intrinsic states are related with the semiconductor surface, extrinsic states are related with external species adsorbed on the surface or dissolved in the lattice. Intrinsic surface states are divided into two types: Tamm states (ionic states) and Shockley (covalent) states. Tamm state will not cause any band bending because they are present very near to band edges. Shockley states are mainly located near the middle of the band gap, which results in positive space charge formation on the n-type semiconductor. In order to maintain the electronic equilibrium between the surface and bulk, some electrons from bulk are transferred to surface states resulting in band bending. A certain amount of band bending is necessary to provide the driving force for the chemical reaction. The main advantage of semiconductor powders and dispersions is the large surface area exposed to the reactants (Memming, 2001).

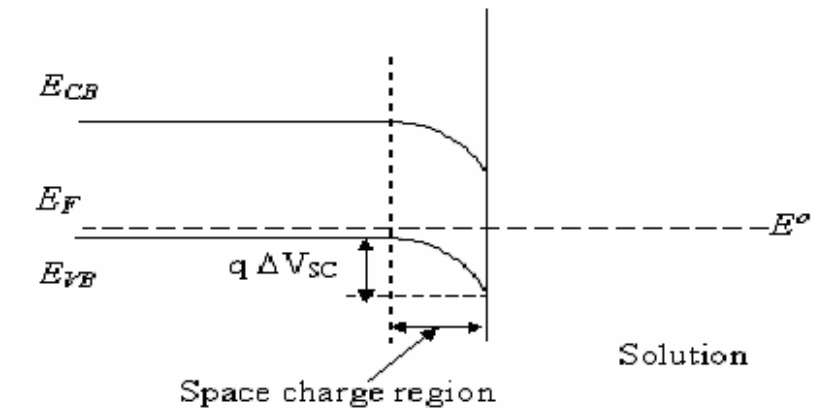

Fig 1.1. Formation of space charge region on semiconductor

When the semiconductor is doped with transition metals or any other species, it will affect not only Fermi energy level but also the thickness of the space charge region. Depending upon the redox potential of the substrate, one can tune the redox properties of the semiconductor by doping with transition metals. When the semiconductor is in contact with an electrolyte containing a redox couple, the Fermi level adjusts to equilibrate with potential of redox species. Contact between the semiconductor and electrolyte results in Schottky barrier. The electric field of this barrier induces spatial separation between electron and hole by driving the photogenerated electron and hole in opposite directions, resulting band bending at the interface. For efficient photocatalytic reaction the electron- hole pair recombination must be suppressed. Either trapping the photogenerated electron or hole or both can lead to this. When semiconductor particle is exposed to light with energy greater or equal to band gap (the energy difference between the minimum of conduction band edge and the maximum of valence band edge) it leads to the creation of electron-hole pairs. Under the influence of the electric field, this electron-hole pair moves into the surface of the conduction and valence band respectively. The electron in the conduction band moves to the surface and reduction reaction takes place either with adsorbed molecule or

surface groups. Self-recombination with the hole in the valence band depresses the activity of the semiconductor.

The reduction and oxidation strength of the photoexcited electron and hole can be measured from the energy of the lower edge of the conduction band and upper edge of the valence band. Depending on the relative positions of the top of valence band, bottom of conduction band and the redox potentials of the species, the oxidation and reduction processes are promoted (Fig. 1. 2)

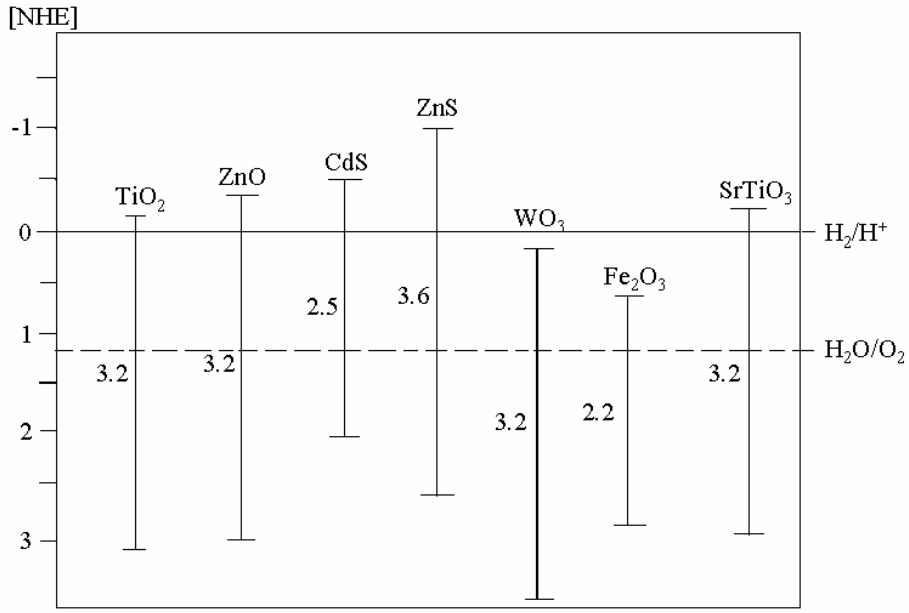

Fig 1. 2. Energy levels of various semiconductors

1.5.2 Photocatalysis by bulk phase semiconductor

In general, the selection of semiconductor for a particular reaction is based on the position of the valence and conduction band edges and redox potential of the adsorbed species of interest. To reduce the adsorbed species, the potential of the bottom of conduction band must be more negative than the adsorbed species; for oxidation reaction the top of valence band should be more positive than the adsorbed species;

Energies of various semiconductors are shown in the Fig. 1.2 with respect to normal hydrogen electrode (NHE).

Since the energy of valence and conduction levels of TiO_2 is optimum to oxidize most of the organic species, and its high oxidation ability of photogenerated holes (E = 2.9V vs NHE at pH = 0) makes it as the best choice for photocatalyst. In addition TiO_2 is inert, resistant to photocorrosion, thus making it as a good photocatalyst. Among three structural modifications of TiO_2 (brookite, rutile and anatase), anatase is the form that is more active. Eventhough there are other semiconductors to fulfill these criteria; some of them suffer from "photocorrosion" under the experimental conditions employed.

1.5.3 Charge carrier trapping

The recombination of excited electron-hole pair should be minimized for efficient charge transfer reaction between semiconductor and adsorbed species. Trapping the excited electron by surface states increases the lifetime of the excited electron; thereby one can reduce the direct recombination of electron - hole pair. Irregularity in the crystal lattice results in the bulk and surface states. In semiconductor, the nature of the states present depends on the method of preparation of the materials. The surface and bulk electron carrier trapping process is pictorially shown in Fig. 1.3. The bulk and surface states are localized. The charge carriers trapped by these states are localized to a particular site on the surface or in the bulk. The distribution of charge carriers to the bulk and surface states mainly depends on the energy difference between the lower limit of the conduction band and the position of the surface states.

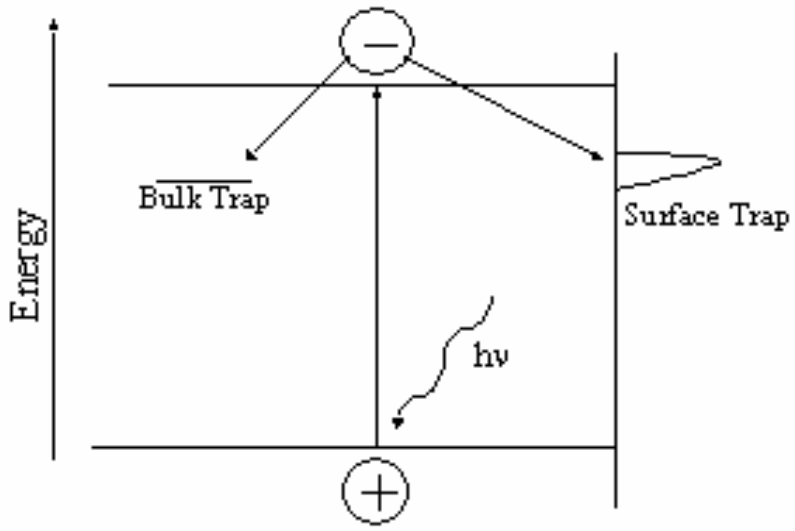

Fig.1.3. Trapping of excited electron by surface and bulk states in semiconductor (Linsebigler *et al*., 1995)

1.5.4 Band bending

When a semiconductor is placed in vacuum the bands are usually flat. When the semiconductor is allowed to contact with solution or the metal, band bending occurs. The double layer is formed at the semiconductor-solution interface and the transfer of mobile charge carrier between semiconductor and solution produce the space charge layer. In the case of n-type semiconductor, the surface was enriched by negative charge**.** In order to maintain the electrical neutrality positive space charge layer has been formed in the semiconductor, which results in band bending (Fig.1.4). The direction of band bending depends on the nature of the excess charge present on the surface of the semiconductor (Hagfeldt and Gratzel, 1995). Fig.1.5 shows the formation of depletion and accumulation layers due to the presence of excess negative and positive charges respectively on the semiconductor surface. When semiconductor surface has the same sign as the majority charge carriers, results in the formation of accumulation layer (a). If on the other hand, majority charge carriers deplete into the solution and results in the formation of depletion layer (b). The excess charge depletes into the solution until the concentration in the surface becomes below the intrinsic

level. As a result, the concentration of the holes in the space charge region becomes higher than the electrons, so the Fermi level comes closer to the valence band. The semiconductor surface acts as p-type semiconductor and the bulk acts as n-type semiconductor this is known as inversion layer (c).

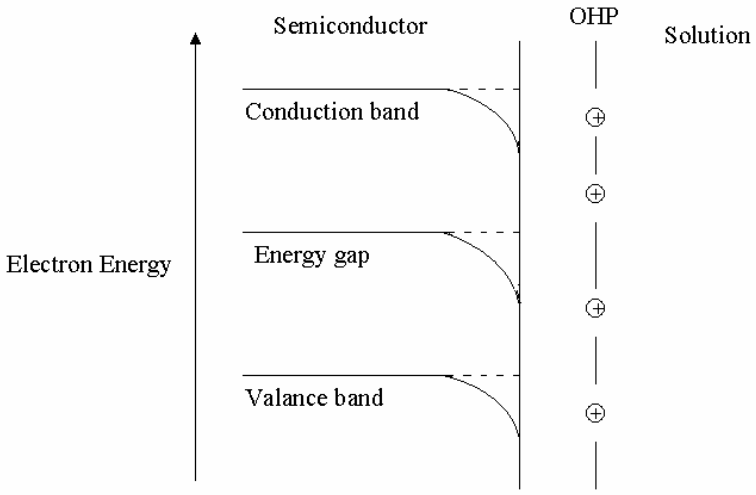

Fig. 1. 4. Band bending on semiconductor near the surface

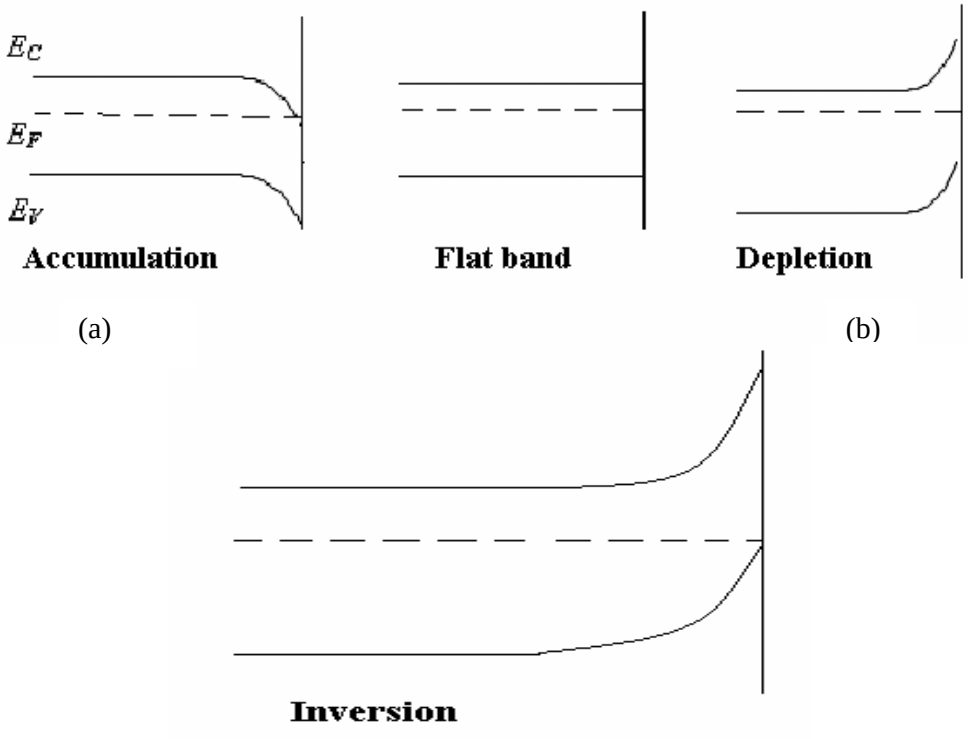

Fig. 1.5. Formation of depletion, accumulation and inversion layers on semiconductor

1.5.5 Photocatalytic reaction on TiO_2 surface.

TiO_2 exists in three different crystal structures namely brookite, anatase, and rutile. Among these, anatase and rutile are commonly used in photocatalysis, with anatase showing higher photoactivity (Augustynski, 1993). The structure of anatase and rutile contains the TiO_6 octahedra. They differ by the distortion pattern of the octahedra. The difference in the lattice structure causes variation in mass densities and electronic band structure. When TiO_2 is exposed to light energy equal to or greater than the band gap, the electrons are excited from the valence band to the conduction band. The excitation by light follows the exponential law

$$I = I_0 \exp(-\alpha l)$$

Where, l is the light penetration length and α - reciprocal absorption length. For TiO_2 α has a value of 2.6×10^4 cm^{-1} at 320 nm (Hagfeldt and Gratzel, 1995).

The relaxation of excited electron will take place in many ways. (i) The excited electron can move into the surface of the semiconductor and react with surface adsorbed molecule having appropriate potential level (equal or more positive than the conduction band) or it can react with surface adsorbed oxygen molecule. (ii) The excited electron can come back to the original state in the valence band and recombine with the hole. (iii) Bulk recombination- the excited electron can combine with hole in the bulk. Various possible relaxation pathways of excited electron in semiconductor are shown in Fig. 1. 6. (Millis and Hunte, 1997)

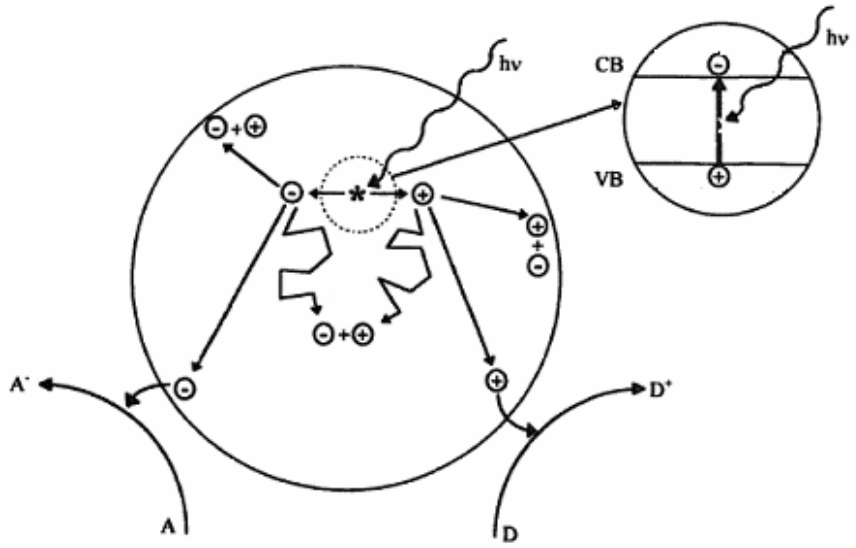

Fig. 1.6. Various possible relaxation pathways for excited electron on a photo semiconductor

The hole produced in the valence band oxidizes the water, surface adsorbed OH group or organic molecule adsorbed on the semiconductor surface. The excited electron in the conduction band reduces the dissolved oxygen to O_2^- then H_2O_2. The H_2O_2 oxidizes the organic species present on the surface of semiconductor. The reduction process takes place in the conduction band. The rate of both oxidation and reduction reactions should be equal. If the rate of reduction is slow, the excess electron will be accumulated in the conduction band, which favors the recombination of electron-hole pair. In the other case, the excess holes will be accumulated in the valence band, resulting in a similar situation. In this situation, the addition of sacrificial agents (electron donor or electron acceptor) is necessary to increase the efficiency of the process. The choice of the sacrificial agents depends on the nature of the process.

1.5.6 Metal doped semiconductors

Normally lower activity is observed when semiconductor is used alone; this is due to high recombination rate of electron – hole pair. When a semiconductor surface is

doped with an appropriate metal, the rate of recombination reduces to a greater extent and the photocatalytic activity is correspondingly enhanced (Escudero *et al.,* 1990; Courbon *et al.,* 1981; Matsumura *et al.,* 1983; Bahnemann *et al.,* 1987; Papp *et al.,* 1993). Because the rate of electron transfer from semiconductor to metal is faster than self-recombination rate. According to Frank – Condon principle the electron transfer reaction takes place faster than any other reaction and the rate depends on density of energy states on both sides of the interface. The photocatalytic activity varies with respect to parameters like nature of the metal (higher electron affinity metal), method of metal loading, extent of metal loading and nature of the semiconductor. Mainly there are two methods followed for metal loading on semiconductor namely impregnation method (Ichou *et al*., 1985) and photocatalytic deposition method (Bucher *et al.*, 1990). The amount of metal loading should be optimum for better photocatalytic activity (0.1 – 1.0 wt %). The higher loading of metal results in the formation of a very narrow space charge region, so that the penetration of light into a semiconductor greatly hindered in the space charge layer thereby increasing the recombination rate (Renault et al., 1986). Usually the metal should have high electron affinity and it should have suitable work function to form ohmic contact with the semiconductor. This can be explained on the basis of metal – semiconductor interface. Two types of contacts are possible for the metal – semiconductor interface, (i) Schottky barrier and (ii) Ohmic contact.

1.5.6.1 Schottky barrier

If a metal and a semiconductor are brought together the energy levels of both metal and semiconductor are readjusted. If the work function of metal is higher than the semiconductor, the electrons will flow from semiconductor to metal until Fermi levels

of both becomes equal. Energy levels of the semiconductor and metal before and after the contact made are shown in Fig.1.7 a & b. ϕ_m and ϕ_s are the work function of metal and semiconductor respectively. $\phi_s = \phi_e + \phi_I$. ϕ_e is the electron affinity, measured from the bottom of the conduction band , ϕ_I is the energy difference between Fermi level and conduction band (Viswanathan, 2002).

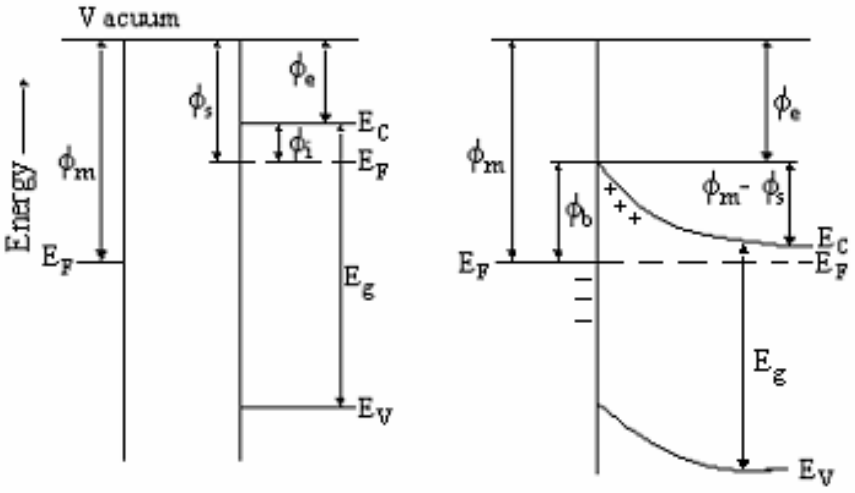

(a) **(b)**

Fig. 1.7. Formation of Schottky barrier on semiconductor – metal interface

Excess positive charge is accumulated in the semiconductor due to the electron transfer from semiconductor to metal, the distribution of this positive charge results in creation of Schottky Barrier. The barrier restricts the further flow of electrons from semiconductor to metal.

1.5.6.2 Ohmic contact

When the work function of the metal is less than that of the n- type semiconductor ($\phi_m < \phi_s$) the contact behaves in a different manner. In this case electron flow from metal to semiconductor results in accumulation of negative charge in semiconductor

and downward bending of conduction band occurs. This is shown pictorially in Fig.1. 8 a & b. The electron can then move in either direction depending on the applied potential (positive or negative). This contact is known as ohmic contact.

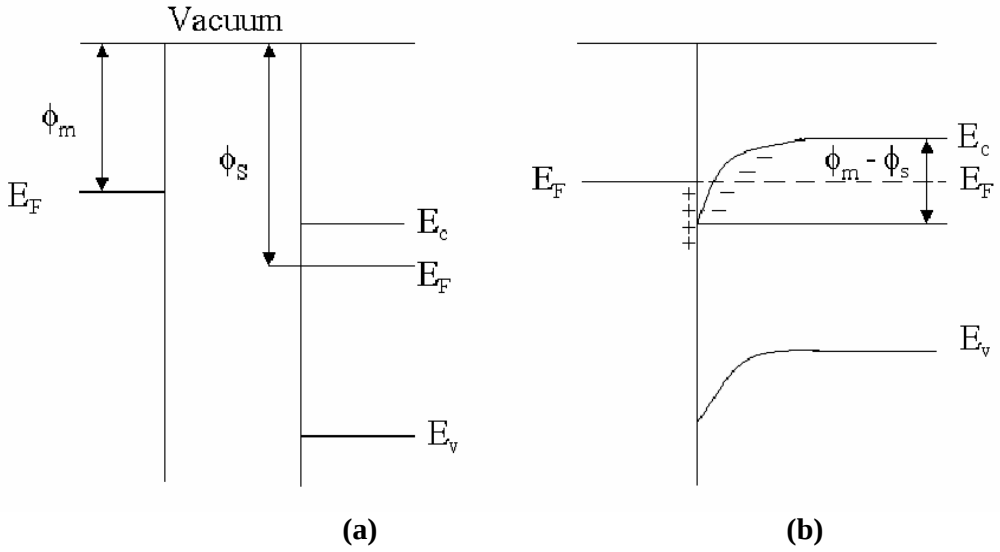

Fig.1. 8. Formation of Ohmic contact

1.5.7 Photocatalytic hydrogen production by semiconductor nanoparticles

Recently, the nanosized-particles have gained attention in various fields, particularly in catalysis, energy conversion, electronics and medicine. Though the nanoparticles are known for a long time, the synthesis, characterization tools and the properties are realized only recently. Most of the studies on the nanoparticles of semiconductor are interdisciplinary in character and are devoted to investigation of their colloidal solutions. When the particle size is comparable to Bohr radius of the excitons in semiconductor, then the optical and redox properties of the semiconductor are changed drastically (Khairutdinov, 1998). Second important observation is the increase in number of surface atoms that results in an increase of surface energy and decrease of the melting temperature of the particle (Goldstein *et al*., 1992). Also the

kinetics of the chemical reactions on the surface of the nanoparticles are different from that observed with bulk semiconductor. Arora *et al.,* (1998) demonstrated that the hydrogen production activity of CdS nanoparticles is strongly dependent on the semiconducting behavior (p- or n type), which is dependent on the stoichiometric composition.

The reduction in the particle size of semiconductors is always associated with an increase in the energy of formation of electron - hole pair and shifts the conduction and valence band towards more negative and more positive potentials respectively. The increase in the band gap favors the water splitting and oxidation of many organic compounds that have slightly more positive potential than the potential of valence band in the bulk semiconductor.

1.5.8 CdS nanoparticles

Cadmium sulfide has band-gap energy of 2.5 eV that suits very well with the solar spectrum. The conduction and valence bands position of CdS are positioned well above and below the water reduction and oxidation potential, respectively. When the particle size is reduced to nano-range, the band gap energy is increased and the position of the valence and conduction bands are also altered, in such a way that the reduction and oxidation potential of CdS nanoparticle are increased. Also, the rate of recombination of photoexcited electron-hole pair is also reduced greatly due to the large band gap and the formation of more number of surface states, which act as electron trap, thereby the recombination rate reduced.

Recently, CdS nanoparticle are under investigation for hydrogen production by water splitting, due to the visible light absorption of nano-size CdS. Various methods have been adopted in literature for the synthesis of CdS nanoparticles and the photocatlytic

activity has been evaluated (Hirai and Ota, 2006; Hirai *et al.,* 2003; Chen *et al.,* 2002; Wang *et al.,* 2003; Kida *et al.,* 2003; Liem *et al.,* 1999). From these studies, it is observed that CdS nanoparticle shows higher photocatalytic hydrogen production activity compared to the bulk CdS. The methods of preparation of CdS also have significant impact on the photocatalytic hydrogen production.

1.5.9 Photocatalytic decontamination of water

The lower energy input for the decomposition of immeasurable amount of industrial pollutants by photocatalytic methods accounts for the extensive investigations in this direction. With this view, various organic and inorganic compounds containing wastewater treatments by photocatalysis have been studied in literature (Herrmann *et al.,* 2002; Muggli and Ding, 2001; Byrne *et al.,* 1998; Vidya *et al.,* 2004; Guo *et al.,* 2002; Nagaveni *et al.,* 2004). In general, treatment of wastewater has various types like mechanical, biological, physical, and chemical processes. The particular treatment depends upon the nature of the pollutant. In the first step, the solid wastes are removed by filtration and then the dissolved organic pollutants are oxidized to CO_2 and water. In photocatalysis the free hydroxyl radicals are produced, these radicals have a high oxidizing power than other oxidants. Hence, this processes is called advanced oxidation technology (AOT). The hydroxyl radical are produced by two different ways as follows

$$OH^-(Surf) + h^+ \rightarrow OH^{\cdot}$$

$$O_2(ads) + e^- \rightarrow O_2^-(ads)$$

$$O_2^-(ads) + H_2O \rightarrow OH^- + HO_2^{\cdot}$$

$$2HO_2^{\cdot} \rightarrow H_2O_2 + O_2$$

$$H_2O_2 \rightarrow 2\,OH^{\cdot}$$

Where the e^- and h^+ are the electrons and holes produced respectively in the conduction band and valence band by excitation of semiconductor. Various oxides and sulphides like TiO_2, Fe_2O_3, ZnO, ZrO_2, WO_3, CdS, ZnS etc have been tried for this purpose as a photocatalyst (Botta *et al*., 1999; Hagfeld and Gratzel, 1995; Fox and Dualy, 1993; Millis and Hunte, 1997; Litter, 1999). Among these materials, TiO_2 has been studied extensively and exploited for the decomposition of pollutants from the wastewater.

1.5.9.1 Visible light photocatalytic activity of doped TiO_2

Though, TiO_2 is more photoactive among the studied catalytic materials, it is less active in the visible region due to its higher band gap (3.2 eV). For the same reason, the light absorption will take place at < 400 nm (UV region). Since the solar spectrum consists only 4-5 % UV light, the efficiency of the process is very poor. In order to over come this, various attempts have been made to activate the TiO_2 in the visible region. The absorption wavelength region of semiconductor is extended to visible region by dye adsorption (Regan and Gratzel, 1991; Boschloo and Hagfeldt, 2005; Alex *et al.,* 2005; Tae *et al.,* 2006). The light absorption by the dye molecule excites electrons from ground state to excited single or triplet state then the excited electron transfers to the conduction band of the semiconductor. In order to achieve the electron transfer process from excited state to conduction band the potential of conduction band should be more positive than the excited state. Some common species which are used as sensitizers include $Ru(bpy)_3^{2+}$(Cho *et al.,* 2001) porphyrin (Majunder et al., 1992)), merocyanine (Abe *et al.,* 2002) and organic compounds (He et al., 1998). The solubility of the dye in water and other solvents, and the stability of the dye on the semiconductor surface are the major disadvantages of the process. In a similar way,

insertion of transition metal ions on the titania structure can significantly enhance the photonic efficiency, either by widening the light absorption range or by modifying the redox potential of the photoproduced radicals (Hoffman *et al.*, 1995; Lin *et al.*, 1999; Anpo, 2000). The doping of metal ions on the TiO_2 lattice will produce additional energy levels between the valence band and conduction band of the semiconductor; thereby the band gap of TiO_2 has been decreased to certain extent and the light absorption will takes place in the visible region. Various metal ions like Fe, Cr, V, Ni, Ce, Cs, Cu, and La have been studied with different amounts of loading (Kang *et al.*, 2003; Wu and Chen, 2004; Zang *et al.*, 2000; Pal *et al.*, 2001; Beydoun *et al.*, 2002). Though, the doping of metal ion increases the activity significantly, none of them shows stable activity after certain time due to the instability of doped metal ion against photocorrosion. Photocorrosion is the phenomenon where the self-decomposition of catalyst occurs when the decomposition potential of the catalyst falls between its band gap. An alternative approach is establishing electronic contacts between different semiconductors *i.e.* coupling of large band gap semiconductor with lesser bad gap semiconductor (Tada *et al.*, 2000). In such case, when a suitable choice (band gap) of the materials brought into contact, the lower band gap material will excite in the visible region and the excited electron will transfer into the conduction band of other semiconductor which is having more positive potential than the former. But, in may cases, the lesser interfacial electron transfer rate of electron from one semiconductor to the other semiconductor limit the process as inactive (Keller and Garin, 2003).

Recently, doping of non-metals such as C, N, S and B on TiO_2 lattice has created considerable attention due to certain added advantages over the metal ion doping (Asahi *et al.*, 2001; Umebayashi *et al.*, 2002). The heteroatom doping in the TiO_2

results in increase in the top of the valence band, thus reducing the band gap. It is assumed that, the heteroatoms are doped as anion and occupies the oxygen positions in the TiO_2 lattice; few experiments and theoretical results also support this hypothesis. Since “p” orbital of oxygen and the heteroatoms are of same energy, certainly there will be a strong orbital overlapping, which results in the reduction of band gap.

1.6 ELECTROLYSIS

Electrolysis of water is a well known process for the water decomposition, when a potential difference between two metal electrodes is 1.23 V in acidic or alkaline medium, hydrogen and oxygen are evolved at the cathode and anode respectively, as a result of electrolysis of water. Though the theoretical potential is 1.23 V for water electrolysis, in practice the actual water decomposition will occurs only above 1.7 V (Vogel, 1961). The extra potential, which is essential for the water decomposition, is called over potential. Overvoltages are evaluated mainly as a function of current and temperature. Overvoltages are composed of activation or charge transfer overvoltage, concentration or diffusion or mass transfer overvoltage and resistance or ohmic overvoltage.

In general, an aqueous solution of caustic potash or soda is used as the electrolyte for water electrolysis. At the same concentrations, the conductivity of caustic potash is higher than that of caustic soda solution. In addition, the solubility of CO_2, which contaminates the electrolyte and decreases its conductivity, is lower in caustic potash solution than the caustic soda solution. But, at higher concentration of absorbed CO_2 results in the formation of carbonate precipitate more easily in caustic potash than the

caustic soda. So, it is necessary to change the electrolyte occasionally which forces to use the cheaper caustic soda solution as electrolyte. The nature of anode and cathode is decided based on their hydrogen and oxygen overvoltages in the electrolytic medium in addition to their stability in the particular medium. The hydrogen and oxygen overvoltages of various electrode materials in 16 % NaOH electrolyte at different current densities are given in Table 1.1. It can be seen from the table, that the iron sheets have lesser hydrogen and oxygen overvoltage. Also iron has higher resistivity towards corrosion in the alkaline medium. In industries, nickel-plated iron sheets or ferronickel alloy sheets are used as anode and cathode for water electrolysis in alkaline medium. Since most of these electrodes are not stable in acidic medium compared to alkali medium. The cathode and anode are separated by a diaphragm, which prevents the mixing of hydrogen and oxygen gases produced at the cathode and anode surfaces respectively. The diaphragm should be stable in the electrolyte and minimize the diffusion of gas molecules without the affecting the conductivity of the medium.

Table 1.1 Hydrogen and oxygen overvoltage (V) in 16 % NaOH electrolyte

Current density A/dm^2	Iron sheet plated with sulfur containing nickel		Ni-steel (5 % Ni)		Smooth Ni sheet		Co plated iron sheet	
	H_2	O_2	H_2	O_2	H_2	O_2	H_2	O_2
1	0.11	0.32	0.21	0.35	0.37	0.55	-	0.31
5	0.16	0.36	0.31	0.40	0.47	0.77	-	0.35
10	0.19	0.38	0.36	0.44	0.51	0.82	0.42	0.37
20	0.21	0.42	0.40	0.48	0.55	0.85	0.47	0.39

The electrolytic cells are commonly divided in to two types *i.e.* uni polar and bi polar. In the first case a diaphragm separates the cathode and anode and both sides of the electrode will be in the same polarity. Whereas, in the second case, an insulator separates the individual electrodes and one side of the electrode will act as cathode and other side will act as anode and each electrodes are separated by a diaphragm. So, even in the case of single common electrolytic cell, the separation of anodic and cathodic compartment is essential for getting maximum efficiency. In view of this, a compartmentalized cell can be designed. In addition to separation of anode and cathode, the compartmentalization enables one to use different electrolytes in the two chambers, namely, anode and cathode chambers, and using a suitable electrolyte in the cathodic and anodic compartments separately, the over potential of hydrogen and oxygen can be reduced to a greater extent.

1.6.1 Effect of temperature and pH on the decomposition potential

The amount of electricity required to produce one mole of hydrogen by splitting one mole of water is 2F is equal to 236.96 kJ. Whereas, heat generated by combustion of one mole of hydrogen will release 285.58 kJ at 25 ^{0}C. The extra energy of 48.63 kJ must be absorbed from the surrounding of electrolytic cell if the water is to be electrolyzed with 1.229 V at 25 ^{0}C. Applying electrical energy of 285.58 kJ, *i.e.* 1.481 V, to a water electrolyser at 25 ^{0}C would generate hydrogen and oxygen isothermally. The values 1.229 and 1.481 V are called as the reversible and thermoneutral voltage. The variation of reversible and thermoneutral voltage with temperature are shown in Fig. 1.9.

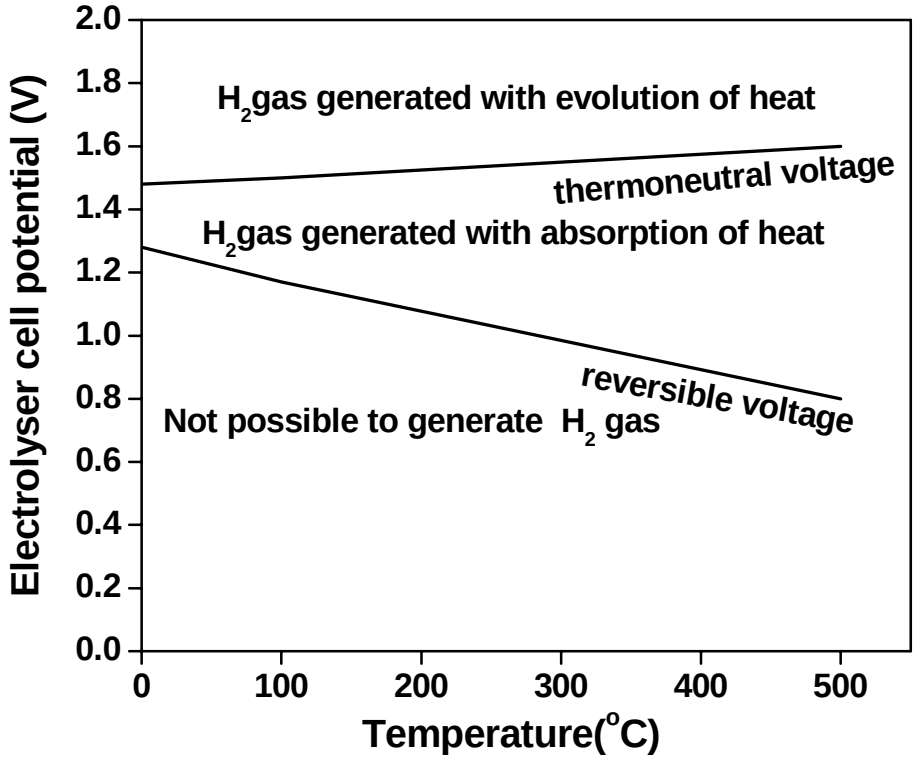

Fig. 1.9. Variation of cell potential as a function of temperature

It can be seen from the Fig.1.9, that when the temperature increases the reversible voltage decreases, whereas the themoneutral voltage slightly increases with temperature. It can also be seen from the figure that, in the region below the reversible voltage, hydrogen production is not possible. In the second region, the hydrogen is evolved with absorption of heat from the surrounding. In the third region, the hydrogen is evolved with liberation of heat, *i.e.* the extra energy as potential above the thermoneutral potential is released as heat energy. In general, the commercial industrial electrolytic cells are operating between 60-80 ^{0}C. The hydrogen and oxygen evolution reversible potentials at various pH are shown in the Fig. 1.10. It can been seen from the figure that the net potential needed for the hydrogen and oxygen evolution at any given pH between 0 to 14 is 1.229 V at 25 ^{0}C.

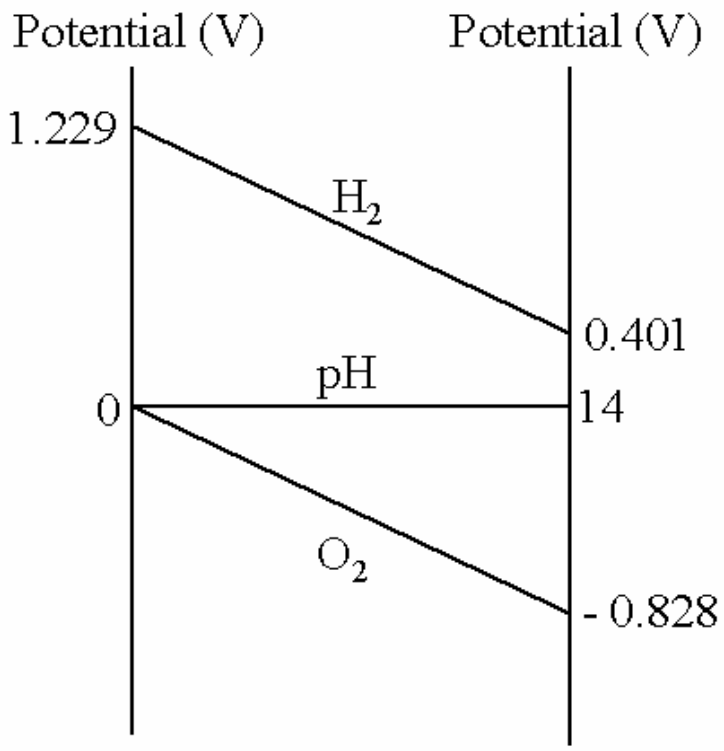

Fig. 1. 10. Hydrogen and oxygen reversible electrode potentials against pH of the electrolyte at 25 ^{0}C

Due to the corrosive action on the electrode materials, especially at the anodes, the acidic solutions are avoided for the water electrolysis.

1.7 ELECTROLYTIC DECONTAMINATION OF WATER

Electrochemical treatments of wastewater have shown several benefits in terms of costs and safety. The process runs at high electrochemical efficiency and operates essentially under the same conditions for a wide variety of wastes. Operation at room temperature and atmospheric pressure reduces the possibility of volatilization and the discharge of unreacted waste from the water. The waste treatment can be stopped within seconds by cutting off power to the electrodes. The removal of undesired components from aqueous phases is based on the choice of the appropriate electrode material, decomposition potential, concentration, nature of the medium and the

presence of other ions in the medium. It has the advantage of being applicable to a wide range of wastewater purification process. Furthermore, electrochemical oxidation offers a means of oxidizing the pollutants to H_2O and CO_2 so that the transfer of the contaminants from one phase to the other is avoided. Electrochemical combustion is therefore presented as a clean and versatile method for removal of pollutants. Generally, the route in which the electrochemical oxidation/removal processes proceeds are;

1. Indirect electrochemical oxidation of inorganic or organic contaminants
2. Direct electrochemical oxidation of the contaminants on the electrode surface
3. Cathodic removal of metal-cations (mostly heavy metals)

In the first case the nascent oxygen or radicals are produced at the anode surface. Subsequently, these will oxidize the pollutant present in the medium. In the second case, the organic or inorganic species present in the system will under go the oxidation directly on the electrode surface when the oxidation potential of the species is lower than the potential of the anode. In the third case, the metal ions present in the medium are reduced and deposited over the cathode surface; this process is efficient to remove trace amounts of the metal ions present in the medium. The reduction potential of metal ions should be more positive to attain the maximum efficiency.

Various electrode materials have been investigated to improve the efficiency of the electrochemical process. Basically, the choice of electrode material must focus on high activation energies for undesired side reactions. If side-reactions are to be reduced cathode materials should have high over-voltages for hydrogen-evolution and the anodes should preferably show high over-voltages for the evolution of oxygen (Bard and Faulkner, 1980).

Among the various chemical compounds studied, the electrochemical oxidation for destruction of phenolic wastes has been investigated under various conditions (Awad and Abuzaid, 1997; Boscoletto *et al*., 1994; Comninellis and Pulgarin, 1993; Comninellis and Nerini, 1995; Chettiar and Watkinson, 1983; Gattrell and Kirk, 1990). Commonly, it is observed that the lower reaction rate for the electrochemical oxidation of phenolic compounds, is due to electrode fouling (Dabrowski *et al*., 1975). Phenol is well known for its ability to foul electrodes and the polymerization on electrodes during oxidation. The oxidation of phenolic compounds at solid electrodes produces phenoxy radicals, which are responsible for coupling to form a passivating polymeric film on the electrodes (Gattrell and Kirk, 1993). Attempts have also been made to improve the efficiency by the addition of salts like NaCl, Na_2SO_4, which will result in the generation of power full oxidizing agents like chloride, hypochlorite or hydrogen peroxide instantly (Zareie *et al.,* 2001).

The main inorganic contaminants in wastewater are metal ions, nitrates, nitrites, nitrogen dioxide, nitric oxide, ozone, ammonia, azide and halide ions. Metal ions like Cd and As have been extensively investigated due to severe hazardous nature even in presence of small quantity in water (Zaw and Emett, 2002; Butter *et al.,* 1998; Dutra *et al.,* 2000).

1.8 OBJECTIVES AND SCOPE OF THE PRESENT INVESTIGATION

The production of hydrogen from naturally available resources like water using sunlight is an attractive proposition. Removal of pollutants from industrial wastewater is another area, which calls for research attention mainly from the points of view of economics and efficiency. This can be achieved by photocatalytic and electrolytic methods; hydrogen can be produced from water using sunlight as the

energy source in the former method and by applying an electric potential in the latter method. Both these methods can be used for the environmental remediation processes. The objectives of the present investigation include;

- Preparation of CdS nanoparticles using zeolite as template and mesoporous CdS nanoparticles by ultrasonic mediated precipitation method.

- Photocatalytic production of hydrogen by CdS nanoparticles and various metal (Pt, Pd, Rh and Ru) loaded CdS nanoparticles using Na_2S and Na_2SO_3 mixture as sacrificial agent

- Preparation of N doped TiO_2 by different routes and N, S co-doped TiO_2 by complex decomposition method.

- Physico-chemical characterization of the prepared materials by XRD, UV-Visible, SEM, TEM, XPS and sorptometric techniques.

- Comparative study of visible light photocatalytic decomposition of methylene blue by anion (N and N&S) doped TiO_2 nanoparticles prepared from various routes.

- Design a compartmentalized electrolytic cell for generation of hydrogen and oxygen to minimize the overpotentials.

- Electrolytic removal of phenol and arsenic from water using a compartmentalized electrolytic cell.

CHAPTER 2

EXPERIMENTAL METHODOLOGY

2.1 CHEMICALS USED

The chemicals used and the sources from which they were obtained are as follows.

Titanium isopropoxide, titanium trichloride and nitrate/chloride/sulphide/sulphate of sodium, cadmium, magnesium (Ar grade) were obtained from Merck India Ltd or Fluka Chemie, Germany. Commercial TiO_2 (P25) was obtained from Degussa, Germany. All the noble metal chlorides were obtained from Arora Matthey Ltd., India.

All other Chemicals used in the investigation were of analytical reagent (AR) grade and were obtained from Qualigens, India or S.D. Fine Chemicals, India. These chemicals were used as such without further purification.

2.2 PREPARATION OF THE CATALYST

2.2.1 Preparation of CdS nanoparticles using zeolite as template

Cadmium sulphide nanoparticles were prepared by precipitation in the zeolite matrix. Three different zeolites (H-Y, HZSM-5 and H-β) with different pore sizes were used for this purpose. In a typical preparation procedure, 1 g of sodium form of the zeolite was taken in a round bottom flask and 100 ml of 1 M $CdNO_3$ solution was added to it. The mixture was stirred for 24 h at room temperature. The zeolite was filtered and washed with distilled water until the filtrate is free from Cd^{2+} ions. The sample was dried and stirred with 100 ml of 1 M Na_2S solution for 12 h and this results in the precipitation of the cadmium ions present inside the zeolite matrix. The precipitated

CdS particles were washed with distilled water until the filtrate is free from the S^{2-} ions. Finally, the zeolite matrix was removed by treatment with 48 % HF solution. The undissolved CdS particles were washed with hot water until the pH of the filtrate becomes neutral. The obtained CdS particles are dried in an air-oven and then calcined at 400°C for 4 h in air. The CdS particles prepared from H-Y, HZSM-5 and H-β are named as CdS-Y, CdS-Z and CdS-B respectively in subsequent discussions.

2.2.2 Preparation of mesoporous CdS nanoparticles

In a typical synthesis, 250 ml of 5 mM Na_2S solution was taken in a 1000 ml glass beaker and kept in an ultrasonicator water bath. Then, 250 ml of 1 mM $Cd(NO_3)_2$ was added into the Na_2S solution using peristaltic pump (Miclins) at the rate of 20 ml/h. The resulting precipitate was filtered and washed with double distilled water until the solution is free from S^{2-} ions. For the sake of comparison, bulk CdS was prepared by conventional precipitation method. In this method, equimolar amount of Na_2S solution was added dropwise to a stirred solution of 1 M $Cd(NO_3)_2$ and this results in the formation of CdS precipitates. The CdS precipitate was washed repeatedly with distilled water until it is free from S^{2-} ions, dried in an air-oven and then calcined at 400°C for 4 h in air. The CdS particles prepared by ultrasonic method and conventional precipitation method are designated as CdS-U and bulk CdS respectively in subsequent discussion.

2.2.3. Preparation of metal loaded CdS catalysts

Generally, 1 wt % of Pt, Pd, Ru and Rh metal loaded CdS was prepared by wet impregnation of corresponding metal chloride solution with CdS particles followed by evaporation to dryness and reduction in hydrogen atmosphere at 723 K.

2.2.4. Preparation of N doped and N, S co-doped TiO_2

2.2.4.1 Preparation of N doped TiO_2 from $TiCl_3$

In a typical synthesis of the N-doped TiO_2, 50 ml of 15% $TiCl_3$ (48.6 mmol) was mixed with 50 ml of Na_2S solution (51.2 mmol). The pH of this acidic solution was adjusted to 8.5 by slow addition of dil. NH_3 solution. The precipitate formed at this pH was continuously stirred for ~ 4 h. The precipitate was filtered and washed with double distilled water until the filtrate was free from chloride and sulfide ions. The sample was calcined in air for 4 h at different temperatures. Pure TiO_2 was also prepared by a similar procedure without the addition of Na_2S solution.

2.2.4.2 Preparation of N doped TiO_2 from thermal decomposition of Ti-salen complex

The Ti- salen complex was prepared by mixing the titanium isopropoxide with salen ligand. Ti–isopropoxide in dichloromethane (DCM) (1:1 molar ratio) was added dropwise into salen in DCM. The mixture was stirred for 6 hours at room temperature and then the solvent was removed by evaporation at reduced pressure. The ligand salen was prepared by mixing equimolar amount of ethylene diamine and salicylaldehyde in ethanol medium. The resulting yellow solid was filtered, washed and dried under vacuum. The metal complex (Scheme 2.1) was calcined in a vacuum sealed glass tube at 400 °C. The sample was heated slowly from room temperature to 400 ^oC and maintained at this temperature for 12h. Then it was allowed to cool to room temperature. Then the sealed tube was broken carefully and the material collected was further calcined in air at 400 ^oC temperature for ~ 12 h.

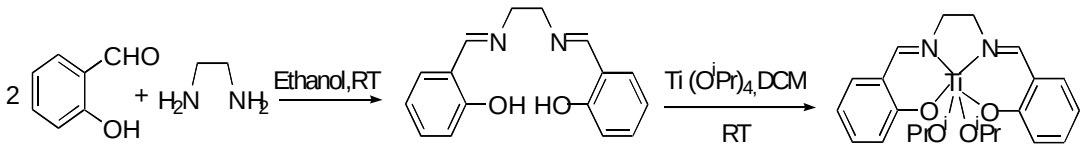

Scheme 2.1. Preparation of Ti-salen metal complex

2.2.4.3 Preparation of N doped TiO_2 from thermal decomposition of Ti- melamine complex

The Ti- melamine complex was prepared by mixing, melamine dissolved in hot water ethanol mixture (1:3 volume) into Ti $(ipro)_4$ in ethanol solution in 3:1 molar ratio of Ti $(ipro)_4$ and melamine. The resulting solution was stirred for 24 h and allowed to age for 5 days. The gel obtained after five days was dried in hot air oven, calcined at various temperatures in air and finally washed with hot water.

2.2.4.4 Preparation of N, S co-doped TiO_2 from thermal decomposition of Ti-benzothiazoline and Ti-aminothiol complexes

The Ti^{4+}- 2(O-hydroxyphenyl) benzothiazoline (TB) complex was prepared (Kanmani, 1998) by dropwise addition of 1:2 molar ratio of titanium isopropoxide in dichloromethane with 2(O-hydroxyphenyl) benzothiazoline in dichloromethane. The mixture was stirred for an hour. The color changes from yellow to red indicating the formation of Ti^{4+}- 2(O-hydroxyphenyl) benzothiazoline complex, and the solvent was removed under reduced pressure. The ligand 2(O-hydroxyphenyl)benzothiazoline was prepared by mixing equimolar amount of 2-amino thiophenol and salicylaldehyde in the ethanol at room temperature. The TB complex obtained (Scheme 2.2a) was ground to fine powder in an agate mortar and calcined in vacuum sealed glass tube at 400 °C for 12 h. Then it was allowed to cool to room temperature, the sealed tube was broken carefully and the content was collected. The collected material was further

calcined in N_2 atmosphere for 6 h and air at various temperatures for 12 h. The prepared samples were named as TB (n), where n denotes the calcination temperature in air. The Ti-aminothiol complex (TS) was prepared by addition of calculated amount of Ti isoproxide and aminothiol in DCM at room temperature. The resulting complexes (Scheme 2.2b) were decomposed at 400 °C in N_2 atmosphere for ~ 12 h and air at various temperatures for ~ 12 h. The prepared samples were named as TS (n) respectively, where n denotes temperature of calcination in air.

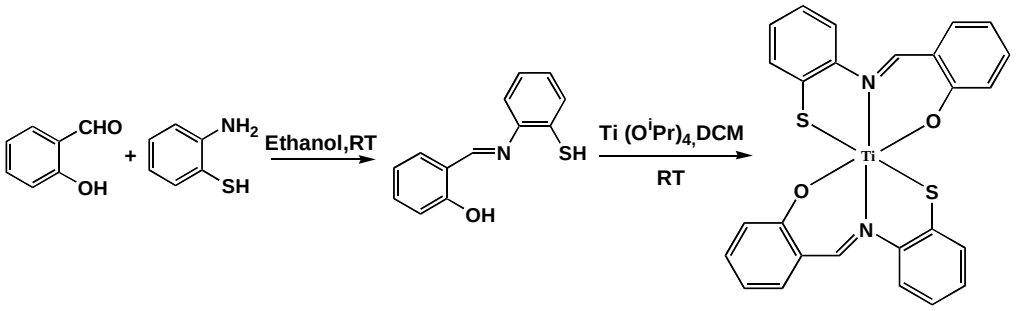

(a) **TB**

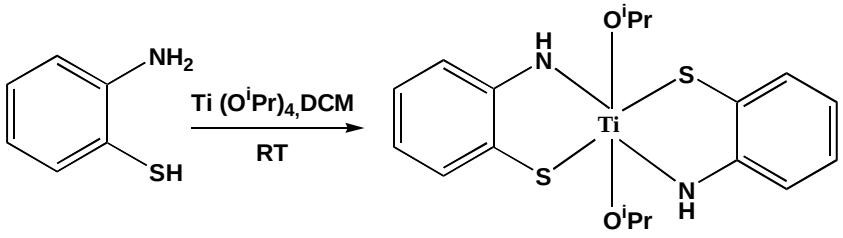

(b) **TS**

Scheme 2.2. Preparation of (a) TB and (b) TS complex

2.3 CHARACTERIZATION

2.3.1 UV-Visible absorption studies

UV-Visible absorption spectra were recorded using a CARY 5E UV-Vis-NIR spectrophotometer in the spectral range of 200-800 nm. The absorption spectra for catalyst samples were recorded as nujol paste.

2.3.2 Powder X-ray diffraction (XRD)

X-ray diffraction patterns of the various samples were recorded using SHIMADZU XD-D1 diffractometer using Ni-filtered Cu K_α radiation (λ =1.5418 Å) in the range of 10 - 80 degrees at a scan rate of 2 degrees per minute using Bragg-Brantan configuration.

2.3.2.1 Particle size determination by X-ray line broadening

The particle size of the materials are calculated by X-ray line broadening technique employing Debye-Scherrer equation (Cullity, 1987)

$$t = \frac{0.89\ \lambda}{\beta \cos \theta_B}$$

Where

t = thickness of particle

λ = wavelength of the radiation used

β = integral breadth of peak (full width at half maximum)

θ_B = Bragg diffraction angle

For these measurements, the X-ray diffraction patterns were recorded at same scan speed (2 degrees per minute), and the reflections corresponding to three highest

intense peaks were taken for the measurements and the average particle size calculated.

2.3.3 Surface area measurements

Surface area and pore volume of the catalyst were measured using CE Instruments model Sorptomatic 1990. The samples were outgassed at 423 K and 10^{-3} torr vacuum for 6 - 10 h depending on the nature of the sample. For adsorption experiments, ultrahigh pure nitrogen is used at liquid nitrogen temperature. BET method was used to evaluate the surface area and pore volume evaluated at the p/p_0 of 0.999.

2.3.4 Transmission electron microscopic studies (TEM)

Transmission electron micrographs were recorded with a JEOL-JEM 100SX microscope, working at a 100 kV accelerating voltage. Samples for TEM were prepared by dispersing the powdered sample in acetone by sonication and then drop drying on a copper grid (400 mesh) coated with carbon film.

2.3.5 Scanning electron microscopic studies (SEM)

Scanning electron micrographs were taken using JEOL, JSM5610LV microscope (acceleration voltage 15 kV). The sample powders were deposited on a carbon tape before mounting on a sample holder. In order to improve the conductivity of the sample, gold sputtering was done for 3 min on all the samples.

2.3.6 X-ray photoelectron spectroscopy (XPS)

Chemical nature of N and S in TiO_2 has been studied using X-ray photoelectron spectroscopy in a VG Microtech Multilab ESCA 3000 spectrometer with a non-monochromatized Al Kα X-ray ($h\nu$ = 1486.6 eV). The catalyst pellet surface was

scraped *in situ* to remove any surface contamination that could arise from atmospheric components like water, CO_2 etc. The energy resolution of the spectrometer was set at 1.1 eV at a pass energy of 50 eV. The binding energy (BE) was calibrated with respect to Au $4f_{7/2}$ core level at 83.9 eV.

2.3.7 Thermogravimetric analysis (TGA)

Thermogravimetric analyses of catalyst precursor, metal complexes were performed to assign the calcination temperatures. TGA analyses were preformed for the calcined catalyst also, to confirm complete decomposition of precursor materials. The analyses were done using Perkin Elmer TGA (Delta series TGA7) instrument with a heating rate of 20 °C min^{-1} under air atmosphere.

2.3.8 Infrared (IR) absorption studies

FT-IR absorption spectra of the samples were recorded using a Bruker FT-IR spectrometer (Model IFS 66v) at room temperature in the range 4000-400 cm^{-1}. The powdered samples were ground with KBr and pressed into pellets (5 ton/cm^2) for recording the spectra.

2.4 PHOTOCATALYTIC ACTIVITY

2.4.1 Photocatalytic production of hydrogen

Photocatalytic hydrogen evolution experiments were performed using a quartz reactor with options for water circulation at the outer wall of the reactor and specific outlet for gas collection. For a typical photocatalytic experiment, 0.1 g of catalyst was added to a 50 ml of aqueous solution containing 0.35 M Na_2SO_3 and 0.24 M Na_2S and placed inside the reactor. Before illumination by a UV source, the solution was purged with nitrogen gas for 30 minutes to remove the dissolved oxygen. Then the mixture

was irradiated with photons from 400 W Hg lamp (ORIEL Corporation, USA). The evolved gas was collected over brine solution using an inverted gas burette.

2.4.2 Photocatalytic decomposition of methylene blue at fixed wavelengths

Photocatalytic decomposition of methylene blue was performed using a quartz reactor with water circulation facility at the outer wall of the reactor and with the specific outlet for the sample collection. For a typical photocatalytic experiment, 25 mg of catalyst was added to 25 ml of aqueous solution containing ~110 ppm methylene blue solution and the solution was irradiated using 400 W Hg lamp (ORIEL Corporation, USA). The experiments were carried out separately, at four different wavelengths namely 365, 405, 436 and 546 nm using the monochromatic filters (Oriel) for 30 min duration. After recovering the catalyst by centrifuging, the light absorption of the clear solution was measured at 662 nm (λ_{max} for MB). The photocatalytic activity was compared with those using Degussa (P25) and pure TiO_2 (anatase) prepared in the laboratory.

2.4.3 Visible light photocatalytic decomposition of methylene blue

Photocatalytic methylene blue decomposition experiments were performed using a quartz reactor as described in previous section. For a typical photocatalytic experiment, 0.1 g catalyst is taken with 50 ml of ~ 50ppm methylene blue solution. The experiments were carried out for 3 h duration with visible light (> 420 nm) using 400 W Hg lamp as light source and HOYA L-42 UV cut off filter (< 420 nm). The concentration of methylene blue was monitored every 30 minutes time interval.

2.5 GAS CHROMATOGRAPHIC (GC) ANALYSIS

The gas products were analysed using chromatograph (Nucon- Model 5765) with molecular sieve 5A as column and thermal conductivity detector (TCD). For the detection of hydrogen, nitrogen was used as the carrier gas and for that of oxygen/moisture, the carrier gas was hydrogen.

The intermediate formation during the electrolysis was analyzed by GC (Nucon-5765) equipped with flame ionizing detector (FID) using SE-30 column. This intermediate species was extracted after 5 hours of electrolysis with diethylether solvent from the electrolyte solution after saturating the electrolyte with NaCl and analyzed using GC.

2.6 DESIGN OF COMPARTMENTALIZED ELECTROLYTIC CELL

A divided electrolytic cell has been designed using glass tubes, with chemically treated disc acting as a separator (Fig. 5.1). The separator prevented the mixing of the anolyte and catholyte, but ensured the passage of current for electrolysis.

2.7 EXPERIMENTAL CONDITIONS FOR THE ELECTROLYTIC REMOVAL OF PHENOL

A smooth platinum sheet (of area 1 cm^2) dipped into 50 ml of 1 M H^+ (aq.) solution acted as the cathodic part of the half cell. The anodic compartment consisted of graphitic carbon (of area 1 cm^2) as the electrode dipped into a 50 ml solution of phenol (~200 ppm) along with a supporting electrolyte (NaCl or NaOH). The decomposition of phenol was carried out at 5 V.

2.8 EXPERIMENTAL CONDITIONS FOR THE ELECTROLYTIC REMOVAL OF ARSENIC

For the removal of arsenic, appropriate concentration of sodium arsenate (As^{3+}) resembling pollutants, was taken along with 1 M H^+ solution in the cathode compartment. The anolyte contained 50 ml of 1M OH^-. Galvanostatic electrolytic reduction was carried out using Ni and Ag sheets (of area 1 cm^2), which were used as anode and cathode respectively.

2.9 PREPARATION OF Co, Ni MODIFIED Pt AND Ti ELECTRODES

Co and Ni were electrochemically deposited on Ti and Pt (1 cm^2) cathodes by using 1 M "$CoCl_3$ and $NiCl_2$" as electrolyte and Pt as anode. Co/Ti or Co/Pt deposition was done using $CoCl_3$ electrolyte. CoNi/Ti or CoNi/Pt deposition was done from electrolyte containing a mixture of $CoCl_3$ and $NiCl_2$. After the electrodeposition process, the electrodes were heated at 673 K for 2 h in air to obtain their corresponding oxides.

2.10 SPECTROPHOTOMETRIC ESTIMATION OF PHENOL

Estimation of phenols was done spectrophotometrically using 4-aminoantipyrine method (Ettinger *et al*., 1951). Phenol solution (100 ml) in phosphate buffer (pH 7.9 ± 0.1) is mixed with 1 ml of 2 % 4-aminoantipyrine followed by 1 ml of 8 % potassium ferricyanide to develop a red colour. After 15 minutes of incubation, absorbance was measured at 500 nm. Phenol concentration of the sample was calculated using a standard graph. A series of known concentrations of phenol (1-10 ppm) was prepared and the absorbance was measured as described above. The standard graph was obtained by plotting the absorbance vs the concentration.

2.11 SPECTROPHOTOMETRIC ESTIMATION OF ARSENIC

Arsine (AsH_3) gas, evolved at the cathode compartment, was absorbed by passing through the pyridine solution containing silver diethyldithiocarbamate. Arsine reacts with solution of silver diethyldithiocarbamate, $AgS.CS.N(C_2H_5)_2$, in pyridine to form a soluble red complex, which has an absorption maximum at 540 nm (Vogel, 1961). The quantity of As removed was calculated using a standard graph, which was obtained by plotting known amount of arsenic containing solution vs absorption intensity (λ_{max})

2.12 CHEMICAL OXYGEN DEMAND (COD) ANALYSIS

COD for the phenolic samples was determined using open reflux method (Clesceri *et al*., 1988). For analysis, 25 ml of phenol solution was taken in a 250 ml single neck round bottom flask. 1 g $HgSO_4$ and several glass beads was added to the above solution, and 5 ml sulfuric reagent (5.5 g $AgSO_4$/ kg H_2SO_4) was added very slowly with mixing to dissolve $HgSO_4$. The resulting mixture was cooled while mixing to avoid possible loss of volatile materials. 25 ml of 0.04167 M $K_2Cr_2O_7$ solution was added to the above solution and mixed well. The flask was attached with water cooling condenser, and 70 ml of sulfuric reagent was added to the mixture through the open end of the condenser. The above mixture was refluxed for 2h, cooled and diluted to about twice its volume with distilled water. The excess $K_2Cr_2O_7$ titrated with 0.25 M Ferrous Ammonium Sulfate (FAS), using 0.10 to 0.15 ml ferroin indicator. Blank experiment was also done as described earlier with distilled water.

$$\text{COD as mg } O_2 /1 = \frac{(A - B) \text{ x } M \text{ x } 8000}{\text{ml of sample}}$$

A = ml FAS used for blank B = ml FAS used for sample

M = molarity of FAS 8000 = milliequivalent weight of oxygen X 1000 mL/L

CHAPTER 3

CHARACTERIZATION AND PHOTOCATALYTIC HYDROGEN PRODUCTION BY CdS NANOPARTICLES

3.1 STUDIES ON TEMPLATED CdS NANOPARTICLES

3.1.1 Introduction

Production of hydrogen from inexhaustible source, water by cheaper route has been under extensive investigations in recent years (So *et al*., 2003; Koca and Sahin, 2003). Among different processes used for hydrogen production, photocatalysis is a method, which has to be improved for viability where sunlight can be utilized as a sustainable energy source for hydrogen production. Selection of a suitable photocatalyst is an important criterion to accomplish the process as workable for maximum quantity of hydrogen production. Essentially, the photocatalyst should have the appropriate conduction and valence band edge positions in order to reduce and oxidize the H^+ and OH^- ions, respectively. For better hydrogen evolution activity, the bottom of conduction band should have more negative potential than the H^+/H_2 redox potential. The values of top edge of valence band should be at more positive with oxidation potential of water. In addition to these criteria, photocatalyst should absorb light especially in the visible region and should have good photo-stability under the irradiation conditions.

Several types of semiconducting materials such as TiO_2, Fe_2O_3, ZnO and CdS have been investigated for hydrogen production (Li *et al*., 2001; Takata *et al*., 1998; Nguyen *et al*., 2005). Among them, CdS shows light absorption in the visible region and has suitable conduction band potential to reduce the H^+ ion effectively. However, the utility of CdS as photocatalyst has been limited due to its anodic decomposition, the so called photocorrosion. Number of attempts have been made to overcome this disadvantage by using suitable sacrificial agents. In general, Na_2S and Na_2SO_3

mixture has been widely used as sacrificial agent (Buhler *et al*., 1984). Coupling of CdS with other semiconductors like TiO_2 and ZnS has also been studied (Sant and Kamat, 2002). It has been observed that, the photocatalytic activity for hydrogen production increases considerably in the coupled semiconductors because of the interparticle electron transfer process (Kakuta *et al*., 1985) In the coupled semiconductor photogenerated electron is transferred with relative ease, from one semiconductor to the other, due to the favourable position of the conduction bands of the semiconductor couple and this results in the efficient electron transfer for H^+ ion reduction. Recently $LaMnO_3$/CdS (Kida *et al*., 2003) and CdS/ETS-4 (Titanosilicate zeolite) (Guna *et al*., 2004), composites have been studied as efficient catalyst for photocatalytic hydrogen production. It has been shown that the supported CdS shows higher activity in the presence of sacrificial agent without undergoing any photocorrosion. The surface characteristics of the support such as the acid-base properties can also play an important role on the photocatalytic activity of CdS. In case of the CdS/MgO photocatalyst, it has been observed that the activity for hydrogen reduction is enhanced with increase in basicity of the support (Supriya and Subrahmanyam, 1998; Subrahmanyam *et al*., 1996). Furthermore, it is known that semiconductor nanoparticles show higher photocatalytic activity compared to the bulk materials (Pal *et al*., 2004; Warrier *et al*., 2004) due to changes in surface area, band gap, morphology and generation of surface defects. Various methods have been adopted in literature for the synthesis of CdS nanoparticles (Chen *et al*., 2002; Wang *et al*., 2003; Parvathy *et al*., 1997; Liem *et al.*, 1999) and CdS particles embedded in the cages, egg membrane and zeolite (Wellmann *et al*., 2001; Pattabi and Uchil, 2000; Peng *et al.*, 2003). The photocatalytic experiments carried out using CdS embedded systems show better activity than the bulk CdS although the nonactive host material can reduce the amount of light absorption. In order to overcome this problem, in this study CdS nanoparticles in zeolite matrix have been prepared, which are subsequently retrieved by treatment with HF solution. The CdS nanoparticles prepared by this

method were used to carry out photocatalytic hydrogen production. The photocatalytic activity of these materials has been found to correlate well with the particle size. The effect of noble metal loading on CdS for the photocatalytic hydrogen evolution has also been studied.

3.1.2 RESULTS AND DISCUSSION

3.1.2.1 UV-Visible spectra

UV-Visible absorption spectra for CdS nanoparticles prepared from different zeolite matrices are shown in Fig. 3.1. Comparing the absorption edge of bulk CdS with that of CdS-Y, CdS-Z and CdS-B samples prepared from different zeolites, it is seen that a blue shift in the onset of absorption is observed in these samples. This phenomenon of blue shift of absorption edge has been ascribed to a decrease in particle size. It is well known that in case of semiconductors the band gap between the valence and conduction band increases as the size of the particle decreases to the nanosize range.

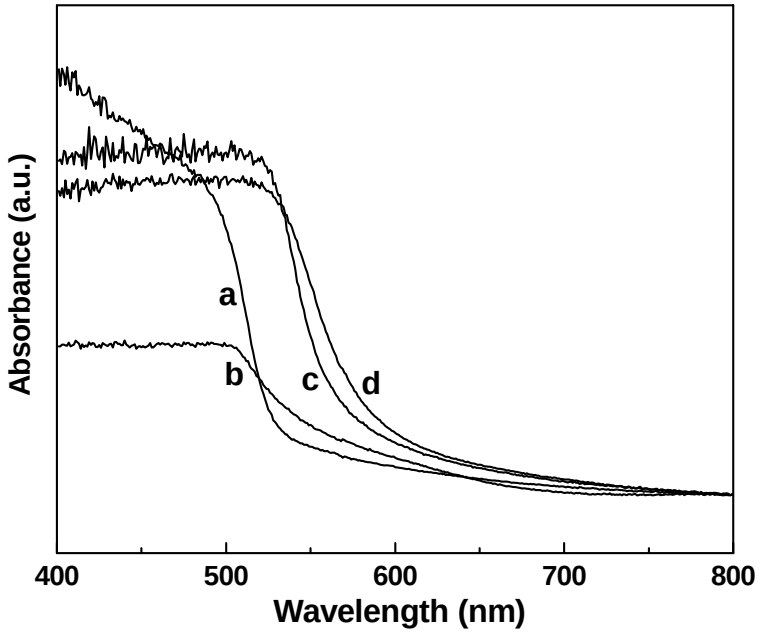

Fig. 3.1 UV-Visible absorbance spectra of (a) CdS-Z, (b) CdS-Y, (c) CdS-B and (d) bulk CdS

This results in a shift in the absorption edge to lower wavelength region (higher energy band gap). The magnitude of the shift depends on the particle size of the semiconductor. In the present study, the CdS-Z samples prepared from the ZSM-5 zeolite matrix shows a blue shift of approximately 65 nm compared to the bulk particles. The smaller pore size and pore volume of the ZSM-5 compared to the other two zeolites is responsible for the formation of CdS with smaller size. The observed size of the CdS nanoparticles are higher than their respective zeolite pore size, this may be due to the agglomeration of CdS nanoparticle during the post treatment with hot HF. From the onset of the adsorption edge, the band gap of the CdS particles were calculated using the method of Tandon and Gupta (Tandon and Gupta, 1970). In Table. 3.1, the band gap is found to increase in the order CdS-Z> CdS-Y> CdS-B> bulk CdS.

Table 3.1 Band gap, particle size, specific surface area and pore volume of CdS samples prepared from zeolite and bulk CdS sample.

Samples	Band Gap (eV)	Particle size (nm)	Specific surface area ($m^2 g^{-1}$)	Pore volume ($cm^3 g^{-1}$)
CdS – Z	2.36	6	46	0.236
CdS – Y	2.25	8.8	36	0.123
CdS -B	2.21	11.6	26	0.073
bulk CdS	2.13	23	14	0.042

3.1.2.2 X-ray diffraction study

X-ray diffraction patterns of the prepared CdS nanoparticles using zeolite templates and HF treated CdS bulk sample are presented in Fig.3.2. The bulk CdS sample was treated with 48 % HF solution for 12 h prior to the XRD study to see any possible change in phase or crystallinity. The bulk CdS sample shows major X-ray reflections with d values of 3.56, 3.35, 3.15 and 2.06 corresponding to the hexagonal phase of cadmium sulfide (JCPDS No 06 - 0314).

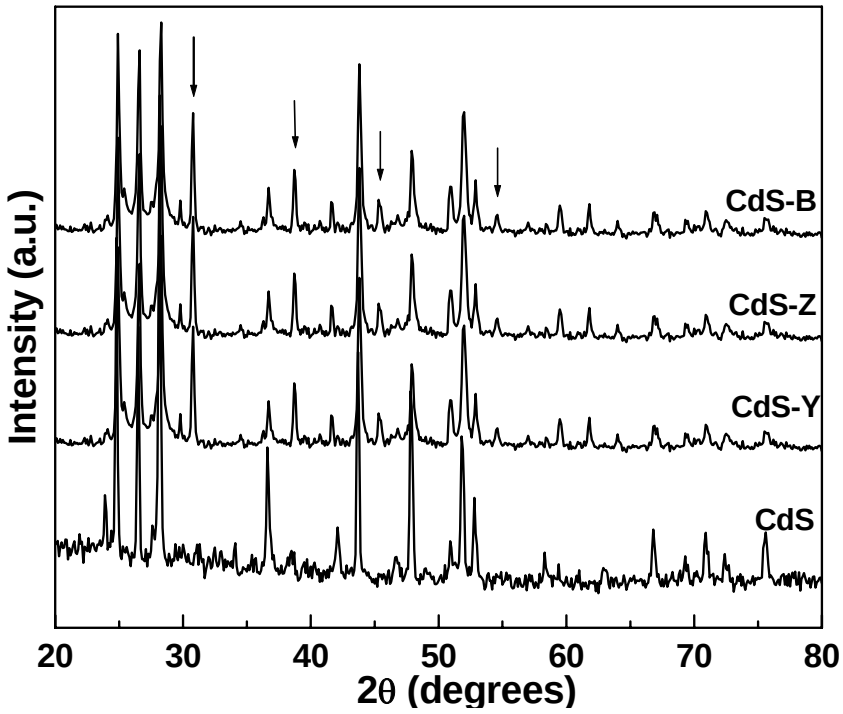

Fig. 3.2. X-ray diffraction patterns of bulk CdS and CdS nanoparticles

In case of the CdS-Y, CdS-Z and CdS-B samples, in addition to the above mentioned peaks, new peaks are observed (indicated by an arrow). These peaks correspond to the cubic phase of the CdS particles (JCPDS No.10 - 0454). Peak broadening has also been observed in case of the CdS nanoparticles prepared from zeolites compared to that of the bulk samples. The HF treated CdS bulk sample shows identical XRD patterns as that of bulk CdS particles indicating that there is no significant change in the crystal structure and phase as a result of the acid treatment. The XRD study demonstrates that nanosize CdS particles with altered phases can be prepared by using the zeolite matrix as a template for synthesis. The XRD pattern for the samples after treatment in hydrogen atmosphere at 400 °C do not indicate any phase or morphological change.

3.1.2.3 Surface area

The specific surface area and pore volume of the CdS samples prepared from different sources are presented in Table. 3.1. As seen from the table, the surface area of the CdS depends on the zeolite matrix from which it has been prepared. The highest surface area and pore volume are observed for the CdS-Z particles prepared from ZSM-5 zeolite. ZSM-5 is a medium pore size zeolite with pore opening in the range of 5-6 Å. During the preparation process, CdS particles are homogeneously precipitated inside the pores of the zeolites. Upon removal of the zeolite matrix, uniform pores are created in the CdS particles. These pores contribute to the higher pore volume and surface area of CdS-Z sample. The same argument can be extended to the CdS-Y and CdS-B samples prepared from the H-Y and H-β zeolites, respectively.

3.1.2.4 Electron microscopic analysis

a. Scanning electron micrograph

Surface morphology of CdS nanoparticles has been studied by scanning electron microscopy. The SEM pictures of the CdS samples are presented in Fig. 3.3. The growth of fine particles of CdS in a regular pattern is observed on the surface of the CdS-Y, CdS-Z and CdS-B samples in Fig. 3.3a, 3.3b and 3.3c. The surface is also relatively rough for the CdS particles prepared from the zeolite matrices. In case of the bulk sample in Fig. 3d the surface is smooth with large outgrowth of CdS particles in an irregular manner.

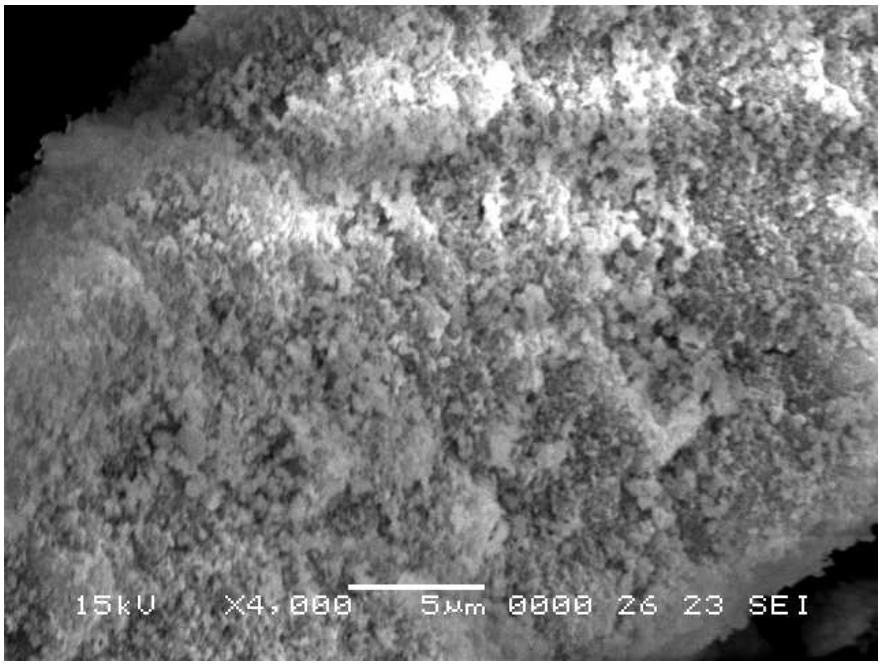

(a)

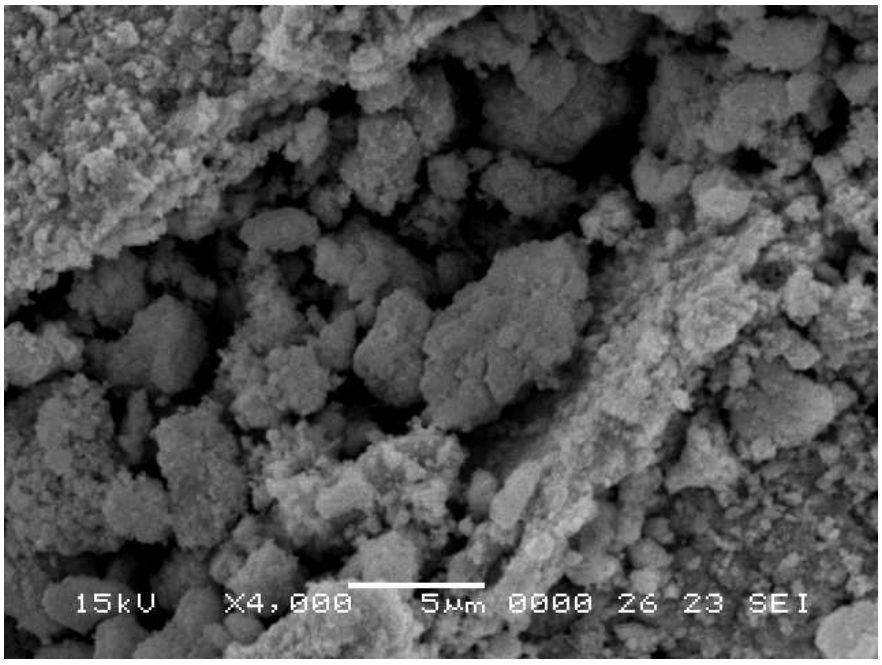

(b)

Fig. 3.3. SEM photographs of (a) CdS-Z (b) CdS-Y

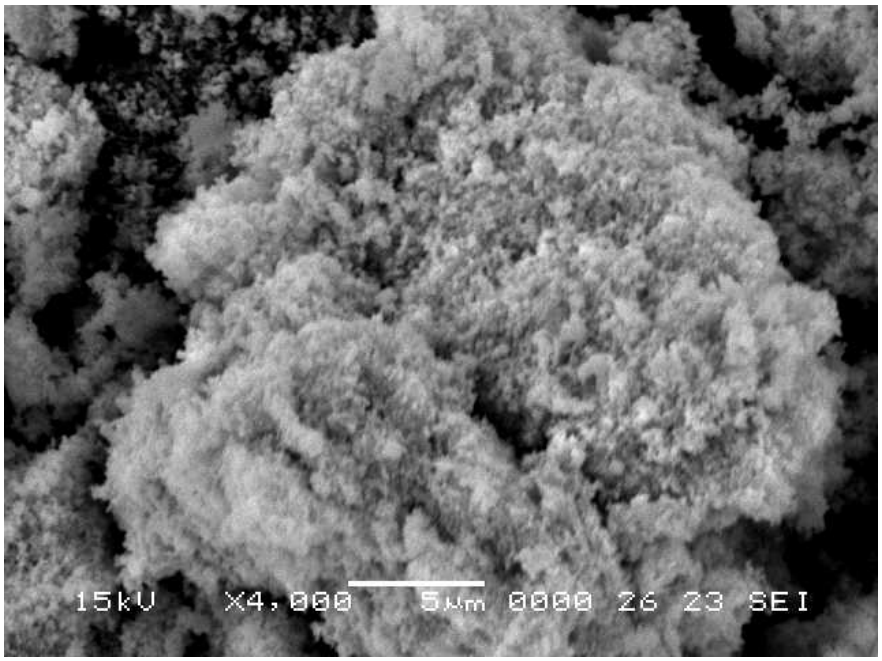

(c)

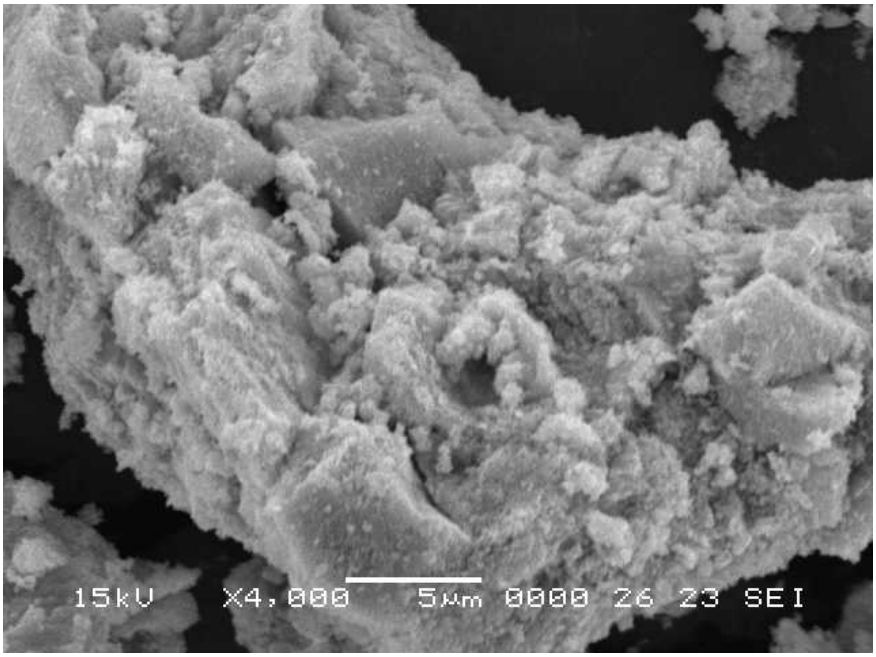

(d)

Fig.3.3. SEM photographs of (c) CdS-B and (d) bulk CdS

b. Transmission electron micrograph

The transmission electron micrographs of the CdS sample from Y zeolite are shown in Fig. 3.4 (a & b). Particles in nanosize range are clearly observed for the CdS-Y, CdS-Z and CdS-B samples. The exact particle size for the bulk and the prepared samples has been calculated from the micrographs and are presented in Table. 3.1. It is observed that the nature of the zeolite matrix plays a vital role in the particle size. The CdS-Y and CdS-Z samples prepared from zeolites showed a smaller particle size compared to other two samples. Fig. 3.4b shows the electron diffraction pattern of CdS-Y nanoparticles, from which the d values are calculated and are tabulated in Table. 3.2.

Table. 3.2. The d values (Å) for CdS-Y, CdS-Z and CdS-B nanoparticles calculated from XRD and electron diffraction methods

CdS-Y		CdS-Z		CdS-B		Literature
XRD	Electron Diffraction	XRD	Electron Diffraction	XRD	Electron Diffraction	
1.53	1.52	1.52	1.57	1.52	1.52	1.52
1.79	1.70	1.79	1.76	1.78	1.79	1.79
2.96	3.16	2.97	3.06	2.93	3.11	2.97

It can be seen from Table.3.2, that there is a good correspondence between the 'd' values calculated form the electron diffraction, X-ray diffraction and literature values for the CdS samples prepared from the zeolite matrix. The other TEM pictures for the CdS-Z and CdS-B are not shown due to poor quality.

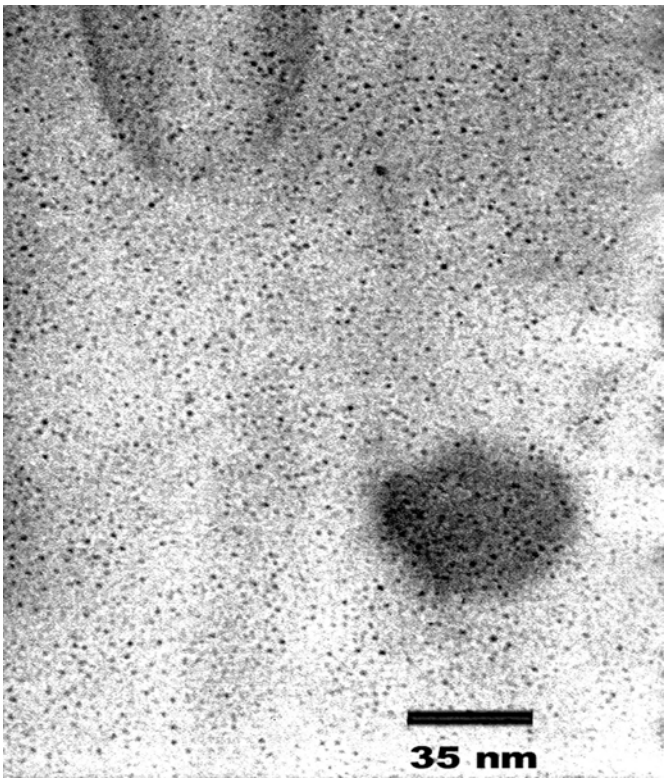

Fig. 3.4 a. TEM images of CdS-Y sample

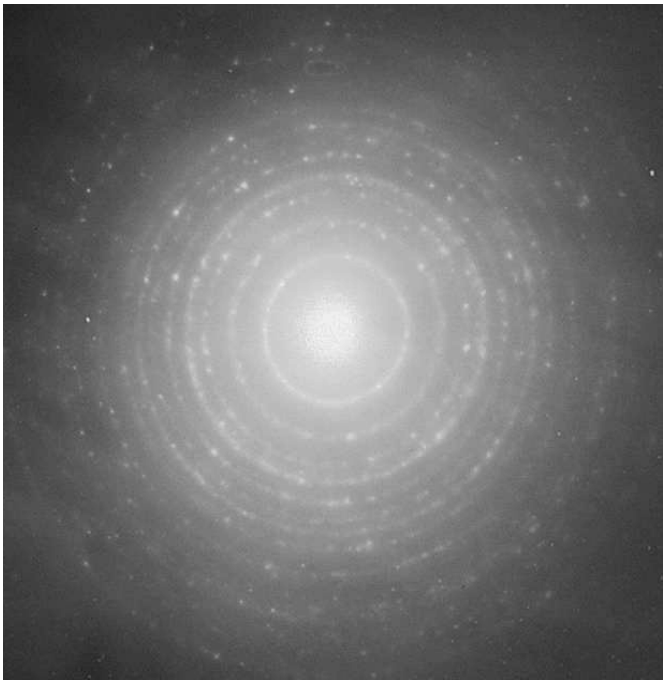

Fig. 3.4 b. Electron diffraction pattern of CdS-Y sample

3.1.3 Photocatalytic activity

Photocatalytic hydrogen evolution reaction has been carried out on these materials under ambient conditions and using 400 W Hg lamp as light source. The amount of hydrogen evolved is presented in Table.3.3. From the results, it can be seen that the amount of hydrogen evolved is higher for the CdS nanoparticles in comparison with that of the bulk CdS sample.

Table 3.3. The rate of hydrogen production with different CdS samples.

S.No	Sample	Rate of hydrogen production ($\mu mol\ h^{-1}\ 0.1g^{-1}$)
1	CdS – Z	68
2	CdS – Y	102
3	CdS – B	67
4	bulk CdS	45

The CdS-Y prepared from HY zeolite matrix, showed a hydrogen evolution rate of 102 μmol h^{-1} when S^{2-}/SO_3^{2-} is used as a sacrificial agent. This value is quite significant in comparison with the other hydrogen evolution rate reported for pure CdS particles in literature (Kakuta *et al.,* 1985). The higher hydrogen evolution rate in the present case can be ascribed to the lower particle size and high surface area of these materials. Fig. 3.5, shows that the amount of hydrogen evolved over different CdS samples for a time period of 6 h. For the sake of comparison, the results with CdS particles present inside the zeolite matrix are also presented. It can be seen that the nanoparticles show higher activity compared to the CdS nanoparticles entrapped inside the zeolite matrix (without removing the zeolite matrix) (curve d). This points to the fact that the inert zeolite matrix reduces the amount of light absorption by CdS

nanoparticles thereby reducing its activity. Also, during this six hour period there is no appreciable decrease in the activity of these nanomaterials. After the catalytic experiments these catalysts were recovered and regenerated by washing with water and subsequently calcining at 673 K for 4 h. The regenerated catalysts show similar activity as that of fresh catalyst indicating that photocorrosion has been reduced substantially by using the sacrificial agent. In the present case, Na_2S/Na_2SO_3 system is quite effective in preventing photocorrosion which has been studied in literature (Buhler *et al.*, 1984).

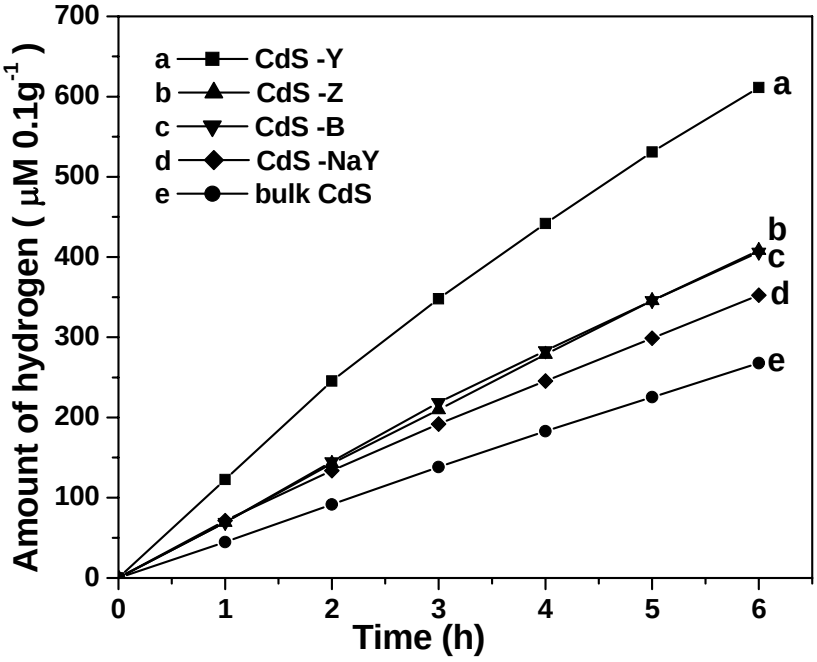

Fig. 3.5. Hydrogen production as a function of time on (a) CdS-Y (b) CdS-Z (c) CdS-B (d) Zeolite-Y containing CdS nanoparticles (CdS-H-Y) and (e) bulk CdS

3.1.4 Effect of noble metal on the photocatalytic activity

It is well known that the photocatalytic activity of CdS increases substantially in presence of noble metal particles (Sakata *et al*., 1982). In order to study the effect of noble metal on the hydrogen evolution rate of these CdS samples, 1 wt% metal loaded

samples have been prepared by wet impregnation method. The hydrogen evolution rate for various noble metal (Pt, Pd, Ru and Rh) loaded CdS nanoparticles and bulk CdS are shown in Fig. 3.6 (a-d). Among the noble metals studied, Pt metal loaded on CdS (irrespective of CdS source) shows higher activity for hydrogen evolution; the Pt / CdS-Z shows the highest activity.

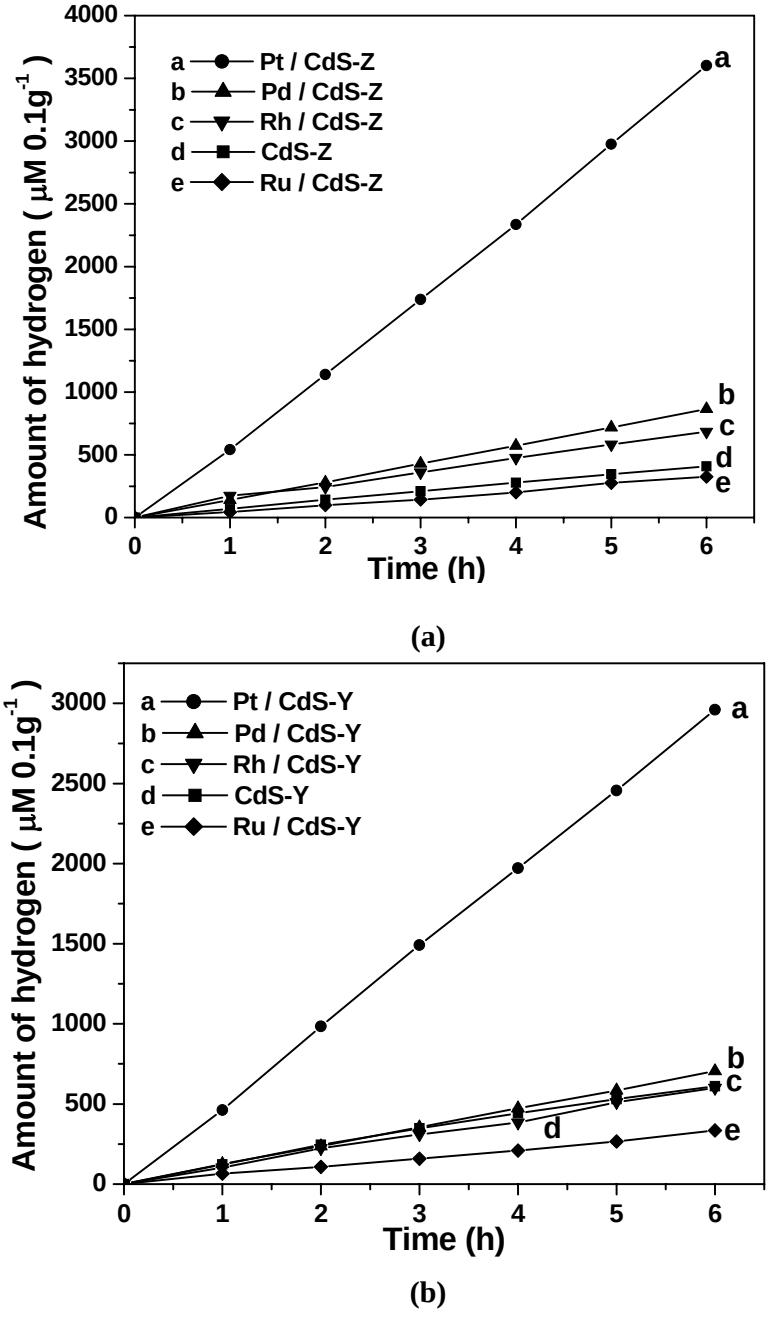

Fig. 3.6. Amount of hydrogen produced on (a) Cds-Z and (b) CdS-Y

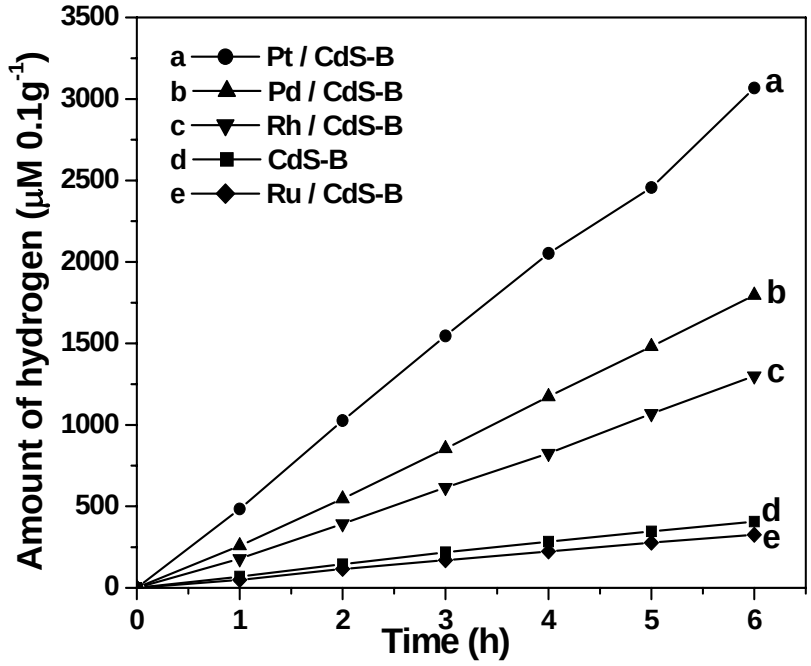

(c)

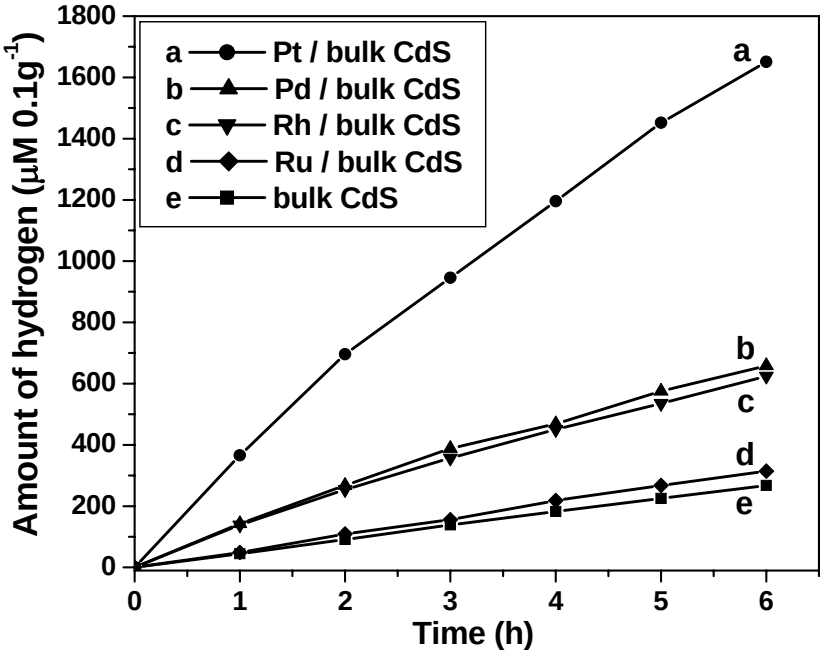

(d)

Fig. 3.6. Amount of hydrogen produced on (c) CdS-B and (d) bulk CdS

The rate of hydrogen production on a noble metal surface can be related to the metal hydrogen bond, redox potential and work function of the noble metal atom (Milazzo, and Caroli, 1978; Ranjit *et al*., 1996). Hydrogen evolution increases linearly with increase in the redox potential of the noble metal. The more positive the redox potential of a metal, it facilitates faster reduction of H^+ ion. Similarly, the hydrogen evolution also depends on the metal-hydrogen bond strength. When the metal hydrogen bond energy is less, the hydrogen evolution barrier is substantially reduced resulting in easy evolution of molecular hydrogen. The work function of the metal is another factor that influences the hydrogen evolution, if it is high, the reduction rate increases. These parameters are crucial for hydrogen evolution reaction and are tabulated in Table.3.4.

Table. 3.4 Redox potential, metal-hydrogen bond strength, work function and rate of hydrogen evolution for different noble metal loaded CdS-Z samples (Milazzo, and Caroli, 1978; Ranjit *et al*., 1996)

Metal	**Redox potential (E^0)**	**Metal- hydrogen bond energy (kCal mol^{-1})**	**Work function (eV)**	**Hydrogen evolution rate* (μmol h^{-1} 0.1g^{-1}).**
Pt	1.188	62.8	5.65	600
Pd	0.951	64.5	5.12	144
Rh	0.758	65.1	4.98	114
Ru	0.455	66.6	4.71	54

*1 wt% metal loaded on CdS-Z sample. The reaction data is presented after 6 h under reaction condition.

From the table, it is observed that there is a direct correlation between these factors and hydrogen evolution. Pt metal with higher redox potential, work function and lower metal hydrogen bond strength is found to be favorable for hydrogen evolution activity. Whereas, in case of the Ru loaded CdS samples it has been observed that the hydrogen production activity is lower than the naked CdS (except for bulk CdS). This

is due to the strong ruthenium-hydrogen bond which inhibits the hydrogen evolution on the ruthenium surface. In this study, with 0.1g of the Pt loaded CdS nanoparticles the hydrogen evolution rate has been found to be 600 μmol h^{-1} which is higher than the value reported so far in the literature (Subrahmanyam *et al*., 1996).

3.1.5 Product analysis

It has been reported in the literature, that in the photocatalysis using sulphide nano particles hydrogen gas is produced by the reduction of H^+ ions by the photo generated electrons from the conduction band of the semiconductor. The elemental sulphur is the other product. This reacts with excess sulphide (S^{2-}) ion present to give a disulphide (S_2^{2-}) ion. This further reacts with sulphite ion to regenerate sulphide ion along with thiosulphate ion (Equation 3.1 & 3.2). Thus in the presence of a mixture of sulphide and sulphite hydrogen will be the only product. The evolved gas has been analyzed and found to be hydrogen along with trace quantity of moisture. The source of moisture may be due to the product gas being generated from the reaction solution, which is in aqueous medium.

$$S + S^{2-} \rightarrow S_2^{2-} \quad (3.1)$$

$$S_2^{2-} + SO_3^{2-} \rightarrow S_2O_3^{2-} + S^{2-} \quad (3.2)$$

3.2 STUDIES ON MESOPOROUS CdS NANOPARTICLES

3.2.1 Introduction

Recently, the mesoporous compounds are under extensive investigation in various fields due to is larger surface area. The photocatalytic activity could be enhanced substantially by increasing the specific surface area of the CdS. Though, there are various methods available for the preparation of mesoporous CdS nanoparticles, simple preparation routes for porous CdS nanoparticles have not yet been established

and also with the available methods, the yield of the CdS nanoparticles is comparatively low. However, various mesoporous materials have been synthesized via conventional approaches using surfactants as templates based on a liquid crystal template mechanism (Perkas *et al*., 2003; Yu *et al*., 2003; Qingmin *et al*., 2001). These methods often require a long time and multiple-step procedures. Recently, sonochemistry has been demonstrated to be an excellent method for the preparation of mesoporous TiO_2 (Yu *et al*., 2002; Yu *et al*., 2003; Yu *et al*., 2005). It arises from acoustic activation, the formation, growth and implosive collapse of bubbles in a liquid. The collapse of bubbles generates localized hot spots with transient temperatures around 5000 K, pressure of about 20 MPa and heating and cooling rates greater than 100 Ks^{-1} (Gedanken *et al*., 2001; Suslick *et al*., 1991). These conditions efficiently muddle up the cations and the anions present in the solution faster and thereby alter the rate of the precipitation reaction. In the recent past, few attempts have also been made to prepare both for the hexagonal and cubic CdS nanoparticles through the ultrasonic mediated precipitation at room temperature (Wang *et al*., 2001; Shao *et al*., 2004; Li *et al*., 2003). However, the mesoporous CdS nanoparticles have not yet been attained. This may be due to the high concentrations of the precursor solutions used, in the literature for the preparation. In the present study, attempt has been made to prepare mesoporous CdS nanoparticles by ultrasonic mediated precipitation using Na_2S and $Cd(NO_3)_2$ as the precursors at room temperature.

3.2.2. RESULTS AND DISCUSSION

3.2.2.1 UV-Visible spectra

UV-Visible absorption spectra for the as prepared mesoporous CdS-U nanoparticle prepared by ultrasonic mediated precipitation and as prepared bulk CdS are shown in Fig. 3.7. It can be seen from Fig.3.7, that, the onset absorption of CdS-U particle

shows blue shift when compared to bulk CdS onset absorption. This can be explained on the basis of the smaller size CdS-U nanoparticles.

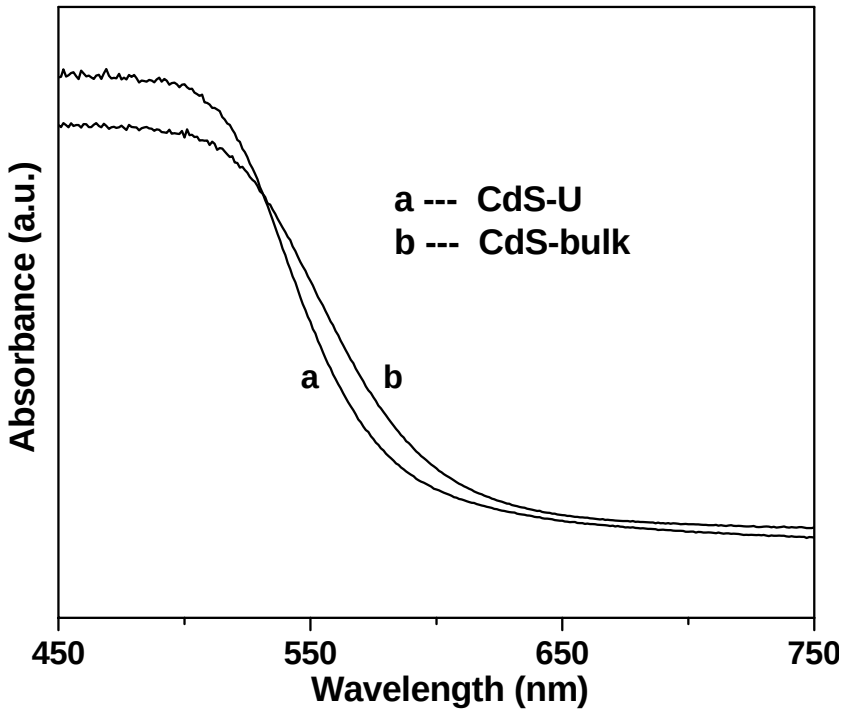

Fig. 3.7. UV-Visible absorbance spectra of as prepared (a) CdS-U nanoparticles and (b) bulk CdS particles

3.2.2.2 X-ray diffraction study

X-ray diffraction patterns of as prepared CdS-U nanoparticle from ultrasonic mediated precipitation is shown in Fig. 3.8. The observed peaks at "d" values of 1.75, 2.04 and 3.32 correspond to the (3 1 1) (2 2 0) and (1 1 1) planes with the lattice constant a = 5.818, show the presence of cubic crystalline phase CdS (JCPDS No.10 - 0454). Peak broadening has also been observed in the as prepared CdS-U nanoparticle. The particle size has been calculated using Debye-Scherrer equation (Cullity, 1987) and the value obtained is 4-6 nm. The as prepared bulk CdS shows no definite X-ray diffraction pattern (not shown) indicating the amorphous nature of the material.

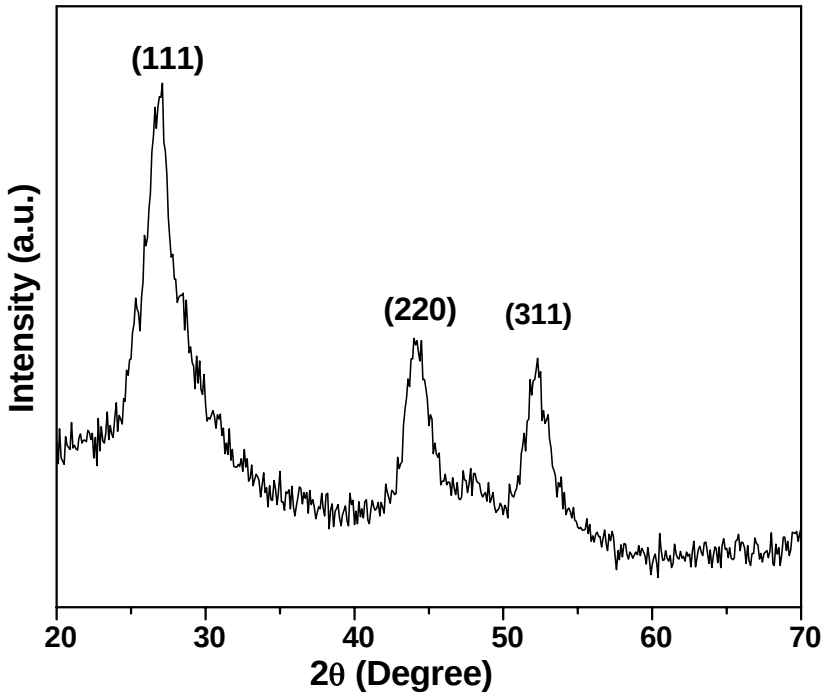

Fig. 3.8. X-ray diffraction pattern of as prepared mesoporous CdS-U nanoparticle

3.2.2.3 Surface area and pore volume studies

The N_2 adsorption and desorption isotherms of as prepared CdS-U sample are shown in Fig.3.9. It can be seen from Fig.3.9, that the hysteresis found in this material is of type IV and can be attributed to the mesoporous nature of the as prepared CdS-U nanoparticle. The pore size distribution has been studied using B.J.H. method and is shown in Fig 3.9 (inset). The bulk CdS has a specific surface area ~ 14 m^2 /g .The specific surface area and pore volume of as prepared CdS-U sample are 95 m^2/g and 0.157 cm^3/g respectively. It can be stated that maximum pore volume is contributed by the pores with an average size of 54 Å.

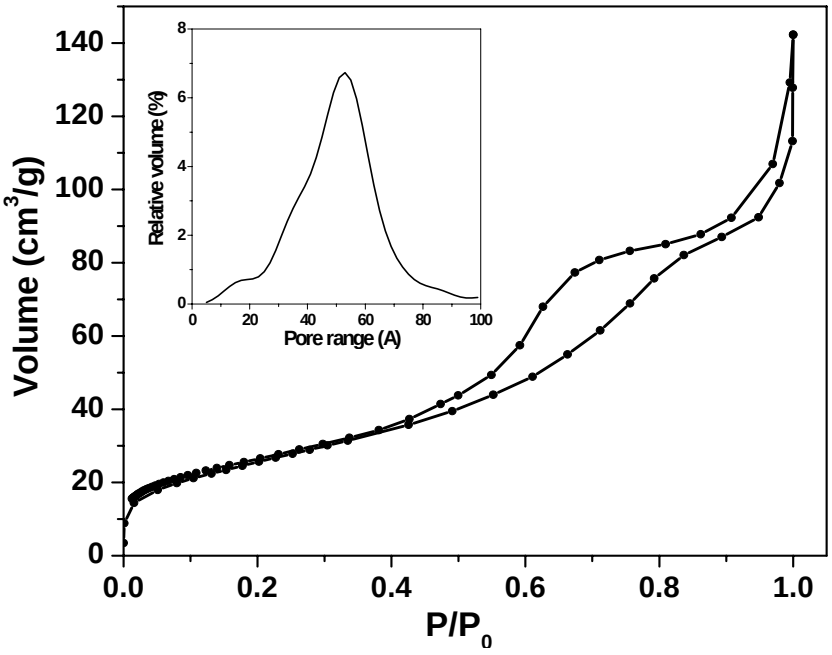

Fig. 3.9. N_2 Adsorption desorption isotherm of as prepared CdS-U particle and pore size distribution of as prepared CdS-U particle (inset)

3.2.2.4 Electron microscopic analysis

Surface morphology of CdS nanoparticles has been studied by scanning electron microscopy. The SEM pictures of the as prepared CdS samples are presented in Fig. 3.10 a and b. The growth of fine spongy particles of CdS-U is observed on the surface of the CdS-U (Fig. 3.10 a), whereas in the case of the bulk sample (shown in Fig.3.10b) the surface is found with large outgrowth of CdS particles. The transmission electron micrograph of the CdS sample is shown in Fig. 3.11. The fine mesoporous CdS particles in the nanosize range are observed for the as prepared CdS-U sample.

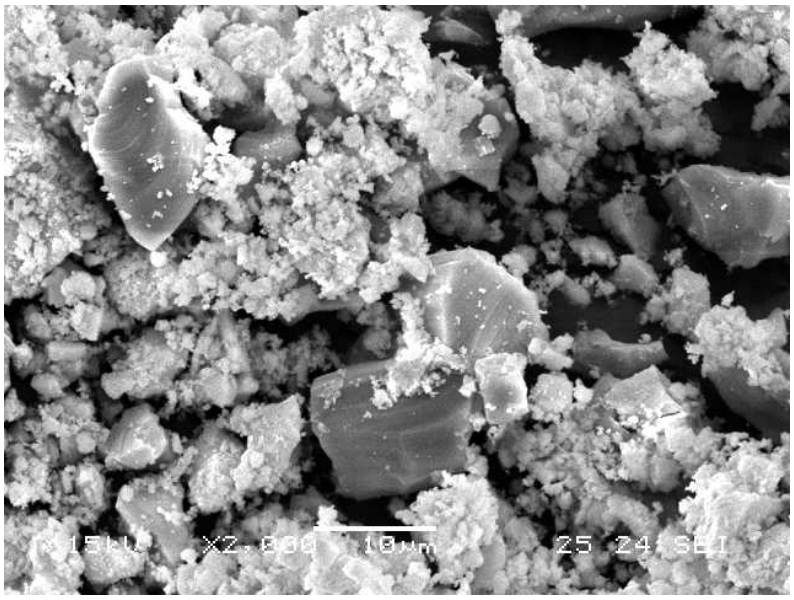

(a)

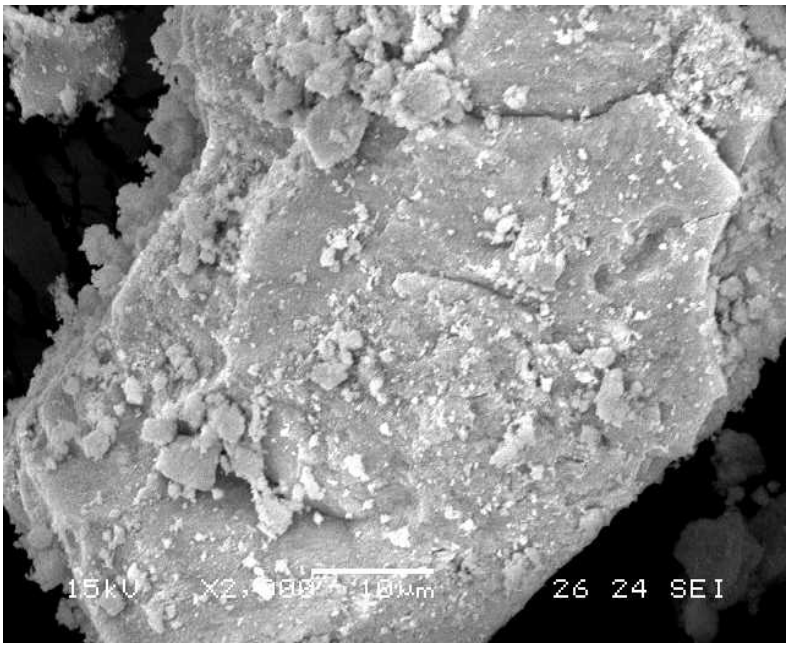

(b)

Fig. 3.10. SEM photographs of as prepared (a) CdS-U (b) bulk CdS

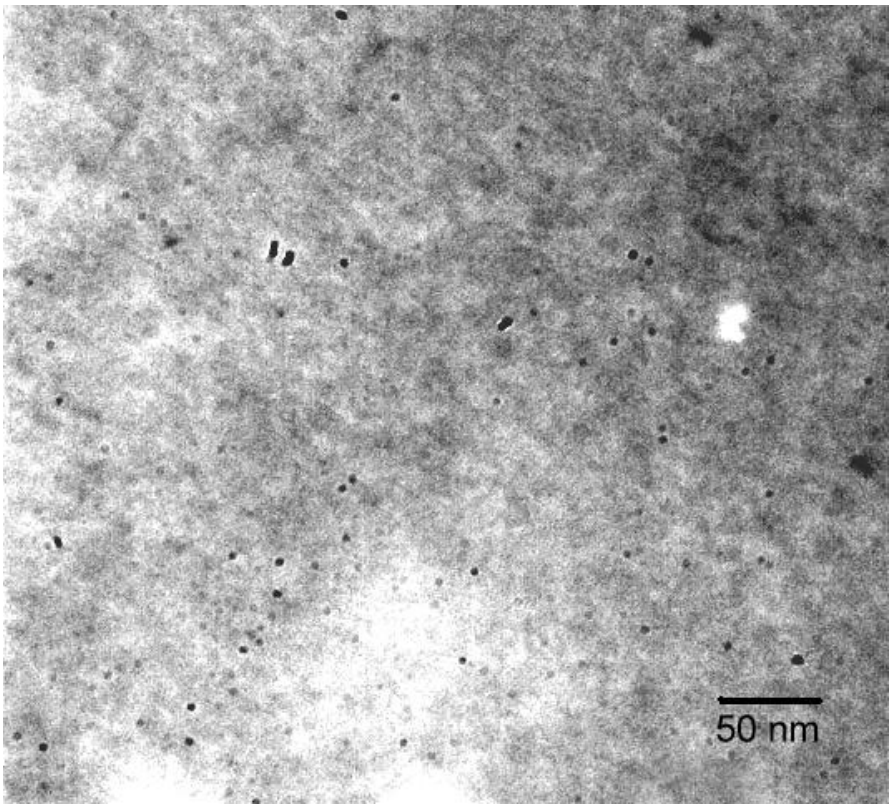

Fig.3.11. TEM image of as prepared CdS-U particles

3.2.3 Photocatalytic activity

Photocatalytic hydrogen evolution reaction has been carried out on these materials under ambient conditions using 400 W Hg lamp as light source. The amount of hydrogen evolved over pure CdS-U and 1 wt % of noble metal loaded CdS particles are shown in Fig. 3.12. From the results, it can be seen that the amount of hydrogen evolved is very much higher for the Pt/CdS-U nanoparticles in comparison with that of other CdS-U samples. In fact, the amount of hydrogen evolved (73 μmole/h/0.1g) over pure CdS-U sample is higher than the CdS samples which were prepared from the zeolite matrix (68 μmole/h/0.1g). Similarly the noble metal loaded CdS-U samples also show higher amount of hydrogen evolution when compared to samples prepared using zeolites. Surprisingly, the Pt/CdS-U particle shows enormous amount of

hydrogen evolution, 1415 μmole/h/0.1g, which is a higher value than the results reported in the literature so far. In fact it is almost 2-3 times higher value than the highest value reported in literature. The higher amount of hydrogen production by the CdS-U samples could be attributed to the presence of mesopores in the CdS-U samples, which will enable the high dispersion of metal atoms over the catalyst surface.

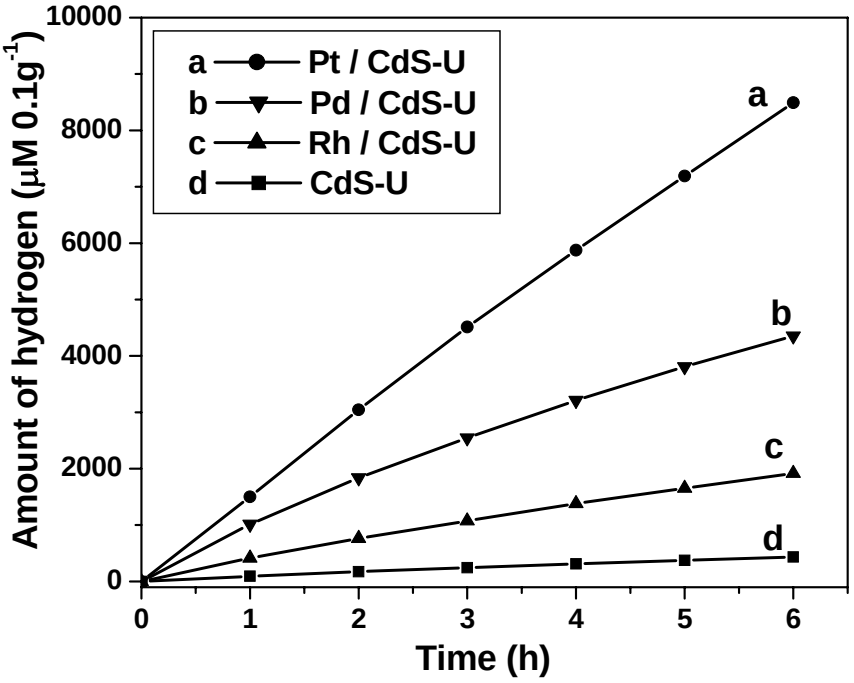

Fig. 3.12 Rate of hydrogen production as a function of time on (a) Pt/CdS-U (b) Pd/CdS-U (c) Rh/CdS-U and (d) CdS-U samples

3.3 PHOTOCATALYTIC ACTIVITY OF CdS-TiO_2 COUPLED SEMICONDUCTOR

3.3.1 Introduction

When two semiconductors are coupled together the rate of recombination of electron hole- pair has been reduced by inter system electron transfer (Barbeni *et al*., 1985; Borgarello *et al*., 1986) and thus one can effectively use major portion of solar light.

This concept was successfully applied to the decomposition of H_2S into H_2 and the production of hydrogen from water (Tambwekar *et al*., 1999; Kakuta *et al*., 1985) and decomposition of organic compounds (Kumar and Jain, 2001; Yin *et al*., 2001; Paola *et al*., 2000; Li and Haneda, 2003). Borrell *et al* (1992) discussed catalytic activity of CdS-based semiconductor for photocatalytic hydrogen production from sulphide/suphite sacrificial agents. Fig.3.13 shows the energy levels of bulk TiO_2 and CdS coupled semiconductor. The lower band gap, CdS absorbs light energy in the visible region and the excited electron is transferred to the conduction band of TiO_2 molecule and this electron is utilized to reduce the desired species.

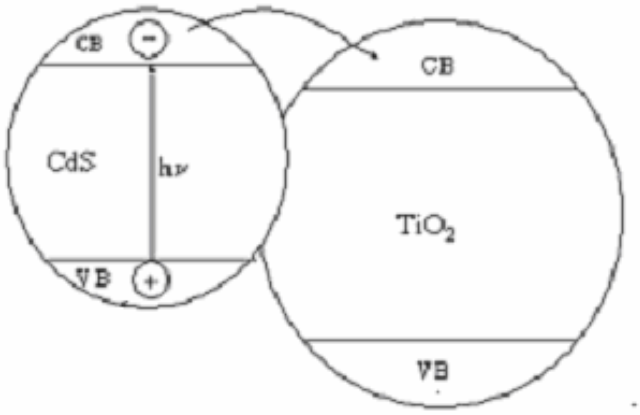

Fig. 3.13. Energy level diagram of CdS-TiO_2 coupled photocatalyst

3.3.2 RESULTS AND DISCUSSION

In the present study, 1 wt % Pt loaded CdS-U (More active for photocatalytic hydrogen production among the prepared catalysts) was coupled with visible light active N-doped TiO_2 (2.2.4.1). It is expected that, the recombination of electron-hole pair will be minimized by the presence of Pt atom and the other semiconductor. Also, visible light active N-TiO_2 was used to couple with CdS-U particles, since it will also excite in visible region thereby the net photoactivity will increase. Various ratio

(wt %) of CdS and N-TiO_2 coupled catalytic system has been prepared by dry impregnation method and the photocatalytic hydrogen production activity have been evaluated using 400 W Hg lamp and tabulated in Table. 3.5.

Table 3.5. Rate of hydrogen evolution on coupled photocatalyst at different weight ratios of CdS: TiO_2

Catalyst	Weight ratio (wt %)	Hydrogen evolution rate ($\mu mol\ h^{-1}\ 0.1g^{-1}$)
CdS-U: N-TiO_2	5:95	51
1 wt % Pt/CdS-U: N-TiO_2	5:95	126
1 wt % Pt/CdS-U: N-TiO_2	10:90	173
1 wt % Pt/CdS-U: N-TiO_2	50:50	581
1 wt % Pt/CdS-U: N-TiO_2	75:25	403
CdS-U: 1 wt % Pt/N-TiO_2	50:50	34
1 wt % Pt/CdS-U: TiO_2 (P25)	50:50	510

It can be seen from the above Table 3.5 that, when amount of Pt/CdS increased from 5 to 50 wt %, the hydrogen evolution rate also increases from 126 to 581 $\mu mol\ h^{-1}$ /0.1g, further increase in the Pt/CdS amount in the coupled system results decreases in the hydrogen evolution rate. The optimum ratio of Pt/CdS-U: N-TiO_2 is 1:1 wt % to obtain maximum hydrogen evolution. Whereas, for the same 1: 1 wt % ratio of CdS-U: Pt/N-TiO_2, the activity is very low. This clearly shows that, when the Pt deposited on the CdS acts as electron sink, and the excited electron are moved to Pt surface, which reduces the water into hydrogen subsequently. In the other case, the Pt deposited of on the N-TiO_2 surface is not capable to trap the excited electron in the CdS conduction band. This situation makes that, Pt as inactive and results in lower photocatalytic activity. It can also be seen that, when N-TiO_2 is replaced with TiO_2

(P25, Degussa) in the CdS-TiO_2 coupled system, there is a significant decrease in the photocatalytic activity. It confirms that the visible light active N-TiO_2 is also participating into the hydrogen evolution reaction. The amount of hydrogen evolved during the reaction period for the various compositions of CdS and TiO_2 is shown in Fig. 3.14.

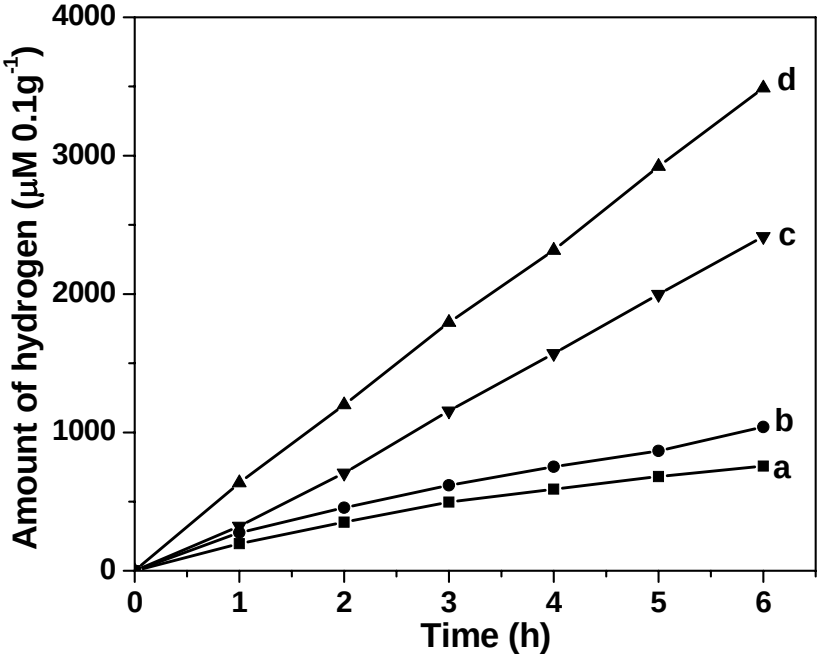

Fig. 3.14 Amount of hydrogen produced on 1 wt % Pt/CdS: N-TiO_2 coupled photocatalyst (a) 5:95 (b) 10:90 (c) 75:24 and (d) 50:50 weight ratio of CdS: TiO_2

It can be clearly seen form the Fig. 3.14 that, there is a steady increase in the hydrogen evolution (for the measured 6 h duration) when the CdS amount is 50 wt % and more. Below which, when the reaction time increased above 2h, the hydrogen evolution rate decreased significantly. It also confirms that the ratio between CdS and TiO_2 should be minimum 1 to attain maximum hydrogen evolution.

3.4 PHOTOCATALYTIC HYDROGEN PRODUCTION UNDER DIRECT SUNLIGHT

3.4.1 Introduction

The production of hydrogen using direct sunlight has significant advantages, since ultimately one has to utilize the catalyst in the direct sunlight. Many photocatalytic systems have been tried for the production of hydrogen form water using direct sunlight (Koca and Sahin, 2002; Alfano *et al.*, 2000). In this present study, attempts have been made to evaluate the photocatalytic activity of CdS-U nanoparticle in the direct sunlight.

3.4.2 RESULTS AND DISCUSSION

Direct sunlight mediated photocatalytic experiments have been carried out with Pt/CdS-U catalyst, which is having higher photocatalytic activity for the hydrogen production in the UV light among the prepared CdS nanoparticles. The experiments have been carried out in the month of February 2006 between 10 AM and 4 PM. For photocatalytic experiments, 0.1 g of 1 wt% Pt loaded CdS-U particles have been taken in a circular reactor (r = 4.5 cm) with 50 ml of aq solution containing 0.35 M Na_2SO_3 and 0.24 M Na_2S as sacrificial agent. The catalyst particles are allowed to settle down in the bottom the reactor. The reaction mixture has been irradiated with direct sunlight for 30 min to attain thermal equilibrium. During this period thermal expansion of gas molecule takes place and the gases evolved during this time have been leaked out. The gas evolved after the equilibrium period have been collected over the gas burette and analyzed using gas chromatography. The complete reaction setup is shown in the following Fig. 3.15 a and b.

(a)

(b)

Fig. 3.15. Direct sunlight assisted photocatalytic hydrogen production set up

The thermal expansion of gases molecule and evaporation of water during the reaction has been evaluated using a blank experiment *i.e.* without the catalyst. The observed values are subtracted from the experimental values. It is observed that 1153 μmol h^{-1} /0.1g of hydrogen evolution have been observed for 1 wt% Pt loaded

CdS-U in the direct sunlight. The reaction has been carried out for 6h continuously and observed that there is no significant decrease in the hydrogen evolution rate during this period. The reaction mixture has been re-used for the second day and it is observed that there is not much of a change in the rate of hydrogen evolution on the second day. After two days, the same catalyst was filtered from the reaction mixture and the photocatalytic hydrogen production activity is measured with 400 W Hg lamp. It has been observed that the photocatalytic activity (1088 μmol h^{-1} /0.1g) remains almost constant even after the direct sunlight experiments.

3.5 CONCLUSIONS

In this study, CdS nanoparticles prepared from zeolite matrices and ultrasonic precipitation methods have been shown to be efficient photocatalyst for hydrogen production. In the first method, the zeolite matrix acts as a templating agent preventing the growth of CdS particles during precipitation process resulting in the formation of nanoparticles. In the second method, the CdS mesoporous nanoparticles are formed due to the high energetic ultrasonic waves. The CdS nanoparticles prepared by both the methods exhibit blue shift in the absorption edge (UV-Vis) due to particle size effect. Mixed cubic and hexagonal phases have been observed in the XRD study for the CdS nanoparticles prepared from the zeolites. Whereas only cubic phase has been observed in the ultrasonic precipitation method. The nanoparticles are of uniform size with a particle size distribution in the range of 6-12 nm and 5 ± 1 nm in zeolite template and ultrasonic precipitation methods respectively. Photocatalytic activity study on these materials, clearly show that the nanoparticles exhibit higher activity compared to the bulk samples. Surface area, morphology and particle size of the CdS are important factors, which affect their performance as catalyst for hydrogen evolution. Presence of noble metals such as Pt and Pd greatly enhance the

photocatalytic activity of the synthesized CdS nanoparticles. Pt/CdS-U nanoparticles shows higher photocatalytic activity among the prepared catalyst. In the CdS-TiO_2 coupled system, Pt/CdS-U: N-TiO_2 shows higher activity when the ratio between the CdS and TiO_2 is 1. The direct sunlight experiment shows that the Pt/CdS-U catalyst is a promising catalyst for hydrogen production and it is proposed for further studies on this to develop for commercial scale hydrogen production purpose using direct sunlight.

CHAPTER 4

CHARACTERIZATION OF VISIBLE LIGHT ACTIVE N-DOPED AND N, S CO-DOPED TiO_2

4.1 N-DOPED TiO_2 BY $TiCl_3$ HYDROLYSIS

4.1.1 Introduction

Recently, the anion doped TiO_2 has attracted considerable attention due to its photocatalytic activity in the visible region (Hattori *et al*., 1998; Yamaki *et al.,* 2002) Even though TiO_2 is a promising photocatalyst for the waste water purification (Hoffmann et *al*., 1995), exploitation for practical circumstances has not been achieved as expected, due to its poor light absorption in the visible region. Attempts have been made to improve the utility of TiO_2, by shifting its onset absorption from UV to visible region. Various noble/transition metal (or) metal ions have been doped into the TiO_2 lattice and the photocatalytic activity has been studied (Herrmann *et al.,* 1984; Karakitsou and Verykios, 1993), but none of them have been found to be satisfactory. Even though the visible light response of anion doped TiO_2 has been discovered in 1986 by Sato (1986), the recent work by Asahi *et al* (2001) has rekindled a great interest in TiO_2 as a visible light photocatalyst. Consequently, in the recent past few preparation methods have been reported in the literature for N, S, P, F, and B doped TiO_2 catalyst (Asahi *et al.,* 2001; Morikawa, *et al*., 2001; Umebayashi *et al.,* 2002; moon *et al.*, 2000; Sakthivel and Kisch, 2004). In parallel, some theoretical calculations have also been performed to suggest that anion doping of TiO_2 has considerable effect on the band gap alteration (Asahi *et al.,* 2001; Umebayashi *et al.,* 2002; Umebayashi *et al.,* 2003). Subsequently, N-doped TiO_2 (N-TiO_2) has been prepared by sputtering, ion implantation, chemical vapor deposition, sol-gel

method, oxidation of TiN and decomposition of N-containing metal organic precursors (Sano *et al.*, 2004; Tokudome and Miyauchi, 2004; Yang *et al.*, 2004; Kobayakawa *et al.,* 2004; Diwald *et al.*, 2004). The photocatalytic activities of such N-doped systems have been studied (Morowetz *et al*., 2004; Torres *et al*., 2004; Bacsa *et al.*, 2005).

Considerable success has been achieved in increasing the photocatalytic activity by decreasing the band gap with N-TiO_2 (Sato, 1986; Asahi *et al.,* 2001; Sakthivel *et al*., 2004; Irie *et al.*, 2003; Gole *et al.*, 2004; Chen and Burda, 2004; Valentin *et al.,* 2005; Nakamura *et al.*, 2004), due to either mixing of nitrogen p states with O 2p states on the top of the valence band or a creation of N-induced mid-gap level. The success in producing N-TiO_2 provides good opportunities for various applications like oxidation of CO, ethanol, acetaldehyde and NO_x removal at room temperature as well as the decomposition of dyes like methylene blue (Asahi *et al.,* 2001; Gole *et al.*, 2004; Sano *et al.,* 2004). However, there seems to be no consensus among the reports (Asahi *et al.,* 2001; Diwald *et al*., 2004; Irie *et al*., 2003; Gole *et al*., 2004; Valentin *et al*., 2005; Nakamura *et al*., 2004) about the state of doped nitrogen in the N-TiO_2 lattice. XPS analysis of N-TiO_2 shows the N 1s core level at binding energy (BE) between 396 and 397 eV and claimed the state of nitrogen to be either nitrogen anion (N^-) (Diwald *et al.*, 2004) or atomic N atoms [Asahi *et al.,* 2001; Sano *et al*., 2004), as explained in the oxidation of TiN (Saha and Tompkins, 1992). Additional N 1s peaks on N-TiO_2 were observed at 400 and 402 eV and are attributed to chemisorbed N_2 or adsorbed organic compounds (Asahi *et al.,* 2001; Saha and Tompkins, 1992). Sakthivel and Kisch (2003 and 2004) observed no anionic-like nitrogen species around 396 eV, rather a N 1s peak at 404 eV that corresponds to hyponitrite type nitrogen. Valentin *et al* (2005). recognized the above controversy in the assignment of

N 1s XPS result. They observed N 1s core level at 400 eV and hinted at a lower valent state for N. However recently, Chen and Burda (2004) observed N 1s core level at 401.3 eV from the detailed XPS investigations of nano N-TiO_2 and suggested that there is N-Ti-O bond formation due to nitrogen doping and no oxidized nitrogen is present. It is to be noted that the preparation procedure adopted was different in the above cases and this could have led to the different observations in XPS. In this chapter, a simple chemical preparation method for N-TiO_2 has been adapted and its photocatalytic activity in the decomposition of methylene blue under UV and Visible radiation has been studied. The results are compared with that of Degussa P25 catalyst and pure anatase TiO_2. A clear N states on the top of valence band could be identified and the consequent band gap reduction. The state of N to be more like an anion is demonstrated from the XPS results.

4.1.2 RESULTS AND DISCUSSION

4.1.2.1 Synthetic strategy

In our procedure, the synthesis of N-doped TiO_2 has been carried out in the presence of Na_2S (aq). The addition of Na_2S solution during the catalyst preparation is essential for N-doping in the TiO_2 lattice. The addition of Na_2S solution increases the ionic strength of the medium and it may also induce *in situ* formation of transient $(NH_4)_XTiS_X$ complex, which on slow hydrolysis results in the N-TiO_2 nanoparticles. In addition, the presence of Na_2S might be effective in purging of any of the dissolved oxygen by H_2S and thereby contributing to the N-doping in a reductive solution atmosphere. It has been confirmed by the blank experiments, by following the above procedure but without Na_2S addition, that the resultant material after calcination at 400 °C for 4 h in air is only pure TiO_2, without N-doping.

4.1.2.2 UV-Visible spectra

The UV-Vis light absorption spectra of N-TiO_2 as a function of calcination temperatures and pure TiO_2 prepared in our laboratory are shown in Fig. 4.1. Inset in Fig. 4.1 shows the optical absorption trailing edge (in eV) and hence band gap narrowing for N-TiO_2 calcined at 400 ^{0}C compared to pure TiO_2. Pure TiO_2 spectrum is provided for comparison. It can be seen from Fig.4.1 that the visible light absorption is high and extended up to 550 nm in the case of N-TiO_2 (Asahi *et al.,* 2001; Gole *et al*., 2004) calcined at 400 °C compared to pure TiO_2. Moreover, the light absorption in the visible region decreases very significantly as the calcination temperature increases above 400 °C. It may be due to the fact that, there is a decrease in the amount of N doping on the TiO_2 lattice with an increase in calcination temperature. It has also been observed in an earlier report (Ohno *et al*., 2003) that an increase in the calcination temperature decreased the amount of heteroatom doping in TiO_2. Inset in Fig. 4.1 shows a clear cut shift in optical absorption edge towards visible region by 0.13 eV on N-TiO_2 at 3.26 eV compared to 3.39 eV. The above shift of 0.13 ± 0.01 eV suggests the localized nature of nitrogen species in the TiO_2 lattice. These nitrogen species occupy some of the oxygen positions in the lattice. This also rules out the occupancy of N in any other positions like interstitial sites, which should give rise to a mid gap band/level between valence and conduction bands. It is to be pointed out that there is an excellent agreement between the energy width of the localized N states observed above and the calculated one to be 0.14 eV from the density functional theory by Valentin *et al* (2005) and in general, by Asahi *et al* (2001). Recent N-induced mid gap levels suggested by Nakamura *et al* (2004) and oxygen vacancy induced state below the conduction band suggested by Ihara *et al* (2003) for N-TiO_2 is in contradiction to the present results. It

is to be noted that the evidence to show the presence of nitrogen is not direct and the average particle size is close to 1 μm as reported by Nakamura *et al* (2004). It is also likely that the electronic structure changes with particle size. Further, the amount of nitrogen is found to be too small and the preparation methods are also different in both the procedures of Nakamura *et al* (2004) and Ihara *et al* (2003) compared to the present method.

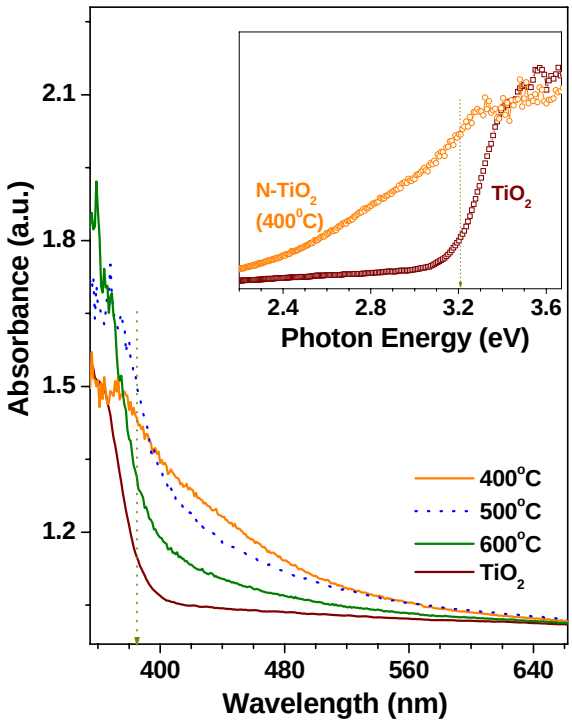

Fig.4.1. UV-Visible absorption spectra of N-doped TiO_2 at different calcination temperatures and pure TiO_2. Inset shows a shift in absorption edge towards visible region on N-TiO_2 compared to TiO_2 and hints at the localized nature of nitrogen

4.1.2.3 X-ray diffraction study

In Fig. 4.2, the XRD patterns of different TiO_2 samples are provided. The presence of anatase phase is observed for the N-TiO_2 sample calcined at 400 °C. The anatase phase has been retained without phase transformation to rutile even after increasing

the calcination temperature to 600 °C. It can also be seen from the XRD patterns that the N-TiO_2 samples show peak broadening compared to pure TiO_2, which indicates the formation of nanoparticles. The crystallite size of the N-TiO_2 particle has been calculated using Debye-Scherrer equation (Cullity, 1987) and the values are given in Table 4.1 along with other physical characteristics.

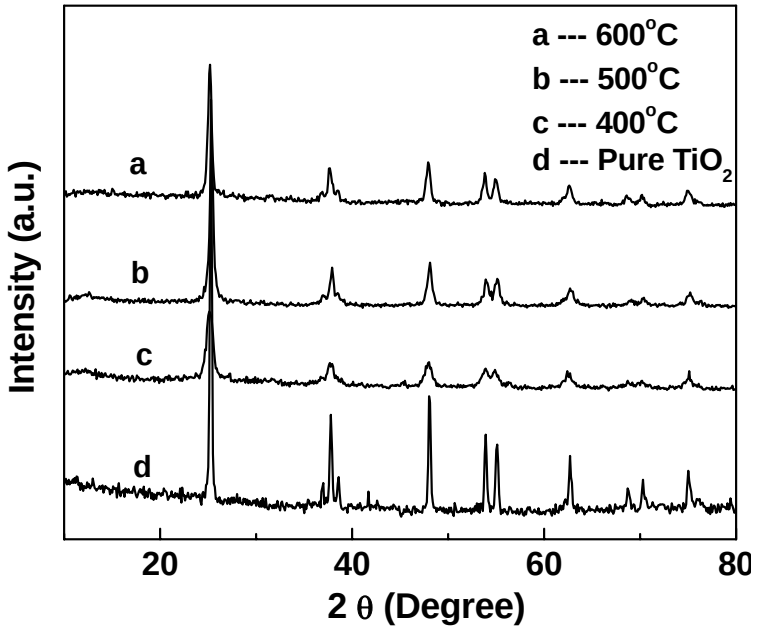

Fig.4.2. X-ray diffraction patterns of N-doped TiO_2 calcined at various temperatures and pure TiO_2 (anatase).

It can be seen from Table 4.1 that as the calcination temperature increases, the particle size increases caused by the agglomeration of particles at high temperatures. In addition to this, there is no change in the "d" spacing values, which implies that in N-TiO_2 samples, N has been introduced into the lattice without changing the average unit cell dimension. A good correspondence between the XRD and optical absorption results of TiO_2 and N-TiO_2 calcined at 600 ^{0}C hints at the progressive loss of N due to heat treatment and moving towards N-free TiO_2.

Table 4.1 Specific surface area, particle size and crystalline phase for N-doped TiO_2 at different calcination temperatures and pure TiO_2

Sample	Calcination Temperature (°C)	Specific Surface area (m^2/g)	Crystallite size (nm)	Anatase crystalline phase (%)
N-TiO	400	73	12	100
N-TiO_2	500	66	15	100
N-TiO_2	600	37	20	100
Pure TiO_2	400	14	35	100

4.1.2.4 Surface area

The specific surface area of the N-doped and bulk TiO_2 samples are given in table 4.1. It can be seen from the table that, the N-doped TiO_2 samples calcined at 400 °C show higher surface area of 73 m^2/g and an increase in a calcination temperature results in the decrease in the values of specific surface area. Thus with increase in temperature, agglomeration of particles will takes place and it can be seen from the increase in the crystallite size of the particle.

4.1.2.5 Electron microscopic analysis

It is well known that when increasing the calcination temperature, agglomeration will be favored, which results in an increase in the particle size and it has been clearly seen from the XRD studies. It is further confirmed from the TEM result given in Fig. 4.3 that uniform size (14 ± 2 nm) of spherical type particles have been observed for the N-TiO_2 calcined at 400 °C. The TEM picture of N-TiO_2 calcined ≥500 °C shows significantly larger particles (not shown here).

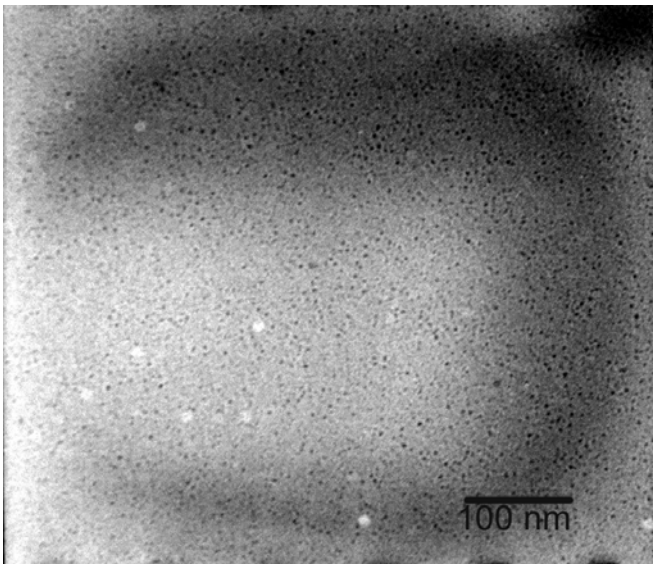

Fig. 4.3. TEM image of N-doped TiO_2 calcined at 400°C

Fig. 4.4 shows the electron diffraction pattern obtained for the N-doped TiO_2 calcined at 400 °C. The'd' values are calculated from the electron diffraction pattern and compared with the'd' values obtained from our XRD data and literature report. Thus, the obtained 'd' values have good correspondence with the 'd' values for the anatase crystalline phase.

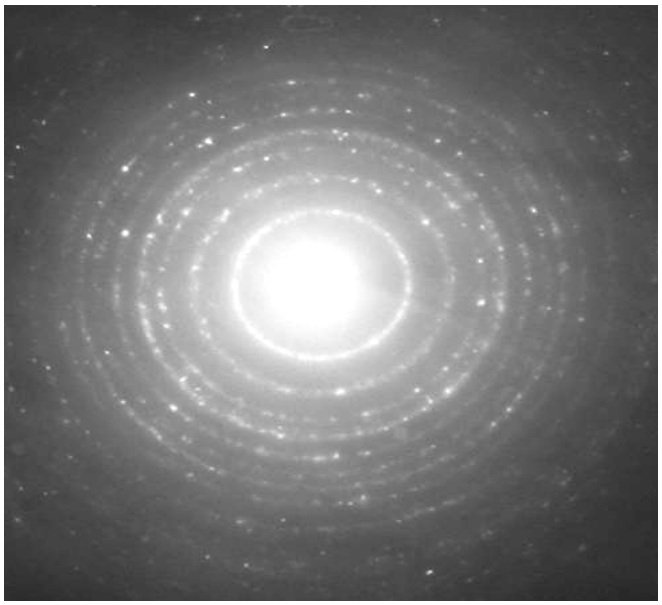

Fig. 4.4. Electron diffraction pattern of N-doped TiO_2 calcined at 400 °C

4.1.2.6 X-ray photoelectron spectroscopy

The XPS spectra of TiO_2 and N-TiO_2 samples recorded are shown in Fig. 4.5 for Ti 2p, N 1s and O 1s core levels. It is to be noted that the above results are after *in situ* scraping the surface of the pellets of both the catalysts within the ESCA spectrometer under ultra high vacuum conditions. This is mainly to remove any contribution from the atmospheric degradation. Indeed, the un-scraped surface displays high carbon (some carbonate also) content along with a relatively low intensity Ti 2p features (not shown). However, carbon and carbonate contamination has been fully removed by scraping the catalyst surface and that enhances the intensity of all intrinsic features. Ti $2p_{3/2}$ core level appears at 459.3 and 458.5 eV for TiO_2 and N-TiO_2 calcined at 400^0C, respectively. Lower BE of Ti 2p in N-TiO_2 shows that the electronic interaction of Ti with anions is considerably different than on TiO_2. This suggests that TiO_2 lattice is considerably modified due to N-substitution. Lower BE of Ti 2p in N-TiO_2 can also be explained on the basis of covalency between the titanium and nitrogen bond. It is known that if the electronegativity of the anion decreases, the percentage ionicity will decrease (Viswanathan, 2003) as a result, the electron density around the anion decreases resulting in the increase in electron density around the cation. Our results on Ti 2p core levels are consistent with that of Chen and Burda (2004) and Saha *et al* (1992). Oxygen 1s core level peak appears around 530 eV in both cases, indicating nature of oxygen to be similar. Nonetheless, a broadening on the higher BE side at 531.5 eV (indicated by arrow) is clearly visible in the case of N-TiO_2 sample. It is deconvoluted and shown in Fig. 4.6. This indicates the presence of another type of oxygen due to the more covalent nature of the N-TiO_2. This might be due to the presence of oxygen and nitrogen from the same lattice units in TiO_2. However a small amount of contamination that might remain on the surface cannot be ruled out.

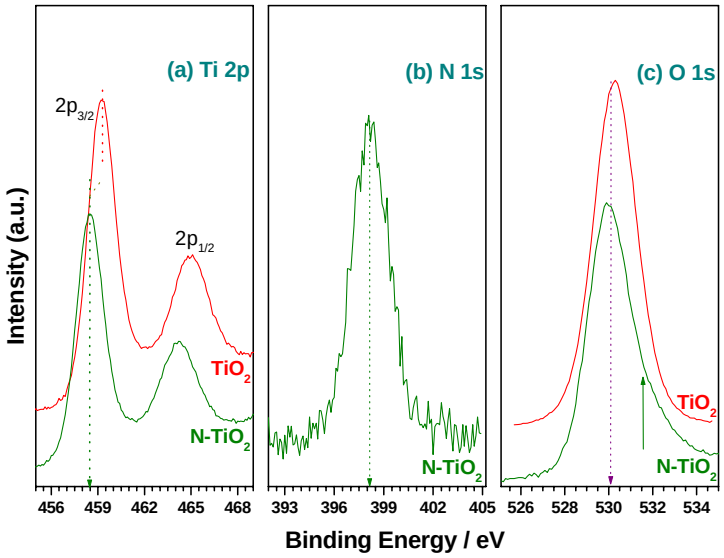

Fig.4.5 X-ray photoelectron spectral details collected from TiO_2 and N-TiO_2 samples (a) Ti 2p, (b) N 1s and (c) O 1s core levels. Note the shift in Ti 2p binding energy after the introduction of N into the TiO_2 lattice

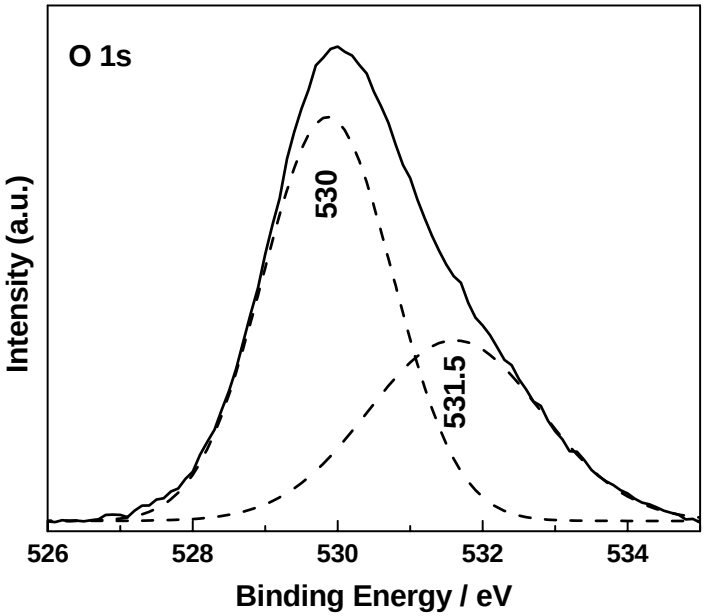

Fig. 4.6. X-ray photoelectron spectrum of O 1s core level (deconvoluted) for N-TiO_2 sample

Nitrogen 1s core level from N-TiO_2 shows a single peak at 398.2 eV. This N 1s peak is attributed to the anionic N^- in O-Ti-N linkages. Nitrogen from simple chemisorbed nitrogen or TiN should appear at ≤397.5 eV and NO or NO_2 type species appear above 400 eV (Saha and Tompkins, 1992; Shinn and Tsang, 1991; Sugai *et al.*, 1991; Rainer *et al.*, 1997; Rodriguez *et al.,* 2000; Gyorgy *et al.*, 2003; Wagner *et al.*, 1979) Additionally, few nitrogen in the TiO_2 lattice also might reduce the electron density on nitrogen due to the high electronegativity of oxygen and hence a relatively higher BE observed compared to TiN. However, the observation of N 1s core level at 398.2 eV after high temperature calcination at 400 ^{0}C supports the conclusion that the nitrogen should be from the TiO_2 lattice as N-Ti-O linkages. Any significant interaction between N and O within the lattice would increase the BE of N 1s level and hence any direct significant interaction between N and O within the lattice is ruled out. It is further supported by the low BE of Ti 2p compared to that of pure TiO_2. A mixed phase of TiO_2-TiN is also ruled out due to the absence of two different Ti peaks in Ti $2p_{3/2}$ core level at ~459.5 eV (TiO_2) and 455 eV (TiN) (Saha and Tompkins, 1992; Gyorgy *et al.*, 2003). From the above observations it can be concluded that the peak observed in the present study at 398.2 eV is due to the N^- anion incorporated in the TiO_2 as N-Ti-O structural feature. It is relevant to point out the contradiction between the recent XPS findings by Chen and Burda (2004) on N-TiO_2 and the present results. It has been reported that N 1s feature appears at 401.3 eV and has been interpreted to be due to N-Ti-O linkages (Gole *et al*., 2004). However, an overall view from the BE of N in different environments hints that the presence of oxidized nitrogen such as Ti-O-N and/or Ti-N-O linkages should appear above 400 eV as reported by Saha and Tompkins (1992) and Gyorgy *et al* (2003). It might also be due to a different preparation procedure followed by Chen and Burda (2004).

It is clear from the above discussion that if the N atom is subtitutionally doped into the TiO_2 lattice, it is not likely to have significant interaction with nearby oxygen atoms. However, an interstitial N-doping in the anatase lattice is likely to have some strong interaction with nearby oxygen and hence a change in effective charge on the nitrogen species and hence a shift in the BE. Present results on N 1s BE at 398.2 eV suggest that it is comparable to N 1s BE (398.8 eV) in NH_3 (Wagner *et al.*, 1979). However, a lower BE results from some partial negative charge on N in N-TiO_2, and also supports for substitutional N-doping. It is likely that the interaction between N and O is strong for interstitial N doping, as in NO type species (Rodriguez *et al.*, 2000). The reported BE of >400 eV for N 1s core level by other investigators indicates either a possible O-N-Ti linkages (Sakthivel and Kisch, 2003: Gole *et al.*, 2004), or some surface oxidation. The above controversies involved in the interpretation of XPS results of N-TiO_2 remain to be clearly resolved.

4.1.3 Visible light photocatalytic activity

The photocatalytic activity of N-TiO_2, pure TiO_2 and Degussa (P25) samples have been studied by measuring the percentage decomposition of methylene blue (MB) in aqueous solution. It can be seen from Fig. 4.7 that the photocatalytic activity of N-TiO_2 samples and Degussa sample have comparable activity while the synthesized TiO_2 has much lower activity under UV condition. In the visible region, the N-TiO_2 samples (calcined at 400 and 500 ^{0}C) show higher activity than the Degussa and pure TiO_2 samples. Nevertheless the activity further decreases as the calcination temperature is increased to 600 ^{0}C. The calcination temperature is found to have influence on the activity of the titania in the visible region only, whereas in the UV region there is no perceptible influence.

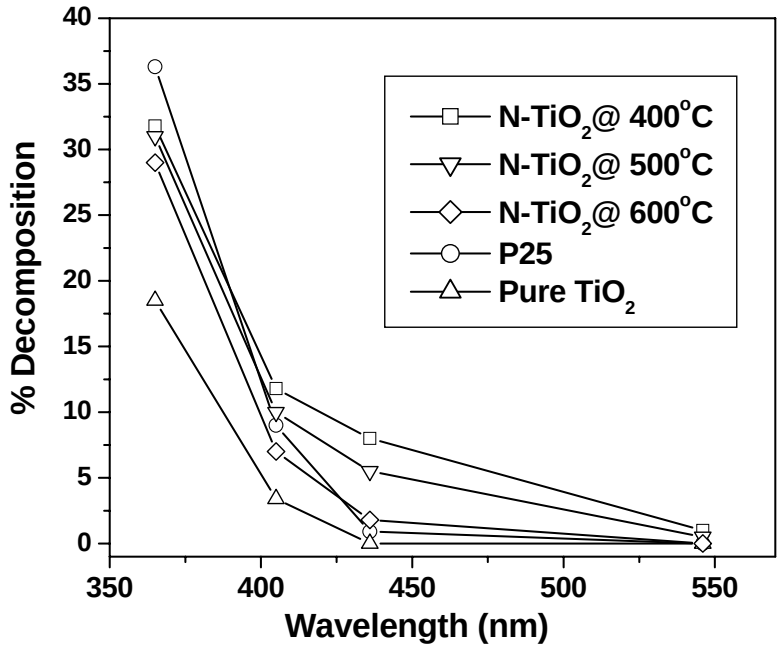

Fig. 4.7. Photocatalytic decomposition profiles of methylene blue over N-TiO_2 (calcined at 400, 500 and 600 ^{0}C) pure TiO_2 and Degussa (P-25) at different wavelengths

In the visible region, it can be seen that as the temperature of calcination is increased from 400 to 600 ^{0}C, the photoactivity is found to decrease. This decrease in activity may be attributed to the removal of the nitrogen from the TiO_2 matrix. This is evident from the shift in the absorption edge to lower wavelength (Fig. 4.1). This shift is not due to the change in the particle size of the catalyst. The observed decrease in the particle size is expected to shift the absorption edge to the visible region. An attempt has been made to compare the photocatalytic activity of our N-TiO_2 with the literature reports on S-doped TiO_2 (Umebayashi *et al.,* 2003) and carbonate doped TiO_2 (Ohno *et al.*, 2004). Even though the experimental parameters, like intensity of light (a major factor), initial concentration of the MB, experimental time, temperature and the amount of catalyst used are very different, the N-TiO_2 sample used in the present study is (after normalizing for the variables) about 10 times more active compared to the carbonate doped sample (Ohno *et al.*, 2004) and roughly 50% active compared to

S-doped TiO_2 (Umebayashi *et al*., 2003) The lower activity of N-doped TiO_2 in the present study compared to the S-doped TiO_2 reported in the literature may be due to the difference in the light intensity. In our experiments monochromatic wavelength has been employed by using monochromatic filters with 400 W Hg lamp, whereas in literature cut off filters have been used with 1000 W Xe lamp as light source, which provides higher intensity of light when compared to our experimental conditions.

4.2 N-DOPED TiO_2 BY THERMAL DECOMPOSITION OF Ti–SALEN COMPLEX

4.2.1 Introduction

In this present study, attempt has been made to prepare N-doped TiO_2 by decomposing Ti containing metal complex. It is believed that when decomposing Ti-salen complex, a few Ti-N bonds will be retained in the resulting TiO_2 samples, which leads the N-doping in the TiO_2 lattice. Also, the thermal decomposition in the vacuum sealed tubes will control the decomposition rate due to the availability of limited amount of oxygen and provides maximum possibilities for the N-doping. In addition, the slow decomposition of metal complex prevents the particle agglomeration to a larger extent and the particles are formed in the nano range. The photocatlytic activity in the visible region has been studied for the methylene blue decomposition.

4.2.2. RESULTS AND DISCUSSION

4.2.2.1. TGA analysis

The thermal decomposition profile of Ti- salen and pure salen ligand in air are shown in Fig. 4.8. The decomposition temperature of pure salen ligand is between 250 to 270 °C, whereas Ti-salen complex decomposes at 400 to 500 °C, in total 40 %

decomposition have been attained up to 800 °C. Based on this TG profile, the samples are calcined at 400 °C in air followed by vacuum, N_2 atmosphere. The TG profile of air calcined sample at 400 °C shows, no significant weight loss, which indicates that complete decomposition of the organic precursor moiety during the calcination process.

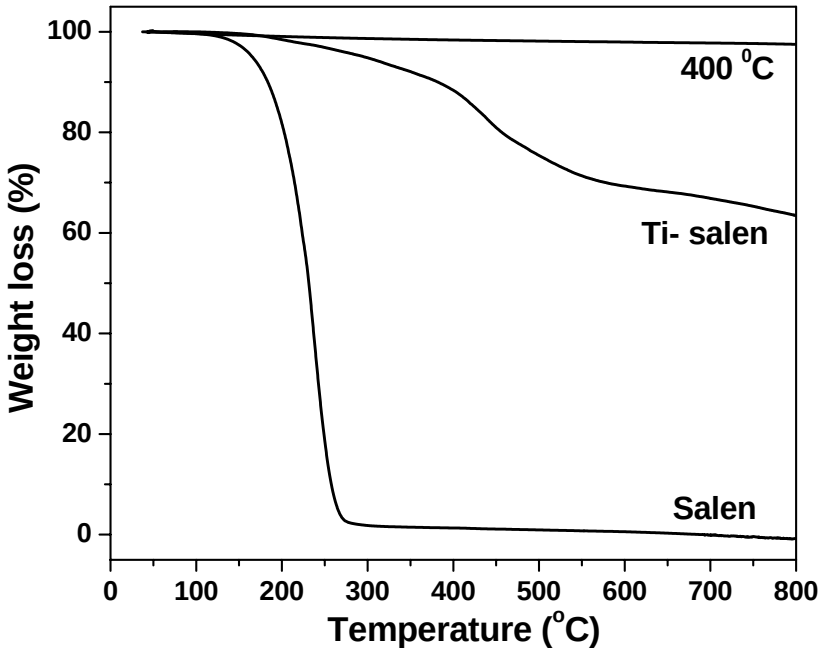

Fig. 4.8. TGA profile of salen, Ti-salen and N-TiO_2 calcined at 400 °C

4.2.2.2. UV-Visible spectra

The UV-Vis light absorption spectra of N–doped TiO_2 and pure TiO_2 are shown in Fig. 4.9. It can be seen from Fig. 4.9 that, the visible light absorption is more in the case of N-doped sample calcined at 400 °C. The light absorption onset is shifting by ~100 nm towards visible region (red shift) for the N-doped samples compared to that of undoped TiO_2.

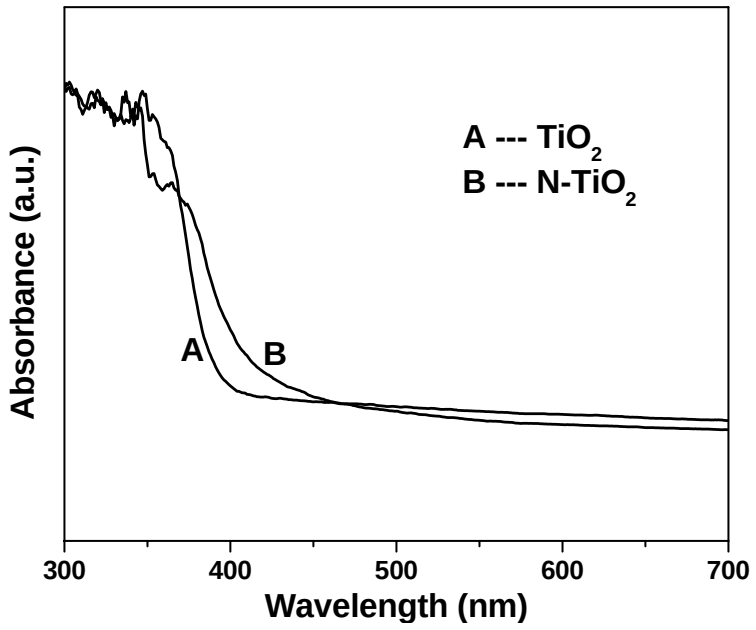

Fig. 4.9. UV-Visible absorption spectra of nitrogen doped TiO_2 and pure TiO_2

4.2.2.3. X-ray diffraction studies

In Fig. 4.10, XRD patterns for the undoped and N-doped TiO_2 samples are shown. The presence of anatase phase is observed for both the N-doped sample calcined at 400 °C and undoped sample. It is known that the anatase phase has higher photocatalytic activity than the rutile phase. It can also be seen from XRD patterns that the N-doped samples show peak broadening when compared to pure TiO_2, which indicates the formation of nanoparticles. In addition to this, there is no change in the "d" spacing values, which implies that in N-doped samples, N has been introduced into the lattice without changing the average unit cell length. It has been proposed that the light absorption in the visible region is due to distortion in the local crystal lattice like S doping on TiO_2 (Ohno *et al.*, 2003).

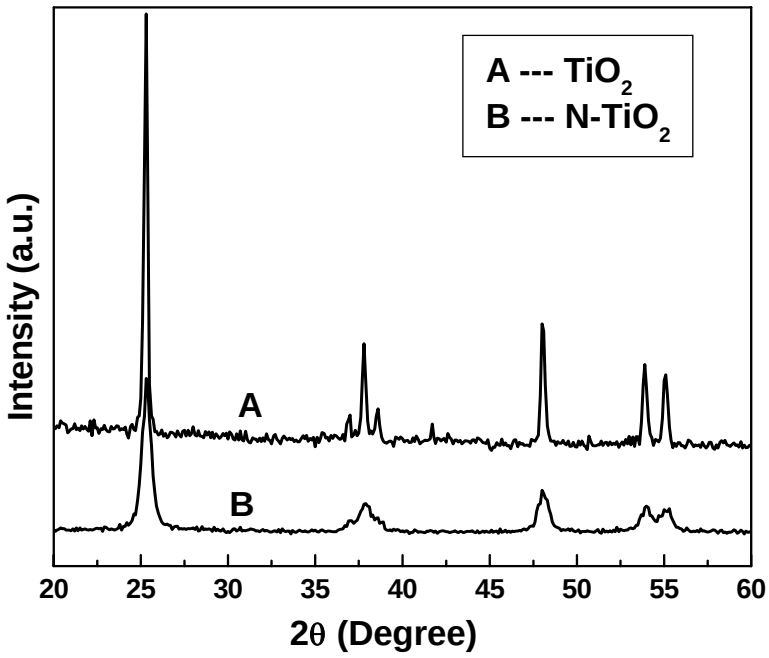

Fig. 4.10. X-ray diffraction patterns of N-doped TiO_2 and undoped TiO_2 calcined at 400 ^oC

4.2.2.4. Surface area

The specific surface area for the N-doped TiO_2 and pure TiO_2 have been calculated. It is observed that, the specific surface area are 68 m^2/g and 14 m^2/g for the N-doped TiO_2 and pure TiO_2 respectively.

4.2.2.5. Electron microscopic analysis

The TEM result is shown in Fig. 4.11. It can be seen from the Fig. 4.11 that spherical type particles have been observed in the range of ~ 14 nm in size for the N- doped samples calcined at 400 °C (for pure TiO_2 the particle size is 35 nm) and also the electron diffraction pattern (not shown) indicates the presence of pure anatase phase, which is more photoactive than rutile phase.

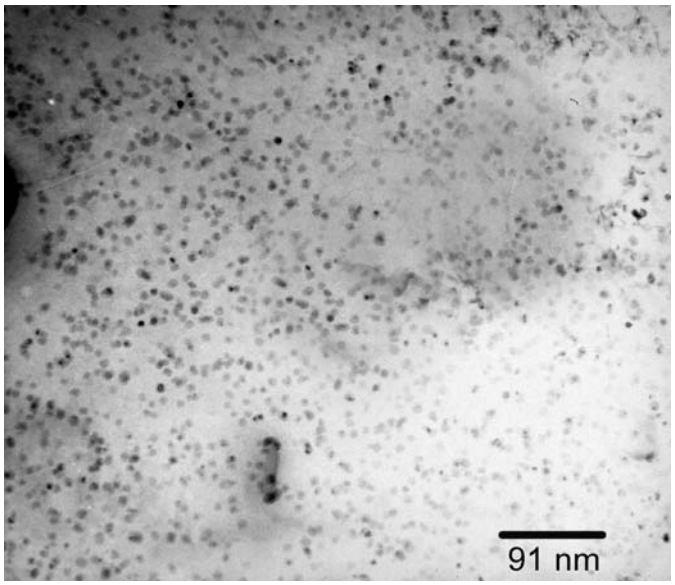

Fig. 4.11. TEM image of N-doped TiO_2 calcined at 400 °C

4.2.2.6. X-ray photoelectron spectroscopy

The XPS spectra of N-doped sample and pure TiO_2 are given in the Fig.4.12. Ti $2p_{3/2}$ core level appears at 459.3 and 458.7 eV for TiO_2 and N-TiO_2 calcined at 400 ^{0}C, respectively. The shift in the binding energy to lower energy for N-doped samples when compared to pure TiO_2 implies that the N replaces the O in the TiO_2 crystal lattice. N-doping in TiO_2 lattice reduces the positive charge on Ti due to its lesser electronegativity when compared to oxygen. In another way also the lowering of the BE of Ti 2p in N-TiO_2 can be explained on the basis of covalency between the Ti and nitrogen bond. It is known that if the electronegativity of the anion decreases, the % ionicity will decrease (Viswanathan, 2003), as a result, the electron density around the anion decreases resulting in the increase in electron density around the cation.

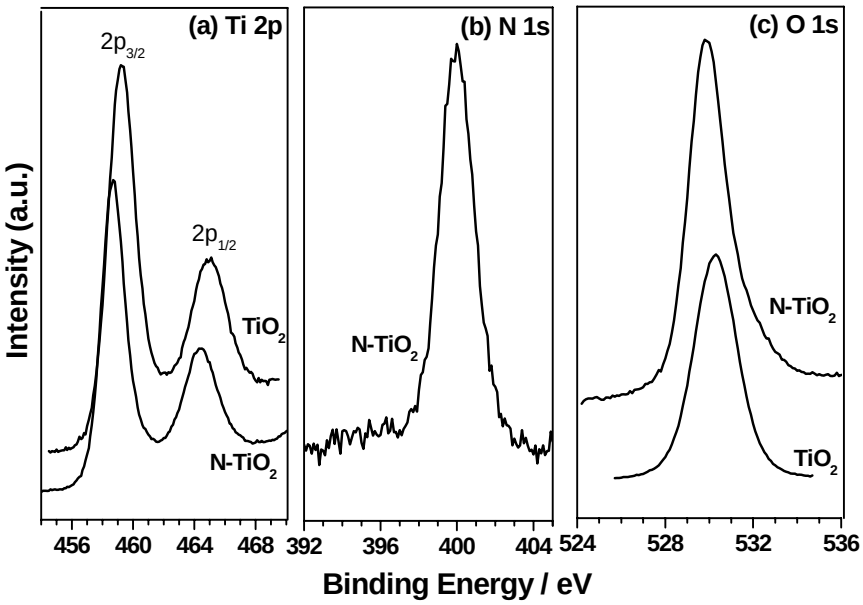

Fig. 4.12 X-ray photoelectron spectra of TiO_2 and N-TiO_2 samples (a) Ti 2p, (b) N 1s and (c) O 1s core levels

Nitrogen 1s core level from N-TiO_2 shows a single peak at 400 eV. Nitrogen from simple chemisorbed nitrogen or TiN should appear at ≤ 397.5 eV and NO or NO_2 type species appear above 400 eV (Saha and Tompkins, 1992; Shinn and Tsang, 1991; Nakamura *et al.*, 2004). The observed peak at 400 eV shows that there is a slight negative charge on the doped N atom. This may be due to nitrogen in the TiO_2 lattice could reduce the electron density on nitrogen due to the high electronegativity of oxygen and hence a relatively higher BE observed compared to TiN. However, the presence of N 1s after high temperature calcination at 400 ^{0}C with a BE at 400 eV typically supports that the nitrogen should be from the TiO_2 lattice as N-Ti-O linkages (Chen and Burda, 2004). Any significant interaction between N and O within the lattice would increase the BE of N 1s and hence any direct significant interaction between N and O within the lattice is ruled out. From the above observations it can be concluded that the peak observed in our study at 400 eV is due to the N incorporated

in the TiO_2 as N-Ti-O lattice, which is having comparatively a lesser negative charge than the N in the TiN.

A broad peak is observed for O 1s core level, broadening on higher BE side is clearly visible in the case of N-TiO_2 sample hinting the presence of another type of oxygen. It is deconvoluted and shown in Fig. 4.13. The peaks at 529.8 eV and 531.1 eV indicates the presence of O in the TiO_2 lattice and presence of O in N-Ti-O environment respectively. This clearly indicates that N-doping on TiO_2 causes an increase in the covalent nature of TiO_2.

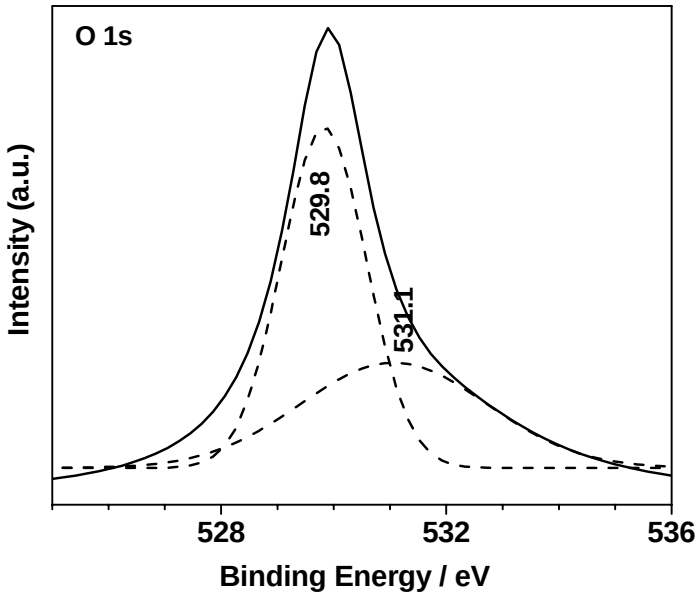

Fig. 4.13 X-ray photoelectron spectrum of O 1s core level (deconvoluted) for N-TiO_2 sample

4.2.2.7. Visible light photocatalytic activity

Photocatalytic decomposition of methylene blue has been carried out both in visible and UV region for N-doped TiO_2. The experiments have also been carried out for commercial sample P25 (Degussa) and laboratory synthesized pure TiO_2 for comparison purposes. The photocatalytic decomposition profile of 50 ppm methylene

blue is shown in Fig. 4.14. It has been observed that the complete decomposition of methylene blue has been achieved within 2.5 hours of irradiation with 400W Hg lamp for the N-doped TiO_2. Also it can be seen from the Fig. 4.14. (inset) that the photocatalytic activity of N-doped sample shows lower activity than in the Degussa catalyst in the UV region at 365 nm, whereas in visible region at 405 and 436 nm the N-doped sample shows higher activity than the Degussa sample. This corroborates our observation with UV-Vis spectra of the two samples, viz, the nitrogen containing TiO_2 has absorption in the visible region and the pure TiO_2 absorbs only in the UV region. It indicates that N-doped samples are more active in the visible region when compared to the Degussa catalyst. It is pertinent to point out that the laboratory synthesized pure TiO_2, even though present as anatase, has a lower photocatalytic activity in the UV-Vis region studied compared to Degussa sample.

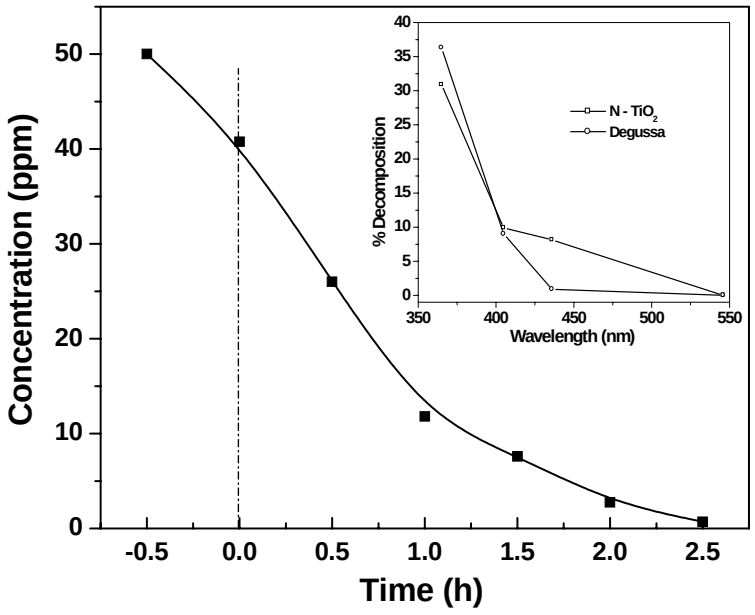

Fig. 4.14. Phototcatalytic decomposition profile of methylene blue over nitrogen doped TiO_2. (In the inset the 30 minute photocatalytic activity of the nitrogen doped and Degussa samples are compared as a function of wavelength).

4. 3 N-DOPED TiO_2 BY THERMAL DECOMPOSITION OF Ti –MELAMINE COMPLEX

4.3.1 Introduction

Though, there are significant reports for the preparation of N-doped in TiO_2 (Asahi *et al.,* 2001; Sakthivel and Kisch, 2003; Gole *et al.,* 2004; Nosaka *et al.,* 2005; Sano *et al.,* 2004), convenient preparation methods are still not available. With this view, in the present study, an attempt has been made to prepare N-doped TiO_2 by decomposing Ti melamine complex and to study photocatalytic activity in the visible region.

4.3.2 RESULTS AND DISCUSSION

4.3.2.1 TGA analysis

The thermal decomposition profile of Ti- melamine and pure melamine in air are shown in Fig. 4.15. The decomposition temperature of pure melamine is between 320 to 350 °C, where as Ti-melamine complex shows three regions 50-150, 300 to 450 and 600-700 °C, in total 40 % decomposition have been attained up to 800 °C. This indicated that complete decomposition of the unbounded/adsorbed melamine on the TiO_2 surface. The TG profile of air calcined sample at 400, 500 and 600 °C supports the above observation.

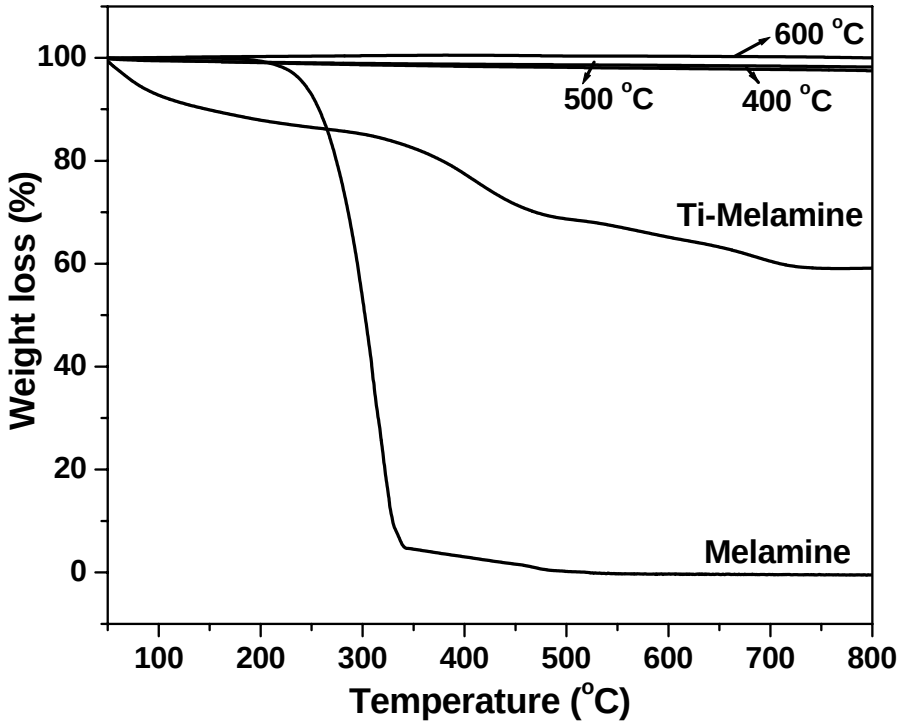

Fig. 4.15. TGA profile of melamine, Ti-Melamine and N-TiO_2 calcined at 400, 500 and 600 °C

4.3.2.2. UV-Visible spectra

The UV-visible absorption spectra of N-doped TiO_2 and bulk TiO_2 samples are shown in Fig. 4.16. It can be seen from the figure, that there is a red shift in the onset absorption (~120 nm) for N-doped samples when compared to undoped TiO_2. The absorption spectrum of 400 °C and 500 °C calcined samples are comparable, whereas the sample calcined at 600 °C shows comparatively lesser shift in the onset absorption. This can be attributed by the reduction in the amount of Nitrogen doped in the samples, as a result of higher calcination temperature.

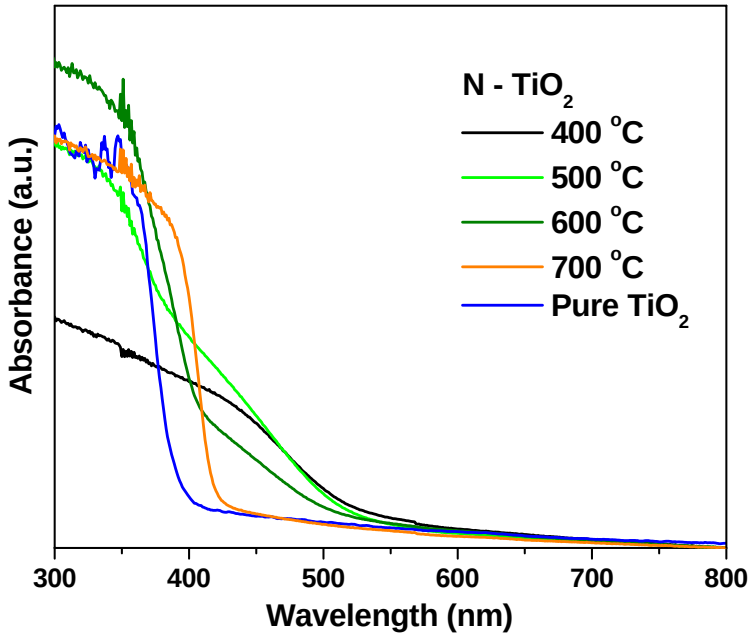

Fig. 4.16. UV-Visible absorption spectrum of N-doped TiO_2 at different calcination temperatures and pure TiO_2

4.3.2.3. X-ray diffraction studies

Fig. 4.17 shows the X-ray diffraction pattern of bulk and N-doped TiO_2 samples. The presence of anatase phase have been observed for the bulk and N-TiO_2 samples with X-ray line broadening in the case of N-doped samples indicating the formation of nanoparticles. But, when the calcination temperature was increased to 600 °C, formation of rutile phase, a high temperature phase, can also be seen (shown as "R") in the Fig.4.17.

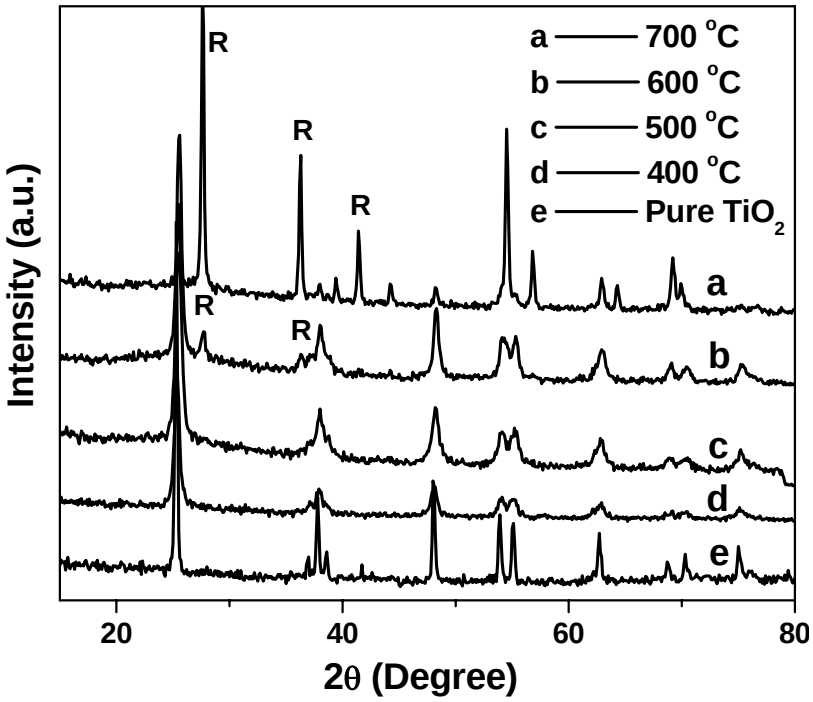

Fig. 4.17. X-ray diffraction patterns of N-doped TiO_2 calcined at various temperatures and pure TiO_2 (anatase)

4.3.2.4 Electron microscopic analysis

The surface morphology of the N-doped TiO_2 nanoparticle has been studied by scanning electron microscopy. The SEM picture (in 2 magnifications) of the N-doped TiO_2 sample are presented in Fig. 4.18. The growth of mixture of spherical and leave like particles of N-doped TiO_2 have been clearly observed for the 400 °C calcined samples. The transmission electron micrograph of the N-doped TiO_2 sample is shown in Fig.4.19. Particles in nanosize range are observed for the N-doped TiO_2 sample calcined at 400 °C in air. In addition, the presence of spherical type particles are seen from the TEM. The exact particle size of 25 nm for the prepared sample calcined at 400 °C has been calculated from the micrograph.

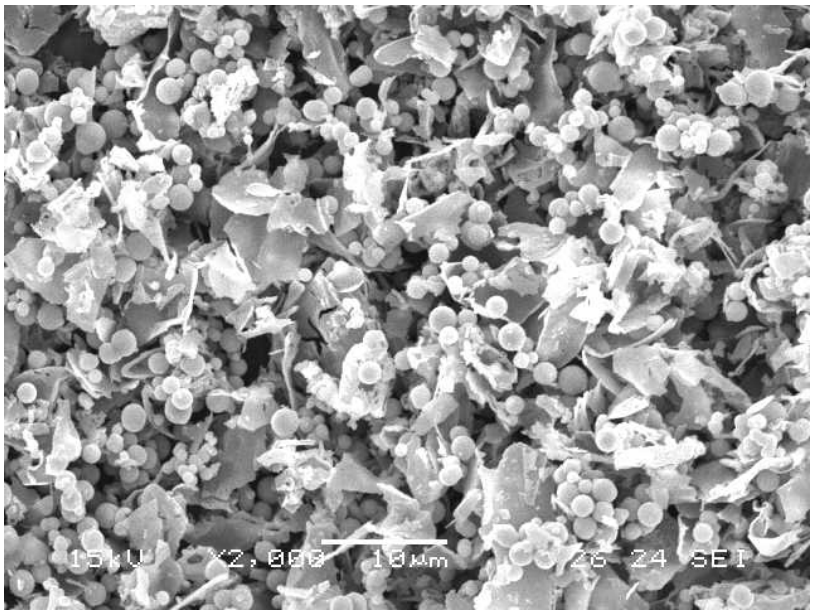

(a)

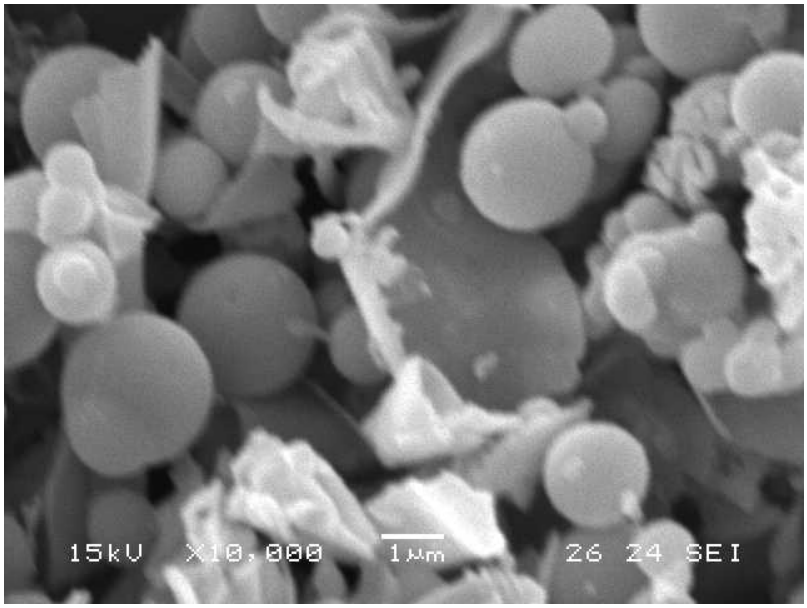

(b)

Fig. 4.18. SEM photographs of N-doped TiO_2 calcined at 400 °C

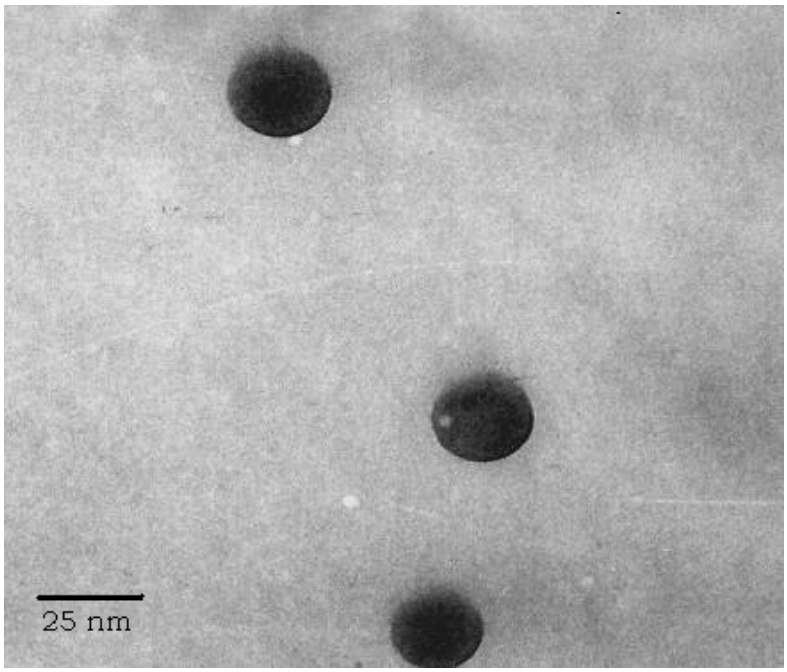

Fig. 4.19. TEM image of N-doped TiO_2 calcined at 400 °C

4.3.2.5 X-ray photoelectron spectroscopy

The chemical state of doped nitrogen in the TiO_2 was studied by X-ray photoelectron spectroscopy and shown in 4.20 a and b. Fig. 4.20b (black line) shows that, the N 1s peak for the N-doped TiO_2 samples calcined at 400 °C. The obtained broad peak centered around 400 eV is deconvoluted. (green line). On deconvolution four different peaks at 396.2, 398.4, 400 and 401.5 eV are discernible. The observed peak at 396.2 eV is attributed to the presence of Ti-N bond in the TiO_2 lattice (Asahi *et al*., 2001; Kobayakawa *et al.*, 2004). The observed peaks at 401.3 eV and 400 eV are respectively, due to the presence of nitrogen in the N-Ti-O environment and presence of N atoms in the organic compounds on the surface (or) in grain boundaries (Sano *et al*., 2004; Chen and Burda, 2004). Nevertheless, the presence of N in the surface of the sample as adsorbed N_2 like species could be seen from the observed peak at 398.4 eV. The present results are in accordance with the values reported in the literature for the N doped TiO_2 sample (Saha and Tompkins, 1992; Li *et al*., 2005a and 2005b).

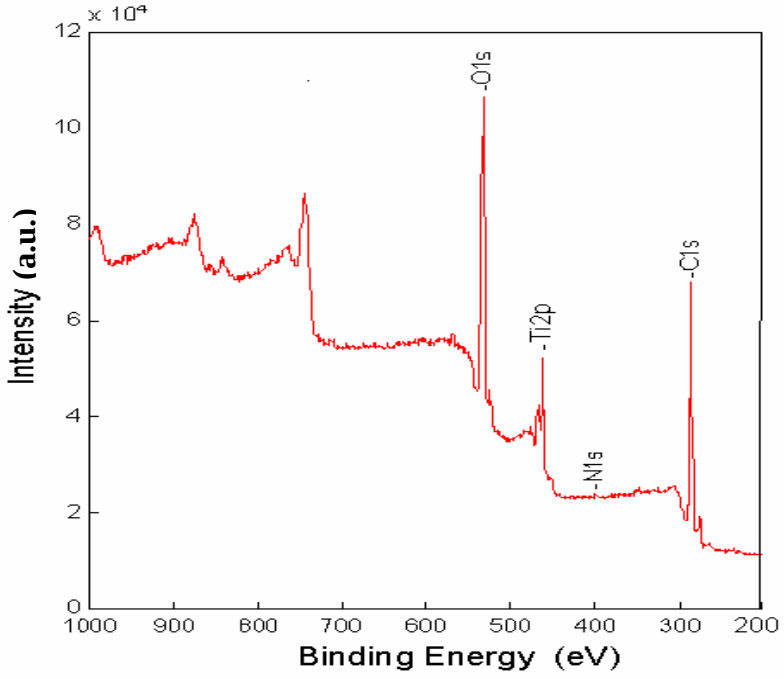

(a)

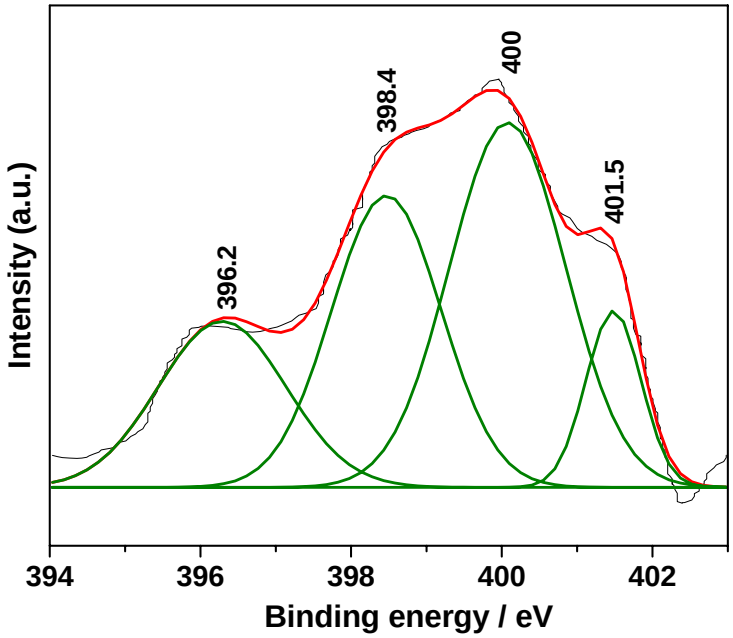

(b)

Fig. 4.20. X-ray photoelectron spectrum of (a) N-TiO_2 and (b) N 1s level for N-TiO_2 samples

4.3.3 Visible light photocatalytic activity

The visible light decomposition profile of methylene blue over N-doped samples is shown in Fig. 4.21. It can be seen that, there is significant change in the decomposition of methylene blue as the calcination of temperature is increased to 600 °C. The rate of decomposition is high in the case of 500 °C calcined sample when compared to other two samples. The lower rate of decomposition of methylene bule for 600 °C calcined sample could be explained by the decreased amount of N in the N- doped TiO_2. The UV-visible absorption spectrum of the corresponding sample also supports our observation. Nevertheless, between 400 and 500 °C calcined samples, the later one is more active than the former due to higher crystalline nature (anatase). In conclusion, ~ 40 % of methylene blue decomposition has been achieved within 3 h by the N-doped TiO_2 sample in the visible region alone. Where as, in UV + Visible region, complete decomposition of methylene bule has been achieved within 1 h for the 400 °C calcined N-doped TiO_2 samples (not shown).

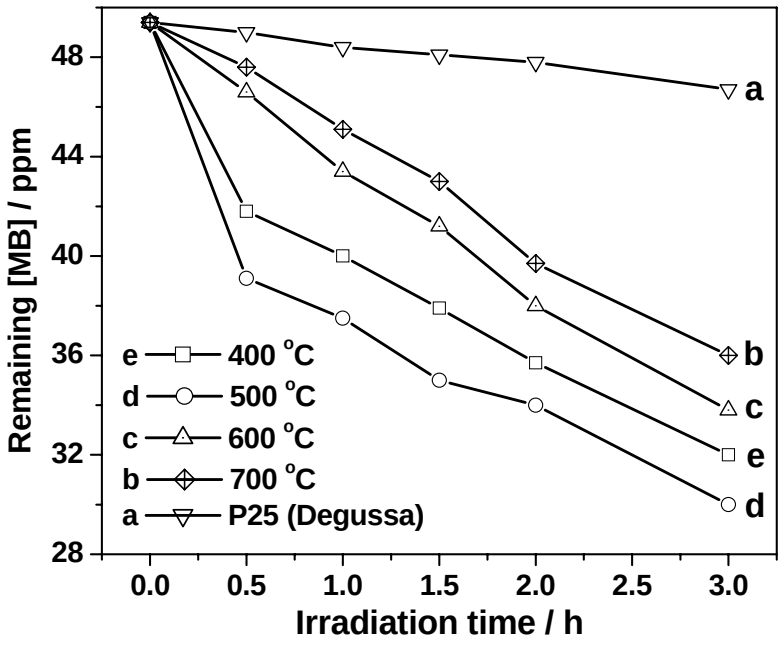

Fig. 4.21. Decomposition profile of methylene blue over N-doped TiO_2 sample in the visible light

4.4 N, S CO-DOPED TiO_2 BY THERMAL DECOMPOSITION OF Ti COMPLEX

4.4.1 Introduction

The eventual goal in photocatalysis is development of visible light active semiconductor based materials in order to utilize solar energy more efficiently. In recent times, the rehabilitated attention in photocatalysis is due to the light absorption by anion doped TiO_2 in the visible region compared to large band gap in pure TiO_2, which confines the utility of TiO_2 in the UV region (Hattori *et al*., 1998; Tamaki *et al.,* 2002). Photocatalytic processes have been examined extensively ever since the possibility of water splitting proposed by Japanese scientists in early 70s (Fujishima and Honda, 1972). A wide variety of materials like oxides, sulphides, and perovskites have been proposed and undertaken for photocatalysis (Hoffmann *et al.*, 1995; Sato *et al.*, 2003; Zou *et al*., 2001). Though generally it is conceived that TiO_2 semiconductor is the best option for promoting photocatalytic process, the maturity for optimization of the properties of the selected materials have not been evolved. Various methods have been implemented to activate TiO_2 in the visible region like sensitization with dye molecule, doping of metal ions in the crystal lattice and coupling with another semiconductor (Boschloo and Hagfeldt, 2005; Bandara *et al.,* 2004). Essentially, in all these cases, the electrons are promoted directly from energy levels of doped component to TiO_2 conduction band (or) injected into the conduction band from the other molecule or semiconductor surface, thereby the energy gap is minimized and charge separation prevents the recombination. But the lesser stability of the doped atom or sensitized molecule, and the less efficient interfacial electron transfer between the two phases make these systems insignificant to exploit photoactivation in visible region.

In the recent past, it has been proved that the anion doping to be quite efficient for the visible light activity (Sato, 1986; Asahi *et al.,* 2001). Various methods like chemical vapour deposition, laser ablation, sol-gel, oxidative decomposition and sputtering techniques have been reported for N, S, F, B and C doping on TiO_2 lattice (Ohno *et al.,* 2004; Tokudome, and Miyauchi, 2004; Kobayakawa *et al.*, 2004; Diwald *et al.,* 2004; Ohno *et al.,* 2003; Umebayashi *et al.,* 2003). Among the anions, much attention has been focused on N (and to a limited extent on S) doping on TiO_2 lattice, and an adequate amount of literature is available to understand the state of the doped N in the TiO_2 lattice (Tokudome, and Miyauchi, 2004; Kobayakawa *et al.*, 2004; Diwald *et al.,* 2004; Nosaka *et al*., 2005; Hong *et al*., 2005; Silveyra *et al.*, 2005). In general, there is a good agreement between the available literature that, in the N-doped TiO_2, the N atoms are occupying the oxygen position in the lattice. Despite the fact that there exists an incongruity for the chemical state of the doped nitrogen in the lattice. Although, it is confirmed/accepted that nitrogen exists with negative charge rather than positive charge. The results presented on N- doped TiO_2 in the previous section also confirms the presence of nitrogen with slight negative charge at the oxygen position in the TiO_2 lattice.

In the case of S-doped TiO_2, Ohno *et al*., (Ohno *et al.*, 2003) have reported a controversial observation that, S atoms are incorporated as cations (S^{6+}) and replaces Ti ions in the TiO_2 lattice. Furthermore, these powders absorb visible light more strongly than the N-doped TiO_2 and other anionic S-doped TiO_2 powders. Apart from this result, it has been widely accepted and also other literature results confirm that, S survive as anion, and replaced the oxygen ions in the TiO_2 lattice (Umebayashi *et al*., 2003). Various theoretical studies have also implied that the doping of heteroatom on TiO_2 lattice shifts the light absorption onset by reducing the band gap

of the TiO_2 (Umebayashi *et al.*, 2002 & 2003). The reduction in the band gap occurs due to the overlap of 2p and 3p orbital of N and S respectively, with the valence band of TiO_2 and results in the formation of additional energy levels just above the valence band.

Recently, attempts have been made by Li *et al* (2005a) to prepare N, F co-doped TiO_2 to study the effect of second heteroatom on the photocatalytic activity of TiO_2 in visible light. They have reported that N, F co-doped TiO_2 shows better activity in the visible region than the N or F doped TiO_2. Both their experimental and theoretical studies of N, F co-doped system shows that, N doping, shifts the onset absorption to visible region and F doping, increases in the acidity of the catalyst. In the present study, attempts have been made to prepare the N, S co-doped TiO_2 and study the effect of second heteroatom in the visible light photocatalytic activity of single anion doped TiO_2.

4.4.2 RESULTS AND DISCUSSION

4.4.2.1 TGA analysis

The thermal decomposition profile of titanium complex (TB) and pure ligand in air are shown in Fig. 4.8. The decomposition temperature of pure ligand is between 300 to 350 °C, whereas TB complex decomposition takes place at 400 to 500 °C, and in total 40 % decomposition have been attained up to 800 °C. Based on this TG profiles, TB complex was calcined in vacuum and N_2 at 400 °C, and the final calcination temperature in air is varied, starting from 400 to 550 °C. The TG profile of calcined samples at 400 and 450 °C in air shows, no significant weight loss, which indicates that complete decomposition of the organic precursor moiety during the calcination process.

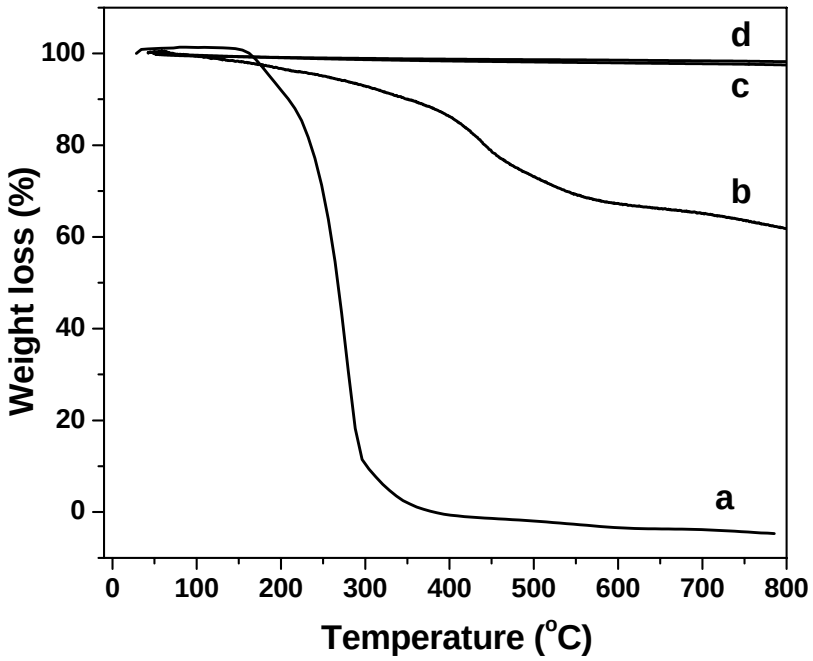

Fig. 4.22. TGA profile of (a) Pure ligand (b) TB complex (c) TB 400 and (d) TB 450

4.4.2.2. UV-Visible spectra

The UV- visible absorption spectrum of pure TiO_2 and N, S co-doped samples calcined at different temperature are shown in Fig.4.23. A shift in the absorption edge towards visible light can be seen (Fig.4.23, inset) for the N, S co-doped TiO_2 samples when compared to pure TiO_2. Although, when compared to N-doped TiO_2, the absorption curve significantly differs for N, S co-doped TiO_2. Unlike N-doped TiO_2 or S-doped TiO_2, there is precipitous increase in the absorption curves for N, S co-doped TiO_2. This indicates that there is a definite role for the addition of second hetero atom in the TiO_2 lattice.

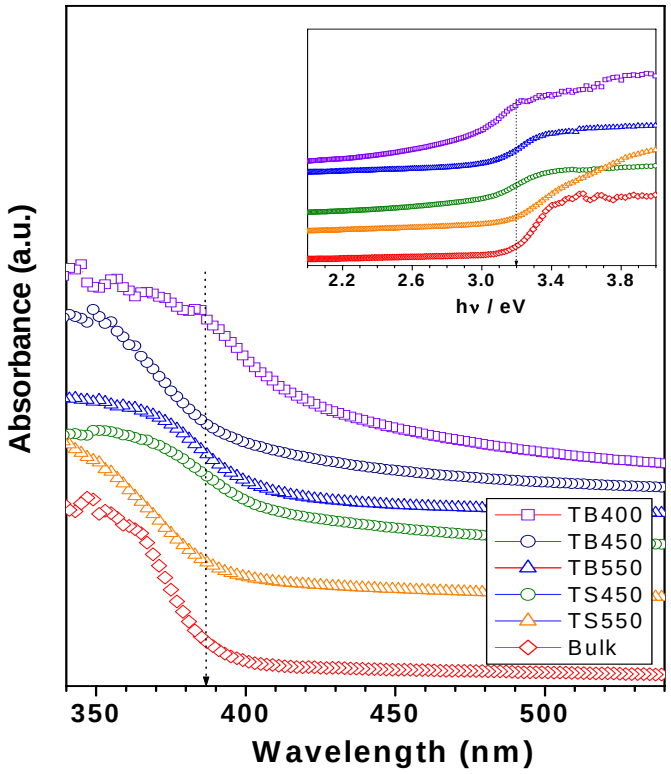

Fig.4.23. UV-Visible absorption spectra of N, S co-doped TiO_2 samples at different calcination temperatures and pure TiO_2. (Inset shows a clear shift in absorption edge towards visible region)

4.4.2.3. X-ray diffraction Studies

The Fig. 4.24 shows the X–ray diffraction patterns of N, S co-doped TiO_2 powders calcined at different temperature in air. For all samples, the more photoactive crystalline phase of TiO_2 *i.e.* anatase phase has been retained in the calcination temperature range studied. Of course, the transformation from anatase to rutile phase will takes place normally around 600-700 °C, and prior results substantiate that doping of N and S will not induce the phase transformation at lower temperatures (Ohno *et al.*, 2003; Silveyra *et al.*, 2005). It has been expected that, due to higher atomic radius of S and N atoms compared to O atom, substitution doping of S/N atoms will lead to increase in the inter planar distance and thereby decrease the

"d" values. Though, no significant change in the "d" values have been observed due to S and N incorporation in the TiO_2 lattice, nevertheless the X-ray line broadening have been observed when compared to pure TiO_2. It can be understood that due to the low at % of S and N atom doping in the TiO_2 lattice, any perturbation in the crystal lattice can be ruled out. Also, the peak broadening can be ascribed by the formation of N, S doped TiO_2 nanoparticles, which are formed by slow decomposition of metal complex in the N_2 atmosphere. The crystallite size of the N, S doped TiO_2 powders are calculated by Debye-Scherrer equation (Cullity, 1987) and given in Table 4.2. It can also been seen from Fig. 4.24, that as calcination temperature increases, peak broadening decreases which can be explained on the basis of particle agglomeration at high temperatures, resulting in larger particles.

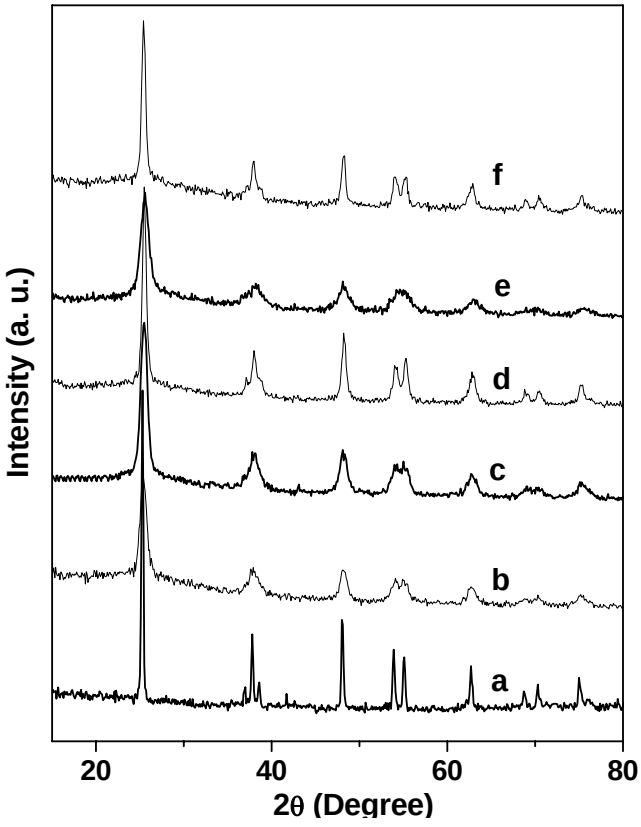

Fig. 4.24 X-ray diffraction patterns of (a) pure TiO_2 (b) TB 400 (c) TB 450 (d) TB 550 (e) TS 450 and (f) TS 550

4.4.2.4 Surface area and pore volume

The specific surface area and pore volume of N, S co-doped and pure TiO_2 are given in the Table 4.2. It can be seen that, as the calcination temperature increases from 400 –550 °C the surface area of the samples decreased. There is a good agreement between increase in the surface area as a consequence of decreases in particle size. In addition, N, S co-doped samples show higher pore volume compared to bulk TiO_2; this can be attributed to the slow decomposition of metal complex in the N_2 and air atmosphere leading to the formation of micropores, which offers the higher surface area.

Table 4.2. Crystallite size, specific surface area and pore volume of N, S co-doped TiO_2

Catalyst	Crystallite size (nm)	Specific Surface area (m^2/g)	Specific pore volume (cm^3/g)
TB 400	8	110	0.1293
TB 450	9	95	0.1908
TB 550	16	81	0.0936
TS 450	8	99	0.1159
TS 550	15	81	0.0932
Pure TiO_2	35	14	0.0696

Higher surface area compared to bulk TiO_2 even at higher calcination temperature confirms/supports the above observation and the slight decrease in the pore volume could be due to sintering of particles at higher temperatures. The sample calcined at 450 °C shows a higher pore volume than the sample calcined at 400 °C, this may be due to the release of doped S, N atom from the bulk to surface, and as a result the amount of S, N atom in the bulk decreases. The significant decrease in the UV-visible absorption onset as calcination temperature is increased from 400 to 450 and 550 °C, hints the removal of doped N, S atoms from the TiO_2 lattice. This will indirectly

support to the contribution of S and N energy levels in the band gap reduction mechanism. The samples calcined at 400 °C are yellow in colour and the intensity of the yellow colour decreased as the calcination temperature is increased to 550 °C, above this temperature the yellow samples turns white in colour. This observation also supports our UV-visible absorbance spectrum of N, S co-doped TiO_2 calcined at various temperatures. A good correspondence between the surface area, pore volume, particle size and UV-visible light absorption can be seen for different temperature calcined N, S co-doped samples.

4.4.2.5 Electron microscopic analysis

The transmission electron micrograph of the N, S co-doped TiO_2 sample is shown in Fig.4.25. Particles in nanosize range are clearly observed for the doped sample. The exact particle size for the prepared sample has been calculated from the micrographs and is presented in the Table 4.2. The SEM pictures of the N, S co-doped TiO_2 samples at different magnifications are presented in Fig. 4.26 a and b. The growth of fine particle of N, S co-doped TiO_2 in a different morphology has been observed.

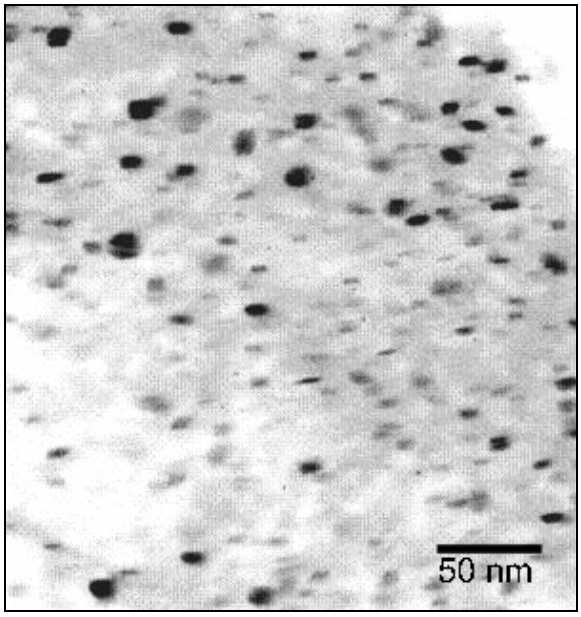

Fig.4.25. TEM image of N, S co-doped TiO_2 sample obtained from TB complex calcined at 400°C (TB 400)

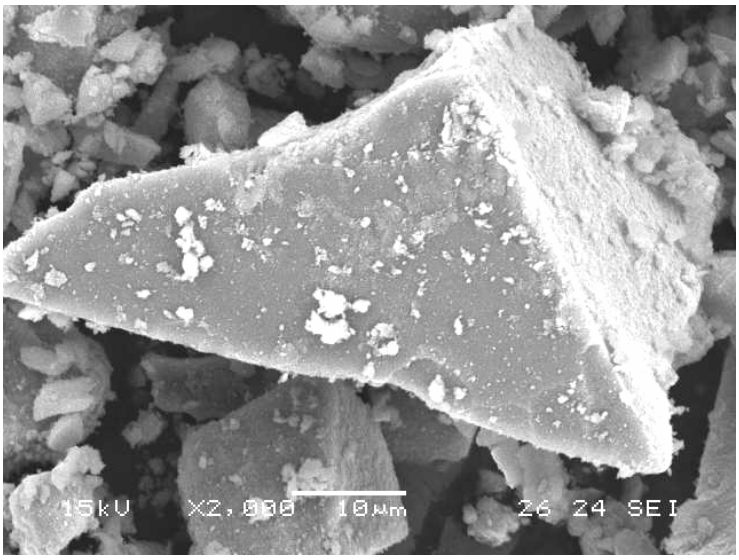

(a)

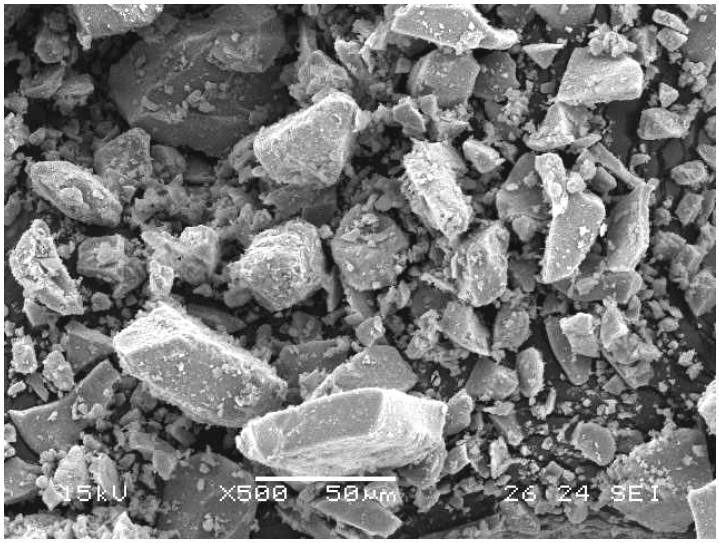

(b)

Fig.4.26. SEM image of N, S co-doped TiO_2 sample obtained from TB complex calcined at 400°C (TB 400)

4.4.2.6 X-ray photoelectron spectroscopy

The XPS spectra for N, S co-doped TiO_2 and Pure TiO_2 sample are recorded and Ti 2p, N 1s, S 2s and O 1s core levels are shown in Fig. 4.27 and 4.28. It is to be noted that these results are after *in situ* scraping of the pellet surfaces of both the

catalysts within the ESCA spectrometer under ultrahigh vacuum conditions, mainly to remove any contribution from the atmospheric degradation. It is to be mentioned here that Ar^+ sputtering lead to preferential removal of lower atomic weight elements first and hence an artificial reduction of cations on the surface (Diwald *et al*., 2004). However, physical scrapping does not alter the oxidation state of any element on the surface. Indeed, the unscraped surface displays high carbon (some carbonate also) content along with a relatively low intensity Ti 2p peak (not shown). However, carbonate and hydroxide contamination was fully removed by scraping the catalyst surface and that enhances the intensity of all intrinsic features. Ti $2p_{3/2}$ core level appears at 459.3 and 458.8 eV for TiO_2 and N, S co-doped TiO_2 samples calcined at 400 °C in air (after N_2 atmosphere), respectively (Fig. 4.27 a). The shift in the BE of Ti 2p in N, S co-doped TiO_2 towards lesser energy shows that the electronic interaction of Ti with N, S anions is considerably different than that of oxygen anion in TiO_2. Also, this observation suggests that TiO_2 lattice is considerably modified due to N, S substitution with oxygen in the TiO_2 crystal lattice. Lower BE of Ti 2p in N, S co-doped TiO_2 samples can also be explained on the basis of covalency between the Ti and anion bond. It is well known that if the electronegativity of the anion decreases, the percentage ionicity will also decrease (Viswanathan, 2003) as a result, the electron density around the anion decreases. Consequently, the covalent nature of the bond between metal and anion will increase, as a result that the net positive charge on the metal will be reduced. It is in good agreement with results reported in the literature and also our previous studies on N-doped TiO_2. In addition, as anticipated based on the literature, the O 1s peaks are observed at 530 eV with an unusual peak broadening at higher binding energy side (Fig. 4.27 b). This peak broadening can be

explained due to the presence of another type of oxygen in the TiO_2 lattice other than O-Ti-O environment.

Fig.4.28 a shows the XPS spectra for the S 2p core level of the N, S co-doped TiO_2 samples calcined at 400 °C in air. The S 2p state had a broad peak because of the overlap of the split sublevels, the $2p_{3/2}$ and $2p_{1/2}$ states, with separation of 1.2 eV due to spin-orbit coupling (Lindberg *et al.,* 1970). Two peaks are observed around 168.9 and 159.3 eV for the N, S co-doped TiO_2 samples. The peak at 168.9 eV can be accounted by the presence of adsorbed SO_2 or SO_3 molecule on the TiO_2 surface (Sayago *et al*., 2001), which is generated through the diffusion of S atoms doped in the bulk TiO_2 and the peak at 159.3 eV can be accounted for the presence of Ti-S bond in the anatase lattice (Gonbeau *et al.,* 1991) Ohno *et al* (2003) and Ohno *et al* (2004) had observed the peak around 170 eV and ascertained the presence of S^{6+} in the S doped TiO_2 and claimed that the S doping resulted in S replacing the Ti in the crystal lattice. Meanwhile, Umebayachi *et al* (2002 and 2003) have reported the above distinctive peak with an addional peak around 168 eV and observed that enhancement in the later peak intensity as etching time increases. This indicates that the S atoms are uniformly doped into the anatase lattice, and due to the calcination or annealing the catalyst at high temperatures, the S atoms, which are doped near the surface are moved to the surface of the catalyst and exists as SO_3 or SO_4. It has been further supported by Hebenstreit *et al* (2001) that, when S replaced O on the TiO_2 (110) surface, the XPS of S modified surface showed S 2p peak at 162 eV. The S 2p peak for S in TiS_2 was situated around 160–161 eV (Fujimori *et al.*, 1988; Lichtman *et al.*, 1981). Based on these results, the observed peak at 160 eV could be ascertained to the doped S^{2-} atom in the TiO_2 lattice and the existence of Ti-S bond in the N, S co-doped TiO_2 samples were confirmed.

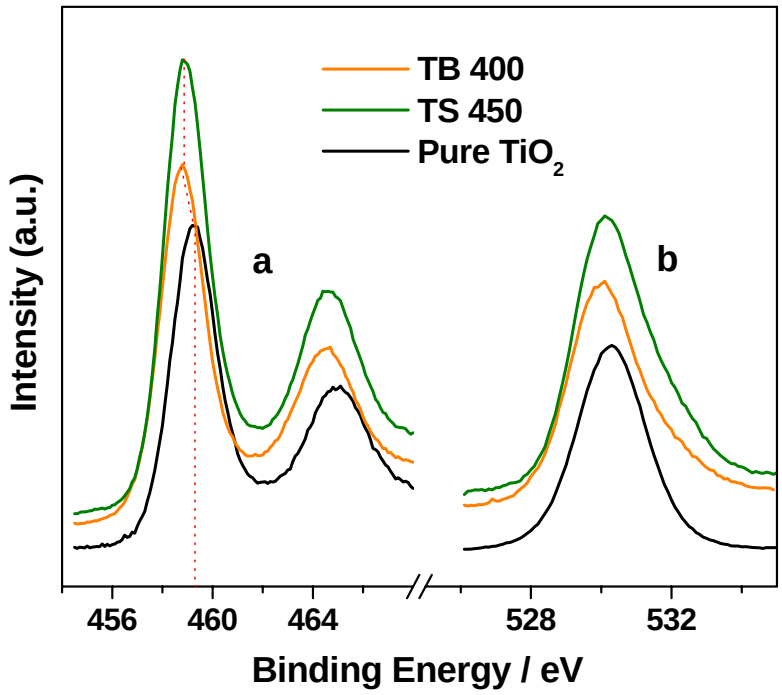

Fig. 4.27. **X-ray photoelectron spectral details collected from N, S co-doped TiO_2 samples (TB 400 and TS 450). (a) Ti 2p and (b) O 1s core levels. (Note the shift in Ti 2pbinding energy after the introduction of N and S into the TiO_2 lattice)**

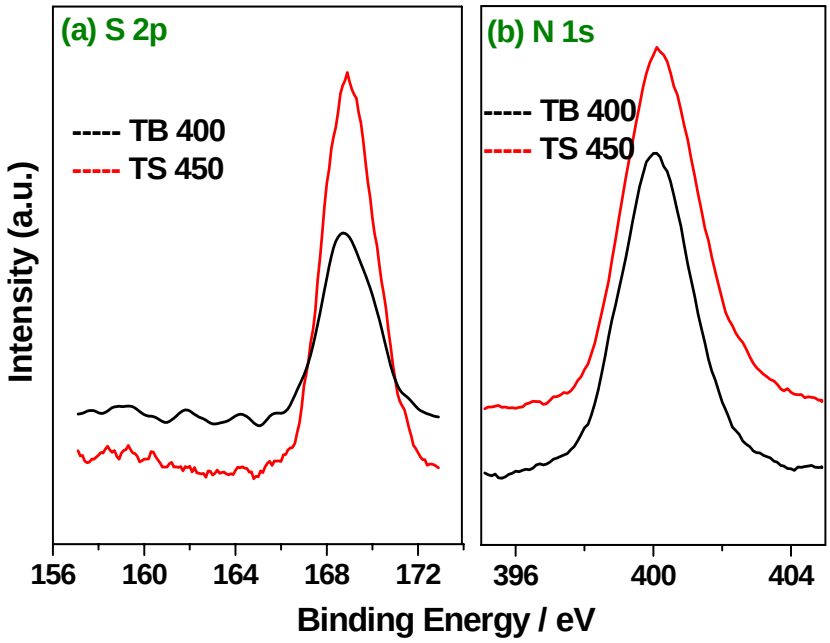

Fig. 4.28. **X-ray photoelectron spectral details collected from N, S co-doped TiO_2 samples (TB 400 and TS 450) (a) S 2p, (b) N 1s.**

Fig. 4.28b, gives the N 1s peak of the N, S co-doped samples. The XPS spectrum of N, S co-doped TiO_2 sample shows that, the N 1s level binding energy at 400 eV. The observed broad peak between 398 to 402 eV confirms that N is present as anion in the TiO_2 lattice. The observed peak maximum at 400 eV, which is also attributed to the presence of N atoms in the organic compounds on the surface or in grain boundaries (Sano *et al.,* 2004).

It is clear from the above discussion that if the N, S atoms are subtitutionally doped into the TiO_2 lattice and have significant interaction with oxygen atoms. Indeed, an interstitial doping of anions in the anatase lattice have some strong interaction with nearby oxygen and hence a change in effective charge on the species and hence a shift in the BE. This speculation is supported by DFT calculations of Valentin *et al* (2005), that the substitutional doping of carbon will alter the electronic structure by producing occupied energy states over the oxygen levels and leads to red shift in the light absorption. Whereas intestinal doping of carbon will create oxygen vacancy, which will result in the formation of mid gap energy levels. In the former case the absorption onset of TiO_2 shifts to 400-500 nm and in the latter case the absorption takes place at above 500 nm. In the present case, based on the UV-visible light absorption spectra of N, S co-doped TiO_2, only substitutional doping of N, S could be possible rather than interstitial doping.

4.4.3 Visible light photocatalytic activity

The visible light photocatalytic activity of N, S co-doped TiO_2, N-TiO_2 and TiO_2 (degussa P25) samples for methlylene blue decomposition are shown in Fig. 4.29. It can be seen from Fig. 4.29 that, when increasing the calcination temperature, there is a significant decreases in the visible light photocatalytic activity. Furthermore, the

method of preparation of N, S co-doped TiO_2 also plays a vital role in the photocatalytic activity. It can be seen that for same calcination temperatures, TB samples are showing higher activity than the TS samples, which can be explained on the basis of amount of hetero atom (N and S) doped in the TiO_2 lattice. It is well known that, the visible light absorption of hetero atom doped TiO_2 depends on the concentration of the dopant present in its lattice, the decrease in the amount of hetero atom results in decrease in the visible light absorption. It is clearly reflected in the UV-visible absorption spectrum (Fig. 4.23) of TB and TS samples calcined at different temperatures.

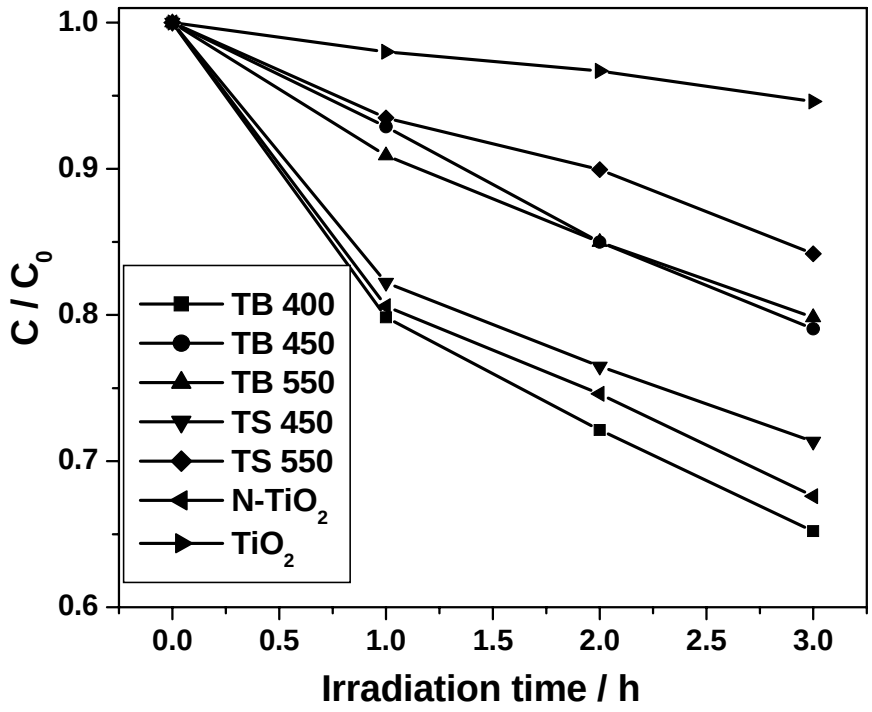

Fig. 4.29. Visible light photocatalytic decomposition profiles of methylene blue over N, S co-doped TiO_2 samples (400 W Hg lamp with HOYA L-42 UV light cut off filter)

Approximately, 30-35 % of methylene blue decomposition has been achieved for the N, S co-doped TiO_2 samples calcined at 400 and 450 °C, whereas only 5-6% decomposition of methylene blue was observed for the commercial TiO_2 (Degussaa, P25). The complete decomposition of methelyne blue has been observed within 2 h irradiation time for the same samples in UV + Visible region (without the filter, data not shown) for the N, S co-doped TiO_2. Nevertheless, it has been observed that, in UV + Visible region, there is no significant difference in the activity between the N, S co-doped samples (TB 400 and TS 450), and commercial TiO_2 (Degussa P25) (Fig. 4.30). This observation supports that the difference in the photocatalytic activity in the visible region for the N, S doped TiO_2 samples is essentially due to the amount of hetero atom doped in the TiO_2 lattice.

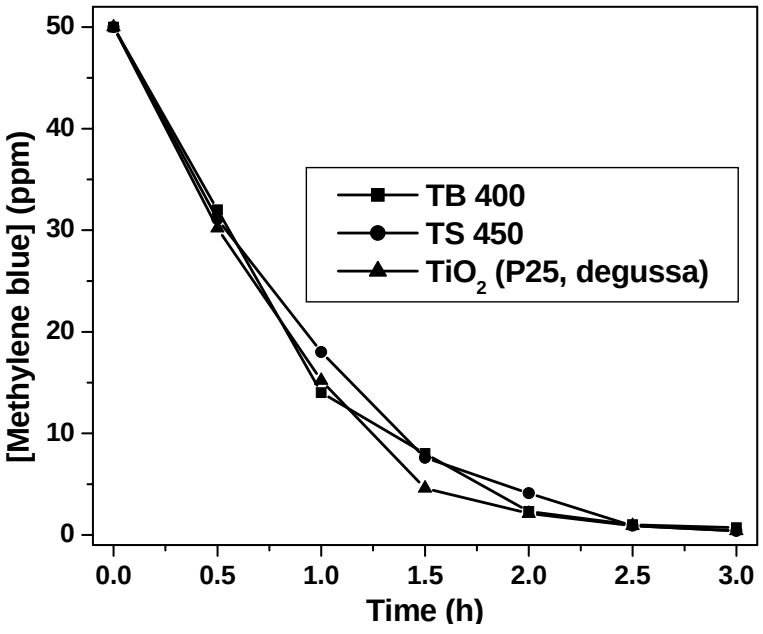

Fig. 4.30. Photocatalytic decomposition profiles of methylene blue in (UV + Visible region) over N, S co-doped TiO_2 samples (400 W Hg lamp)

4.5 THEORETICAL STUDIES ON THE POSITION AND EFFECT OF HETERO ATOM (N and S) SUBSTITUTION IN TiO_2

4.5.1 Introduction

The studies on chemical state of the doped hetero atom and its contribution to the band gap reduction in hetero atom doped TiO_2 are essential for further developments in photocatalysis. In this view, few density functional theory (DFT) calculations have been performed and reported in literature (Asahi *et al.,* 2001; Umebayashi *et al*., 2002; Ohno *et al*., 2004 Umebayashi *et al*., 2003). Asahi *et al* (2001) have studied the effect of hetero atom (F, N, C, S and P) doping in TiO_2 and the results show that substitutional doping of N atom reduces the band gap. Umebayashi *et al*. (2002, 2003) have studied the band gap narrowing of anatase and rutile TiO_2 by substitutional doping of S in the oxygen position. Similarly, Ohno *et al* (2004) have also studied by substituting the S in the Ti position. The presence of S as anionic (S^{2-}) and cationic (S^{6+}) form in the TiO_2 lattice has been supported both by XPS and theoretical results in the former and latter case, respectively. Unfortunately, the contribution of sulphur energy levels on the conduction band has been absolutely omitted in both cases. Nevertheless, the conclusion arrived from these studies are not able to explain the rationale for the observed band gap reduction in the case of N and S doped TiO_2.

With this background, the present study has focused on both (i) Cluster model DFT study and (ii) First principle band calculations using super cell approach, to understand and explain the band gap narrowing in the doped TiO_2. The cluster ($Ti_5O_{14}H_8$) model used for the DFT calculation, and primitive unit cell of the TiO_2 anatase crystal structure for density of states studies are shown in Fig. 4.31 and Fig. 4.32, respectively. The observed results are explained on the basis of mixing of titanium and oxygen orbitals with the doped hetero atom.

4.5.2 Computational model and methodology

Cluster model ($Ti_5O_{14}H_8$) used for the quantum chemical calculations were taken from the crystal lattice of anatase TiO_2 which consist of 5 Ti atom and 14 oxygen atoms and the edge position is saturated with hydrogen to avoid the edge effect (Fig. 4.31). The effect of N and S substitution in the oxygen position of the cluster has been studied. All DFT calculations were carried out by Becke three parameter hybrid functions with the LYP correlation function (B3LYP) and an effective core potential basis set of 6-31g (d, p) level (Becke *et al.,* 1993; Lee *et al.,* 1988) using the Gaussian 98 program (GAUSSIAN 98. 1998). In the calculation, geometry of the cluster has been optimized by Universal Force Field (UFF 1.02) approach using Cerius2 software (Rappe *et al.,* 1992). Using force field optimized parameters (DFT) single point energy and band population analysis calculations were carried out.

To study the details of the band gap engineering due to doping of N and S in the crystal lattice, DOS (Density of States) has been calculated by utilizing primitive unit cell of the TiO_2 anatase crystal structure (Fig. 4.32). The doping effects were modeled by replacing one oxygen atom with one doping atom. The plane - wave - based Density Functional Theory (DFT) calculation (Blaha *et al.,* 1990; Perdew *et al.,* 1996; Kohn and Sham, 1965) carried out using CASTEP program in Materials Studio supplied by Accelerys with, the core orbital replaced by ultrasoft pseudopotentials, and a kinetic energy cutoff of 300 eV. All the electronic band structures and the optical absorption spectra were calculated on the corresponding optimized crystal geometries. The Generalized Gradient Approximation (GGA) with the PW91 exchange correlation function was adopted.

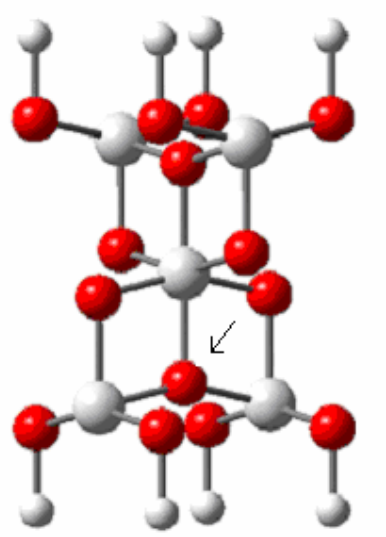

Fig. 4. 31. Model of the cluster (Ti_5 O_{14} H_8)

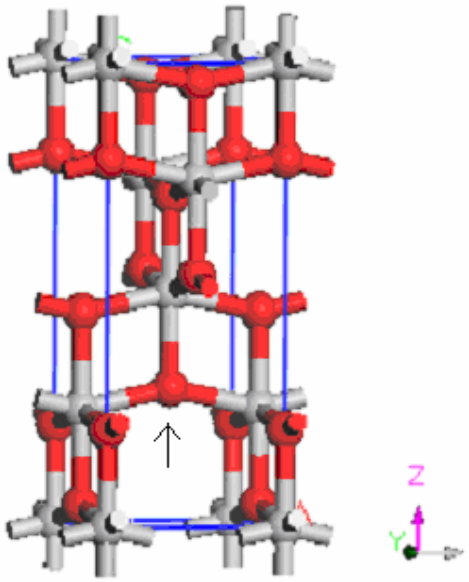

Fig. 4. 32. Model of the primitive TiO_2 crystal

4.5.3 RESULTS AND DISCUSSION

4.5.3.1 Density of states and band gap

The total density of states for hetero atom (N, S, N & S) doped and undoped TiO_2 are shown in Fig. 4.33. The band gap reduction can be seen in the case of hetero atom doped TiO_2 when compared to undoped TiO_2. The reduction in the band gap is attributed due to the orbital mixing of hetero atom with oxygen 2p and Ti 3d orbital. It is well knon that, the valence and conduction bands of TiO_2 are mainly formed due to the major contribution by completely filled oxygen 2p orbital and the empty Ti 3d orbital, respectively. Due to energetic equality, the 2p and 3d orbital of the doped hetero atom are significantly contributing to the valence and conduction band by mixing with Ti and oxygen orbital. In another way, when substituting O with N or S, the electronegativity difference between the cation (Ti) and the anion (S or N) has reduced significantly, which will increase the covalent nature of the bond. The increase in the covalent nature results in reduction of the band gap due to the destabilization of filled 2p orbital and stabilizing unfilled 3d orbital of anion (O) and the cation (Ti), respectively. The density of states of N doped TiO_2 shows broadening in the top of the valence band and bottom of the conduction band. It is clearly seen from Fig. 4.34, that, both the valence and conduction band structure have been altered (curve b). Whereas in the sulphur doped TiO_2 (curve c), the conduction band was altered significantly when compared to valence band due to the formation of additional energy levels at the bottom of the conduction band, which results in broadening of the conduction band. The S 3p orbital has higher energy compared to N 2p and O 2p, and extent of overlapping with O 2p will be lesser than N 2p. In

addition, it is speculated that the overlapping of empty S 3d orbital with the Ti 3d orbital in addition to 2p orbital results the conduction band broadening. The cluster model study shows that, contribution of S orbital in the conduction band is more when compared to valence band, 9.16% and 2.36 % for the former and latter cases, respectively, which is supporting our speculation. This is further confirmed from the N, S codoped TiO_2 (curve d), where it can be seen that both the conduction and valence band are altered by the orbital mixing of doped N and S atom. There is no difference in the conduction and valence band between the sulphur doped and N, S co-doped TiO_2, though the top of the valence band is destabilized like N-doped TiO_2. Ohno *et al,* have also observed the valence band broadening for the S doped TiO_2, and ascribed due to the overlapping of S 3s states with O 2p states (Ohno *et al.,* 2004). The band gap are in the order of TiO_2 > N-TiO_2 > S-TiO_2 ≥ N, S co-doped TiO_2. This observation shows good correspondence with band gap calculated form the cluster model calculation (Table 4.3) and the literature reports (Umebayashi *et al.,* 2003; Umebayashi *et al,* 2002). Also, the magnitude of band gap reduction can be explained based on the electronegativity strategy (Viswanathan, 2003) that, sulphur is more electronegative than nitrogen atom and shows more covalent nature, and shows more reduction in the band gap than N-TiO_2. Similarly, in N, S doped TiO_2, two oxygen atoms has replaced by N and S, which results more covalent character, and more reduction in the band gap.

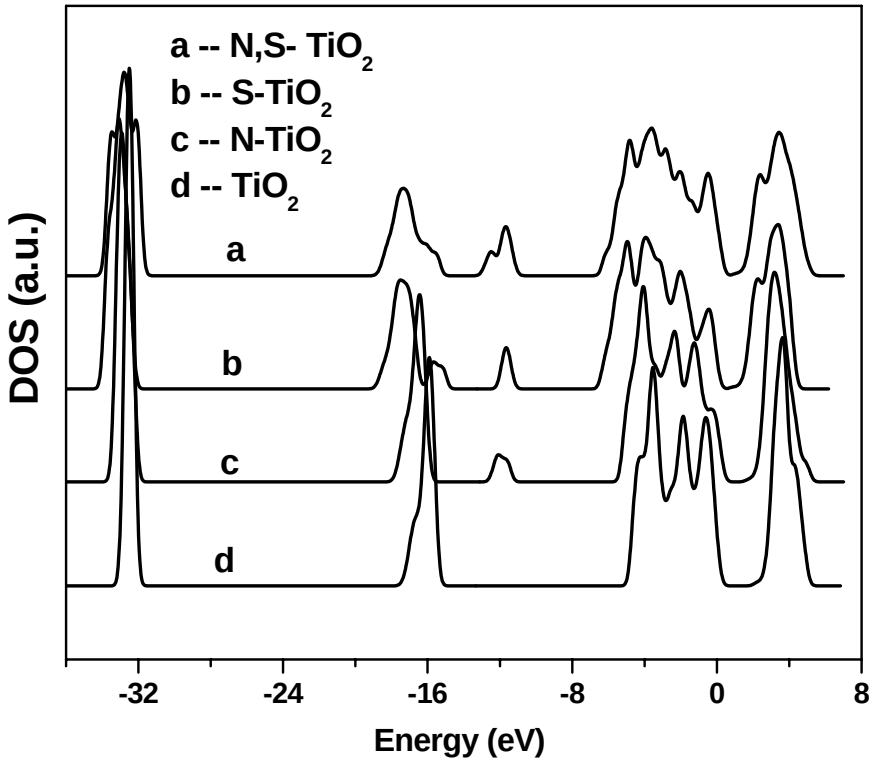

Fig.4.33. Total density of states for (a) N, S codoped TiO_2 (b) S-doped TiO_2 (c) N-doped TiO_2 and (d) Undoped TiO_2

It can also be seen from Fig. 4.34, that the total width of the valence and conduction band increases significantly for the doped TiO_2 compared to undoped TiO_2. Between the S and N doped TiO_2, the former has more bandwidth both in valence and conduction band than the later (shown as A & B in Fig.4.34). This also suggests that the S 3s, 3p and 3d orbital are mixing with TiO_2 valence and conduction band orbital and leads to the narrowing of valence and conduction bands. The band gap, orbital contribution and the stabilization energy obtained from the cluster ($Ti_5O_{14}H_8$) model DFT studies are tabulated in Table 4.3.

Table 4.3. Band gap, stabilization energy and % orbital contribution of pure and heteroatom (N, S) doped $Ti_5O_{14}H_8$ cluster

Cluster	$Ti_5O_{14}H_8$		$Ti_5O_{13}NH_8$		$Ti_5O_{13}SH_8$	
	VB	**CB**	**VB**	**CB**	**VB**	**CB**
Ti	8.3	83.5	22.55	77.87	36.54	78.41
O	89.61	15.78	31.99	16.76	60.72	12.24
N	-	-	45.06	0.26	-	-
S	-	-	-	-	2.36	9.16
H	1.92	0	0	4.9	0	0
ΔE	-6.3859		-6.2595		-6.1961	
B.G	2.00		1.31		1.17	

It can be seen from the table that, when oxygen in the cluster (shown by arrow) is replaced by N or S, the band gap is reduced to 2.00, 1.31 and 1.71 for the undoped, N and S doped TiO_2 respectively. Our previous experimental results (N-TiO_2) and literature reported experimental band gap values for N and S doped TiO_2 have good correspondence with the above band gap ratio (Madhusudan Reddy *et al.,* 2005; Diwald et al., 2004). The stability of the cluster also reduced for the N and S doped TiO_2, the magnitude is more for the S doped TiO_2 compared to N doped TiO_2 due to the larger size of the S atom compared to N or O size. The % orbital contribution of Ti in the conduction band is almost same for the doped and undoped cluster, whereas the valence band contribution increases in the order of undoped < N doped < S doped TiO_2. This may be due to the mixing of Ti 3d orbital with N 2p and S 3p orbital, which is having more energy than O 2p orbital. The oxygen orbital contribution in the conduction band is more or less constant for the all the three cluster. Whereas, it is decreased for the N doped cluster due to the significant contribution of N 2p orbital in the valence band. In S doped cluster, the oxygen contribution has higher than the

N doped cluster, but still lower than the undoped TiO_2. This can be attributed by the inefficient mixing of S 3p orbital with O 2p orbital due to higher energy of the former energy level.

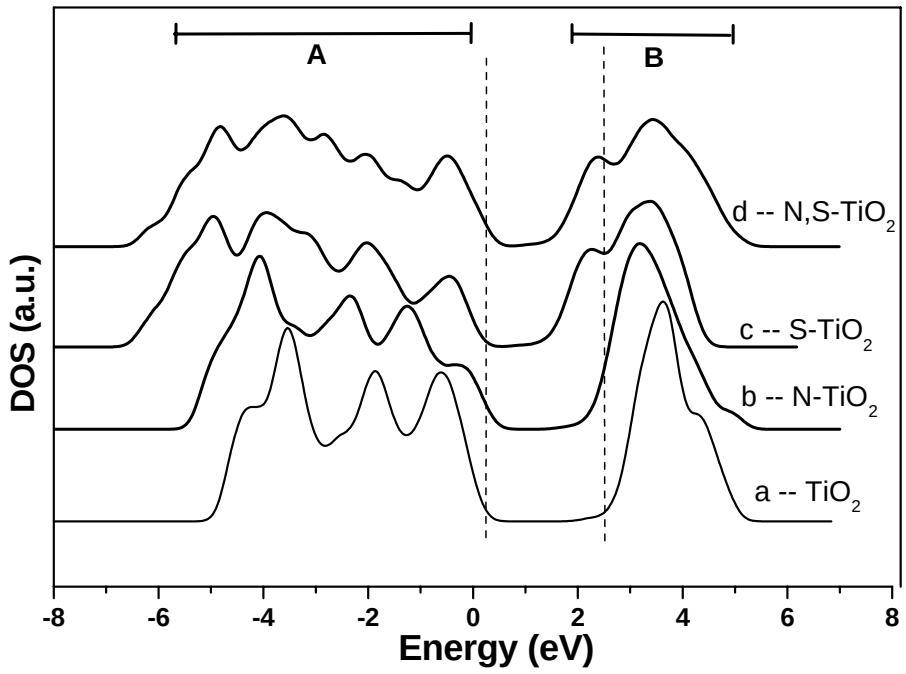

Fig.4.34. Total density of states for (a) Undoped TiO_2 (b) N-doped TiO_2 (c) S-doped TiO_2 and (d) N, S co-doped TiO_2

4.5.3.2 Position of doped S atom in the S-doped TiO_2

Fig.4.35, shows the density of states of pure, sulphur doped in oxygen and Ti position. It can be seen from Fig. 4.35 that, when oxygen atom is replaced with S, the valence band and conduction band structure is altered significantly, in addition to increase in the bandwidth. Formation of additional energy levels at the bottom of the conduction band has been observed. Whereas, when S replaces Ti, both the valence and conduction band has stabilized more. Though, the band gap appears to be reduced to almost same as in the case of others, due to the small number of states, the light

absorption will takes place only in the UV region and the band gap will be more than undoped TiO_2. This observation suggests that, S replaces the oxygen and doped as S^{2-} in the TiO_2 lattice rather than as S^{6+} by replacing titanium in the TiO_2 lattice. The cluster model study shows that the stabilization energy is low for the S doped TiO_2 when compared to N doped and undoped TiO_2. It is relatively difficult to prepare the sulphur doped TiO_2, the size of the sulphur atom is also another important factor, the recent number publications has confirmed these statement.

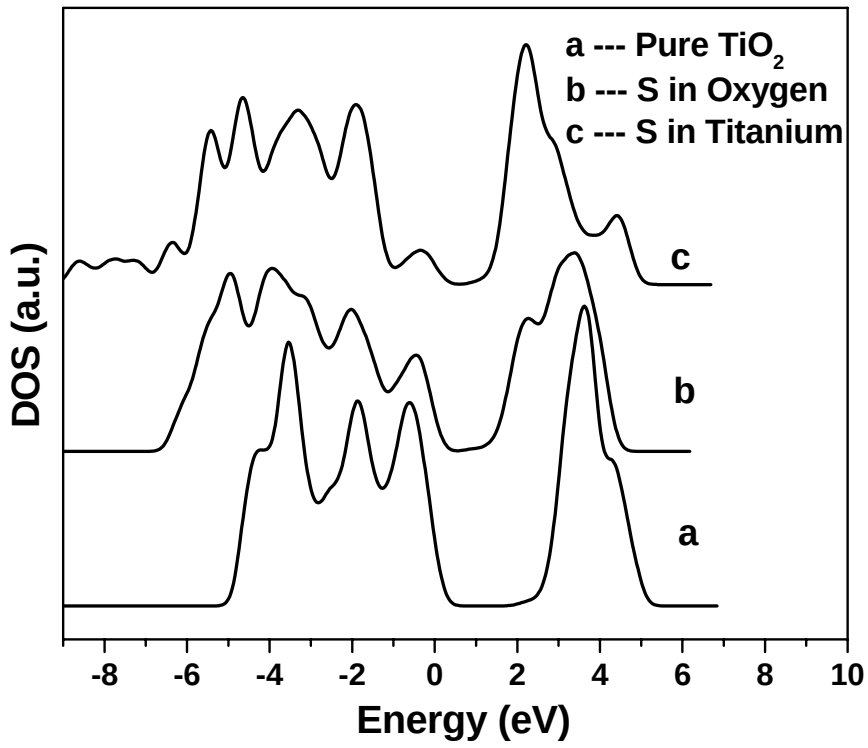

Fig. 4.35. Total density of states for (a) Undoped TiO_2 (b) S-doped in oxygen position of TiO_2 and (c) S doped in the Ti position in TiO_2

The band gap reduction in the TiO_2 could be achieved by substitutional doping with heteroatoms like N and S in the TiO_2. The magnitude of band gap reduction increases with decrease in the electronegativity difference between Ti- heteroatom bonds. The present results strongly emphasize that, S doping has more impact on the band gap

reduction, and the doping of S atom in the TiO_2 replaces only the oxygen atom, but not the Ti atom in the lattice. Also, the doping of S in the Ti position has no significance in the band gap reduction, and the photocatalytic activity.

4. 6 CONCLUSIONS

N-doped TiO_2 nanosize photocatalyst with a homogeneous size and spherical shape has been prepared by three different routes namely (i) simple hydrolysis of $TiCl_3$ (ii) thermal decomposition Ti- salen complex and (iii) thermal decomposition of Ti-melamine complex. The light absorption onset of N-doped sample in the visible region is clearly observed. The advantages of the first method over other methods of preparation are (i) use of inexpensive chemical precursors for the synthesis of N-doped TiO_2, and (ii) formation of TiO_2 as uniform sized nanoparticles. Studies of optical absorption, identified the substitutional N-doping and localized N-states in TiO_2 lattice. XPS results indicate the status of N to be anion like (N^-) and the chemical environment of N is as in N-Ti-O in the TiO_2 lattice. The methods of preparation strongly affect the visible light absorption capacity, and the chemical nature N in the doped TiO_2. Also, the calcination temperature plays an important role in the absorption of visible light. The photocatalytic activity induced by visible light for the prepared N-doped samples was evaluated by decomposition of methylene blue. The N-TiO_2 sample shows higher photocatalytic activity as compared to Degussa P25 and pure TiO_2.

Visible light active N, S co-doped TiO_2 nanosize powders have been prepared by thermal decomposition of Ti based metal complex in vacuum. Investigations on absorption of visible light by the doped samples indicate a clear red shift in the onset absorption spectrum and hence the reduction in the band gap. The chemical nature of

the doped N and S atoms in the TiO_2 lattice is identified using XPS spectrum. Higher visible light induced photocatalytic activity for the N, S co-doped samples than that of the TiO_2 (degussa P25) has been examined by methylene blue decomposition. This high activity is ascribed to a synergetic effect of doped N, S atoms in the TiO_2 lattice. The theoretical calculation shows that, the band gap reduction in the TiO_2 could be achieved by substitutional doping with hetero atoms like N and S in the TiO_2. The magnitude of band gap reduction increases with decrease in the electronegativity difference between Ti- hetero atom bonds. Also, the observed results emphasize that, S doping has more impact on the band gap reduction, and the doping of S atom in the TiO_2 replaces only the oxygen atom, but not the Ti atom in the lattice. However, the doping of S in the Ti position has no significant influence in the band gap reduction.

CHAPTER 5

STUDIES ON THE ELECTROLYTIC GENERATION OF HYDROGEN – DESIGN OF COMPARTMENTALIZED CELL

5.1 INTRODUCTION

Hydrogen is widely recognized as the promising energy carrier now and in the future. The hydrogen production methods from water have received much attention in the recent years. Even though the hydrogen production by electrolysis of water is one of the classical and important reactions, due to the hydrogen and oxygen over potentials the electrolysis requires more than the theoretical decomposition potential of water. The theoretical value for water decomposition is 1.23 V. The decomposition potential of water in different media, using platinum electrode (in the presence of various mineral acids, except HCl, and /or alkalis), is around 1.70 V. This extra potential to be applied is due to the sum of the hydrogen over potential (0.05 – 0.1 V) and oxygen over potential (~ 0.5 V in acid medium and ~1.0 V in alkaline medium) (Vogel, 1961) Due to this, the industrial electrolytic plants operate at an applied potential of ~1.75 V using nickel/stainless steel electrodes in alkaline medium. The energy efficiency of the process is much dependent on this extra potential one has to apply in order to make the process economically viable.

The energy required to produce hydrogen via electrolysis (assuming 1.23 V) is about 32.9 kW-hr / kg. A kilogram is about 2.2 lb. For 1 mole (2 g) of hydrogen the energy is about 0.0660 kW-hr / mole. For commercial electrolysis systems that operate at about 1 A/cm^2, a voltage of around 1.80 -2.00 V is required. This translates into about

46.8 kW-hr / kg, which corresponds to an energy efficiency of 70%. Lowering the voltage for electrolysis, which will increase the energy efficiency of the process, is an important area of research. Various attempts have been made by researchers to reduce the over potential (Suffredini *et al.,* 2000; Rossmeisel *et al.,* 2005;Hu *et al.,* 1997;Campillo *et al.,* 2002; Millet *et al.,* 1996; Stojic *et al.,* 2003; Kreuter and Hofmann**,** 1998; Ulleberg, 2003). But, no significant success has been attained so far.

In the present study, an attempt has been made to design a simple compartmentalized electrolytic cell. The study involves the utilization of a compartmentalized electrolytic cell for electrolysis of water. The effect of other parameters like, electrolyte concentration, nature of the electrode and nature of the separator material have been studied.

5.2 RESULTS AND DISCUSSION

5.2.1 Cell design

A compartmentalized electrolytic cell has been designed as shown in Fig. 5.1. The compartmentalization enables one to use different electrolytes in the two chambers, namely, anode and cathode chambers. The advantage of this is that the over-potentials at the cathode and anode are minimized. As a result of this, decomposition potential is drastically reduced. The separator prevents mixing of the electrolytes as well as the products of electrolysis; but does not affect the passage of current.

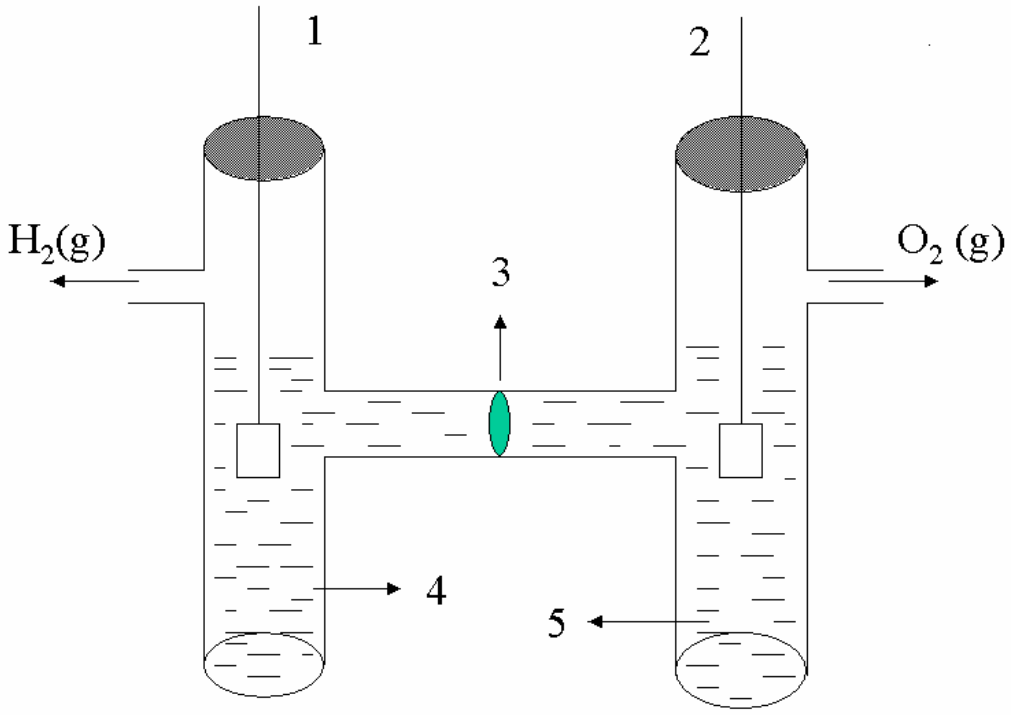

Fig. 5.1. Single unit electrolytic cell

1. Cathode
2. Anode
3. Separator disk
4. Catholyte
5. Anolyte

5.2.2 Cell current

The cell current obtained at different applied potentials for common electrolytic cell with acid or alkali as common electrolyte, and the compartmentalized electrolytic cell where different electrolyte used as anolyte and catholyte are shown in Fig. 5.2. The vertical line shows the theoretical decomposition potential of water at ambient condition.

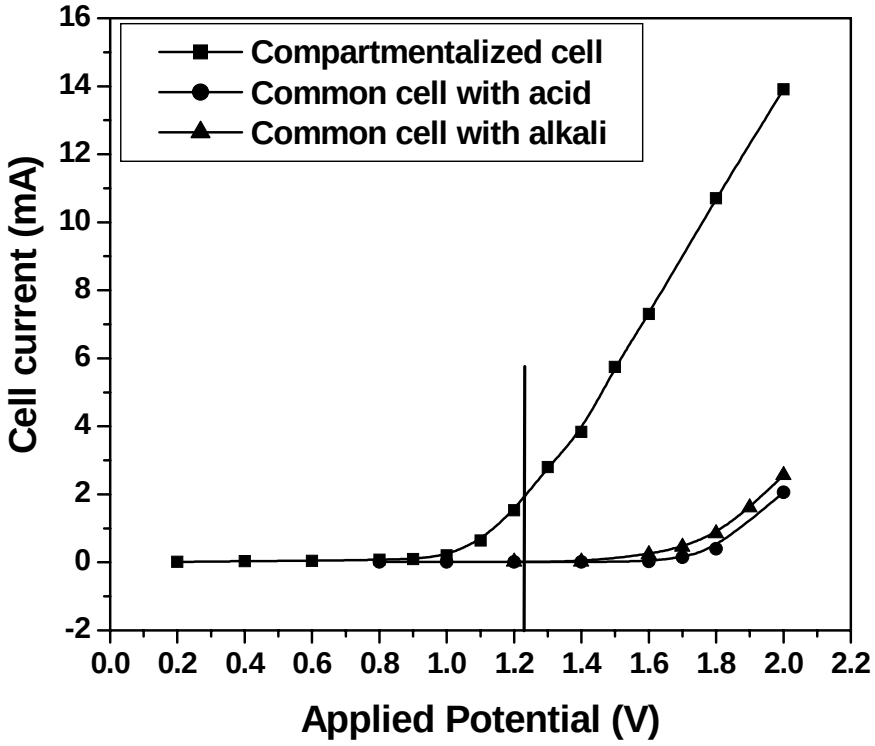

Fig. 5.2. Cell current vs applied potential for common and compartmentalized electrolytic cell

It can be seen from the figure that, in common electrolytic cell, either acid or alkali as electrolyte, the decomposition occurs around at 1.8 V. whereas, in compartmentalized electrolytic cell, the decomposition starts at 1.0 –1.1 V. Moreover, the observed cell current at 1.8 V is much larger for compartmentalized electrolytic cell when compared to common electrolytic cell. Among the common electrolyte, the alkali shows slightly higher cell current than the acid.

The Fig.5.3a, shows the photographs of compartmentalized electrolytic cell, where alkali as common electrolyte in both sides of the compartment. The Fig. 5.3b, shows the compartmentalized electrolytic cell, where different anolyte and catholyte were used in the anode and cathode compartment respectively. The cell current and applied potential (1.2 V) are shown separately using different digital multimeters, it can be

seen clearly that, for an applied potential of 1.2 V the observed cell current are 0.01 and 1.56 mA for common electrolyte and two different electrolytes (compartmentalized) cell, respectively.

(a)

(b)

Fig. 5.3. Photographs of (a) Common electrolytic cell (b) Compartmentalized electrolytic cell.

5.2.3 Effect of nature of the electrolyte on decomposition potential

It is well known that the nature of the electrolyte and concentration of the electrolyte play a major role in the electrolytic processes. The decomposition potential of water is dependent on the nature of the electrolyte. The decomposition potential of water for various electrolytes with common electrolyte cell is given in the Table 5.1. Though, there is a slight variation in the decomposition potential, almost all of them are fall around 1.7 V.

Table 5.1. Decomposition potential of water in different media (Vogel, 1961)

S. No	Medium	Decomposition potential (V)
1	HNO_3	1.69
2	H_2SO_4	1.67
3	HCl	1.31
4	NaOH	1.69
5	KOH	1.67
6	NH_3(aq)	1.74

5.2.4 Effect of electrolyte concentration on cell current

With single common electrolyte, the effect of acid concentration or alkali concentration on the cell current have studied by varying the concentration of the electrolyte from 0.5 N to 10 N and the results are shown in the Fig. 5.4 a and b. It can be seen from Fig. 5.4a, that when the alkali concentration is increased from 0.5 N to 10 N, there is a slight increase in the cell current. Similar observation has been made

(Fig. 5.4b) when increasing the acid concentration from 0.5 to 2 N the cell current increases. Pt is used as anode and cathode in these studies.

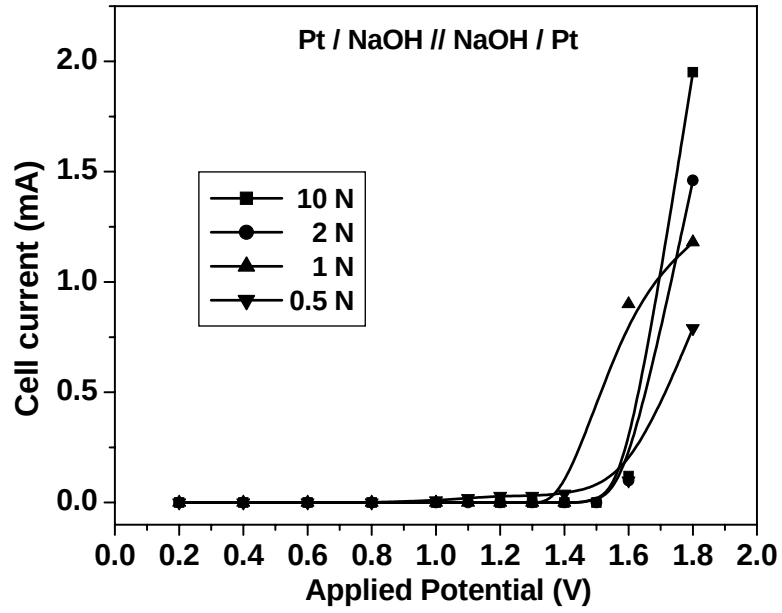

(a)

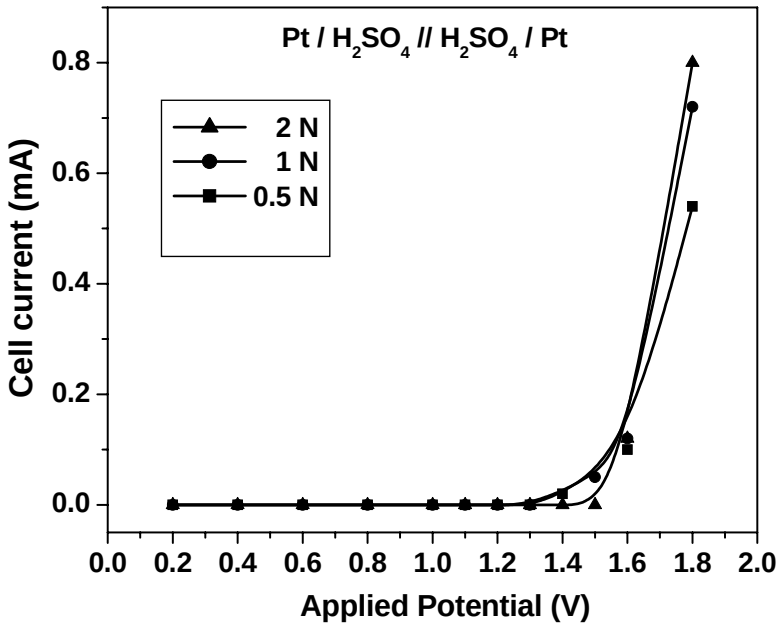

(b)

Fig. 5.4. Variation in the cell current-voltage profile for different concentrations of (a) NaOH and (b) H_2SO_4 in the single common electrolyte cell

The effect of concentration in the compartmentalized cell has been calculated by varying the concentration of anolyte from 0.5 to 20 N and keeping the catholyte concentration as 0.5, 1 and 2 N as constant separately. The variation in the cell current for each catholyte concentration is shown in Fig. 5.5 a, b and c. Fig. 5.5a shows, for 0.5 N anolyte concentration, the increase in the cell current when the concentration of anolyte was increased from 0.5 to 10 N. It can be seen that, as the concentration of the electrolyte increases, the cell current also increases, but there is no significant change in the decomposition potential with respect to concentration.

Fig. 5.5 b and c, shows the cell current Vs applied voltage curve for various anolyte concentration and at a constant catholyte concentration of 1 N and 2 N respectively. The similar trends have been seen for both the cases as in previous case.

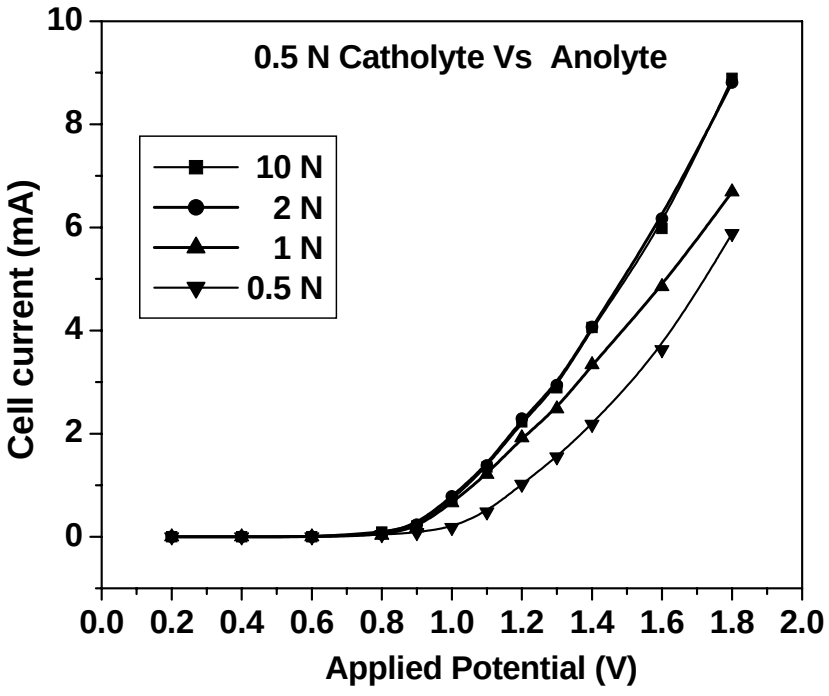

(a)

Fig.5.5. The cell current vs applied voltage curve for various anolyte concentrations and at a constant catholyte concentration of (a) 0.5 N

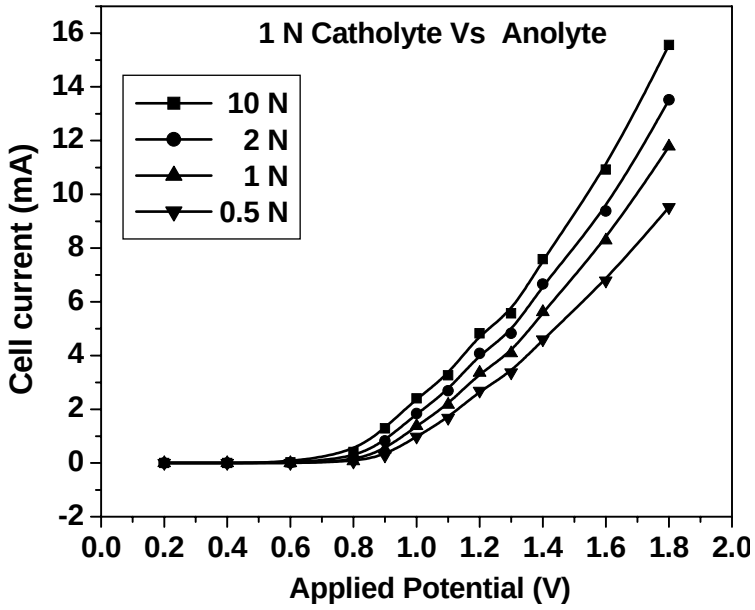

(b)

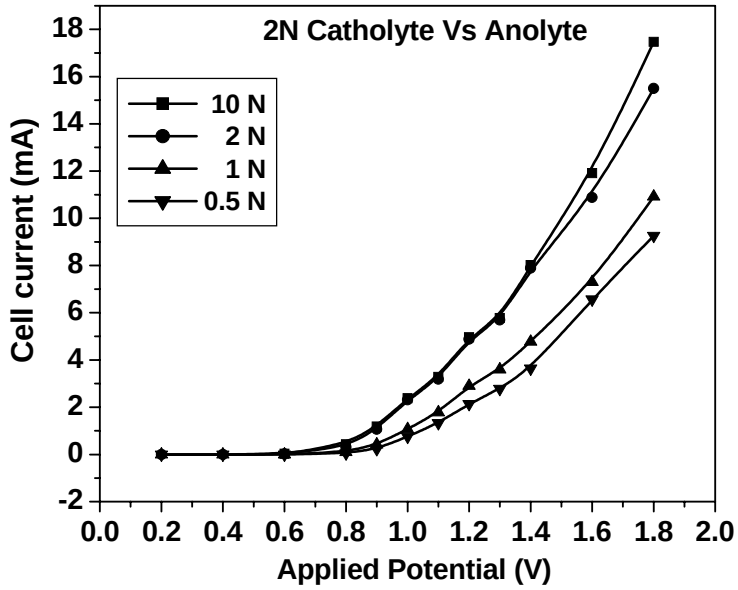

(c)

Fig.5.5. The cell current vs applied voltage curve for various anolyte concentrations and at a constant catholyte concentration of (b)1 N and (c) 2 N

The variation in the cell current at 1, 1.2 and 1.4 V applied potential for various anolyte and catholyte concentrations (when the anolyte concentration is varied, the catholyte concentration is kept constant) are shown in Fig. 5.6a, b & c respectively. It can be seen from the figures, when the catholyte concentration is 0.5 N, the rate of electrolysis is very low for all the concentrations of anolytes. On the other hand, when it is kept at 2 N, the rate of electrolysis increases dramatically as shown by the increased cell current. Nevertheless between 2 N and 10 N anolyte concentrations, no substantial rise in cell current is observed. When the catholyte concentration is 1 N, there is a gradual increase in the cell current as anolyte concentration increases from 0.5 N to 10 N. Based on the above observation, 1 N has kept constant as anolyte and catholyte concentration for our further studies.

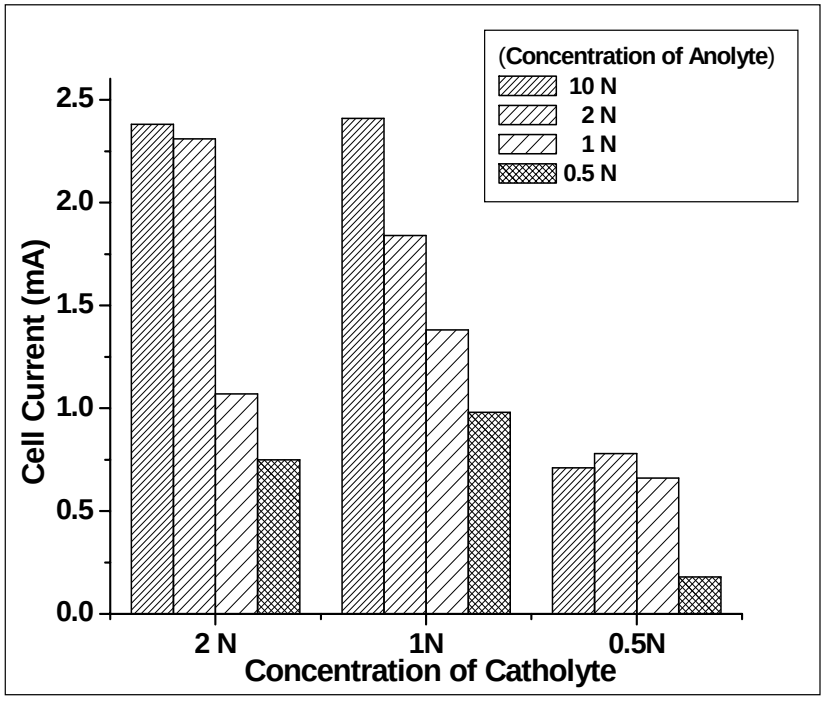

(a)

Fig. 5.6. Variation in the cell current for various concentrations of anolyte and catholyte at (a) 1.2 V

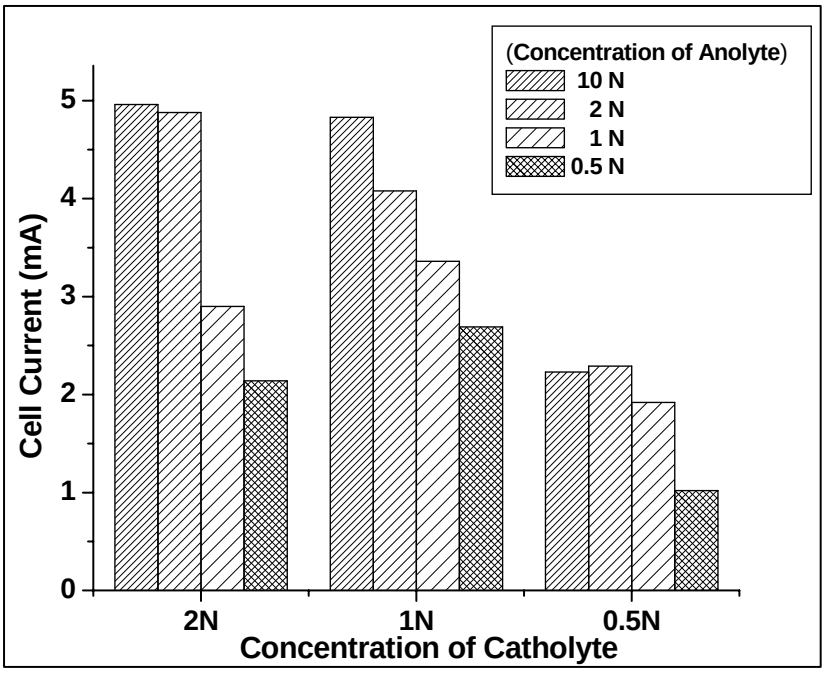

(b)

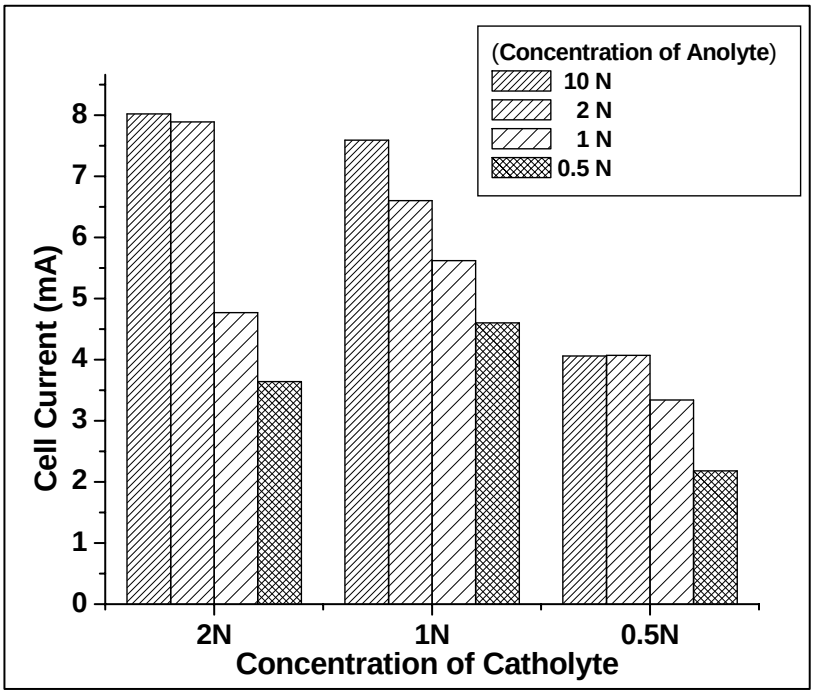

(c)

Fig. 5.6. Variation in the cell current for various concentrations of anolyte and catholyte at (b) 1.4 V and (c) 1.6 V

5.2.5 Nature of the anode material

In order to increase the cell current and reduce the applied potential various modifications have been carried out in the electrode surface. In this present study, the Pt and Ti electrodes are modified with Co and Ni oxides. The electrochemically deposited Co and Ni have been converted to oxide by calcining at 673 K in air for 2 h. Fig. 5.7 shows the applied potential vs the current plot of water electrolysis carried out with Pt cathode and Pt, Pt/Co and Pt/Co/Ni as anode. The decomposition potential for various electrodes are tabulated and are given in Table. 5.2. It can be seen from Table. 5.2 and Fig. 5.7, the decomposition of water has been achieved at an applied DC potential of 1 V. The coating of the metal oxides cobalt oxide and nickel oxide on Pt electrode shows a slight shift to a lesser decomposition potential, but one can observe significant increase in the cell current than in the case of pure Pt anode.

Table 5.2. Water decomposition potential in a divided cell with different electrolytes

Electrode		Decomposition potential (V)
Anode	**Cathode**	
Pt	Pt	0.9
Pt/Co	Pt	1.0
Pt/Co/Ni	Pt	0.9
Ti/Co	Pt	0.8
Ni	Ag	1.0

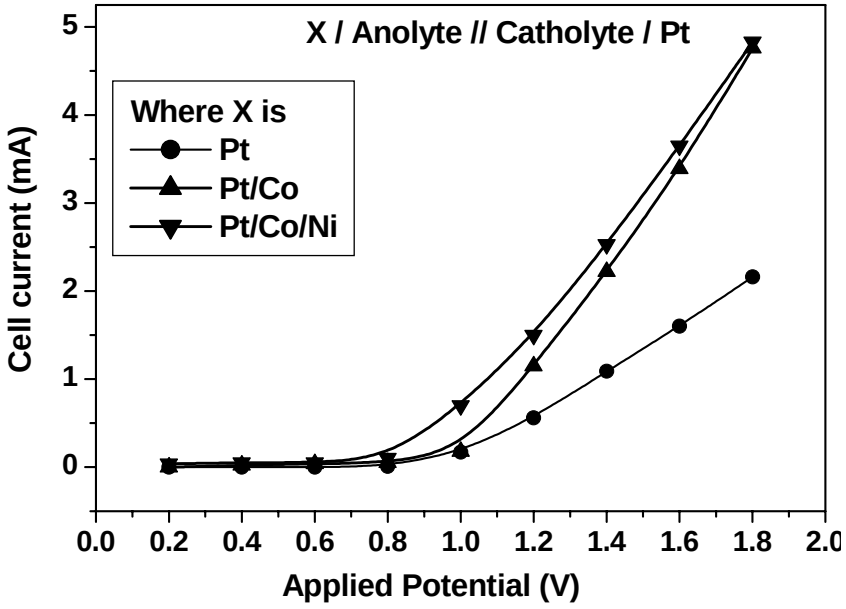

Fig. 5.7. Variation in the cell current for various Pt based anode materials

Similarly, the cell current has been measured for modified Ti anodes and shown in Fig. 5.8. Though pure Ti anode shows lesser activity when compared to Pt anodes, the modified Ti anodes show notably higher cell current than the pure Pt anode.

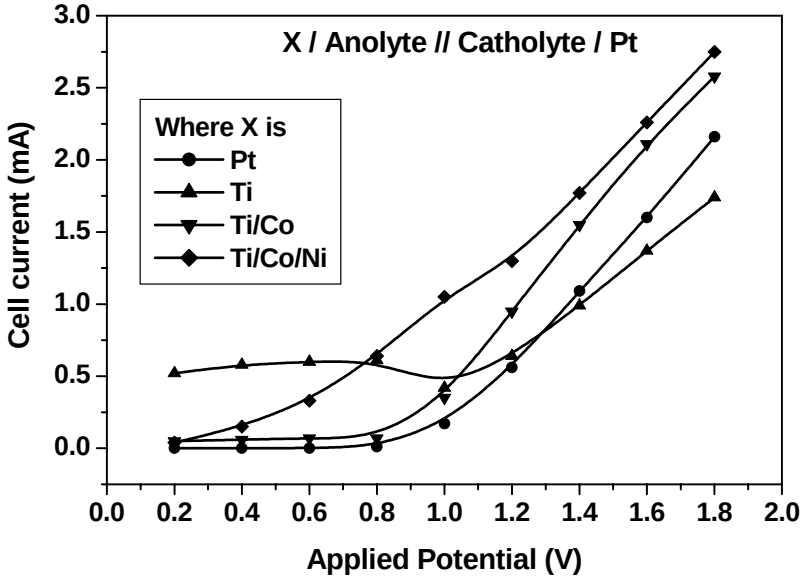

Fig. 5.8. Variation in the cell current for various titanium based anode materials

5.2.6 Product estimation

To ensure that the gases evolved at the cathode and anode compartments are only hydrogen and oxygen, the products of electrolysis, at a constant current of 1 mA have been collected separately for 26 h continuously, using Pt electrodes. The collected gas products have analyzed by gas chromatography. The evolved gases are shown to be only hydrogen and oxygen. Fig.5.9 shows the amount of gases (hydrogen and oxygen) produced in the cathode and anode compartments. The ratio between the volumes of hydrogen and oxygen gas is 2:1, which clearly indicates the absence of any other side products or side reactions during the water electrolysis.

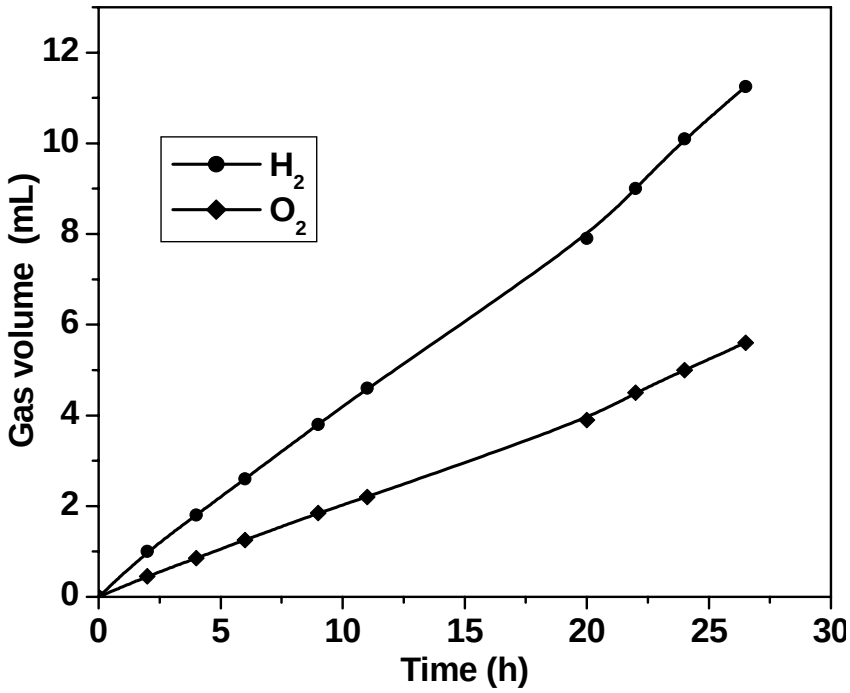

Fig. 5.9. Volume of hydrogen and oxygen generated at the cathode and anode compartments at various time

When the cell current is increased to 2 mA, for 15 h of electrolysis, ~ 12 and ~ 5.5 ml of hydrogen and oxygen gas are generated in the cathode and anode compartments respectively. Which is almost twice the volume of gas, which has been produced for 15 h at 1 mA as constant current.

5.3. MULTIPLE ELECTROLYTIC CELL

A multiple electrolytic cell has been designed as shown in Fig. 5.10. The cell performance was studied with Ag and Ti as cathode and anode, the optimum concentration (1 N) of anolyte and catholyte have been used. The anode and cathodes are connected in parallel mode.

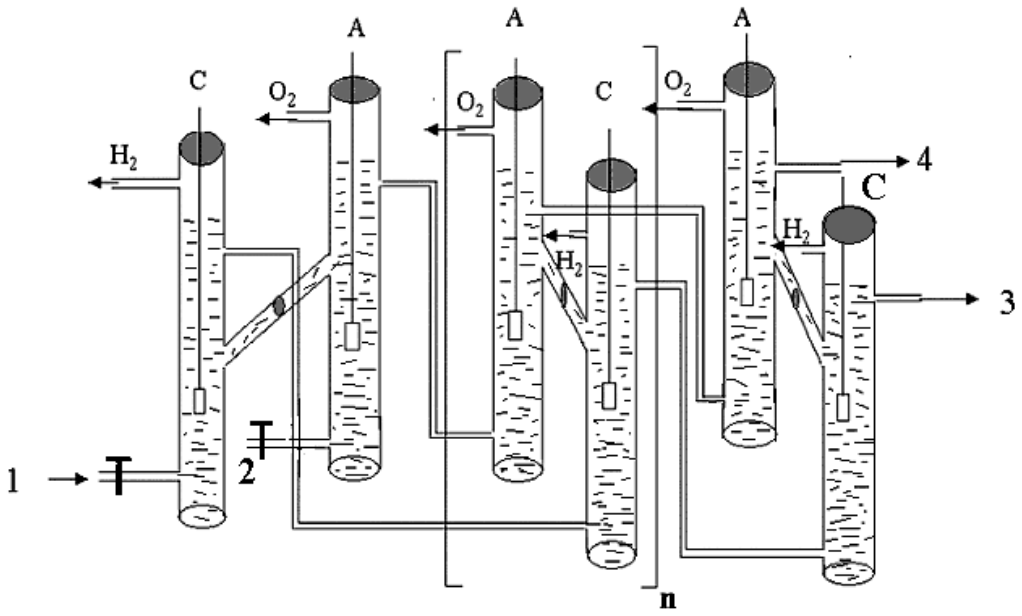

Fig 5.10. Multiple unit electrolytic cell

1.Catholyte inlet

2. Anolyte inlet

3. Catholyte outlet

4. Anolyte outlet.

n = Number of multiple cells

A - Anode (Ti)

C – Cathode (Ag)

The cell current obtained for one single cell and multiple electrolytic cells are shown in the Fig. 5.11. It can be seen that, there is a noticeable increase in the cell current for the multiple cell.

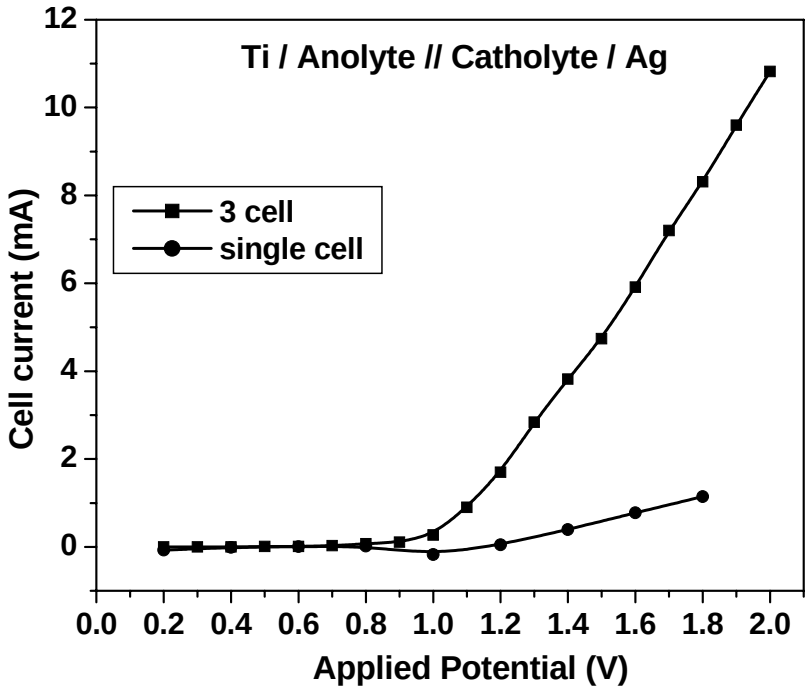

Fig. 5.11. Variation in the cell current for single and multiple electrolytic cell as a function of applied potential

5.4 EFFECT OF CELL DESIGN ON CELL CURRENT

The cell design has significant contribution in the efficiency of the electrolytic cell. In this view, various types electrolytic cells have been designed and studied for the water electrolysis (uni polar, bipolar, divided electrolytic cells). Also, the type and design of electrolytic cell depends on the mode of operation, nature of the electrode material, nature of the electrolyte. In our present study, to increase the cell current, the cell design has been modified and shown in Fig. 5.12. The advantages of this modified cell over the previous one are

1. The distance between anode and cathode is reduced significantly

2. The nature and size of the separator disk can be varied according to our requirement.

3. Performance various other separator can be easily examined using this cell

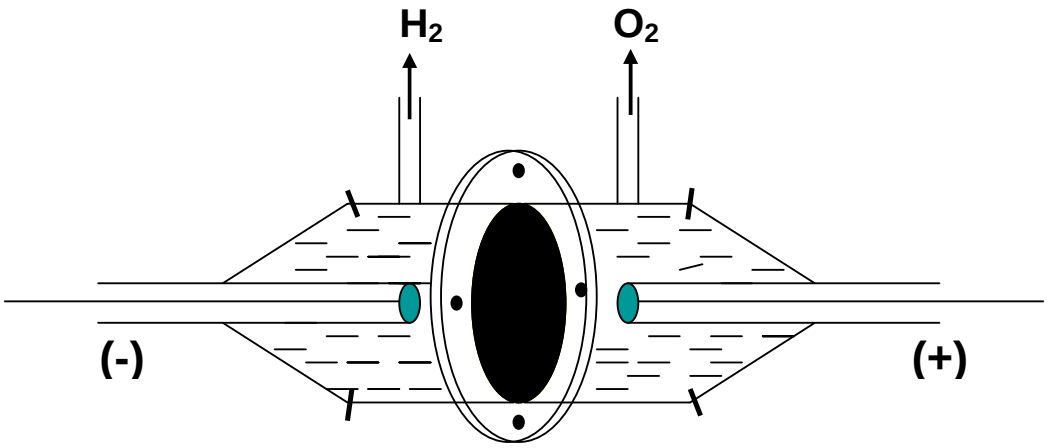

Fig. 5.12. Modified divided electrolytic cell

Various types of separator materials have been studied with the modified electrolytic cell, and it is observed that, there is significant increment in the cell current (not shown). This increase in the cell current is attributed to the increase in the area of the separator and minimum distance between the electrodes.

5.5 CONCLUSIONS

By using compartmentalized electrolytic cell, hydrogen generation has been achieved at an applied DC potential of ~1 V. Also, the restrictions on the choice of electrode material are minimized due to the separation of the catholyte and anolyte. The obtained cell current for titanium based anodes are comparable with the Pt electrodes. The concentrations of the electrolyte are lesser than the concentration of the electrolyte used in the commercial electrolytic cells. In addition, the mixing of gas products generated at the cathode and anode surface will be reduced greatly.

CHAPTER 6

ELECTROCHEMICAL DEGRADATION OF AQUEOUS PHENOL AND REMOVAL OF ARSENIC FROM WATER

6.1 ELECTROCHEMICAL DEGRADATION OF AQUEOUS PHENOL

6.1.1 Introduction

Concern for environmental pollution from industrial waste water is high, and many groups world wide are engaged in this area. One of the many methods employed for the removal of organic pollutants is "electrochemical oxidation of the organic pollutants". Researchers have reviewed the work in this area with a special emphasis on the merits of the electrochemical methods over the other processes like chemical oxidation, photocatalytic decomposition (Rajeshwar *et al*., 1994; Juttner *et al*., 2000). Different anodes like graphitic carbon electrode (Kannan *et al*., 1995; Liu and McCreery, 1995; DuVall and McCreey, 1999; DuVall and McCreey, 2000), metal oxide electrodes (Tahar and Savall, 1998; Wu and Zhou, 2001; Azzam *et al*., 2000) and metal electrodes (Canizares *et al*., 2002) have been employed. The major problem in the electrochemical oxidation of phenol is the formation of a polymer film on the electrode surface and this results in unwanted reduction of current density. For characterization of these polymeric films, Fourier Transform Infrared Spectroscopy (FTIR) has been widely used (Ezerskis and Jusys, 2002; Zareie *et al*., 2001). The formation of these films depends mainly on the nature of the electrodes, the ions in the electrolyte and the pH of the medium. It is reported that the formation of polymeric film on the electrode surface is favored by the alkaline medium than by acidic or neutral medium (Comninellis and Pulgarin, 1991; Canizares *et al*., 1999).

Scanning tunneling microscopy has been used to study the morphology of the film formed during the electro-oxidation of phenol (Wang *et al*., 1991)

The effect of various experimental factors like nature of the electrode, pH, temperature and the nature of medium on the electro-oxidation of phenol has been reported (Pulgarin *et al*., 1999; Ribordy *et al*., 1997; Iniesta *et al*., 2001). Recently, attempts have been made to study the relationship between the structure and reactivity of p-substituted phenols for electrochemical oxidation at Pt anodes and it is suggested that compounds with electron donor substituents will readily undergo electro-oxidation on Pt electrodes (Torres *et al*., 2003). When nickel or stainless steel is used as the anode, the efficiency has been found to be perceptibly slow due to the electro coagulation of the metal in the organic polymer matrix. In a similar type of electrooxidation, platinum metal anode has been reported to be efficient during electrolysis for the removal of organic wastes (Ezerskis and Jusys, 2001). But the stability of the electrode in saline medium is a point to be kept in mind in addition to prohibitive cost of platinum. Photochemical decomposition of hazardous wastes like phenol and chlorophenols is another cheap and efficient way to clean up the environment (Peiro *et al*., 2001). In an earlier work on the removal of phenolic compounds by electro-assisted process, a combination of photo-electrocatalysis has been reported. The combined process of electrocatalysis and photocatalysis has significant synergetic effect at the suitable applied potential of 3 V (Wu *et al*., 2002).

With this background, an attempt has been made in this chapter to investigate the electro- oxidation of aqueous phenol as a test pollutant in a divided electrolytic cell. The advantage of the compartmentalization is the use of anolyte and catholyte with different compositions. This in turn will open up new avenues, to employ more stable

electrodes involving chemically biased electrolytic cells. This setup further enables one to employ lower voltage conditions (5 V which is less than the voltage employed by previous studies) (Wu *et al.*, 2002). By using FTIR technique, it has been shown that phenolic species are strongly adsorbed on the carbon anode (especially in alkaline medium), which inhibits the rate of mineralization of phenol.

6.1.2 RESULTS AND DISCUSSION

6.1.2.1 Removal of phenols from water

The concentration profile of phenol as a function of electrolysis time is shown in Fig 6.1. The initial rate of degradation of phenol is almost independent of nature of the supporting electrolyte (0.1 N NaCl or 0.5 N NaOH or 0.5 N NaCl + 0.25 N NaOH). However, after 4 hours of electrolysis, decomposition of phenol is faster in the neutral chloride medium than in the alkaline medium.

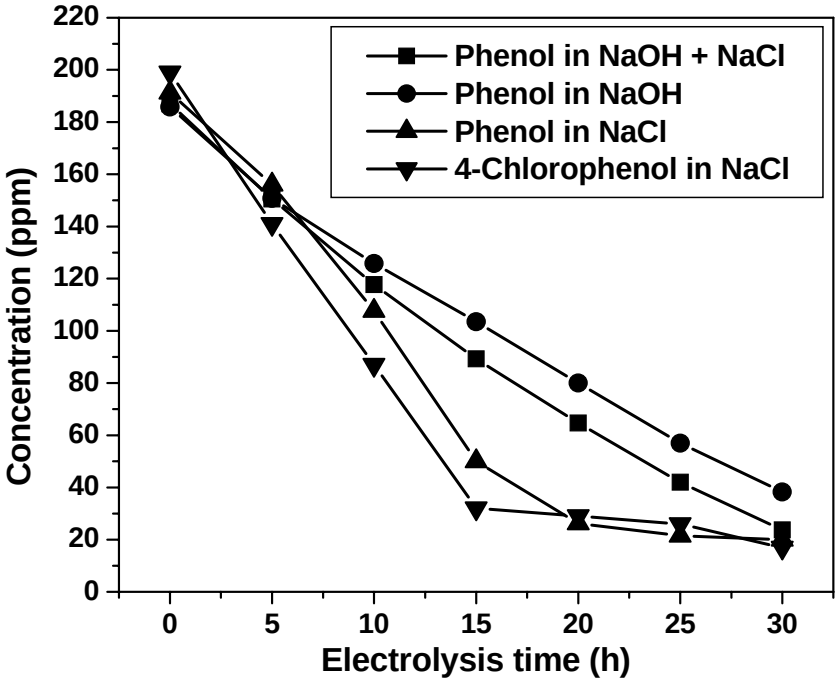

Fig. 6.1. Concentration of phenol and p-chlorophenol as a function of electrolysis time in different media at an applied cell potential of 5 V

Also it can be seen that, in the case of NaCl alone as supporting electrolyte, the decomposition of phenol and 4-chlorophenol are almost constant after 20 h of electrolysis. There is no significant change in the concentration in both the cases. Whereas, in presence of NaOH (NaOH or NaCl + NaOH mixture), the concentration of phenol has been observed to decrease even after 25 h of electrolysis.

6.1.2.2 Cell current and anode potential

In Fig 6.2, variations of the anode potential and cell current are plotted as a function of time when NaCl alone is used as the supporting electrolyte. The experiments have been carried out at a constant cell potential of 5.0 V. At the start of the experiment the anode potential constitutes around 2 V. Though cell potential is maintained at a constant value of 5.0 V throughout the 40 h of electrolysis, when NaCl is used as the supporting electrolyte, the anode potential is found to decrease as electrolysis proceeds and while the cell current is observed to increase. This feature indicates the greater extent of electrolysis as the time progresses. Also, it can be seen that, this significant increment in the cell current is observed for only 20 h of electrolysis. Beyond 20 h of electrolysis, there is no significant increment in the cell current. It is in agreement with the concentration profile for phenol decomposition in the NaCl medium. Also, the availability of the phenol on the electrode surface will be less due to the low concentration of the pollutant after 20 h electrolysis.

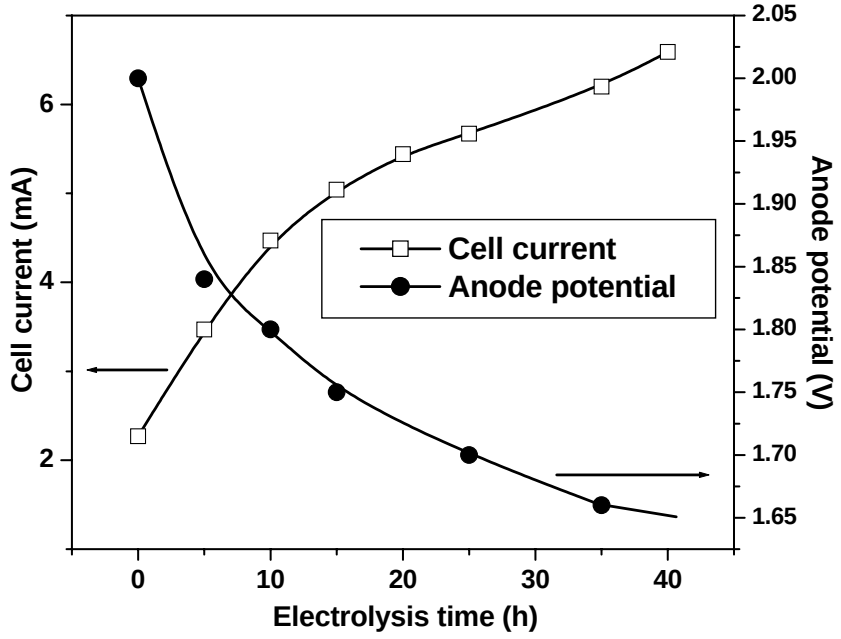

Fig. 6.2. Variation of anode potential and cell current as a function of electrolysis time at an applied cell potential of 5 V (in NaCl medium)

But, when NaOH is present in the anolyte, the anode potential has been observed to be more or less constant at 1.5 ± 0.2 V. The cell current on the contrary shows a decreasing trend as shown in Fig 6.3. Though, the initial cell current is high, it is gradually decreased to greater extent when the electrolysis time is increased. From the constant cell current and the observed decrease in the cell current, it can be concluded that, the active electrode surface (anode) is blocked. Also, it can be noticed from the decomposition profile of phenol in presence of NaOH, the decrease in the phenol concentration is constant, though the cell current is decreased. This observation indicates that, phenols are converted to some other form rather than decomposition on the electrode surface. This shows that the electrolytic degradation of phenol is dependent on the nature of the electrolyte medium.

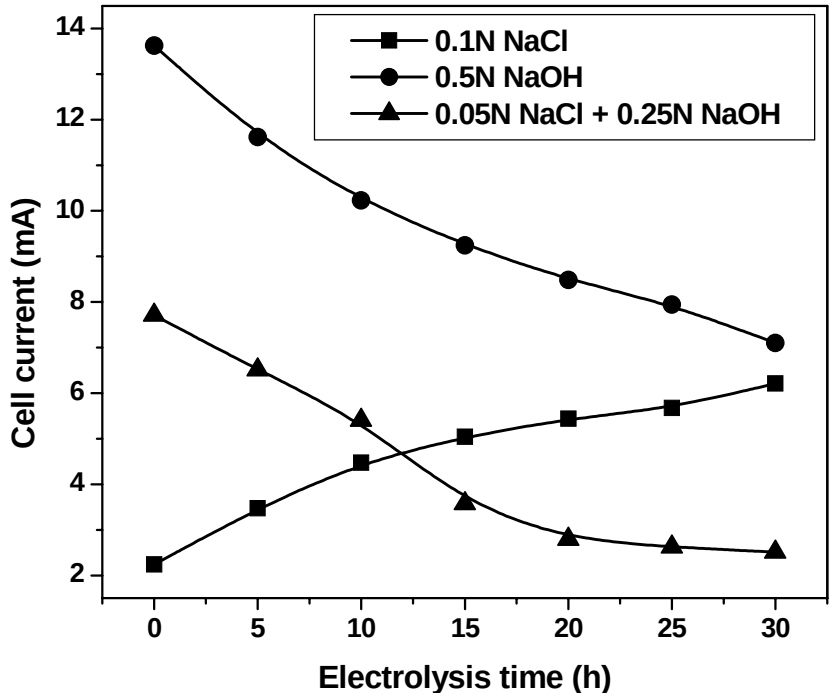

Fig. 6.3. Cell current vs time in different media at an applied cell potential of 5 V

6.1.2.3 Formation of passive film on the electrode surface

Presence of alkali in the electrolyte favours polymeric products to be coated on carbon electrode. This film can hinder or slow down the electrolytic process. A recent study reports the formation of non-passivating polymer film on carbon electrode surface during the electrolysis of phenol at high initial concentrations in NaCl medium (Zareie *et al*., 2001). But in the present study, the non-passive film formation has not been observed in presence of NaCl electrolyte. This may be due to lesser concentration of phenol taken for this study. When NaCl is present as the electrolyte the chlorine generated *in situ* will form hypochlorite or hypochlorous acid which are powerful oxidizing agents. In addition to this, the formation of p-chlorophenol will also assist the rate of decomposition of phenol, because the p-chlorophenol is found to be decomposing faster than phenol. In Fig 6.1, the concentration profiles of phenol and p-chlorophenol in the NaCl medium show that the decomposition rate of

p-chlorophenol is higher than that of phenol. In Table 6.1, electrolysis time, concentration of phenol and p-chlorophenol and COD are tabulated for the electrolysis experiment with NaCl alone as the supporting electrolyte.

Table 6.1 Phenol and COD concentration as a function of electrolysis time at an applied cell potential of 5 V (in NaCl supporting electrolyte)

S. No	Time (h)	Phenol Concentration (ppm)	p-Chlorophenol Concentration (ppm)	Phenol COD (ppm)	p-chlorophenol COD (ppm)
1	0	191	199	399	341
2	20	26	29	134	147
3	30	20	17	125	132
4	40	12	-	93	-

6.1.2.4 FT-IR studies

In order to find whether phenolic species are coated on carbon surface, FT-IR spectra have been recorded for carbon powder under different conditions. The spectra are shown in Fig 6.4, represents the conditions in the NaCl medium and Fig. 6.5, represents the conditions in the alkaline medium. In Fig 6.4 & 6.5, spectrum 'a' in, represents IR spectrum for carbon electrode powder material washed with distilled water and dried at 175 ^{0}C for 4 h in an air oven and pelletized with KBr. Spectrum 'b' is for the carbon powder, collected from the electrode immediately after electrolysis. The powder is washed and boiled with distilled water to remove traces of physically bound phenol, filtered and then dried at 175 ^{0}C for 4 h in hot air oven. The dried sample has been pelletized with KBr for recording the IR. Another sample of carbon has been collected from the electrode after the polarity of the carbon electrode had been reversed and employed as a cathode for a short period (~ 5 minutes). During this process it is expected to remove any of the weekly bound phenol. The powder is

collected form the electrode surface and washed with distilled water. Then it is boiled with distilled water to remove traces of physically bound phenol, washed, filtered and dried at 175 ^{0}C for 4 h in hot air oven and pelletized with KBr. This is shown in spectrum 'c' of Fig 6.4 and 6.5.

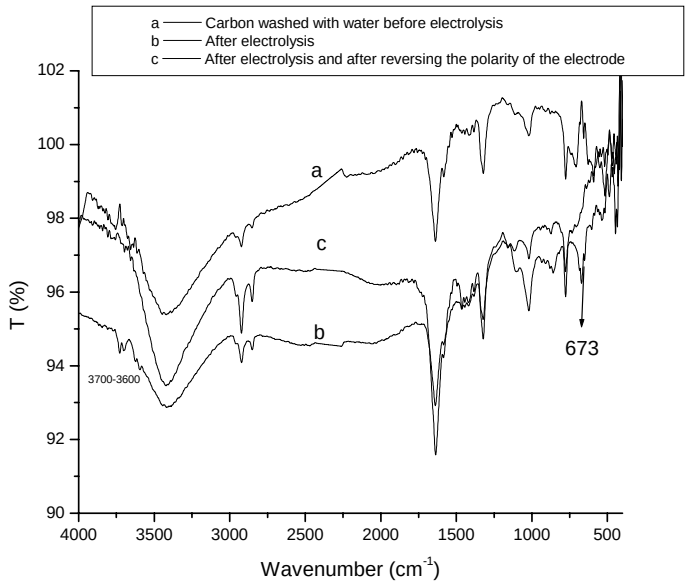

Fig. 6.4. IR spectrum of carbon electrode before and after the electrolysis in NaCl medium

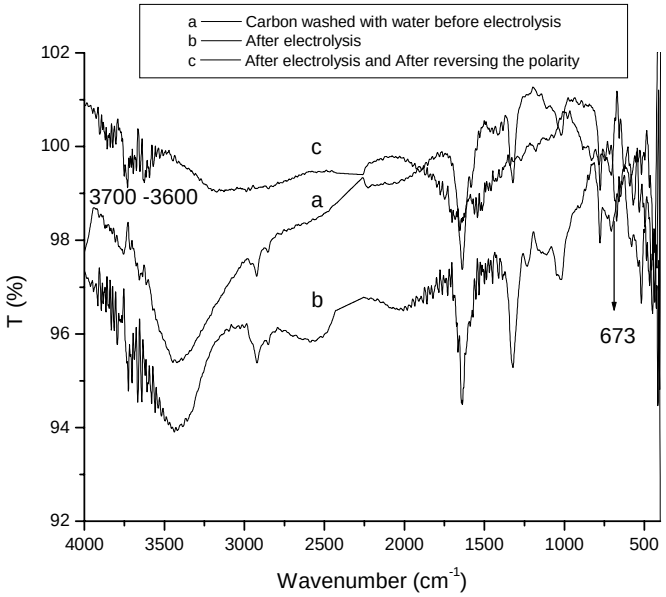

Fig. 6.5. IR spectrum of carbon electrode before and after the electrolysis in NaOH medium

The O-H stretching frequency is in the range of ~ 3600 – 3700 $cm^{-1}$and the C-H bending frequency is in the range of ~ 650 – 700 cm^{-1} and these are observed on the electrode surface after the electrolysis with NaCl as the supporting electrolyte. These absorption frequencies disappear on reversing the electrode potential. This proves that the phenol is adsorbed on the electrode surface during electrolysis. At the same time this is not strongly bound as these frequencies disappear when the potential has been reversed. Similar kind of experiments carried out in the alkaline medium, shows that the species adsorbed on the surface are still retained even after the reversal of potential. This clearly indicates that the surface is coated with phenolic species (may be polymeric). As shown in spectrum 'c' in Fig. 6.5, it is worthwhile to keep in mind that the phenate ion eliminates the bridging through hydrogen bond

Generally, the reaction sequence for phenol decomposition is as follows:

Phenol → Intermediate compounds → Final products (CO_2 + H_2O + polymers)

6.1.2.5 Formation of 4 chlorophenol intermediate

In order to check whether any chlorinated phenol is formed as intermediates, UV-visible λ_{max} for phenol and chloro-phenols have been recorded and the values are given in Table 6.2. The phenol and o-chlorophenol have λ_{max} at 268 and 272 nm respectively. While the p-chlorophenol has the value around 278 nm and the phenoxide has value around 286 nm. The λ_{max} value of samples electrolyzed in NaCl is also included. The sample has initial λ_{max} pertaining to phenol. On electrolysis there is a shift in the λ_{max} value to 276 – 278 nm. At the end of electrolysis the λ_{max} shifts back to the original. From this it may be concluded that p – chlorophenol is formed as an intermediate species during the initial stages of electrolysis. The formation of p-chlorophenol intermediate has also been confirmed by gas chromatography by

analyzing the electrolyzed solution (after 5 hours of electrolysis). The disappearance of p-chlorophenol at the end of the electrolysis is observed.

Table 6.2. λ_{max} of phenolic compounds

S.No	Compounds	λ_{max}(nm)
1	Phenol	268
2	Phenoxide ion	286
3	O-Chlorophenol	272
4	P-Chlorophenol	276
5	Sample-1 (after 5 h electrolysis)	276
6	Sample-2 (after 15 h electrolysis)	274

6.1.2.6 Proposed reaction mechanism

Based on the results of our study, the possible pathway for the decomposition of phenol is shown in the Scheme 6.1, which is similar to the one reported in the literature (Torres *et al*., 2003; Gattrell and Kirk, 1990). In the presence of NaCl, the pathways I and II are favoured and the pathway III is restricted; but in alkaline medium, the pathway I is completely restricted due to the absence of chloride ion in the medium and II & III are favoured. However, polymerization of phenol occurs only in the alkaline medium under the specific conditions when the phenoxide ion is more stable (pathway I).

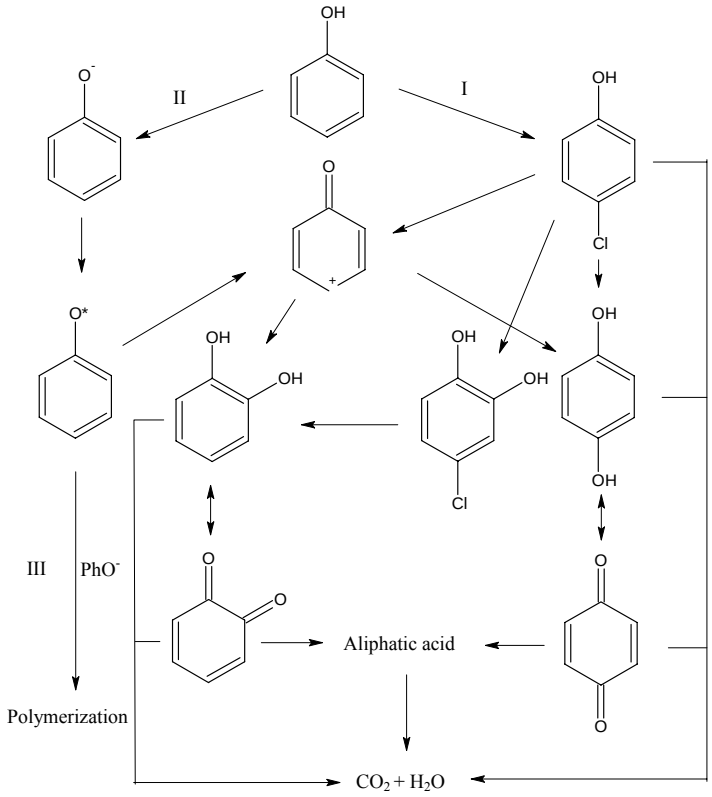

Scheme 6.1. Proposed pathway for the decomposition of phenol

6.1.2.7 Efficiency of phenol removal

a. Current efficiency

The volume of hydrogen produced at cathode compartment, during the entire duration of electro-decomposition of phenol with NaCl as supporting electrolyte is shown in Fig 6.6. The amount of hydrogen generated indicates that, this process has a current efficiency exceeding 97 %. Thus with the present cell one gets a value added by-product in the form of hydrogen. The chemical reaction for the phenol mineralization is,

$$C_6H_6O + 7\ O_2 \rightarrow 6CO_2 + 3H_2O$$

Theoretically 7 moles of oxygen is needed to oxidize each mole of phenol. This will be equivalent to 14 moles of hydrogen at the cathode. In our experiments, the anolyte contained 8 mg of phenol, which is equivalent to 0.085 mmole of phenol. This will liberate 1.19 mmole of hydrogen. The hydrogen gas volume at 300 K for this amount will be around 30 ml. The fact that more hydrogen is liberated indicates that either side reactions are accompanying phenol degradation or not all the liberated oxygen is used in the phenol degradation. Thus it can be seen as added advantages of using a divided cell. The generation of hydrogen, as a by-product and fuel of the future will be a valuable by-product.

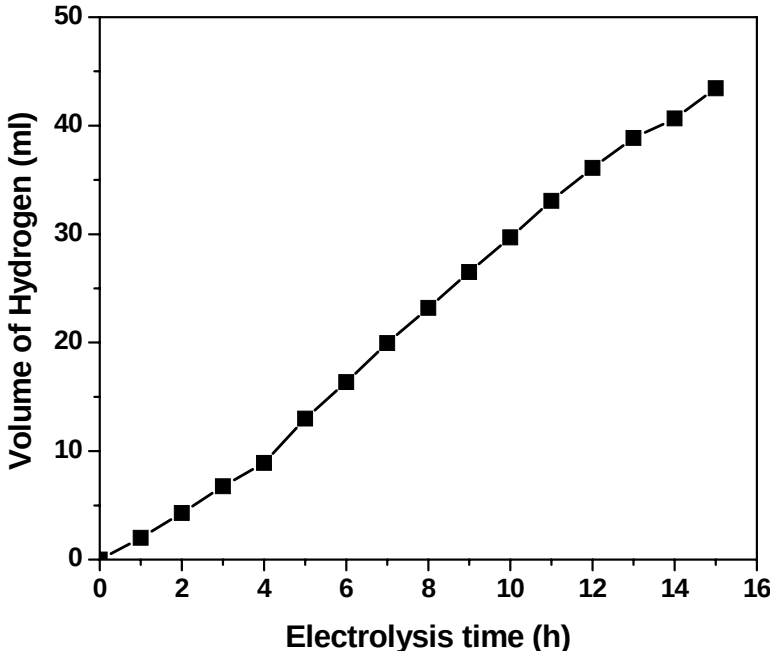

Fig. 6.6. Volume of evolved hydrogen at the cathode during the decomposition of phenol at an applied cell potential of 5 V

b. The average current efficiency (ACE)

The average current efficiency (ACE) for phenol removal has also been calculated by using the following formula.

$$ACE = \frac{\text{Experimental change in number of moles of phenol}}{\text{Theoretical change in number of moles of phenol}}$$

The experimental change in the number of moles of phenol was calculated by taking the difference between the initial and final COD values. For this calculation, the cell current was taken as average of cell current obtained in the period of 0 to 40 h for every 5 h from the Fig. 6.2. It was observed that the ACE for the removal of phenols in the NaCl medium are 63 % for phenol and 85% for chlorophenol, respectively.

6.2 REMOVAL OF ARSENIC FROM WATER BY ELECTROLYSIS

6.2.1 Properties of arsenic

Elemental arsenic (As) occurs in two solid modifications, yellow and silver-gray crystalline metallic solid that exhibits low thermal conductivity. Although arsenic is often referred to as a metal, it is classified chemically as a non-metal or metalloid belonging to Group 15 (VA) of the periodic table. The principle valances of arsenic are +3, +5 and -3. Arsenic and its compounds are poisonous and it is finding increasing uses as a doping agent in solid-state devices such as transistors (Weast and Astle, 1978). Gallium arsenide is used as a laser material to convert electricity directly into coherent light.

6.2.2 Occurrence of arsenic

Arsenic is found widely in nature and is most often combined with oxygen, chlorine or sulphur. It is found in trace quantities in all living organisms, the atmosphere, water and geological formations. It is usually found in ores containing gold, silver, cobalt, nickel and antimony. There are over 150 known arsenic-bearing minerals and the most of them are of inorganic origin. A few are listed in Table 6.3.

Table 6.3. Important arsenic bearing minerals

Mineral	Arsenic Content, %
Arsenopyrite	46
Lollingite	73
Orpiment	61
Realger	70
Native Arsenic	90 - 100

Compounds of arsenic can be typically divided into two categories: inorganic and organic forms. Inorganic arsenic occurs naturally in many kinds of rocks as highlighted in Table 6.3, the most commonly found inorganic form is with sulphide ores, such as arsenopyrite. Organic compounds of arsenic occur due to its affinity to combine easily with carbon to form a wide variety of organic compounds with one or more As-C bonds. The most commonly occurring organic forms are monomethylarsonic acid (MMA) and dimethylarsinic acid (DMA).

Elevated arsenic concentrations are found in groundwater due to anthropogenic activities and natural processes. Anthropogenic activities include mining, use of arsenical pesticides, herbicides and crop desiccants, release of industrial effluents, and disposal of chemical waste (Bang *et al.,* 2005; Chakravarty *et al.,* 2002; Smedley and Kinniburgh, 2002). The release of arsenic from natural processes can be caused by the reduction of iron hydroxides and the oxidation of pyrite minerals including orpiment (As_2S_3) and realgar (As_2S_2) (Meng *et al.,* 2001; Nickson *et al.,* 2000).

6.2.3 Methods for removal of arsenic from water

Removal of arsenic from drinking water is one of the main aims of water purification because of its execrable health threat. Arsenic is removed from water mainly by

adsorption (Daus *et al*., 2004; Zhang *et al*., 2003), precipitation (Roberts *et al*., 2004), ion exchange, UV-Oxidation process (Zaw and Emett, 2002), electrocoagulation (Ratna Kumar *et al*., 2004) and membrane filtration. Activated alumina (Kim *et al*., 2004) is the most commonly used adsorbent for the removal of arsenic from aqueous solutions. Though there are many methods known to remove arsenic from water they have their own limitations like slow kinetics, instability, saturation and the contamination by other metal ions in the medium. Electrochemical reduction of arsenic ion to arsine is one of the methods, in which one can achieve maximum efficiency compared to many other methods. This part will also emphasis the cathodic removal of arsenic from the water.

6.2.4 RESULTS AND DISCUSSION

In the case of arsenic removal, H^+ ions are reduced to atomic hydrogen at the cathodic compartment and this nascent hydrogen favours the reduction of arsenic from its higher oxidation state, namely, As (III) and As (IV). The reduced arsenic atoms will combine with hydrogen atoms, which results in the formation of Arsine (AsH_3) gas.

6.2.4.1 Removal of arsenic

Two different concentrations of arsenic solution have been taken for the analysis (200 μg/l and 1082 μg/l). This experiment has been carried out in galvanostatic conditions at 20mA and 30mA current. The quantities of arsenic present in the test solutions are electrolyzed with different currents are given in Table 6.4. It can be seen from Table 6.4, that the solutions containing initial concentration of 1082 and 200 μg/l of arsenic are brought down to 210 and 13 μg/l respectively at 20 mA as applied cell current and time period of 48 h. For 30 mA of applied cell current, the solutions

containing the same initial concentration of arsenic are brought down to 156 and 6 μg/l respectively at 48 h of electrolysis. The lower level of arsenic concentration (6 μg/l) has been achieved by employing this method. The achieved value is found to be lower than the permissible value (10 μg/l) of drinking water standard proposed by the World Health Organization (www.who.int) and hence it is proposed that this electrolysis is an inexpensive and suitable method of removal of arsenic in potable water.

Table 6.4. Effect of cell current and initial concentration on arsenic removal

Current (mA)	Time of electrolysis (h)	Initial concentration (μg/l)	Final concentration (μg/l)
20	48	1082 200	210 13
30	48	1082 200	156 6

It can be seen clearly form the table that, when the initial concentration is high, the complete removal of arsenic from the solution has not been achieved even when the electrolysis has been carried out for more than 48 h, where as, when a fresh solution, which have the same concentration of 200 μg/l has taken, one can able to reduce the arsenic concentration up to 6 μg/l. This can be attributed due to the formation of equilibrium between the deposited arsenic metal on the electrode surface and dissolution of deposited arsenic metal from the electrode surface, which results in a decrease in the removal efficiency.

Fig. 6.7 shows the decomposition profile of arsenic in the cathodic compartment and it can be seen that, at the initial stages of the reaction, the removal rate is very high up

to 12 h of electrolysis and after 12 h of electrolysis, there is no significant change in the removal rate for both the initial concentrations.

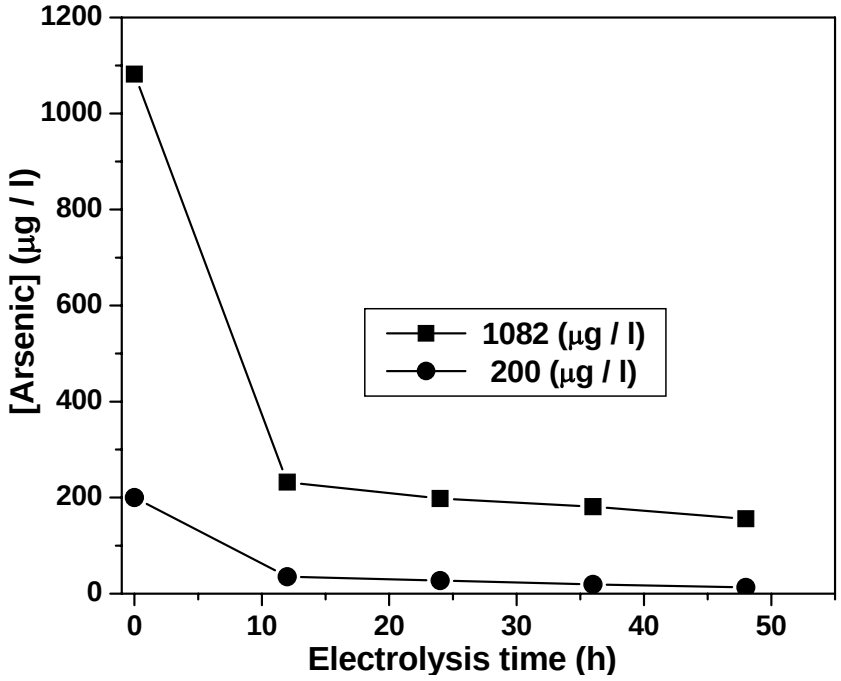

Fig. 6.7. Amount of arsenic collected from the cathode compartment with time of electrolysis for different initial concentrations

6.3 CONCLUSIONS

In the present study a relatively lower voltage of 5 V has been found to be sufficient to degrade phenol. This has been made possible due to the compartmentalization of the cell. As a consequence of this, nascent oxygen generated *in situ* at the anode compartment is providing an additional route for the degradation process. The electrochemical decomposition of phenol was found to be dependent on the medium in which it is carried out. Among the alkaline and NaCl media, the decomposition is faster in the latter. In the NaCl medium, the formation of p-chlorophenol intermediate and absence of non-passive film formation on the electrode surface were identified and was confirmed using UV-Visible, IR and Gas chromatography. The formation of

passive film (polymer) on the carbon electrode surface in alkaline medium resulted in slower degradation of phenol. The IR study confirms that the polymer is strongly adsorbed on the electrode surface. This indicated that the polymerization of phenol was favoured only in the alkaline medium. The major advantage of the divided electrolytic cell was that it produced a valuable co-byproduct of pure hydrogen, with > 97% efficiency. This process will enable the user to employ lower voltages and hence the energy consumed will be concomitantly lower than the values reported in the earlier literature.

The arsenic removal has been profitably achieved by using divided electrolytic cell with Ag and Ni electrodes. The left over arsenic in the solution, after the electrolysis is very much within permissible level. The removal of arsenic is very much effected by the initial concentration of the arsenic present in the electrolytic medium.

CHAPTER 7

SUMMARY AND CONCLUSIONS

In this study, CdS nanoparticles prepared from zeolite matrices and ultrasonic precipitation methods have been shown to be efficient photocatalyst for hydrogen production. In the first method, the zeolite matrix acts as a template preventing the growth of CdS particles during precipitation process resulting in the formation of nanoparticles. In the second method, the CdS mesoporous nanoparticles are formed due to the high energetic ultrasonic waves. The CdS nanoparticles prepared by both the methods exhibit blue shift in the absorption edge (UV-Vis) due to particle size effect. Mixed cubic and hexagonal phases have been observed in the XRD pattern for the CdS nanoparticles prepared from the zeolites. Only cubic phase has been observed in the samples prepared in the ultrasonic precipitation method. The nanoparticles are of uniform size with a particle size distribution in the range of 6-12 nm and 5 ± 1 nm in zeolite template and ultrasonic precipitation methods, respectively. Studies on the photocatalytic activity of these materials show that the nanoparticles exhibit higher activity compared to the bulk samples. Surface area, morphology and particle size of the CdS are important factors, which affect their performance as catalyst for hydrogen evolution. Presence of noble metals such as Pt and Pd greatly enhances the photocatalytic activity of the synthesized CdS nanoparticles. Pt/CdS-U nanoparticles show higher photocatalytic activity (both in UV light and direct sunlight). In the CdS-TiO_2 coupled system, Pt/CdS-U: N-TiO_2 shows higher activity when the ratio between the CdS and TiO_2 is 0.5.

N-doped TiO_2 nanosize photocatalyst with a homogeneous size and spherical shape has been prepared by three different routes namely (i) Simple hydrolysis of $TiCl_3$ (ii) Thermal decomposition Ti- salen complex in vacuum and (iii) Thermal decomposition of Ti-melamine complex. Similarly, the N, S co-doped TiO_2 sample has been prepared by thermal decomposition of Ti based metal complex in vacuum. The light absorption onset of heteroatom doped sample in the visible region is clearly observed. The advantages of the first method over other methods for preparation of N-doped TiO_2 are (i) use of inexpensive chemical precursors for the synthesis of N-doped TiO_2, and (ii) formation of TiO_2 as uniform sized nanoparticles. XPS results indicate the status of N to be anion like (N^-) and the chemical environment of N is as in N-Ti-O in the N- doped TiO_2 lattice. The methods of preparation strongly affects the visible light absorption capacity, and the chemical nature N in the doped TiO_2. In the N, S co-doped TiO_2, the N and S are present as anions and replace some of the oxygens in the TiO_2 lattice. The visible light induced photocatlytic activity of the prepared heteroatom doped samples are evaluated for decomposition of methylene blue. The heteroatom doped TiO_2 sample shows higher photocatalytic activity when compared to Degussa P25 and pure TiO_2. The theoretical results using DFT calculation, shows that the band gap reduction in the TiO_2 could be achieved by substitutional doping with heteroatoms like N and S in the TiO_2. The magnitude of band gap reduction increases with decrease in the electronegativity difference between Ti- heteroatom bonds. Also, the observed results strongly emphasis that, S doping been more impact on the band gap reduction, and the doping of S atom in the TiO_2 replaces only the oxygen atom, but not the Ti atom in the lattice. Also, the doping of S in the Ti position has no significance in the band gap reduction, and the photocatalytic activity.

By using compartmentalized electrolytic cell, hydrogen generation has been achieved at an applied DC potential of ~1 V. Also, the restrictions on the choice of electrode materials are minimized due to the separation of the catholyte and anolyte. The obtained cell current for titanium based anodes are comparable with that of the Pt electrodes. The concentrations of the electrolyte are lesser than the concentration of the electrolyte used in the commercial electrolytic cells. In addition, the mixing of gas products generated at the cathode and anode surface will be considerably reduced.

By using compartmentalized electrolytic cell, the electrolytic decomposition of phenol has been carried out in the anodic compartment. The electrochemical decomposition of phenol was found to be dependent on the medium in which it is carried out. Among the alkaline and NaCl media, the decomposition is faster in the latter. In the NaCl medium, the formation of p-chlorophenol intermediate and absence of non-passive film formation on the electrode surface were identified and was confirmed using UV-Visible, IR and Gas chromatography. The formation of passive film (polymer) on the carbon electrode surface in alkaline medium resulted in slower degradation of phenol. The IR study confirms that the polymer is strongly adsorbed on the electrode surface. This indicated that the polymerization of phenol is favoured only in the alkaline medium. The major advantage of the divided electrolytic cell is that it produced a valuable co-byproduct of pure hydrogen, with > 97% efficiency. The arsenic removal has been profitably achieved by using divided electrolytic cell with Ag and Ni electrodes. The left over arsenic in the solution, after the electrolysis is within permissible levels. The removal of arsenic is very much effected by the initial concentration of the arsenic present in the electrolytic medium.

The significant conclusions arrived at from these studies are

- Particle size, crystalline nature, surface area and morphology of CdS nanoparticles influence the rate of photocatalytic hydrogen production.

- Noble metal (Pt, Pd, Ru and Rh) loaded CdS nanoparticles show enhanced photocatalytic activity. In particular, Pt metal loaded on mesoporous CdS nanoparticle shows higher activity for photocatalytic hydrogen production.

- Different synthetic routes are evaluated for the preparation of N doped, and N, S co-doped TiO_2, which are active in the visible region. They have been characterized systematically. It is shown that, N and S doping results in substitution at anionic sites and hence alters the optical response. These doped TiO_2 systems are found to be suitable photocatalyst for methylene blue decomposition employing visible light radiation.

- Hydrogen generation has been observed at ~ 1.0 V using a novel compartmentalized electrolytic cell with chemically treated disk as separator.

- Compartmentalized electrolytic cell has been devised both for electrolytic degradation of phenol and removal of arsenic from water. It is shown that that this method is effective and also yields pure hydrogen or oxygen as valuable by-products.

Suggestions for Future studies

Platinum loaded mesoporous CdS can be developed for hydrogen production by water splitting using direct sunlight as energy source. The preparation methods, amount of metal loading and experimental conditions have to be optimized to achieve higher photocatalytic efficiency.

Visible light active TiO_2 based photocatalyst can be prepared for environmental application by doping with hetero atom, and the amount of hetero atom doping in the TiO_2 should be optimized to use TiO_2 in the visible light application.

Compartmentalized electrolytic cell can be utilized for hydrogen production and environmental application, by designing cells having larger electrode surface. Studies can also be undertaken with different chemical treatments for the separator.

REFERENCES

1. **Abe, R., K. Sayama** and **H. Arakawa** (2002) "Efficient hydrogen evolution from aqueous mixture of I− and acetonitrile using a merocyanine dye-sensitized Pt/TiO2 photocatalyst under visible light irradiation". *Chemical Physics Letters*, **362**, 441-444.

2. **Ait-Ichou, I., M. Formenti, B. Pommier** and **S. J. Teichner** (1985) "Photocatalytic dehydrogenation of isopropanol on Pt/TiO2 catalysts". *Journal of Catalysis*, **91**, 293-307.

3. **Alfano, O.M., D. Bahnemann, A.E. Cassano, R. Dillert** and **R. Goslich** (2000) "Photocatalysis in water environments using artificial and solar light". *Catalysis Today*, **58,** 199-320

4. **Anpo, M** (2000) "Applications of Titanium Oxide Photocatalysts and Unique Second-generation TiO2 Photocatalysts Able to Operate Under Visible Light Irradiation for the reduction of Environmental Toxins on a Global Scale". *Studies in Surface Science and Catalysis*, **130**, 157-163.

5. **Arora, M.K., A. S. K. Sinha** and **S.N. Upadhyay** (1998) "Active Cadmium Sulfide Photocatalysts for Hydrogen Production from Water". *Industrial Engineering Chemical Research,* **37,** 3950-3955.

6. **Asahi, R., T. Morikawa, T. Ohwaki, K. Aoki** and **Y. Taga** (2001) "Visible light photocatalysis in Nitrogen-doped titanium oxides". *Science,* **293**, 269-271.

7. **Augustynski, J** (1993) "The role of the surface intermediates in the photoelectrochemical behaviour of anatase and rutile TiO_2". *Electrochemica Acta*, **38**, 43-46.

8. **Awad, Y.M** and **N.S. Abuzaid** (1997) "Electrochemical treatment of phenolic wastewater: Efficiency, design considerations and economic evaluation". *Journal of Environmental Science and Health Part A-Environmental Science and Engineering & Toxic and Hazardous Substance Control,* **32**, 1393-1414.

9. **Azzam, M.O., M. Al-Tarazi** and **Y. Tahboub** (2000) "Anodic Destruction of 4-Chlorophenol Solution". *Journal of Hazardous Materials,* **75**, 99-113.

10. **Bacsa, R., J. Kiwi, T. Ohno, P. Albers and V. Nadtochenko** (2005) "Preparation, Testing and Characterization of Doped TiO_2 Active in the Peroxidation of Biomolecules under Visible Light". *Journal of Physical Chemistry*, B.**109,** 5994-6003.

11. **Bahnemann, D.W., J. Monig** and **R. Chapman** (1987) "Efficient photocatalysis of the irreversible one-electron and two-electron reduction of halothane on platinized colloidal titanium dioxide in aqueous suspension". *Journal of Physical Chemistry,* **91,** 3782-3788.

12. **Bandara, J., C.C. Hadapangoda** and **W.G. Jayasekera** (2004) "TiO_2/MgO composite photocatalyst: the role of MgO in photoinduced charge carrier separation". *Applied Catalysis B: Environmental,* **50,** 83-88.

13. **Bang, S., G.P. Korfiatis** and **X. Meng** (2005) "Removal of arsenic from water by zero-valent iron". *Journal of Hazardous Materials*, **121,** 61–67.

14. **Barbeni, M., E. Pelizzetti, E. Borgarello, N. Serpone, M. Graetzel, L. Balducci** and **M. Visca** (1985) **"**Hydrogen from hydrogen sulfide cleavage. Improved efficiencies via modification of semiconductor particulates". *International Journal of Hydrogen Energy*, **10,** 249-253.

15. **Bard, A.J., M. Stratmann** and **S. Licht** (2002) "Encyclopedia of Electrochemistry". Volume 6. (Semiconductor electrodes and Photoelectrochemistry) Wiley-VCH Verlag GmbH, Weinheim.

16. **Bard, J.B.** and **L.R. Faulkner** (1980) Electrochemical Methods, Wiley.

17. **Becke A.D** (1993) "Density-functional thermochemistry. III. The role of exact exchange". *Journal of Chemical Physics*, **98,** 5648-5652.

18. **Benemann, J.R** and **N.M. Weare** (1974) "Hydrogen evolution by nitrogen-fixing Anabaena cylindrica cultures". *Science,* **184,** 174-175

19. **Beydoun, D., H. Tse, R. Amal, G. Low** and **S. McEvoy** (2002) "Effect of copper (II) on the photocatalytic degradation of sucrose". *Journal of Molecular Catalysis A: Chemical,* **177**, 265–272.

20. **Blaha, P., K. Schwarz, P. Sorantin** and **S.B. Trickey** (1990) "Full-potential, linearized augmented plane wave programs for crystalline systems". *Computer Physics Communications,* **59**, 399-415.

21. **Borgarello, E., N. Serpone, M. Graetzel** and **E. Pelizzetti** (1986) "Photodecomposition of H_2S in aqueous alkaline media catalyzed by RuO_2-loaded alumina in the presence of cadmium sulfide. Application of the inter-particle electron transfer mechanism". *Inorganica Chimica Acta,* **112**, 197-201.

22. **Borrell, L., S. Cervera-March, J. Gimenez** and **R. Simarro** (1992) "A comparative study of CdS-based semiconductor photocatalysts for solar hydrogen production from sulphide + sulphite substrates". Solar *Energy Materials and Solar Cells,* **25,** 25-39.

23. **Boschloo, G** and **A. Hagfeldt** (2005) "Activation Energy of Electron Transport in Dye-Sensitized TiO_2 Solar Cells". *Journal of Physical Chemistry,* B. **109,** 12093-12098.

24. **Boscoletto, A.B., F. Gottardi, L. Milan, P. Pannocchia, V. Tartari, R. Amadelli, A. de Battisti, A. Barbieri, D. Patracchini** and **G. Battaglin** (1994) "Electrochemical treatment of bisphenol-A containing wastewaters". *Journal of Applied Electrochemistry*, **24**, 1052 - 1058.

25. **Botta, S.G., J.A. Navio, M.C. Hidalgo, G.M. Restrepo** and **M.I. Litter** (1999) "Photocatalytic properties of ZrO_2 and Fe/ZrO_2 semiconductors prepared by a sol–gel technique". *Journal of Photochemistry and Photobiology A: Chemistry,* **129,** 89–99.

26. **Bucher, J.P., J.J. Van der Klink** and **M. Graetzel** (1990) **"**Platinum-195 NMR study of platinum/titania and platinum/silica catalysts: strong metal-support interaction". *Journal of Physical Chemistry*, 94, 1209 – 1211.

27. **Buhler, N., K. Meier** and **J.F. Reber** (1984) "Photochemical hydrogen production with cadmium sulfide suspensions". *Journal of Physical Chemistry,* **88**, 3261-3268.

28. **Butter, T.J., L.M. Evison, I.C. Hancock, F.S. Holland, K.A. Matis, A. Philipson, A.I. Sheikh** and **A.I. Zouboulis** (1998) "The removal and recovery of cadmium from dilute aqueous solutions by biosorption and electrolysis at laboratory scale". *Water Research,* **32,** 400-406.

29. **Byrne, J.A., B.R. Eggins, N.M.D. Brown, B. McKinney** and **M. Rouse** (1998) "Immobilisation of TiO_2 powder for the treatment of polluted water". *Applied Catalysis B: Environmental*, **17,** 25-36.

30. **Campillo, B., P.J. Sebastian, S.A. Gamboa, J.L. Albarran** and **L.X. Caballero** (2002) "Electrodeposited Ni–Co–B alloy: application in water electrolysis". *Materials Science and Engineering,* C. **19,** 115-118.

31. **Canizares, P., F. Martinez, M. Diaz, J. Garcia-Gomez** and **M.A. Rodrigo** (2002) "Electrochemical Oxidation of Aqueous Phenol Wastes Using Active and Nonactive Electrodes". *Journal of Electrochemical Society,* **149**, D118-124.

32. **Canizares, P., J.A. Dominguez, M.A. Rodrigo, J. Villasenor** and **J. Rodrguez** (1999) "Effect of the Current Intensity in the Electrochemical Oxidation of Aqueous Phenol Wastes at an Activated Carbon and Steel Anode**".** *Industrial Engineering Chemical Research*, **38,** 3779-3785.

33. **Chakrabarti, S** and **B.K. Dutta** (2004) "Photocatalytic degradation of model textile dyes in wastewater using ZnO as semiconductor catalyst". *Journal of Hazardous Materials,* **112,** 269-278.

34. **Chakravarty, S., V. Dureja, G. Bhattacharyya, S. Maity** and **S. Bhattacharjee** (2002) "Removal of arsenic from groundwater using low cost ferruginous manganese ore". *Water Research,* **36**, 625-632.

35. **Chen, G** (2004) "Electrochemical technologies in wastewater treatment". *Separation and Purification Technology*, **38,** 11–41.

36. **Chen, X** and **C. Burda** (2004) **"**Photoelectron Spectroscopic Investigation of Nitrogen-Doped Titania Nanoparticles". *Journal of Physical Chemistry,* B. **108,** 15446-15449.

37. **Chen, Y.T., J.B. Ding, Y. Guo, L.B. Kong** and **H.L. Li** (2002) "A facile route to preparation of CdS nanorods". *Materials Chemistry and Physics*, **77**, 734–737.

38. **Chen, Z., Y. Yan** and **S.S.E.H. Elnashaie** (2004) "Catalyst Deactivation and Engineering Control for Steam Reforming of Higher Hydrocarbons in a Novel Membrane Reformer". *Chemical Engineering Science,* **59,** 1965-1978.

39. **Chettiar. M** and **A.P. Watkinson** (1983) "Anodic-Oxidation of Phenolics found in Coal Conversion Effluents". *Canadian Journal of Chemical Engineering*, **61**, 568-574.

40. **Cho, Y., W. Choi, C.H. Lee, T. Hyeon** and **H.I. Lee** (2001) "Visible Light-Induced Degradation of Carbon Tetrachloride on Dye-Sensitized TiO_2". *Environmental Science and Technology,* **35**, 966 -970.

41. **Clark, C.M** (1960) "Oxidation and Reduction Potential of Organic Systems". (The Williams and Wilkins company,Baltimore, USA) pp 451.

42. **Clesceri, L.S., A.E. Greenberg** and **A.D. Eaton** (Ed.), (1998) *Standard Methods for the Examination of Water and Waste Water, 20th Edition,* Washington, Part 5000, pp. 14-15.

43. **Comninellis, Ch** and **A. Nerini** (1995) "Anodic oxidation of phenol in the presence of NaCl for wastewater treatment". *Journal of Applied Electrochemistry*, **25**, 23- 28.

44. **Comninellis, Ch** and **C. Pulgarin** (1993) "Electrochemical oxidation of phenol for wastewater treatment using SnO_2, anodes". *Journal of Applied Electrochemistry*, **25**, 108-112.

45. **Comninellis, Ch.** and **C. Pulgarin** (1991) "Anodic Oxidation of Phenol for Wastewater Treatment". *Journal of Applied Electrochemistry*, **21**, 703-708.

46. **Courbon, H., J.M. Herrmann** and **P. Pichat** (1981) "Photocatalytic isotopic exchange between cyclopentane and deuterium over a bifunctional Pt/TiO2 catalyst". *Journal of Catalysis*, **72**, 129-138.

47. **Cullity, B** (1987) "Elements of X-ray Diffraction". Addision-Wesley, Readin, Massachusetts. p.294.

48. **Dabrock, B., H. Bahl** and **G. Gottschalk** (1992) "Parameters affecting solvent production by *Clostridium pasteurianum*". *Applied and Environment Microbiology*, **58,** 1233–1239.

49. **Dabrowski, A., J. Mieluch, A. Sadkaoski, J. Wild, P. Zoltowski** (1975) "Pilot-plant study of electrochemical phenol-waste purification". *Przemysl Chemiczny,* **54,** 653-655.

50. **Daneshvar, N., D. Salari** and **A. R. Khataee** (2004) "Photocatalytic degradation of azo dye acid red 14 in water on ZnO as an alternative catalyst to TiO_2". *Journal of Photochemistry and Photobiology A: Chemistry,* **162,** 317-322.

51. **Das, D** and **T.N. Veziroglu** (2001) "Hydrogen Production by Biological Processes: A Survey of Literature". *International Journal of Hydrogen Energy,* **26,** 13-28.

52. **Daus, B., R. Wennrich** and **H. Weiss** (2004) "Sorption materials for arsenic removal from water: a comparative study". *Water Research*, **38**, 2948–2954.

53. **Diwald, O., T.L. Thompson, G. Goralski, S.D. Walck** and **J.T. Yates Jr** (2004) **"**The Effect of Nitrogen Ion Implantation on the Photoactivity of TiO_2 Rutile Single Crystals". *Journal of Physical Chemistry,* B. **108,** 52-57.

54. **Dutra, A.J.B., A. Espinola** and **P.P. Borges** (2000) "Cadmium removal from diluted aqueous solutions by electrowinning in a flow-by cell". *Minerals Engineering,* **13,** 1139-1148.

55. **DuVall, S.H** and **R.L McCreey** (1999) "Control of Catechol and Hydroquinone Electron-Transfer Kinetics on Native and Modified Glassy Carbon Electrodes". *Analytical Chemistry,* **71**, 4594-4602.

56. **DuVall, S.H** and **R.L. McCreey** (2000) "Self-catalysis by Catechols and Quinones during Heterogeneous Electron Transfer at Carbon Electrodes". *Journal of the American Chemical Society*, **122,** 6759-6764.

57. **Ergican, E., H. Gecol** and **A. Fuchs** (2005) "The effect of co-occurring inorganic solutes on the removal of arsenic (V) from water using cationic surfactant micelles and an ultrafiltration membrane". *Desalination*, **181,** 9-26.

58. **Escudero, J.C., S.C. March, J. Giménez** and **R. Simarro** (1990) "Preparation and characterization of Pt (RuO_2)/TiO_2 catalysts: Test in a continuous water photolysis system". *Journal of Catalysis*, **123**, 319-332.

59. **Ettinger, M.B., C.C. Ruchhoft** and **R.J. Lishka** (1951) "Sensitive 4-aminoantipyrine method for phenolic compounds". *Analytical Chemistry*, **23**, 1783-1788.

60. **Ezerskis, Z**. and **Z. Jusys** (2001) "Oxidation of Chlorophenols on Pt Electrode in Alkaline Solution Studied by Cyclic Voltammetry, Galvanostatic Electrolysis, and Gas Chromatography-Mass Spectrometry". *Pure and Applied Chemistry,* **73,** 1929-1940.

61. **Ezerskis, Z.** and **Z. Jusys** (2002) "Electropolymerization of Chlorinated Phenols On a Pt Electrode in Alkaline Solution, Part III: A Fourier Transformed Infrared Spectroscopy Study". *Journal of Applied Electrochemistry*, **32,** 755-762.

62. **Fox, M.A** and **M.T. Dulay** (1993) "Heterogeneous photocatalysis". *Chemical Reviews*, **93,** 341-357.

63. **Frisch M. J., G.W.Trucks, H.B. Schlegel, G.E. Scuseria, M.A. Robb, J.R. Cheeseman, V.G. Zakrzewski, J.A. Montgomery, R.E. Stratmann, J.C. Burant, S. Dapprich, J.M. Millam, A.D. Daniels, K.N. Kudin, M.C. Strain, O. Frakas, J. Tomasi, V. Barone, M. Cossi, R. Cammi, B. Mennucci, C. Pomelli, C. Adamo, S. Clifford, J. Ochterski, G.A. Petersson, P.Y. Ayala, Q. Cui, K. Morokuma, D.K. Malick, A.D. Rabuck, K. Raghavachari, J.B. Foresman, J. Cioslowski, J.V. Ortiz, B.B. Stefanov, G. Liu, A. Liashenko, P. Piskorz, L. Komaromi, R. Gomperts, R.L. Martin, D.J. Fox, T. Keith, M.A. Al-laham, C.Y. Peng, A. Nanayakkara, C. Gonzalez, M. Challacombe, P.M.W. Gill, B.G. Johnson, W. Chen, M.W. Wong, J.L. Andres, M. Head-Gordon, E.S. Replogle** and **J.A. Pople.** (1998) *Gaussian98*, revision A.9: Gaussian Inc.: Pittsburgh, PA.

64. **Fujimori, A., S. Suga, H. Negishi** and **M. Inoue** (1988) "X-ray photoemission and Auger-electron spectroscopic study of the electronic structure of intercalation compounds M_xTiS_2 (M=Mn, Fe, Co, and Ni)". *Physical Review*, B. **38,** 3676-3689.

65. **Fujishima, A** and **K. Honda** (1972) "Electrochemical photolysis of water at a semiconductor electrode". *Nature*, **238**, 37 - 38.

66. **Fumiaki, T., J.D. Chang, N. Mizukami, S.T. Tatsuo** and **H. Katsushige** (1996) "Continuous hydrogen production by Clostridium sp. Strain No. 2 from cellulose hydrolysate in an aqueous two-phase system". *Journal of Fermentation and Bioengineering*, **82,** 80–83.

67. **Fumiaki, T., J.D. Chang, N. Mizukami, S.T. Tatsuo** and **H. Katsushige** (1993) "Isolation of a hydrogen-producing bacterium *Clostridium beijerinckii* strain AM21B from termites". *Canadian Journal of Microbiology*, **39,** 726–730.

68. **Funk, J.E** and **R.M. Reinstrom** (1966) "Energy requirements in the production of hydrogen from water". *Industrial and Engineering Chemistry: Process Design and Development*, **5,** 336-342.

69. **Gaffron, H** and **J. Rubin** (1942) "Fermentative and photochemical production of hydrogen in algae". *Journal of General Physiology*, **26,** 219-240.

70. **Ganesan, R** and **B. Viswanathan** (2001) "Redox properties of metal complexes encapsulated in various zeolites". *Indian Journal of Chemistry*, **40 A**, 1255-1257.

71. **Gattrell, M.** and **D.W. Kirk** (1990) "The electrochemical Oxidation of Aqueous Phenol at a Glassy Carbon Electrode". *Canadian Journal of Chemical Engineering*, **68,** 997-1003.

72. **Gattrell. M** and **D.W. Kirk** (1993) "A Study of the Oxidation of Phenol at Platinum and Preoxidized Platinum Surfaces". *Journal of the Electrochemical Society*, **140**, 1534-1540.

73. **Gedanken, A., X. Tang, Y. Wang, N. Perkas, Y. Koltypin, N. Perkas, Y. Koltypin, M.V. Landau, L. Vradman** and **M. Herskowitz** (2001) "Using sonochemical methods for the preparation of mesoporous materials and for the deposition of catalysts into the mesopores". *Chemistry- A European Journal,* **21**, 4546-4552.

74. **Goldstein, A.N. C.M. Echer** and **A.P. Alivisatos** (1992) "Melting in semiconductor nanocrystals". *Science,* **256,** 1425-1427.

75. **Gole, J.L., J.D. Stout, C. Burda, Y. Lou** and **X. Chen** (2004) "Highly Efficient Formation of Visible Light Tunable $TiO_{2-x}N_x$ Photocatalysts and Their Transformation at the Nanoscale". *Journal of Physical Chemistry,* B. **108,** 1230-1240.

76. **Gonbeau, D., C. Guimon, G.P. Guillouzo, A. Levasseur, G. Meunier** and **R. Dormoy** (1991) "XPS study of thin films of titanium oxysulfides". *Surface Science,* **254,** 81-89.

77. **Gopinath, C. S** (2006) Comment on "Photoelectron Spectroscopic Investigation of Nitrogen-Doped Titania Nanoparticles". *Journal of Physical Chemistry,* B. **110,** 7079-7080

78. **Green, A.N.M., E. Palomares, S.A. Haque, J.M. Kroon** and **J.R. Durrant** (2005) "Charge Transport versus Recombination in Dye-Sensitized Solar Cells Employing Nanocrystalline TiO_2 and SnO_2 Films". *Journal of Physical Chemistry,* B. **109,** 12525-12533.

79. **Greenbaum, E** (1988) "Energetic efficiency of hydrogen photoevolution by algal water splitting". *Biophysical Journal,* **54,** 365-368.

80. **Greenbaum, E., J.W. Lee, C.V. Tevault, S.L. Blankinship** and **L.J. Mets** (1995) "CO_2 fixation and photoevolution of H_2 and O_2 in a mutant of Chlamydomonas lacking photosystem I". *Nature*, **376,** 438-441.

81. **Grimm, J., D. Bessarabov** and **R. Sanderson** (1998) "Review of Electro-assisted methods for water purification" *Desalination,* **115,** 285-294.

82. **Guan, G., T. Kida, K. Kusakabe, K. Kimura, X. Fang, T. Ma, E. Abe** and **A. Yoshida** (2004) "Photocatalytic H_2 evolution under visible light irradiation on CdS/ETS-4 composite". *Chemical Physics Letters,* **385**, 319–322.

83. **Guo, Y., C. Hu, S. Jiang, C. Guo, Y. Yang** and **E. Wang** (2002) "Heterogeneous photodegradation of aqueous hydroxy butanedioic acid by microporous polyoxometalates". *Applied Catalysis B: Environmental*, **36,** 9–17.

84. **Gururnathan, K** (2004) "Photocatalytic hydrogen production using transition metal ions-doped γ-Bi_2O_3 semiconductor particles". *International Journal of Hydrogen Energy,* **29,** 933 – 940

85. **Gyorgy, E., A. Perez del Pino, P. Serra** and **J.L. Morenza** (2003) "Depth profiling characterization of the surface layer obtained by pulsed Nd:YAG laser irradiation of titanium in nitrogen". *Surface Coatings and Technology,* **173,** 265-270.

86. **Hagfeldt, A** and **M. Graetzel** (1995) "Light-Induced Redox Reactions in Nanocrystalline Systems". *Chemical Reviews***, 95**, 49-68.

87. **Hansel, A** and **P. Lindblad** (1998) "Towards optimization of Cyanobacteria as biotechnological relevant producers of molecular hydrogen a clean and renewable energy source". *Applied Microbiology and Biotechnology*, **50,** 153–160.

88. **Hart, D** (1997) "Hydrogen power: the commercial future of the ultimate fuel". London: Financial Times Energy Publishing.

89. **Haryanto, A., S. Fernando, N. Murali** and **S. Adhikari** (2005) "Current Status of Hydrogen Production Techniques by Steam Reforming of Ethanol: A Review". *Energy and Fuel*, **19,** 2098-2106.

90. **Hattori, A., M. Yamamoto, H. Tada** and **S. Ito** (1998) "A promoting effect of NH_4F addition on the photocatalytic activity of sol-gel TiO_2 films". *Chemistry Letters, **27,*** 707-708.

91. **He, J., J. Zhao, H. Hidaka** and **N. Serpone** (1998) "EPR Characteristics of a dye/colloidal TiO_2 system under visible light irradiation". *Journal of the Chemical Society, Faraday Transactions,* **94,** 2375 -2378.

92. **Hebenstreit, E.L.D., W. Hebenstreit** and **U. Diebold** (2001) "Structures of sulfur on TiO_2 (110) determined by scanning tunneling microscopy, X-ray photoelectron spectroscopy and low-energy electron diffraction". *Surface Science,* **470,** 347-360.

93. **Herrmann, J.M., C. Guillard, J. Disdier, C. Lehaut, S. Malato** and **J. Blanco** (2002) "New industrial titania photocatalysts for the solar detoxification of water containing various pollutants". *Applied Catalysis B: Environmental*, **35,** 281–294.

94. **Herrmann, J.M., J. Disdier** and **P. Pichat** (1984) "Effect of chromium doping on the electrical and catalytic properties of powder titania under UV and visible illumination". *Chemical Physics Letters*, **108,** 618-622.

95. **Heyndrickx, M., P.D. Vos** and **J.D. Ley** (1991) **"**Fermentation characteristics of *Clostridium pasteurianum* LMG 3285 grown on glucose and mannitol". *Journal of Applied Bacteriology*, **70,** 52–58.

96. **Hirai, T** and **M. Ota** (2006) "Immobilization of CdS nanoparticles from reverse micellar system onto mesoporous organosilicates and their photocatalytic properties". *Materials Research Bulletin*, **41,**1 9-28.

97. **Hirai, T., M. Nanba** and **I. Komasawa** (2003) "Dithiol-mediated incorporation of CdS nanoparticles from reverse micellar system into Zn-doped SBA-15 mesoporous silica and their photocatalytic properties". *Journal of Colloid and Interface Science,* **268,** 394-399.

98. **Hoffmann, M.R., S.T. Martin, W. Choi** and **D.W. Bhanemann** (1995) **"**Environmental Applications of Semiconductor Photocatalysis". Chemical Reviews, **95,** 69-96.

99. **Hong, Y.C., C.U. Bang, D.H. Shin** and **H.S. Uhm** (2005) "Band gap narrowing of TiO_2 by nitrogen doping in atmospheric microwave plasma". *Chemical Physics Letters,* **413,** 454-457.

100. http://srdata.nist.gov/xps/

101. http://www.who.int/mediacentre/factsheets/fs210/en/index.html

102. **Hu, W., X. Cao, F. Wang** and **Y. Zhang (1997) "**A Novel Cathode for Alkaline Water Electrolysis". *International Journal of Hydrogen Energy,* **22,** 621-623.

103. **Ihara. T., M. Miyoshi, Y. Iriyama, O. Matsumoto** and **S. Sugihara** (2003) "Visible-light-active titanium oxide photocatalyst realized by an oxygen-deficient structure and by nitrogen doping". *Applied Catalysis B: Environmental,* **42,** 403-409.

104. **Iniesta, J., J. Gonzalez-Garcia, E. Exposito, V. Montiel** and **A. Aldaz** (2001) "Influence of Chloride Ion On Electrochemical Degradation of Phenol In Alkaline Medium Using Bismuth Doped and Pure PbO_2 Anodes". *Water Research*, **35,** 3291-3300.

105. **Irie, H., Y. Watanabe** and **K. Hashimoto** (2003) "Nitrogen-Concentration Dependence on Photocatalytic Activity of $TiO_{2-x}N_x$ Powders". *Journal of Physical Chemistry, B.* **107,** 5483-5486.

106. **Juttner, K., U. Galla** and **H. Schmieder,** (2000) **"**Electrochemical approaches to environmental problems in the process industry". *Electrochimica Acta,* **45,** 2575-2594.

107. **Kakuta, N., K.H. Park, M.F. Finlayson, A. Ueno, A.J. Bard, A. Campion, M.A. Fox, S.E. Webber** and **J.M. White** (1985) **"**Photoassisted Hydrogen production using visible light and coprecipitated ZnS-CdS without a noble metal". *Journal of Physical Chemistry*, **89**, 732-734.

108. **Kamat, P.V** (1993) "Photochemistry on Nonreactive and Reactive (Semiconductor) Surfaces". *Chemical Reviews,* **93,** 207-300.

109. **Kang, M., S.J. Choung** and **J.Y. Park** (2003) "Photocatalytic performance of nanometer-sized Fe_xO_y/TiO_2 particle synthesized by hydrothermal method". *Catalysis Today*, **87**, 87–97.

110. **Kanmani, A.S** (1998) PhD thesis, IIT Madras

111. **Kannan, K., S.N. Sivadurai, L. John Brechmans** and **R. Vijayavalli** (1995) "Removal of Phenolic Compounds by Electrooxidation Method". *Journal of Environmental Science & Health,* A. **30,** 2185-2203.

112. **Karakitsou, K.E** and **X.E. Verykios** (1993) "Effects of altervalent cation doping of titania on its performance as a photocatalyst for water cleavage". *Journal of Physical Chemistry, **97,*** 1184-1189.

113. **Kato, H** and **A. Kudo** (1998) "New tantalate photocatalysts for water decomposition into H_2 and O_2". *Chemical Physics Letters,* **295,** 487-492.

114. **Keller, V** and **F. Garin** (2003) "Photocatalytic behavior of a new composite ternary system: WO_3/SiC-TiO_2. Effect of the coupling of semiconductors and oxides in photocatalytic oxidation of methylethylketone in the gas phase". *Catalysis Communications,* **4,** 377–383.

115. **Khairutdinov, R.F** (1998) "Chemistry of semiconductor nanoparticles". *Russian Chemical Reviews*, **67**, 109-122.

116. **Kida, T., G. Guan** and **A. Yoshida** (2003) "$LaMnO_3$/CdS nanocomposite: a new photocatalyst for hydrogen production from water under visible light irradiation". *Chemial Physics Letters,* **371**, 563–567.

117. **Kim, Y., C. Kim, I. Choi, S. Rangaraj** and **J. Yi** (2004) "Arsenic Removal Using Mesoporous Alumina Prepared via a Templating Method". *Environmental Science and Technology*, **38,** 924-931.

118. **Kiwi, J., K. Kalyansundaram,** and **M. Graetzel** (1982) *Struct. Bonding* (Berlin) 49 37.

119. **Kobayakawa, K., Y. Murakami** and **Y. Sato** (2004) "Visible-light active N-doped TiO_2 prepared by heating of titanium hydroxide and urea". *Journal of Photochemistry and Photobiology A: Chemistry,* **170,** 177-179.

120. **Koca, A** and **M. Sahin** (2003) "Photocatalytic hydrogen production by direct sunlight: A laboratory experiment". *Journal of Chemical Education,* **80**, 1314-1315.

121. **Kohn, W.** and **L.J. Sham**, (1965) "Self-Consistent Equations Including Exchange and Correlation Effects". *Physical Reviews*, **140**, A-1133–A1138.

122. **Kohno, M., S. Ogura, K. Sato** and **Y. Inoue** (2000) "A tracer study of a radical produced by UV irradiation on $BaTi_4O_9$ photocatalyst surface". *Chemical Physics Letters,* **319,** 451-456.

123. **Kreuter, W** and **H. Hofmann** (1998) "Electrolysis: the important energy transformer in a world of sustainable energy". *International Journal of Hydrogen Energy,* **23,** 661–666.

124. **Kumar, A** and **A.K. Jain** (2001) "Photophysics and photochemistry of colloidal CdS–TiO_2 coupled semiconductors - photocatalytic oxidation of indole". *Journal of Molecular Catalysis A: Chemical,* **165**, 265-273.

125. **Kumar, N and D. Das** (2000) "Enhancement of hydrogen production by *Enterobacter cloacae* IIT-BT08". *Process Biochemistry*, **35,** 589–593.

126. **Lee C., W. Yang** and **R.G. Parr** (1998) "Development of the Colle-Salvetti correlation-energy formula into a functional of the electron density". *Physics Reviews,* B. **37**, 785-789.

127. **Li, D., H. Haneda, S. Hishita** and **N. Ohashi** (2005a) "Visible-Light-Driven N-F-Codoped TiO_2 Photocatalysts. 1. Synthesis by Spray Pyrolysis and Surface Characterization". *Chemistry of materials*, **17,** 2588-2595.

128. **Li, D., H. Haneda, S. Hishita** and **N. Ohashi** (2005b) **"**Visible-Light-Driven N-F-Codoped TiO_2 Photocatalysts. 2. Optical Characterization, Photocatalysis, and Potential Application to Air Purification". *Chemistry of Materials,* **17,** 2596-2602.

129. **Li, H., Y. Zhu, S. Chen, O. Palchik, J. Xiong, Y. Koltypin, Y. Gofer** and **A. Gedanken** (2003) "A novel ultrasound-assisted approach to the synthesis of CdSe and CdS nanoparticles". *Journal of Solid State Chemistry,* **172**, 102-110.

130. **Li, Y., G. Lu** and **S. Li** (2001) "Photocatalytic hydrogen generation and decomposition of oxalic acid over platinized TiO_2". *Applied Catalysis A: General,* **214,** 179–185.

131. **Li. D** and **H.Haneda** (2003) "Photocatalysis of sprayed nitrogen-containing Fe_2O_3–ZnO and WO_3–ZnO composite powders in gas-phase acetaldehyde decomposition". *Journal of photochemistry and photobiology A: Chemistry*, **160,** 203-212.

132. **Licht, S., B. Wang, S. Mukerji, T. Soga, M. Umeno** and **H. Tributsch** (2001) "Over 18% solar energy conversion to generation of hydrogen fuel; theory and experiment for efficient solar water splitting". *International Journal of Hydrogen Energy,* **26,** 653-659.

133. **Lichtl, R.R., M.J. Bazin** and **D.O. Hall** (1997) "The biotechnology of hydrogen production by Nostoc flagelliforme grown under chemostat conditions". *Applied Microbiology and Biotechnology,* **47,** 701–707.

134. **Lichtman, D., J.H. Craig, V. Sailer** and **M. Drinkwine** (1981) "AES and XPS spectra of sulfur in sulfur compounds". *Applications of Surface Science*, **7,** 325-331.

135. **Liem, N., K. Richard, B. Weon** and **K.M. Rajesh** (1999) "Glutathione as a matrix for CdS nanocrystallites". *Chemosphere,* **38,** 155-173.

136. **Lin, J., J.C. Yu, D. Lo** and **S.K. Lam** (1999) "Photocatalytic Activity of Rutile Ti1−xSnxO2Solid Solutions". *Journal of Catalysis*, **183**, 368-372.

137. **Lindberg, B. J., K. Hamrin, G. Johansson, U. Gelius, A. Fahlman, C. Nordling** and **K. Siegbanh (1970)** "Molecular spectroscopy by means of ESCA. III. Sulfur compounds correlation of electron binding energy with structure". *Physica Scripta,* **1,** 286-298.

138. **Linsebigler, A.L., G. Lu,** and **J.T. Yates, Jr.** (1995) "Photocatalysis on TiO_2 Surfaces: Principles, Mechanisms, and Selected Results". *Chemical Reviews,* **95**, 735-758.

139. **Litter, M.I** (1999) "Heterogeneous photocatalysis transition metal ions in photocatalytic systems". *Applied Catalysis B: Environmental,* **23,** 89–114.

140. **Liu, H., S. Grot** and **B.E. Logan** (2005) "Electrochemically assisted microbial production of hydrogen from acetate". *Environmental Science and Technology*, **39,** 4317–4320.

141. **Liu, Y.C** and **R.L. McCreery** (1995) **"**Reactions of Organic Monolayers on Carbon Surfaces Observed with Unenhanced Raman Spectroscopy". *Journal of American Chemical Society,* **117**, 11254-11259. .

142. **Madhusudan Reddy, K., B. Baruwati, M. Jayalakshmi, M. Mohan Rao** and **S.V. Manorama**. (2005) "S-, N- and C-doped titanium dioxide nanoparticles: Synthesis, characterization and redox charge transfer study". *Journal of Solid State Chemistry*, **178**, 3352–3358.

143. **Majunder, S.A. Prairie, M.R. Ondrias, M.R. and Sheluntt, J.A.** "Enhancement of Solar Photocatalytic Detoxification by Adsorption of Prophyrines onto TiO_2". Solar Engineering 1992,Edited by. William Stine, Jan Kreider and Koichi Wantanabe, New York, NY: ASME (1992): pp 9-14.

144. **Mathew, T., N.R. Shiju, K. Sreekumar, B.S. Rao** and **C.S. Gopinath** (2002) "Cu-Co synergism in $Cu_{1-x}Co_xFe_2O_4$ catalyst and XPS aspects". *Journal of Catalysis,* **210,** 405-417.

145. **Matsumura, M., Y. Sato** and **H. Tusbomura** (1983) "Photocatalytic hydrogen production from solutions of sulfite using platinized cadmium sulfide powder". *Journal of Physical Chemistry,* **87,** 3807-3808.

146. **Matsunaga, T., T. Hatano, A. Yamada** and **M. Matsumoto** (2000) "Microaerobic hydrogen production by photosynthetic bacteria in a double-phase photobioreactor". *Biotechnology and Bioengineering*, **68,** 647–651.

147. **Memming, R** (2001) "Semiconductor Electrochemistry". Wiley-VCH Verlag GmbH, Weinheim.

148. **Meng, X.G., G.P. Korfiatis, C. Jing and C. Christodoulatos** (2001) **"**Redox transformations of arsenic and iron in water treatment sludge during aging and TCLP extraction". *Environmental Science and Technology,* **35,** 3476-3481.

149. **Milazzo, M** and **S.Caroli** (1978) "Tables of Standard Electrode Potentials". A Wiley-Interscience Publication, John Willey & Sons, New York.

150. **Millet, P., F. Andolfatto** and **R. Durand** (1996) "Design and performance of a solid polymer electrolyte water electrolyzer". *International Journal of Hydrogen Energy,* **21,** 87-93.

151. **Millis, A**. and **S.L. Hunte** (1997) "An overview of semiconductor photocatalysis". *Journal of Photochemistry and Photobiology A: Chemistry* **108,** 1-98.

152. **Moon, S.C., H. Mametsuka, S. Tabata** and **E. Suzuki** (2000) "Photocatalytic production of hydrogen from water using TiO_2 and B/TiO_2". *Catalysis Today,* **58,** 125-132.

153. **Moreno, G.P** (2002) "Electrochemical Applications of CVD Diamond". (chapter 5) PhD. Thesis, University of Bristol

154. **Morikawa, T., R. Asahi, T. Ohwaki, A. Aoki** and **Y. Taga** (2001) "Band-gap narrowing of titanium dioxide by nitrogen doping". *Japanese Journal of Applied Physics*, Part 2. **40,** 561-563.

155. **Morowetz, M., W. Balcerski, A.J. Colussi** and **M.R. Hoffmann** (2004) "Oxidative Power of Nitrogen-Doped TiO_2 Photocatalysts under Visible Illumination". *Journal of Physical Chemistry,* B. ***108,*** 17269-17273.

156. **Muggli, D.S** and **L. Ding** (2001) "Photocatalytic performance of sulfated TiO_2 and Degussa P-25 TiO_2 during oxidation of organics". *Applied Catalysis B: Environmental,* **32,** 181–194.

157. **Nagaveni, K., G. Sivalingam, M.S. Hegde** and **M. Griridhar** (2004) "Photocatalytic Degradation of Organic Compounds over Combustion-Synthesized Nano-TiO_2". *Environmental Science and Technology*, **38,** 1600-1604.

158. **Nakamura, R., T. Tanaka** and **Y. Nakato** (2004) "Mechanism for Visible Light Responses in Anodic Photocurrents at N-Doped TiO_2 Film Electrodes". *Journal of Physical Chemistry,* B. **108,** 10617- 10620.

159. **Nakashima, T**., **Y**. **Ohko, D**.**A. Tryk** and **A**. **Fujishima (2002) "**Decomposition of endocrine-disrupting chemicals in water by use of TiO_2 photocatalysts immobilized on polytetrafluoroethylene mesh sheets". *Journal of Photochemistry and Photobiology,* A. **151,** 207–212.

160. **Naskar, S., S. Arumugom Pillay** and **M. Chanda** (1998) "Photocatalytic degradation of organic dyes in aqueous solution with TiO_2 nanoparticles immobilized on foamed polyethylene sheet". *Journal of Photochemistry and Photobiology A: Chemistry,* **113,** 257-264.

161. **Nguyen, T.V., K.J. Kim** and **O.B. Yang** (2005) "Photocatalytic water decomposition for hydrogen production over silicotungstic acid–silica photocatalyst". *Journal of Photochemistry and Photobiology A: Chemistry*, **173**, 56-63.

162. **Nickson, R.T., J.M. McArthur, P. Ravenscroft, W.G. Burgess** and **K.M. Ahmed** (2000) "Mechanism of arsenic release to groundwater, Bangladesh and West Bengal". *Applied Geochemistry*, **15,** 403-413.

163. **Nosaka, Y., M. Matsushita, J. Nishino** and **A.Y. Nosaka** (2005) "Nitrogen-doped titanium dioxide photocatalysts for visible response prepared by using organic compounds". *Science and Technology of Advanced Materials*, **6,** 143-148.

164. **O'Regan, B.,** and **M. Graetzel** (1991) "A low-cost, high-efficiency solar cell based on dye-sensitized colloidal TiO_2 films". *Nature*, ***353***, 737-740.

165. **Ohno, T., M. Akiyoshi, T. Umebayashi, K. Asai, T. Mitsui** and **M. Matsumura** (2004) "Preparation of S-doped TiO_2 photocatalysts and their photocatalytic activities under visible light". *Applied catalysis A: General,* **265**, 115-121.

166. **Ohno, T., T. Mitsui** and **M. Matsumura** (2003) " Photocatalytic Activity of S-doped TiO_2 Photocatalyst under Visible Light". *Chemistry Letters,* **32,** 364-365.

167. **Ohno, T., T. Tusbota, K. Nishijima** and **Z. Miyamota** (2004) "Degradation of Methylene Blue on Carbonate Species-doped TiO_2 Photocatalysts under Visible Light". *Chemistry Letters,* **33,** 750-751.

168. **Pal, B., T. Hata, K. Goto** and **G. Nogami** (2001) "Photocatalytic degradation of *o*-cresol sensitized by iron–titania binary photocatalysts". *Journal of Molecular Catalysis A: Chemical,* **169,** 147–155.

169. **Pal, B., T. Torimoto, K. Iwasaki, T. Shibayama, H. Takahashi** and **B. Ohtani** (2004) "Size and Structure-Dependent Photocatalytic Activity of Jingle-Bell-Shaped Silica-Coated Cadmium Sulfide Nanoparticles for Methanol Dehydrogenation". *Journal of Physical Chemistry,* B.**108,** 18670-18674.

170. **Paola, A.D., L. Palmisano** and **A. Augugliaro** (2000) "Photocatalytic behavior of mixed WO_3/WS_2 powders". *Catalysis Today*, **58**, 141-149.

171. **Papp, J., H.S. Shen, R. Kershaw, K.Dwight** and **A. Wold** (1993) "Titanium(IV) oxide photocatalysts with palladium". *Chemistry of Materials,* **5,** 284-288.

172. **Parvathy, N.N., G.M. Pajonk** and **A. Venkateswara Rao** (1997) "Synthesis of various size CdS nanocystals in porous silica matrix and their spectral and physical properties". *Nanostructured Materials,* **8**, 929-943.

173. **Pattabi, M** and **J. Uchil** (2000) "Synthesis of Cadmium Sulphide nanoparticles". *Solar Energy Materials and Solar Cells,* **63,** 309-314.

174. **Peiro, A.M., J.A. Ayllon, J. Peral** and **X. Domenech** (2001) "TiO_2-photocatalyzed degradation of phenol and *ortho*-substituted phenolic compounds". *Applied Catalysis B. Environmental,* **30,** 359-373.

175. **Peng, T., H. Yang, K. Dai, X. Pu** and **K. Hirao** (2003) "Fabrication and characterization of CdS nanotube arrays in porous anodic aluminum oxide templates". *ChemIcal Physics Letters,* **379**, 432–436.

176. **Perdew, J.P., K. Burke** and **M. Ernzerhof** (1996) "Generalized Gradient Approximation Made Simple". *Physical Reviews Letter*, **77,** 3865–3868.

177. **Perkas, N., O. Palchik, I. Brukental, I. Nowik, Y. Gofer, Y. Koltypin** and **A. Gedanken** (2003) "A Mesoporous Iron-Titanium Oxide Composite Prepared Sonochemically". *Journal of Physical Chemistry,* B. **107**, 8772-8778.

178. **Pozzo, R.L., M.A. Baltanas** and **A.E**. **Cassano** (1997) "Supported titanium oxide as photocatalyst in water decontamination: State of the art". *Catalysis Today,* **39**, 219-231.

179. **Pulgarin, C., N. Adler, P. Peringer** and **Ch. Comninellis** (1999) "Electrochemical detoxification of a 1,4-benzoquinone solution in wastewater treatment". *Water Research,* **28,** 887-893.

180. **Qingmin, Z., L. Yan, H. Fuzhi** and **G. Zhennan** (2001) "Mesoporous cadmium sulfide templated by hexagonal liquid crystal". *Journal of Material Science Letters,* **20**, 1233-1235.

181. **Rachman, M.A., Y. Furutani, Y. Nakashimada, T. Kakizono** and **N. Nishio** (1997) "Enhanced hydrogen production in altered mixed acid fermentation of glucose by *Enterobacter aerogenes*". *Journal of Fermentation and Bioengineering*, **83,** 358–363.

182. **Rainer, D. R., S.M. Vesecky, M. Koranne, W.S. Oh** and **D.W. Goodman** (1997) "The CO + NO reaction over Pd: a combined study using single-crystal, planar-model-supported and high surface area Pd/Al_2O_3 catalyst". *Journal of Catalysis,* **167,** 234-241.

183. **Rajeshwar, K., J.G. Ibanez** and **G.M. Swain** (1994) "Electrochemistry and the Environment". *Journal of Applied Electrochemistry,* **24,** 1077-1091.

184. **Ranjit, K.T., T.K. Varadarajan** and **B. Viswanathan** (1996) 'Photocatalytic reduction of initrogen to ammonia overnoble-metal-loaded TiO_2". *Journal of Photochemistry and Photobiology A: Chemistry,* **96**, 181-185.

185. **Rappe A.K., C.J Casewit, K.S Colwell, W.A Goddard** and **W.M Skiff** "UFF, a full periodic table force field for molecular mechanics and molecular dynamics simulations". *Journal of American Chemical Society*, **144,** 10024-10035.

186. **Ratna Kumar, P., S. Chaudhari, K.C. Khilar** and **S.P. Mahajan** (2004) "Removal of arsenic from water by electrocoagulation". *Chemosphere*, **55**, 1245–1252.

187. **Renault, N.J., P. Pichat, A. Foissay** and **R. Mercier** (1986) "Study of the effect of deposited platinum particles on the surface charge of titania aqueous suspensions by potentiometry, electrophoresis, and labeled-ion adsorption". *Journal of Physical Chemistry,* **90,** 2733-2738.

188. **Ribordy, P., C. Pulgarin, J. Kiwi** and **P. Peringer** (1997) "Electrochemical Versus photochemical pretreatment of industrial wastewaters". *Water Science and Technology*, **35 (4)**, 293-302.

189. **Roberts, L.C., S.J. Hug, T. Ruettimann, M.D. Billah, A.W. Khan** and **M.D. Rahman** (2004) "Arsenic Removal with Iron (II) and Iron (III) in Waters with High Silicate and Phosphate Concentrations". *Environmental Science and Technology*, **38**, 307-315.

190. **Rodriguez, J. A., T. Jirsak, J. Dvorak, S. Sambasivan** and **D. Fischer** (2000) "Reaction of NO_2 with Zn and ZnO: Photoemission, XANES, and Density Functional Studies on the Formation of $NO_3^{"}$. *Journal of Physical Chemistry,* B. **104,** 319-328.

191. **Rossmeisl, J., A. Logadottir** and **J.K. Nørskov (2005) "**Electrolysis of water on (oxidized) metal surfaces". *Chemical Physics*, **319,** 178-184.

192. **Rozendal, R.A., H.V.M. Hamelers, G.J.W. Euverink, S.J. Metz** and **C.J.N. Buisman (2006) "**Principle and perspectives of hydrogen production through biocatalyzed electrolysis". *International Journal of Hydrogen Energy*, (In press)

193. **Saha, N.C** and **H.G. Tompkins** (1992) "Titanium nitride oxidation chemistry: An x-ray photoelectron spectroscopy study". *Journal of Applied Physics,* **72**, 3072-3079.

194. **Sakata, T., T. Kawai** and **K. Hashimoto** (1982) "Photochemical diode model of platinum/titanium dioxide particle and its photocatalytic activity". *Chemical Physics Letters,* **88**, 50-54.

195. **Sakthivel, S** and **H. Kisch** (2003) "Photocatalytic and Photoelectrochemical Properties of Nitrogen-Doped Titanium Dioxide". *CHEMPHYSCHEM,* **4,** 487-490;

196. **Sakthivel, S., M. Janczarek** and **H. Kisch** (2004) "Visible Light Activity and Photoelectrochemical Properties of Nitrogen-Doped $TiO_2^{"}$. *Journal of Physical Chemistry*, B, **108,** 19384-19387.

197. **Sano, T., N. Negishi, K. Koike, K. Takeuchi** and **S. Matsuzawa** (2004) "Preparation of a visible light-responsive photocatalyst from a complex of Ti^{4+} with a nitrogen-containing ligand". *Journal of Material Chemistry,* **14,** 380-384.

198. **Sant, P.A** and **P.V. Kamat** (2002) "Interparticle electron transfer between size-quantized CdS and TiO_2 semiconductor nanoclusters". *Physical Chemistry Chemical Physics,* **4**, 198-203.

199. **Sato, J., H. Kobayashi** and **Y. Inoue** (2003) "Photocatalytic Activity for Water Decomposition of Indates with Octahedrally Coordinated d^{10} Configuration. II. Roles of Geometric and Electronic Structures". *Journal of Physical Chemistry,* B.**107,** 7970-7975.

200. **Sato, S** (1986) "Photocatalytic activity of NO_x-doped TiO_2 in the visible light region". *Chemical Physics Letters,* **123,** 126-128.

201. **Sayago, D.I., P. Serrano, O. Bohme, A. Goldoni, G. Paolucci, E. Roman** and **J.A. Martin-Gago** (2001) "Adsorption and desorption of SO_2 on the TiO_2 (110)-(1x1) surface. A photoemission study". *Physical Review*, B. **64,** 205402/1-205402/7.

202. **Shao, M., Z. Wu, F.Gao, Y. Ye** and **X. Wei** (2004) "Surfactant-free route to hexagonal CdS nanotubes under ultrasonic irradiation in aqueous solution at room temperature". *Journal of Crystal Growth*, **260**, 63-66.

203. **Shinn, N.D** and **K.L.Tsang** (1991) "Strain-induced surface reactivity: Low temperatureCr/W(110) nitridation". *Journal of Vacuum Science and Technology.* A. **9,** 1558-1562.

204. **Silveyra, R., L.D.L.T. Saenz, W.A. Flores, V.C. Martınez** and **A.A. Elguezabal** (2005) "Doping of TiO_2 with nitrogen to modify the interval of photocatalytic activation towards visible radiation". *Catalysis Today,* **107–108,** 602-605.

205. **Smedley, P.L** and **D.G. Kinniburgh** (2002) "A review of the source, behaviour and distribution of arsenic in natural waters". *Applied Geochemistry*, **17**, 517-568.

206. **So, W.W., K.J. Kim** and **S. Moon** (2003) **"**Photo-production of hydrogen over the CdS-TiO_2 nano-composite particulate films treated with $TiCl_4$**".** *International Journal of Hydrogen Energy,* **29**, 229-234.

207. **Stal, L.J** and **R. Moezelaar** (1979) "Fermentation in cyanobacteria FEMS". *Microbiological Research*, **21,** 179–211.

208. **Stojic, D.L., M.P. Marceta, S.P. Sovilj** and **S.S. Miljanic** (2003) "Hydrogen generation from water electrolysis—possibilities of energy saving". *Journal of Power Sources,* **118,** 315–319.

209. **Subrahmanyam, M., V.T. Supriya** and **P. Ram Reddy** (1996) "Photocatalytic H_2 production with CdS-based catalysts from a sulphide/sulphide: an effort to develop MgO-supported catalyst". *International Journal of Hydrogen Energy,* **21**, 99-106.

210. **Suffredini, H.B., J.L. Cerne, F.C. Crnkovic, S.A.S. Machado** and **L.A. Avaca** (2000) "Recent developments in electrode materials for water electrolysis". *International Journal of Hydrogen Energy,* **25,** 415-423.

211. **Sugai, S., H. Watanabe, T. Kioka, H. Miki** and **K. Kawasaki** (1991) "Chemisorption of NO on Pd (100), (111) and (110) surfaces studied by AES, UPS and XPS". *Surface Science*, **259,** 109-115.

212. **Supriya, V.T** and **M. Subrahmanyam** (1998) "Enhanced photocatalytic H_2 production over ZnS-CdS supported on super basic oxides". *International Journal of Hydrogen Energy*, **23**, 741-744.

213. **Suslick, K.S., S.B. Choe, A.A. Cichowlas** and **M.W. Grinstaff** (1991) "Sonochemical synthesis of amorphous iron". *Nature*, **353**, 414-416.

214. **Tada, H., A. Hattori, Y. Tokihisa, K. Imai, N. Tohge** and **S. Ito** (2000) "A Patterned-TiO_2/SnO_2 Bilayer Type Photocatalyst". *Journal of Physical Chemistry*,B. **104**, 4585 - 4587.

215. **Tae, E.L., S.H. Lee, J.K. Lee, S.S. Yoo, E.J. Kang** and **K.B. Yoon** (2005) "A Strategy To Increase the Efficiency of the Dye-Sensitized TiO2 Solar Cells Operated by Photoexcitation of Dye-to-TiO_2 Charge-Transfer Bands". *Journal of Physical Chemistry,* B, 109, 22513-22522.

216. **Tahar N. B** and **A. Savall** (1998) "Mechanistic Aspects of Phenol Electrochemical Degradation by Oxidation On a Ta/PbO_2 Anode". *Journal of Electrochemical Society*, **145,** 3427-3434.

217. **Takahashi, H., M. Kakihana, Y. Yamashita, K. Yoshida, S. Ikeda, M. Hara** and **K. Domen** (1999) "Synthesis of NiO-loaded $KTiNbO_5$ photocatalysts by a novel polymerizable complex method". *Journal of Alloys and Compounds,* **285,** 77-81.

218. **Takata, T., A. Tanaka, M. Hara, J.N. Kondo** and **K. Domen** (1998) "Recent progress of photocatalysts for overall water splitting". *Catalysis Today*, **44**, 17-26.

219. **Tambwekar, S.V., D. Venugopal** and **M. Subrahmanyam** (1999) "H_2 production of (CdS–ZnS)–TiO_2 supported photocatalytic system". *International Journal of Hydrogen Energy,* **24,** 957-963.

220. **Tanaka, T., K. Teramura, T. Yamamoto, S. Takenaka, S. Yoshida** and **T. Funabiki** (2002) "TiO_2/SiO_2 photocatalysts at low levels of loading: preparation, structure and photocatalysis". *Journal of Photochemistry and Photobiology A: Chemistry*, **148**, 277–281.

221. **Tandon, S.P** and **J.P. Gupta** (1970) "Measurement of forbidden energy gap of semiconductors by diffuse reflectance technique". *Physica Status Solidi*, **38**, 363-367.

222. **Tokudome, H** and **M. Miyauchi** (2004) "N-doped TiO_2 Nanotube with Visible Light Activity". *Chemistry Letters,* **33,** 1108-1109.

223. **Torres, G. R., T. Lindgern, J. Lu, C. Granqvist** and **S. Lindquist** (2004) "Photoelectrochemical Study of Nitrogen-Doped Titanium Dioxide for Water Oxidation". *Journal of Physical Chemistry*, B, **108,** 5995-6003.

224. **Torres, R. A., W. Peringer** and **C. Pulgarin** (2003) "Electrochemical Degradation of p-Substituted Phenols of Industrial Interest on Pt Electrodes. Attempt of a Structure–Reactivity Relationship Assessment". *Chemosphere,* **50**, 97-104.

225. **Ulleberg, O** (2003) "Modelling of advanced alkaline electrolyzers: a system simulation approach". *International Journal of Hydrogen Energy,* **28,** 21–33.

226. **Umebayashi, T., T. Yamaki, H. Itoh** and **K. Asai** (2002) "Band gap narrowing of titanium dioxide by sulfur doping". *Applied Physics Letters,* **81,** 454-456.

227. **Umebayashi, T., T. Yamaki, S. Tanaka** and **K. Asai** (2003) "Visible light-induced degradation of methylene blue on S-doped TiO_2". *Chemistry Letters,* **32,** 330-331.

228. **Umebayashi, T., T. Yamaki, S. Yamamoto, A. Miyashita, S. Tanaka, T. Sumita** and **K. Asai** (2003) "Sulfur-doping of rutile-titanium dioxide by ion implantation: Photocurrent spectroscopy and first-principles band calculation studies". *Journal of Applied Physics,* **93,** 5156-5160.

229. **Valentin, C. D., G. Pacchioni, A. Selloni, S. Livraghi** and **E. Giamello** (2005) "Characterization of Paramagnetic Species in N-Doped TiO_2 Powders by EPR Spectroscopy and DFT Calculations" *Journal of Physical Chemistry,* B. ***109,*** 11414-11419.

230. **Valentin, C.D., G. Pacchioni** and **A. Selloni** (2005) **"**Theory of Carbon Doping of Titanium Dioxide". *Chemistry of Materials,* **17,** 6656-6665.

231. **Velzen, D.V** and **H. Langenkamp** (1977) "Development studies on thermochemical cycles for hydrogen production". *International Journal of Hydrogen Energy,* **2,** 107-121.

232. **Vidya, K., V.S. Kamble, P. Selvam** and **N.M. Gupta** (2004) "Uranyl-anchored MCM-41 as a highly efficient photocatalyst for the complete oxidation of methanol under sunlight". *Applied Catalysis B: Environmental,* **54,** 145–154.

233. **Viswanath, R.P** (2004) "A Patent for Generation of Electrolytic Hydrogen by a Cost Effective and Cheaper Route". *International Journal of Hydrogen Energy,* **29**, 1191-1194.

234. **Viswanathan, B** (2003) "Photocatalytic processes – Selection Criteria for the Choice of Materials". *Bulletin of Catalysis Society of India,* **2,** 71-74.

235. **Viswanathan,** B. (2002) "Photocatalysis". (Chapter 20) in a handbook of Catalysis Principles and Applications, Edited by: B.Viswanathan, S. Sivasanker and A.V. Ramaswamy. Narosa publishing house.

236. **Vogel**, **I.** (1961) "A Text Book of Quantitative Inorganic Analysis". 3rd Edition, Longmans, Green and Co Ltd, London, 593-594.

237. **Vogel**, **I.** (1961) "A Text Book of Quantitative Inorganic Analysis". 3rd Edition, Longmans, Green and Co Ltd, London, 798-799.

238. **Wagner, C.D., W.M. Riggs, L.E. Davis, J.F. Moulder** and **G.E. Muilenberg** (1979) "Handbook of x-ray photoelectron spectroscopy". Perkin-Elmer Corporation, Eden Prairie, Minnesota.

239. **Wang, G.Z., W. Chen, C.H. Liang, Y.W. Wang, G.W. Meng** and **L.D. Zhang** (2001) "Preparation and characterization of CdS naoparticles by ultrasonic irradiation". *Inorganic Chemistry Communication,* **4**, 208-210.

240. **Wang, J., T. Martynez, D.R. Yaniv** and **L.D. McCormick** (1991) "Scanning Tunneling Microscopic Investigation of Surface Fouling of Glassy Carbon Surfaces due to Phenol Oxidation**".** *Journal of Electroanalytical Chemistry,* **313**, 129-140.

241. **Wang, W., Z. Liu, C. Zheng, C. Xu, Y. Liu** and **G. Wang** (2003) "Synthesis of CdS nanoparticles by a novel and simple one-step, solid-state reaction in the presence of a nonionic surfactant". *Materials Letters*, **57,** 2755-2760.

242. **Warrier, M., M.K.F. Lo, H. Monbouquette** and **M.A. Garcia-Garibay** (2004) "Photocatalytic reduction of aromatic azides to amines using CdS and CdSe nanoparticles". *Photochemistry Photobiologocal Science,* **3**, 859-863.

243. **Weast, R.C** and **M.J. Astle** (Ed.), (1978) "CRC handbook of chemistry and physics". 59th Edition, CRC press, Florida. pp B-10.

244. **Wellmann, H., J. Rathousky, M. Wark, A. Zukal** and **G. Schulz-Ekloff** (2001) "Formation of CdS nanoparticles within functionalized siliceous MCM-41". *Microporous and Mesoporous Materials*, **44-45**, 419-425.

245. **Wu, J.C.S** and **C.H. Chen** (2004) "A visible-light response vanadium-doped titania nanocatalyst by sol–gel method". *Journal of Photochemistry and Photobiology*, A: **163**, 507–513.

246. **Wu, Z** and **M. Zhou** (2001) **"**Partial Degradation of Phenol by Advanced Electrochemical Oxidation Process". *Environmental Science and Technology,* **35**, 2698-2703.

247. **Wu, Z., Y. Cong, M. Zhou, Q. Ye** and **T. Tan** (2002) "Removal of Phenolic Compounds by Electro-assisted Advanced Process for Wastewater Purification". *Korean Journal of Chemical Engineering,* **19**, 866-870.

248. **Yamaki, T., T. Sumita** and **S. Yamamoto** (2002) "Formation of $TiO_{2-x}F_x$ compounds in fluorine-implanted TiO_2". *Journal of Materials Science Letters,* **21,** 33-35.

249. **Yang, M., T. Yang** and **M. Wong** (2004) "Nitrogen-doped titanium oxide films as visible light photocatalyst by vapor deposition". *Thin Solid Films*, **469**, 1-5.

250. **Yin, H., Y. Wada, T. Kitamura, T. Sakata, H. Mori** and **S. Yanagida** (2001) "Enhanced photocatalytic dechlorination of 1,2,3,4-tetrachlorobenzene using nanosized CdS/TiO_2 hybrid photocatalyst under visible light irradiation". *Chemistry Letters*, **4,** 334-335.

251. **Yokoi, H., T. Tokushige, J. Hirose, S. Hayashi** and **Y. Takasaki** (1997) **"**Hydrogen production by immobilized cells of aciduric *Enterobacter aerogenes* strain HO-39". *Journal of Fermentation and Bioengineering,* **83,** 481–484.

252. **Yu, C., B. Tian** and **D. Zhao** (2003) "Recent advances in the synthesis of non-siliceous mesoporous materials". *Current Opinion in Solid State and Materials Science,* **7**, 191-197.

253. **Yu, J., M. Zhou, B. Cheng, H. Yu** and **X. Zhao** (2005) "Ultrasonic preparation of mesoporous titanium dioxide nanocrystalline photocatalysts and evaluation of photocatalytic activity". *Journal of Molecular Catalalysis A: Chemical,* **227**, 75-80.

254. **Yu, J.C., J.G. Yu, W.K. Ho, Z.T. Jiang** and **L.Z. Zhang** (2002) "Effects of F-Doping on the Photocatalytic Activity and Microstructures of Nanocrystalline TiO_2 Powders". *Chemistry of Materials,* **14,** 3808-3816.

255. **Yu, J.G., J.C. Yu, W.K. Ho, M.K.P. Leung, B. Cheng, G.K. Zhang** and **X.J. Zhao** (2003) "Effects of alcohol content and calcination temperature on the textural properties of bimodally mesoporous titania". *Applied Catalysis A: Genaral,* **255**, 309-320.

256. **Zang, L., W. Macyk, C. Lange, W.F. Maier, C. Antonius, D. Meissner** and **H. Kisch** (2000) "Visible-Light Detoxification and Charge Generation by Transition Metal Chloride Modified Titania". *Chemistry of European Journal,* **6,** 379-384.

257. **Zareie, M.H., B.K. Korbahi** and **A. Tanyolac** (2001) "Non-passivating polymeric Structures in Electrochemical Conversion of Phenol in the Presence of NaCl". *Journal of Hazardous Materials*, **87**, 199-212.

258. **Zaw, M** and **M.T. Emett** (2002) "Arsenic removal from water using advanced oxidation processes". *Toxicology Letters*, **133,** 113-118.

259. **Zhang, Y., M. Yang** and **X. Huang** (2003) "Arsenic (V) removal with a Ce (IV)-doped iron oxide adsorbent". *Chemosphere*, **51**, 945–952.

260. **Zou, Z., J. Ye** and **H. Arakawa** (2001) "Photocatalytic and photophysical properties of a novel series of solid photocatalysts, Bi_2MNbO_7 ($M=Al^{3+}$, Ga^{3+} and In^{3+})". *Chemical Physics Letters,* **333**, 57-62.

LIST OF PUBLICATIONS

PATENT FILED

1 **Viswanath, R.P.** and **M. Sathish** "Divided cell for water electrolysis" A Indian patent has been filed for water electrolysis using a divided cell. 810/Che/2003.

REFEREED JOURNALS

1. **Sathish, M., B. Viswanathan** and **R.P. Viswanath** (2004) "Decontamination of water by photocatalytic means". *Photo/Electrochemistry & photobiology in the Environment, Energy and Fuel*, 1-29

2. **Sathish, M** and **R.P. Viswanath**. (2005) "Electrochemical degradation of aqueous phenol using graphite electrode in a divided electrolytic cell". *Korean Journal of Chemical Engineering*, **22,** 358-363.

3. **Sathish, M., B. Viswanathan, R.P. Viswanath** and **C.S. Gopinath** (2005) "Synthesis, characterization, electronic structure, and photocatalytic activity of nitrogen-doped TiO_2 nanocatalyst". *Chemistry of Materials*, **17,** 6349-6353.

4. **Sathish, M** and **R.P. Viswanath** (2006) "A Novel Electrolytic Cell for Water Electrolysis in Hydrogen Generation". *Preprints- American Chemical Society, Division of Petroleum Chemistry,* **51,** 69-70.

5. **Sathish, M** and **R.P. Viswanath** (2006) "Effect of CdS particle size on the photo generation of hydrogen". *Preprints- American Chemical Society, Division of Petroleum Chemistry,* **51,** 57-60.

6. **Sathish, M., B. Viswanathan** and **R.P. Viswanath** (2006) "Alternate synthetic strategy for the preparation of CdS nanoparticles and its exploitation for water splitting". *International Journal of Hydrogen Energy,* **31,** 891-898.

7. **Sathish, M.**, **B. Viswanathan** and **R.P. Viswanath** (2007) "Influence of hetero-atom doping of TiO_2 nanoparticle on the red shift and the related catalytic activity". *International Journal of Nanoscience, **6**, 137-141*.

8. **Sathish, M., B. Viswanathan** and **R.P. Viswanath** (2007) "Characterization and photocatalytic activity of N-doped TiO_2 prepared by thermal decomposition of Ti–melamine complex". *Applied Catalysis* B, **74,** 308-313.

9. **Sathish, M., M. Sankaran, B. Viswanathan** and **R.P. Viswanath** (2007) "On the position and effect of hetero atom (N or/and S) substitution in TiO_2" *Indian Journal of Chemistry A* (In press).

10. **Sathish, M** and **R.P. Viswanath** (2007) "Photocatalytic generation of hydrogen over mesoporous CdS nanoparticle: effect of particle size, noble metal and support" *Catalysis Today* (Accepted)

11. **Sathish, M** and **R.P. Viswanath** (2007) "Ultrasonic Mediated Synthesis of Mesoporous Crystalline CdS Nanoparticle" *Chemistry Letters* (Accepted)

12. **Sathish, M., R.P. Viswanath** and **C.S. Gopinath**, "Preparation, characterization and photocatalytic activity of visible light active N, S co-doped TiO_2 nanoparticles" *Journal of Physical Chemistry C* (communicated).

PRESENTATIONS IN SYMPOSIUM/CONFERENCE

1. **Thomas, R., K. Mohandoss, P. Wilson, M. Sathish** and **R.P. Viswanath**. "Synthesis and catalytic studies of magnesia supported chromia catalysts derived from sonochemico-aerogel route". 17th National Symposium on Catalysis, Central Salt & Marine Chemicals Research Institute (CSMCRI), Gujarat, January 18-20, 2005.

2. **Sathish, M** and **R.P. Viswanath.** "Electrolytic decomposition of water borne pollutants". International conference on Environment, Ecology & Pollution (Green- Tech-2005) Arunai Engineering College. Thiruvannamalai. January 6-7, 2005.

3. **Sathish, M., B. Viswanathan** and **R.P. Viswanath.** "Template synthesis and photocatalytic activity of CdS nanoparticles". National Seminar on "Applied research on Solid state chemistry and Nanotechnology" NSASN – 2005. Annamalai University. Chidambaram. February 25-26, 2005.

4. **Sathish**, **M.**, **B. Viswanathan** and **R.P. Viswanath.** "Influence of hetero-atom doping of TiO_2 nanoparticle on the red shift and the related catalytic activity". International Conference on Materials for Advanced Technologies (ICMAT-2005) Singapore. July 3-8, 2005.

5. **Sathish, M., B. Viswanathan** and **R.P.Viswanath** "Synthesis, characterization and photocatalytic activity of visible light active N-doped TiO_2". National Workshop on Catalysis for Energy at Banaras Hindu University, Varanasi. February 23-25. 2006.

6. **Viswanath, R.P** and **M Sathish**. "A Novel Electrolytic Cell for Water Electrolysis in Hydrogen Generation". presented in petroleum chemistry division, 231stACS National Meeting at Atlanta, USA from March 26th to 30. 2006.

7. **Viswanath, R.P** and **M. Sathish**. "Effect of CdS particle size on the photo generation of hydrogen". presented in petroleum chemistry division, 231st ACS National Meeting at Atlanta, USA from March 26th to 30. 2006.